Hydrodynamic instabilities of miscible and immiscible magnetic fluids in a Hele-Shaw cell

Maksim Igonin

UNIVERSITÉ PARIS 7 – DENIS DIDEROT
INSTITUT DE PHYSIQUE DE L'UNIVERSITÉ DE LETTONIE

2004/2005 *Numéro attribué par la bibliothèque*

THÈSE

de Doctorat en Cotutelle

pour l'obtention du Diplôme de

DOCTEUR DE L'UNIVERSITÉ PARIS 7
ET DE L'UNIVERSITÉ DE LETTONIE
SPÉCIALITÉ: Physique des liquides

présentée et soutenue publiquement par

Maksim IGONIN

le 29 novembre 2004

Sujet de la thèse :

Instabilités hydrodynamiques des liquides magnétiques miscibles et non miscibles dans une cellule de Hele-Shaw

Jury :

M. Jean-Claude BACRI	Directeur de thèse
M. Andrejs CĒBERS	Directeur de thèse
M. Agris GAILĪTIS	Rapporteur
M. Pascal KUROWSKI	Examinateur
M. Jean-Pierre BRANCHER	Rapporteur

Parīzes 7. Universitāte
Latvijas Universitātes Fizikas Institūts

Maksims IGOŅINS

Samaisošos un nesamaisošos magnētisko šķidrumu hidrodinamiskās nestabilitātes Hele-Šou šūnā

Doktora disertācija

Zinātniskie vadītāji:
Žans-Klods BAKRĪ un Andrejs CĒBERS

University Paris 7 – Denis Diderot
Institute of Physics, University of Latvia

Maksim IGONIN

Hydrodynamic instabilities of miscible and immiscible magnetic fluids in a Hele-Shaw cell

PhD thesis

Supervised by
Jean-Claude BACRI and Andrejs CĒBERS

Acknowledgements

This work *en cotutelle* has been done at the University of Latvia (in the Institute of Physics in Salaspils and at the Chair of theoretical physics) and in the Laboratoire des Milieux Désordonnés et Hétérogènes (Groupe ferrofluide) of the University Paris 6 – Pierre et Marie Curie.

I am indebted to Professor Jean-Pierre Brancher and Professor Agris Gailītis, who did an honour to me agreeing to referee my thesis.

I would like to thank my Latvian supervisor Professor Andrejs Cēbers for suggesting interesting and challenging problems for the thesis. I am grateful to my French supervisor Professor Jean-Claude Bacri for his generous hospitality and patience. My understanding of the subject owes much, of course, to their vast experience gained during decades of a front-line research. It is my pleasure to acknowledge also the attention of Professor Régine Perzynski to my studies and her valuable comments. I appreciate very much the encouragement and support provided by Dr. Martin Devaud and Dr. Sandris Lācis.

I am grateful to Valentin Leroy (and Julie) and to Evelyne Kolb for their help, advice, and for making my studies in Paris particularly pleasant. I thank Gregory Pacitto for showing me what a ferrofluid is and for his help in my desperate attempts to learn some French. For creating a friendly and motivating atmosphere in the Laboratory, I thank also Eric Janiaud, Florence Elias, Florence Gazeau, Claire Wilhelm, Peter Lee, Marcelo Sousa, and many others.

In Riga, I am thankful to Ansis Mežulis for cooperation and for the introduction into experimental techniques. I would like to thank Ivars Driķis for his continuous effort to develop the local computing infrastructure available to colleagues, and for the qualified advice on software. I also thank M. M. Maiorov, G. Kroņkalns, V. A. Ivin, and Andrei for discussions and help.

I owe the debt of sincere gratitude to my teachers in the Moscow Institute of Physics and Technology, my alma mater, for having shaped my mind and having sustained my interest in hydrodynamics.

I gratefully acknowledge the financial support of my studies in France (nine months) by the Embassy of France in Latvia, without which this work would have been impossible. Financial support provided under the EU FP5 project G1MA-CT-2002-04046 (six months of PhD training) is gratefully acknowledged as well.

Above all, I thank my parents for their support, patience, and love.

Contents

Contents **iii**

Introduction **1**

1 Governing equations **4**
1.1 About ferrofluids 4
1.2 Gap-averaging, diffusion, and stresses 5
1.3 The Darcy law and the Brinkman equation 13
1.4 Magnetic ponderomotive force 19

2 Stability of a miscible interface **24**
2.1 Miscible interfaces in a Hele-Shaw cell 24
2.2 Miscible problem and continuous spectrum 27
2.3 Labyrinthine instability 33
2.3.1 Derivation of the dispersion relation 34
2.3.2 Stability diagram and asymptotic analysis 38
2.3.3 Physical mechanism of oscillations 44
2.3.4 Labyrinthine instability of a diffused interface 48
2.4 Peak instability in a Hele-Shaw cell 57
2.4.1 Perturbations and sharp interface: normal field 58
2.4.2 A periodic stripe pattern in the normal field. 62
2.4.3 A diffused interface in the normal field 65
2.4.4 A comparison to FRS experiments 70

3 ST instability with an immiscible MF **73**
3.1 The free-boundary problem 73
3.1.1 The context of the problem 73
3.1.2 Formulation of the problem 76
3.1.3 Alternative formulations 81
3.1.4 Integral equation 83
3.1.5 Magnetic force and finger 86

3.2 The numerical method 90
3.2.1 Modelling with BIE 90
3.2.2 Interface and curvature 97
3.2.3 Discretization of integrals 101
3.2.4 Characterization and validation 105
3.3 Numerical results for the perpendicular field 112
3.3.1 Magnetic Saffman–Taylor fingers 112
3.3.2 Dendritic patterns 126
3.4 Numerical results for the normal field 138

Conclusion **144**

List of Figures **146**

List of Tables **148**

Bibliography **149**

Introduction

The work treats theoretically the dynamics of magnetic fluids in a Hele-Shaw cell.

As the magnetic fluid (MF, or a ferrofluid) is a suspension of magnetic nanoparticles in a carrier liquid, its nature is twofold. On the one hand, it is a fluid with peculiar body and interfacial forces acting upon it; on the other hand, diverse diffusion phenomena occur in magnetic colloids. In some situations it is possible that both qualities come into play. Namely, the particle ensemble subjected to a macroscopically non-potential force can entrain the carrier liquid, thus exciting a convective instability. The applied field being uniform, the instability is due to the self-magnetic (demagnetizing) field of an inhomogeneous ferrofluid: a "superparamagnetic" MF parcel is entrained into a stronger resulting field, i.e. where the demagnetizing influence of the MF sample diminishes. Advection by the MF motion and diffusion redistribute the particles and, in their turn, affect the self-magnetic field.

In a thin plane layer with rigid transparent walls (a Hele-Shaw cell), miscible instabilities with MF's can be observed directly (with a microscope). In the field applied perpendicularly to the cell, an intricate labyrinthine pattern (Fig. 1) developed [1] at a narrow straight "diffusion front" between MF and its pure carrier liquid. A peak pattern was observed for another field orientation. The pattern length scale was approximately as small as the layer thickness (less than 10^{-2} cm). Having formed rapidly, both patterns were gradually blurred out by diffusion.

In the forced Rayleigh scattering experiments [2] with transient optical gratings induced in thin MF layers, very recently reported was the first experimental evidence of a microconvection [3]. That the subject requires investigation is further exemplified by the controversy [4] around the nature of the effects observed in a MF layer heated by a perpendicular laser beam.

We cautiously adopt the approach of averaging across the gap in our work. We note that even the linear stability of miscible interfaces was almost unexplored until recently. However, a careful analysis of this sort can reveal a lot. In many known miscible and immiscible instabilities in a Hele-

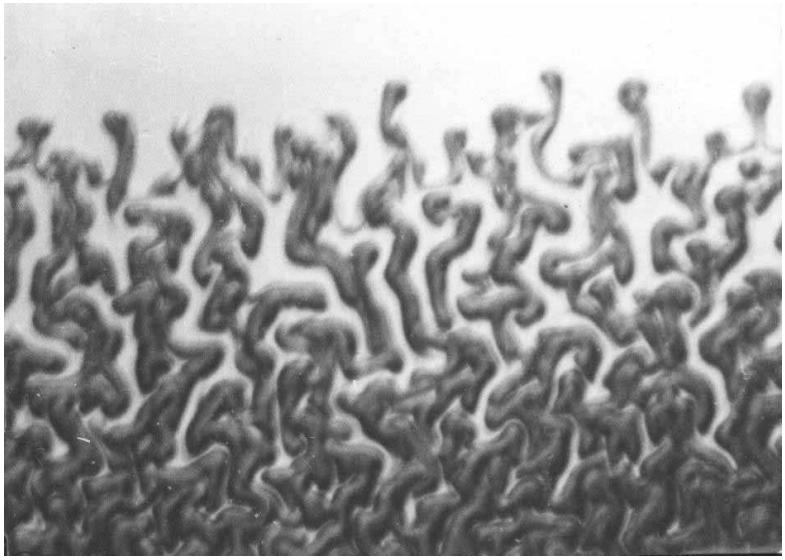

Figure 1: Magnetic microconvection on a diffused interface (top view of the cell). Courtesy of M. M. Maiorov and A. Cēbers. See [1] for details.

Shaw cell, the driving force is such that the shortest wavelengths are the most amplified, and other effects regularize the problem. What selects a finite length scale at the interface? A common opinion is that diffusion and surface tension prevent small-scale perturbations from growing. As we will demonstrate, at strong forcing the length is comparable to the gap thickness and cannot decrease, for which responsible is the viscous dissipation that is usually treated incompletely in the Hele-Shaw flow because of the Darcy approximation. Interfaces between *magnetic* fluids are especially sensitive to the thickness of the cell. The reason is that the self-magnetic field and the inhomogeneous force it causes translate the transverse dimension into the plane of the Hele-Shaw cell.

This is why the convection in a thin MF layer typically occurs on a microscale. Hereby the above-mentioned convective instabilities [1] leading quickly to a highly intricate patterns (Fig. 1) can drastically increase the length of the interface between miscible MF's. By exciting a microconvection, an external field thus allows to importantly enhance mixing inside the sample. Let us recall now that the simple and convenient configuration of a Hele-Shaw cell is ubiquitous both in experimentation and technology (by the way, ferroparticles can be functionalized, drug-loaded, etc.). However, the flows in a Hele-Shaw cell are viscosity dominated and therefore laminar and difficult to mix. Being quite important in technological applications, laminar mixing on a microscale is a subject of intensive research in what is currently known

as *"microfluidics"* [5].

Until recently, in studies of interfacial instabilities in Hele-Shaw cells immiscible magnetic fluids forming sharp, well-defined interfaces were a subject of theoretical analysis (e.g. [6]) and experimental treatment (e.g. [7]). However, the notions of the miscible "interface" and the true immiscible one turn out to be not completely antagonistic. Under discussion [8, 9] is the role of the non-conventional Korteweg stresses that emerge at high concentration gradients and reduce to the classical surface tension in the limit of vanishing interface thickness. Although our particular results do not concern this issue, important analogy between the miscible and immiscible interfaces should indeed take place and be traceable.

In the second half of our study, we model the non-linear dynamics of *immiscible* MF interfaces in the same configuration as before. This is the classical problem [10] modified by the presence of a magnetostatic force due to the self-magnetic field of a ferrofluid. Historically, the interest to the original problem of "viscous fingering" was motivated by its relation to the oil-extraction process. Later (in 1980's), it proved to be interesting in its own right for both physicists and mathematicians, for the interface was observed to form beautiful complex patterns. The Hele-Shaw flow is currently recognized as the simplest physical process capable of pattern formation [11]. In ferrofluids, the evolving patterns are modified substantially by the long-range magnetostatic repulsion to become interesting "dendritic" structures [12, 7], different from both the viscous fingers and the crystalline dendrites. Theoretically, some of their features can be explained using the notion of the effective surface tension [6, 13]. Nevertheless, numerical modelling is indispensable for providing a complete understanding of the process. Efficient modelling in the Darcy approximation is possible owing to the fact that the immiscible problem can be rendered one-dimensional in effect, and we describe the corresponding computational techniques. Of course, in a system that complex, it is difficult even to pose a question that can be answered, but we have made a try to get some insight into the physics.

Chapter 1

Governing equations

1.1 About ferrofluids

The particular subject of the present work is a magnetic fluid (MF, also known as ferrofluid). For a general reference on MF's, see [14, 15]. Here we give only a superficial account of some most basic ideas.

Conceptually, ferrofluid is a colloidal suspension of magnetic particles. In order to prevent the dipolar particles from agglomeration, the energy of their dipole-dipole interaction should not exceed the thermal one, for which the particles should be small enough. The upper bound for particle sizes is of the order of 10 nm, so that the volume of a particle is a single magnetic domain. Besides, as in any colloid, the van der Waals attraction should be counteracted, which is achieved by adsorbing either a surfactant coat (the steric stabilization), or ions of the same sign (the charge stabilization) on the surface of a particle. For details, see texts on the physical chemistry of colloids. The size of a particle should not be too small, however, to facilitate the preparation and to have an acceptable magnetic susceptibility. Sometimes we will distinguish between the magnetic and hydrodynamic radii of a particle; the latter is somewhat higher because the surface layer of the material is non-magnetic, and besides, particles can be coated with a surfactant.

Being both a magnetic media and a fluid, MF can exhibit peculiar features not known for other existing materials. Thus, its free horizontal surface in a (strong enough) perpendicular magnetic field undergoes the static "peak" instability. The peaks form either a hexagonal or square lattice [14, 15], which was a subject of intensive theoretical analysis [16]. The known fluid-mechanical instabilities are also modified in the case of magnetized ferrofluids, as we will see. One more peculiarity is associated with the possibility to materialize, by ferrofluids in rapidly rotating fields, the hydrodynamics "with

a spin" (or internal rotations), when the stress tensor is non-symmetric. The reason is that the magnetization of a particle requires certain time to align with the applied field, either by rotating with respect to the material of the particle, or by rotating the particle as a whole in the viscous fluid. We, however, will be dealing solely with a quasi-static field.

We will not give any further generalities on magnetic fluids. We mention now only some facts that are of immediate relevance to our subject. (Later some more information about ferrofluids will also be given.)

The field interacts with MF through the magnetic ponderomotive force. (The force will be addressed in detail in §1.4.) Now consider the fact the force, in fact, acts upon the particles. A particle moves with some velocity relative to the carrier liquid, and the Stokes drag on it equals, on the average, the force exerted upon the particle. However, the particles can also drive the carrier, in which case an overall MF flow results. Its velocity is determined by the friction at the walls of the cell (according to the Darcy law, §1.3). The friction experienced by a given MF volume at the walls is (more or less) balanced by the force that all particles in the volume exert on the carrier. It gives the ratio of two velocities: the one of MF relative to the walls and the one of particles relative to the carrier. The ratio is very large unless the concentration is very low. Specifically, for the magnetophoretic particle transport to be neglected with respect to the advective one, the condition

$$\varphi \gg (a/h)^2 \tag{1.1}$$

must hold [17], where a is the average radius of a particle, φ is the volume fraction of the suspended matter, and h is the gap spacing. Obviously, the condition is not restrictive at all, given the concentration of normally employed ferrofluids. The estimate is only a necessary condition since it assumes that the force on magnetic particles entrains MF, for which it must be non-potential. Otherwise, the pressure gradient can counter-balance the particle force, which is the case, by the way, for the one-dimensional MF concentration distributions whose stability (against two-dimensional convection) we will analyze later (§§2.3, 2.4). Nevertheless, in the present study the magnetodiffusion will not be taken into account.

1.2 Gap-averaging, diffusion, Korteweg stresses

In this paragraph we will discuss the process of mixing by diffusion in a Hele-Shaw geometry. This material refers to general miscible fluids.

Let us consider the Brownian diffusion of ferromagnetic particles in MF. The velocity $\vec{v}$ will be that of the center of mass of the suspension (i.e. of

MF as a whole). Then for the velocity the equation of continuity holds

$$\partial\rho/\partial t + \operatorname{div}(\rho\vec{v}) = 0\,, \tag{1.2}$$

ρ being the density of MF, and the momentum equation (see §1.3 later) can be written down for the mixture in the same form as it is for a single fluid (Chapter VI of [18]). In addition, the conservation of species gives

$$\partial(\rho C)/\partial t + \operatorname{div}(\rho C\vec{v}) + \operatorname{div}\vec{\jmath} = 0\,,$$

where C is the mass fraction of magnetic particles, $\vec{\jmath}$ is the density of the diffusive mass flux associated with the diffusive fluxes $\vec{\jmath}_0$, $\vec{\jmath}_1$ of the carrier liquid and magnetic particles, respectively, [18]. Then

$$\mathrm{d}c/\mathrm{d}t + c\,\operatorname{div}\vec{v} + (1/m_{\mathrm{p}})\operatorname{div}\vec{\jmath} = 0\,, \tag{1.3}$$

where c is the number of magnetic particles per unit volume, and m_{p} is the mass of a particle. It is reasonable to assume that the density ρ of MF varies linearly with c (a "simple mixture"):

$$\rho(c) = \rho_0\left(1 + \frac{c}{c^*}\right)\,,$$

where ρ_0, ρ_1 are the densities of the carrier liquid and the magnetic material, respectively, and

$$\frac{1}{c^*} = m_{\mathrm{p}}\left(\frac{1}{\rho_0} - \frac{1}{\rho_1}\right)\,.$$

(I.e. by introducing a particle into a certain volume, the mass of the volume increases by $\mathrm{d}\rho/\mathrm{d}n = V_{\mathrm{p}}(\rho_1 - \rho_0)$, V_{p} being the volume of a particle.) Then from Eq.(1.2) it follows that

$$\mathrm{d}c/\mathrm{d}t + (c + c^*)\operatorname{div}\vec{v} = 0\,.$$

Finally, comparing with Eq.(1.3), we obtain

$$\operatorname{div}\vec{v} = \left(\frac{1}{\rho_0} - \frac{1}{\rho_1}\right)\operatorname{div}\vec{\jmath}. \tag{1.4}$$

Thus a very basic argument, involving only conservation laws and a simple $\rho(c)$ dependence, reveals an obvious but usually forgotten fact that even if both components of a flowing inhomogeneous mixture are incompressible, the mass-averaged flow velocity does not satisfy $\operatorname{div}\vec{v} = 0$. (In the present context, the mixture is called "incompressible" if the density of none of the

constituents varies with pressure.) The velocity is divergence-free (solenoidal) only if the densities ρ_0 and ρ_1 are equal.

Nevertheless, we still will assume that variations in the particle concentration throughout MF result in a negligible change in the density. Putting $\operatorname{div}\vec{v}=0$ leads to a considerable simplification of the further analysis.

Among several variables any of which can describe the composition of a mixture (such as the mass or molar concentration, volume fraction, etc.), it is the mass fraction C that is associated to our reference frame of the center of mass (§§4.3, 4.17 of [19]). The first Fick's law introduces the diffusion coefficient D in the usual way if the fluxes (taken relative to our reference frame) are expressed through C: $\operatorname{div}\vec{\jmath}=-\rho D\vec{\nabla}C$. (However, the range of validity of the first Fick's law remains unclear to us.) But in dilute ferrofluids, and since the density difference will anyway be neglected, the composition variables are interchangeable, e.g. we can write the equations in terms of the volumic molar concentration c (i.e. the number of particles per unit volume, as defined above). The incurred error will be indeed negligible. For example, from Eqs.(1.3), (1.4) we have

$$\frac{\mathrm{d}c}{\mathrm{d}t}+\frac{1}{m_\mathrm{p}}\left[1+\varphi\left(\frac{\rho_1}{\rho_0}-1\right)\right]\operatorname{div}\vec{\jmath}=0\,, \tag{1.5}$$

which simplifies to the standard convection–diffusion equation

$$\frac{\mathrm{d}c}{\mathrm{d}t}+\frac{1}{m_\mathrm{p}}\operatorname{div}\vec{\jmath}=0$$

if the ferrofluid is dilute enough:

$$\frac{1}{\varphi}\gg\frac{\rho_1}{\rho_0}-1\,. \tag{1.6}$$

Of course, the *volume*-averaged velocity is solenoidal without any approximations, as noted in [20, 21]. As the Hele-Shaw flow that will be of interest to us is free from inertia, it may seem appealing to reformulate the problem in terms of the volume-averaged velocity. However, the advantage is quite illusory. For example, the correct boundary conditions for mixtures are not known as yet [22]. (The no-slip of which velocity holds?) This uncertainty affects the friction term involving velocity in the averaged equations of motion (§1.3). So one anyway resorts to approximations of the above sort.

That the assumption $\operatorname{div}\vec{v}=0$ is generally wrong for mixtures and, in particular, for miscible fluids, was studied extensively by D. D. Joseph with collaborators. (Our simple Eq.(1.4) is essentially Eq.(2.30) of [23].) Another closely related issue are the so-called gradient stresses that may arise in

the regions of high concentration and density (not present in the Navier–Stokes stress tensor of a Newtonian fluid). In the work [24] the history of the subject is presented over more than a century with many excerpts and experimental illustrations. It appears that many researchers recognized the existence of what can phenomenologically be described as a transient surface tension at the miscible "interface." Back in 1901, Korteweg composed a general stress tensor for compressible and incompressible fluids and showed that it leads to boundary conditions mimicing those at a curved interface with surface tension. This "capillary" tensor is a second order tensor composed non-linearly of the first and second gradients of density and/or concentration; for details, see the works cited below. In [25], by introducing a modified velocity that turns out to be divergence-free, the momentum equation is represented in the form of the Navier–Stokes equation with two viscosities, a non-trivial driving force, and a modified pressure (a conventional one plus a "concentration pressure"). Under some assumptions (of constant coefficients), four of the five Korteweg coefficients entering the stress tensor effectively drop out. Non-linear stability of a vertically stratified fluid is analyzed by energy methods. It is suggested that the Taylor dispersion problem (see below) and the Hele-Shaw problems with miscible fluids be reworked to take the gradient stresses and the non-solenoidality into account. The Hele-Shaw case is indeed investigated in [20], where a linear analysis of a Rayleigh–Taylor instability is carried out. The effect of $\operatorname{div} \vec{v} \neq 0$ proved to be minor if the diffusion coefficient is small. The step-like concentration distribution in the Hele-Shaw geometry does not evolve into the one-dimensional error-function one if the non-solenoidal velocity due to mixing is taken into account [22]. In [25, 20] some constraints are obtained on the coefficients appearing in the Korteweg stress tensor to avoid, on the one hand, the ill-posedness and, on the other hand, an unconditional non-linear stability. Let us note that even the signs of the Korteweg coefficients are not yet established, although the order of magnitude of the transient surface tension is more or less clear from experiments, [24]. In [23], the (in-)validity of putting $\operatorname{div} \vec{v} = 0$ is discussed further. The pressure difference across a plane mixing layer is found to be zero even allowing for the Korteweg stresses; the diffusion in a pipe is also considered. For the spherical diffusion fronts, the $t^{-1/2}$ scaling is obtained.

In a review [8], the diffuse-interface models are presented in several situations. For a single-component fluid, of interest can be the behaviour near a critical point (that the interface thickness grows without bound was shown already by van der Waals with a simpler model) or at the contact line (as of a droplet creeping along the wall). For the binary fluid, the modified Cahn–Hilliard equation enters the governing equations, the spinodal decomposition being a typical application. Interestingly, the question about the

non-solenoidality of the velocity arises in this context as well and has strong consequences: it is argued by some authors that the thermodynamical role of pressure changes. It is also demonstrated how the classical Laplace–Young condition with a variable surface tension is recovered in the sharp-interface limit.[1] (See also [26].) The work also identifies some "subtle differences" between the applicable models. Another important point elucidated in [8] is the connection between the Korteweg stress tensor and the Cahn–Hilliard term in the density of the free energy $f = f_0(c, T, \ldots) + \beta(\vec{\nabla} c)^2$ [this is a spatial development of f; the shape of $f_0(c, \ldots)$ is responsible for the (im-) miscibility]. In [27, 28], the diffuse-interface models are also reviewed. For a Hele-Shaw flow, the Hele-Shaw–Cahn–Hilliard model (HSCH) is analyzed in particular. The average velocity being non-solenoidal is taken into account, non-conventional stresses enter the Darcy equation (§1.3), and the concentration is governed by the Cahn–Hilliard equation that becomes the convection–diffusion equation (CDE) in the limit of a slow concentration variation. (Note that Joseph *et al.* use CDE in the above-cited works.)

Above we have discussed the still somewhat exotic Korteweg stresses. The classical approach due to Taylor, however, would be to treat the particles as a passive scalar, i.e. as an admixture having no influence on the flow. This results in the convection–diffusion equation for the velocity and concentration averaged across the flow, but with an effective diffusion coefficient D_{eff} that exceeds the molecular one D: for a capillary tube [29], $D_{\text{eff}} - D = (Ur)^2/(48D)$, where U is the average velocity and r is the radius, while for a Hele-Shaw cell of a thickness h the result is $D_{\text{eff}} - D = (Uh)^2/(210D)$. The higher the diffusivity, the lower the difference, since the diffusion spreads the scalar away from the center into the near-wall region of low advection velocity. However, normally the fluid viscosity is strongly concentration dependent.

At this point we would like to present a brief overview of the past theoretical work on miscible flows in a Hele-Shaw cell and porous media. (See the next paragraph on the relation between the two types of flow. The mechanical dispersion is the porous-media counterpart of the diffusion in a Hele-Shaw cell.) A review of the early results can be found in [30]. We would note in particular the asymptotic stability analysis of [31] of a vertical miscible displacement and the study [32] (discussed later on p. 17). Much of the research concentrated around the porous-media flow. The work [33] became seminal for much of the research that followed. There, a popular approximate framework (so-called QSSA, also of use in the present work, see p. 27)

[1] As the second part of the present work concerns immiscible ferrofluids, the Korteweg stresses could serve as a common basis for the whole work.

for the stability analysis of time-dependent flows with diffusion (dispersion) is established. It is partially validated by the comparison to the solution of the initial-value stability problem (§2.2). The anisotropy of the dispersion is taken into account in [33]. The radial geometry is analyzed in [34]. Velocity-dependent dispersion is found to have a destabilizing effect in [35]. An asymptotic solution for thin diffused interfaces (but still with QSSA) is found. It is stated explicitly that the sharp-interface stability result depends on the jump of the concentration derivative of the viscosity rather than on the jump in viscosity (the latter is the case for an immiscible interface). The conditions are found at which there is no short-wave cutoff (i.e. however large the wavenumbers, they all are unstable despite the transversal dispersion). In [36, 37], the gravity effect is in addition taken into account, the density of the fluid being an arbitrary function of the concentration; the dispersion is considered an arbitrary function of velocity. In [37] the cross-over between the diffusive regime (no instability) and the convective one (fingers) is traced experimentally. The presence of a tangential velocity discontinuous at the interface is found to stabilize the displacement in the presence of gravity in [38]. In [39] the effect of the non-monotonic concentration–viscosity dependence ("profile"), such as that of a water solution of propanols, is investigated. At some conditions, the diffusive smearing of a stable basic state can render it unstable. Asymptotic analysis of [35] for almost sharp interfaces is extended for any concentration–viscosity dependence. However, this work is also important for stressing the presence of the continuous spectrum in the stability problem (we will develop this subject in §2.2). Identified is the physical reason why it is the concentration derivative of the viscosity, and not the viscosity itself, that determines stability. In this regard, let us note that in the review [30] referenced above, the viscosity difference (in the form of the viscosity Atwood ratio, Eq.(3.18)) is erroneously listed among the parameters that determine stability. In [21] the conditions for the equivalence of the flow under gravity, on the one hand, and by displacement, on the other, are established with respect to the concentration dependence of viscosity and density. (Note that with immiscible interfaces, the two flows are equivalent, see references in [21] and, for the flow in a Hele-Shaw cell, see §3.1.2.) Numerical simulations are presented e.g. in [40, 21, 41]. The above studies mainly concern the porous-media flows. The interest to the Hele-Shaw miscible flow as such was sporadic ([42, 32, 20]) until the late 1990's.

At the moment, the miscible interfaces are a subject of growing interest, as exemplified by [9]. In [43] (extended in [44]), miscible displacements are studied experimentally in capillaries. If the finger of the less-viscous displacing fluid, whose thickness is the main concern of the work, occupies more than half of the cross-section of the capillary, a thin spike (needle) is observed

to grow from its tip. (The intruding finger exists at large Péclet numbers $\mathrm{Pe} = Uh/D$ and for a finite time because of mixing; U is e.g. the average displacement velocity.) The flow structure (recirculations) giving rise to the spike is investigated (Fig. 12 of [43]). In the accompanying numerical study [45], where a constant diffusion coefficient, the linear concentration–density dependence, and the exponential concentration–viscosity one are assumed, an analogous protrusion is obtained in simulations for the geometry of a Hele-Shaw cell as well. In this work, a noteworthy argument is presented that, contrary to intuition and if viscosity is concentration dependent, the conventional viscous stresses can mask the velocity-independent Korteweg stresses at *high* Péclet numbers. The numerical analysis is extended to include the new effects in [46], where it was found that taking the Korteweg stresses, but not the velocity non-solenoidality, into account allows to reproduce the experimental observations. The results of simulations by a different numerical technique [47] are in good agreement with [45] (under the same assumptions, but at no gravity). The Stokes [45] or even Navier-Stokes [47] equations are used in these simulations of a Hele-Shaw flow; see [48, 28] for the numerical modelling of the gap-averaged Darcy flow with the Korteweg stresses. Apart from the above-cited earlier works (see [24] and references therein), many attempts are made to conduct, with miscible fluids, the classical experiments known for the immiscible case, with the aim to establish the effective surface tension. Thus, Rayleigh–Taylor fingers, drop formation, and other phenomena with miscible interfaces are analysed in [49]. The interfaces vibrated horizontally or vertically and the known interfacial singularity above a pair of horizontal parallel immersed counter-rotating cylinders, are carefully studied experimentally [50, 51] in the miscible case. Direct measurements of the effective surface tension are also done [52].

For the concentration-dependent fluid viscosity, when the velocity profile at displacement deviates from parabolic, an asymptotic integro-differential equation is obtained for the velocity in [53] by making use of the small ratio of the gap width to the extension of the mixing region along the cell. At finite Péclet numbers, having adopted the "quarter-power" concentration–viscosity dependence and constant diffusivity, they [53] study the distribution of the concentration across the cell at various viscosity ratios. It is established that if $\mathrm{Pe} \lesssim 10\delta$, then the angle between the isolines of concentration and the normal to the cell will not exceed $\delta \ll 1$. In the limit of zero diffusion, regardless of the (monotonic, however) concentration–viscosity relation, the gap-averaged concentration develops a "shock," i.e. at the tip of the tongue its thickness changes abruptly to zero, which possibility is noted already in [42]. The necessary condition for this not to happen is that $M < 3/2$, where M is the ratio of displaced fluid's viscosity to that of the injected fluid. The

asymptotic analysis is checked against the simulations [47, 46].

In an experimental study [54] of a miscible Saffman–Taylor instability in a vertical Hele-Shaw cell, the theory [53] finds an unexpected outcome. The experiment is conducted with the heavier fluid resting below the lighter one, which stabilizes the interface at no displacement. Then the upper fluid is pumped into the gap, and a downward displacement occurs. The heavier fluid is also the more viscous one. The Péclet number is quite high, $> 10^4$, so that the diffusion can be neglected. If M exceeds ≈ 2 and, in addition, if the non-dimensional injection rate is above critical $U_{\rm c}(M)$ [$U_{\rm c}(M)$ decreases with M], then the horizontal, in the plane of the cell, uniformity of the displacement gets broken, and thin jets of the lower fluid divide the falling one into plane fingers. The width of the fingers is found to be $\approx 5h$ (see the next paragraph on what we believe is the reason for this relation), and they resemble in shape the "deep cells" occurring at directional solidification of binary liquids (e.g. [55]). The distribution of the gap-averaged concentration c of the upper fluid is recorded in [54]. Obviously, c gives also the thickness of the downward tongue. After short transients, the concentration field propagates downwards in a self-similar manner and in some cases indeed decreases in a non-smooth manner along the vertical. Found in [54] is an unexpected relation between the occurrence of the fingering in the plane of the cell and the occurrence of the shock at the vertical c curve (i.e. of the jump in the tongue thickness measured across the gap). Namely, the fingering instability sets in if, and only if, the tongue thickness abruptly goes to *zero* (a "frontal" shock). Thus, the flow in the perpendicular direction remains uniform if the thickness varies smoothly downwards or if it changes abruptly, but to a non-zero value (an "internal" shock). The latter case refers to the protrusion simulated numerically in [45]. In [56] the theory of [53] is extended to include the buoyancy effects. A theoretical diagram in M–U coordinates is delineated which distinguishes between the three cases. The diagram shows a satisfactory agreement with the experimental data. However, the origin of the correlation between the shape of the concentration isolines in the vertical perpendicular section of the cell and the onset of convection in the plane of the cell remains practically unexplained; a three-dimensional stability analysis is required to understand the instability. Using some experimental relations, an ad-hoc analysis is attempted in their later note [57].

As for the object of our study, although we routinely call it a "miscible magnetic fluid" ("miscible" in all proportions), it is essentially a single fluid with an inhomogeneous concentration of suspended ferroparticles. The surface-tension-like effects are due to attractive dipole–dipole particle interactions at concentration gradients and discontinuities. The same effects are in operation at field-induced phase separation of MF's in thin layers at a

diffused boundary between the concentrated and dilute MF phases (see e.g. [58, 59, 60, 61, 62, 63, 64]). In [58, 65, 66] a general model of magnetic suspensions is developed where the free energy of the suspension contains the Cahn–Hilliard term. However, we will eventually adopt the simplest MF model in which interparticle interactions are neglected. Hence it would be inconsequent to take the Korteweg stresses into account and, at the same time, use the Langevin law for the MF magnetization. Very recently, a miscible radial gap-averaged MF flow in the perpendicular field was simulated with the Korteweg stresses [67]; for the same problem simulated without them, see [68]. The subject of these works is particularly close to ours. Now the lack of the quantitative experimental data for ferrofluids becomes apparent.

As this paragraph has shown, the common reduction of the problem to a two-dimensional one by averaging the concentration and the assumed Poiseuille velocity profile across the gap simplifies the analysis at the cost of leaving possibly important effects out of account. The suspended particles can be a "very active" scalar. In our further analysis, we will put aside non-conventional Korteweg stresses, neglect the Taylor dispersion, and in most cases we will neglect the concentration dependence of the viscosity; D will be a constant isotropic diffusion coefficient. Thus, analyzing a miscible Hele-Shaw flow in a technically tractable way and interpreting the results of such analysis requires known caution for the reasons clear from the above exposition. In the next paragraph we will consider the conventional viscous stresses; even their treatment in the Hele-Shaw context is commonly incomplete, but our results will prove the necessity to take them fully into account. So, having said all the above, we eventually adopt for the concentration the simplest CDE with the gap-averaged variables and the solenoidal average velocity field.[2]

1.3 The Darcy law and the Brinkman equation for a Hele-Shaw flow

Let us consider an incompressible fluid of a constant viscosity η flowing between parallel plates at a velocity $\vec{v} = (v_x, v_y, v_z)$, the plates being $z = \pm h/2$. It is well-known and simple to check that the equations $v_y = v_z = 0$,

$$v_x(z) = -\frac{1}{2\eta}\frac{\mathrm{d}p}{\mathrm{d}x}\left(\frac{h^2}{4} - z^2\right), \tag{1.7}$$

[2] "Presumably the practitioners of these arts know what they are doing and recognize that they are making an approximation ..." (D. D. Joseph, [23].)

describe the planar Poiseuille flow driven by a constant pressure gradient $\mathrm{d}p/\mathrm{d}x$. At any gradient, this is a solution to the full stationary Navier–Stokes equations (NSE) with the no-slip conditions at the plates (we lay aside the question of its stability).

Now imagine that the flow for some reason is not unidirectional. The exact solution becomes prohibitively complicated, if feasible at all, because of the non-linear term in NSE. However, at low enough velocity the term is negligible throughout the entire flow domain (§2.7 of [69]), so that NSE simplifies to the linear Stokes equation:

$$-\vec{\nabla}p + \eta\Delta\vec{v} = 0\,. \tag{1.8}$$

With some reservations, this equation admits an important reduction that we are going to describe now.

Consider a flow that approaches the Poiseuille one at infinity. Let us try the possibility of the same kind of z dependence in the entire flow domain:

$$\begin{aligned} v_x &= \frac{6}{h^2}\left(\frac{h^2}{4} - z^2\right) u_x(x,y)\,, \\ v_y &= \frac{6}{h^2}\left(\frac{h^2}{4} - z^2\right) u_y(x,y)\,, \end{aligned} \tag{1.9}$$

where the coefficient is so chosen that $\vec{u}$ is the z-averaged velocity (v_x, v_y). In addition, let us demand that

$$\operatorname{div}_\perp \vec{u} = 0\,, \quad \vec{u} = \vec{\nabla}_\perp\phi\,, \tag{1.10}$$

where $\phi(x,y)$ is some sufficiently smooth function, and the index "$\perp$" refers to an operator in two dimensions x, y. Physically, the assumption is that the flow responds to the local pressure gradient as if it were globally constant. Then by the continuity

$$0 = \operatorname{div}\vec{v} = \frac{6}{h^2}\left(\frac{h^2}{4} - z^2\right)\operatorname{div}_\perp\vec{u} + \frac{\partial v_z}{\partial z}$$

we have $v_z = 0$, and $p = \mathrm{inv}(z)$ from Eq.(1.8). Substituting Eq.(1.9) into Eq.(1.8), we obtain

$$-\frac{\partial p}{\partial x} + \frac{6\eta}{h^2}\left(\frac{h^2}{4} - z^2\right)\Delta_\perp u_x - \frac{12\eta}{h^2}\,u_x = 0\,, \tag{1.11}$$

and analogously for $\partial p/\partial y$, u_y. The term in the middle vanishes, for Eqs.(1.10) lead to $\Delta_\perp u_x = \Delta_\perp u_y = 0$. Thus,

$$\begin{aligned} -\frac{\partial p}{\partial x} - \frac{12\eta}{h^2}\,u_x &= 0\,, \\ -\frac{\partial p}{\partial y} - \frac{12\eta}{h^2}\,u_y &= 0\,. \end{aligned} \tag{1.12}$$

It is remarkable that the pressure gradients are indeed independent of z. Besides, this relation proves that $\vec{u}$ can be potential.

We have demonstrated that Eqs.(1.9), (1.10) solve the incompressible Stokes equation (1.8). A z-independent potential force density can be added to Eq.(1.8) and absorbed into the pressure gradient, changing nothing in the analysis. Essentially, we have found that with such driving force, a three-dimensional *laterally unbounded* flow exactly reduces, by the substitution (1.9), to a two-dimensional one at a gap-averaged velocity. The unboundedness is essential for the following reason. Imagine a cylindric obstacle situated between the plates perpendicularly to them, filling the gap entirely; at the boundary of the obstacle some conditions are posed in terms of the velocity $\vec{v}$ (§4.8 of [70]). Then, apart from reducing the number of dimensions, the substitution also effectively reduces the order of the differential equation. Not all boundary conditions posed for the Stokes equation (1.8) can be satisfied at solving the reduced Eq.(1.10). (The exact analogy can also break at free surfaces and discontinuities.) The no-flux (non-permeability) condition can be satisfied, but not together with the no-slip condition. However, the flow "feels" the presence of the no-slip condition only within a thin belt of thickness $\sim h$ around the obstacle. Indeed, if v_x and v_y are required to vanish at the boundary as well as at the plates, their second derivatives in Eq.(1.8) across the gap and along the plates can be estimated to relate as $(l/h)^2$, where l is a distance from the boundary. Therefore at $l \gg h$ the boundary condition has no impact on the pressure gradient and, by Eq.(1.12), on velocity. The same result is valid near the lateral sides of a Hele-Shaw cell [71].

Eq.(1.12) for the gap-averaged velocity is exactly (to within the coefficient) a two-dimensional version of the Darcy law that is widely used to describe, at coarse enough scales, the groundwater flow [72] in porous media with permeability $\alpha = 12\eta/h^2$ (we will call it the friction coefficient). Due to this direct analogy, the Hele-Shaw device (cell) was often employed to model the percolation processes. However, originally it was introduced by H. J. S. Hele-Shaw back in 1898 to model steady two-dimensional incompressible potential inviscid flows around various obstacles (§330 of [73]; see photos in [74]). At a sufficiently narrow separation between the plates (compared to the dimensions L of the obstacle in the x, y plane, $L \gg h$), the difference in the boundary conditions is negligible and the above approach can indeed be reverted. Of course, the pressure p of the Hele-Shaw flow will have nothing in common with the pressure $p_{\rm iv}$ of the inviscid flow (see §3.9 in [75]) that is calculated from the velocity through a non-linear relation:

$$\rho(\vec{u}\cdot\vec{\nabla})\vec{u} = -\vec{\nabla}p_{\rm iv}\,,$$

ρ being the density. Phenomena such as a flow with non-zero circulation

around the obstacle (i.e. with a multiple-valued potential) and flow detachment cannot be reproduced in a Hele-Shaw cell (§3.9 of [75], §4.8 of [70]). About a century ago, A. N. Krylov suggested to use the device to model stresses in 2D elasticity problems arising in shipbuilding, while Hele-Shaw himself employed the device to solve some potential problems in electrodynamics.

As for the criterion to neglect inertia in NSE, a simple comparison of the non-linear term in NSE against the friction at the plates in Eq.(1.12) gives $\mathrm{Re}^* \ll 1$, where Re^* is the "reduced" Reynolds number calculated with h^2/L as the length scale [76, 70]. Another issue regarding the validity of Eq.(1.12) is the possibility to omit the non-stationary term $\rho\,\partial\vec{u}/\partial t$ (or $\rho\,\partial\vec{v}/\partial t$ in NSE) while preserving the $\partial c/\partial t$ term in the convection–diffusion equation. It is not difficult to retain both and solve, e.g., the stability problem. Then it turns out that the reverse time scale of the flow (e.g. the instability growth increment) λ must remain sufficiently small in the sense that $\lambda\rho_0 \ll \alpha$, i.e. $\lambda h^2/D \ll \eta/(\rho D) = \mathrm{Sc}$ (the Schmidt number Sc is of the order of 10^7 in the typical case). Such rapid processes are of no interest for us. Were λ not small, the non-stationary term $\partial\vec{u}/\partial t$ would become significant, and besides, the vorticity would have no time to diffuse in the transverse direction to form the stationary velocity profile.

What happens at a general driving force not satisfying the above conditions – at a non-potential and/or z-dependent one? Then the reduction does not take place. For example, if the force is z-independent but non-potential, neither is the average velocity $\vec{u}$, cf. Eq.(1.12). The middle term in Eq.(1.11) no longer vanishes at an arbitrary z, while the other terms are z-independent, so there is no solution. This indicates that the velocity profile in fact deviates from the parabolic one. Of course, if the spatial scale L of the flow in the plane of the cell is large compared to h, the term can be neglected with respect to the friction at walls, and the Darcy law is recovered. Without the assumption that $L \gg h$, averaging the Stokes equation across the gap gives

$$-\frac{\partial < p >}{\partial x} + \eta\Delta_\perp u_x - \alpha\, u_x + f_x = 0 \qquad (1.13)$$

(and analogously for the y-components), where $\vec{f}$ is a gap-averaged driving force. Here it is assumed that it is possible to introduce a friction coefficient α such that $\eta < \partial^2 v_x/\partial z^2 >= -\alpha u_x$, where $u_x =< v_x >$. Although this is generally not the case, and Eq.(1.13) cannot be justified in this way, the equation looks rather reasonable from the physical point of view. The near-wall friction is the only viscous effect that is allowed for by the Darcy law. The Brinkman term $\eta\Delta_\perp u_x$ in Eq.(1.13) describes the viscous dissipation due to the flow non-uniformity in the plane of the cell and the associated

additional shear stresses. Like the Darcy law, Eq.(1.13) is known in the context of porous media flows, where it is named after Brinkman (sometimes it is referred to as the Darcy-Stokes equation). It describes both a free fluid flow and a flow in porous media and is useful at analyzing flows bounded by permeable walls.

For the Hele-Shaw flow, however, a rigorous argument for Eq.(1.13) was missing until recently. In [77] a unidirectional Stokes flow in a Hele-Shaw cell was analyzed in several particular situations. In one of them, the flow in a vertical Hele-Shaw cell was directed along the gravity force, and the density was non-uniformly distributed perpendicularly to the flow, but was constant along the flow and across the gap. Then the volume-averaged gravity force is non-potential (as can be seen by taking its curl). Still, the gap-averaged Stokes equation was demonstrated to reduce indeed to Eq.(1.13), but at long enough wavelength and with the Brinkman term multiplied by a constant prefactor $12/\pi^2 \approx 1.2$. The exact form of the Brinkman term is complicated and non-local (integral) [77]. The prefactor is not known in the more complicated cases involving magnetic forces that will be under consideration. Moreover, we don't know the shape of the velocity profile when the magnetic forces are in operation; one cannot expect it to be the Poiseuille one, so the expression for α in Eq.(1.13) is also not known exactly. Therefore we will follow the previous research and leave the Brinkman term equal to unity in Eq.(1.13).

In another case studied in [77], it was viscosity that varied perpendicularly to the flow. Note that our equations presented in this paragraph hold at constant viscosity. The case of a variable viscosity will be modelled in the present work only with the Darcy law (1.12). Nevertheless, it is noteworthy that the same conclusions as stated above hold in this case as well [77].

The Darcy law was conventional at describing the Hele-Shaw flow. However, the Brinkman equation is more adequate to describe the microconvection occurring on the scale of the gap width of the Hele-Shaw cell. First of all, one recalls the early work [32], both analytical and experimental one, where the viscous shear in the plane of the Hele-Shaw cell is considered as the only dissipation mechanism in the radial miscible flow (i.e neither surface tension nor diffusion are in operation). At a large radius, when the interface becomes almost straight, the most unstable mode is found to scale linearly with the gap width, which conclusion is substantiated by experimental results [32]. In [78] the same miscible Hele-Shaw experiment is conducted with a rectilinear displacement; again, the results (Fig. 11(a) of [78]) give $(1 \dots 3)h$ for the finger width. (As for the immiscible case, let us note the experimentally observed [79] saturation of the radius of curvature of the anomalous Saffman–Taylor fingers at the value of $(2.2 \pm 0.1)h$ at high capillary numbers.) In some

other situations [80, 81, 82, 83, 84, 85] the introduction of the Brinkman term in Eq.(1.13) was considered essential for a Hele-Shaw flow. In the context of the Rayleigh–Taylor instability with non-magnetic miscible or immiscible fluids in a Hele-Shaw cell, recently a comparison [86, 87] was done between the stability results given by experiments, a three-dimensional numerical linear analysis and non-linear simulations (all with the Stokes equation and the 3D CDE), on the one hand, and the stability results of [88] for the sharp interface (based on the Brinkman equation and the 2D CDE), on the other hand. (Contrary to the works discussed in §1.2, the concentration was assumed viscosity independent in these studies.) In [88, 89], a linear stability analysis of a sharp interface was conducted analytically in both the miscible and immiscible cases, and the Brinkman equation was found to render the most dangerous wavenumber of the instability equal to $\sqrt{6\left(\sqrt{5}-1\right)}\Big/h$ (the corresponding wavelength is $\approx 2.3h$) in the limit of large Péclet or capillary (§3.1.2) numbers. A slightly more general dispersion relation was obtained, using different characteristic time and space scales, in [90] [their Eqs.(6), (9)] for an arbitrary Schmidt number Sc, and verified using their 3D lattice-gas code [47]. The comparison [88, 86, 87] of the Brinkman results to the more general Stokes ones revealed a "somewhat surprising" [86] general ability of the Brinkman formulation to capture stability details – despite its gap-averaging (and QSSA, see p. 27 later). The non-linear simulations [86] demonstrated the transition between the two-dimensional Hele-Shaw mode of instability with a gap-invariant concentration field to the three-dimensional regime with a strongly z-dependent driving force and non-Poiseuille velocity profile. (We have already discussed on p. 11 the velocity profile at the viscously driven displacement.) Naturally, the transition occurs at high values of the dimensionless group $(\Delta\rho)gh/(\alpha D)$, $\Delta\rho$ being the density difference and g being the free-fall acceleration.

The effect of the wavelength "saturation" at $\sim h$ was also found and likewise attributed to the additional viscous stresses in our early communication [91] in the context of miscible MF's (see §2.3.4, Figs. 2.10, 2.11 later). It is noteworthy that an analogous effect for chemical fronts in a Hele-Shaw cell is contained in Eq.(16) of [81] as their driving parameter tends to infinity, which is due to the adopted Brinkman equation (cf. [92]). We would like to note here also the analytical work [93] which explored the Rayleigh–Taylor instability of a horizontal mixing front in an unbounded three-dimensional geometry (see also [94]). It was found that a new type of dissipation (viscosity) added into a stability problem with another stabilizing mechanism (diffusion), can couple with the latter, seriously modifying the behaviour of the most unstable mode by introducing a short-wavelength cut-off. [Note

that our dimensionless Cm number (Eq.(2.19)) that will govern the stability of our problem also involves a *product* ηD.]

We would like to stress once again that h being the length scale of an unstable interface in a Hele-Shaw cell at high Péclet or capillary numbers is consistent with the experimental evidence (for more references, see [88, 87]). Significant part of the forthcoming results are obtained assuming the flow is governed by the Brinkman equation.

1.4 The magnetic ponderomotive force

In this paragraph we will present the expressions for magnetic ponderomotive force and magnetic field that will be used throughout the following work.

In the approximation of magnetostatics for a non-conducting ferrofluid the Maxwell equations give

$$\operatorname{div} \vec{B} = 0\,, \tag{1.14}$$

$$\operatorname{rot} \vec{H} = 0\,. \tag{1.15}$$

Relaxation of the magnetization $\vec{M}$ will be considered instantaneous, so that $\vec{M} \parallel \vec{H}$.

The general formula for the ponderomotive-force density in a liquid magnetic reads (Eq.(4.33) of [14] in Gaussian units[3])

$$\vec{f}_{\mathrm{m}} = -\vec{\nabla}\left[\int_0^H \left(\frac{\partial(Mv)}{\partial v}\right)_{H,T} \mathrm{d}H\right] + M\vec{\nabla}H\,, \tag{1.16}$$

where $v = 1/\rho$ is the reverse density. This expression was derived in mid-sixties, since before the advent of magnetic fluids it would have had no practical applications. If $M = ((\mu-1)/4\pi)H$ with $\mu = \mathrm{const}$, the simpler classical expression due to Korteweg and Helmholtz is recovered:

$$\vec{f}_{\mathrm{m}} = \frac{1}{8\pi}\vec{\nabla}\left[H^2\rho\left(\frac{\partial\mu}{\partial\rho}\right)_T\right] - \frac{H^2}{8\pi}\vec{\nabla}\mu \tag{1.17}$$

(Eq.(4.47) of [14], Eq.(35.3) of [95]). However, Eq.(1.16) was derived for a single-phase media, and is not obviously valid for a multi-phase dispersed media such as magnetic fluids. Indeed, the variables T, ρ, and H are no longer enough to define the thermodynamic state of MF; for example, the concentration c can also vary independently, while in the approach of Cowley & Rosensweig the product cv is effectively fixed. Then M becomes a function

[3]The CGS system of units is in use throughout the present work.

of the following three variables: c, T, and H. This point was made in [96], where the expression for $\vec{f}_{\rm m}$ was derived in the form of Eq.(1.16), but with the fragment

$$\left(\frac{\partial(Mv)}{\partial v}\right)_{H,T} = M - \rho\left(\frac{\partial M}{\partial \rho}\right)_{H,T}$$

replaced by the expression

$$M - c\left(\frac{\partial M}{\partial c}\right)_{H,T} .$$

The two formulations of the magnetic force were apparently in contradiction. However, it was reconciled by V. V. Gogosov and his collaborators (see Gogosov's footnote comment at pp. 130–131 of [14], pp. 90–91 of [97], and references therein). It turns out that

$$\rho\left(\frac{\partial M}{\partial \rho}\right)_{H,T} = c\left(\frac{\partial M}{\partial c}\right)_{H,T} , \tag{1.18}$$

where the derivative in the left-hand side is taken also at a constant *mass* concentration of the magnetic phase (equal to cv times particle mass), which condition is implicit in Eq.(1.16). We assume again that MF is quite dilute so that the particle dipole-dipole interaction may be neglected: $cm_*^2/k_{\rm B}T \ll 1$, where m_* is the magnetic moment of a particle, $k_{\rm B}$ is Boltzmann's constant, and T is the temperature. (Equivalently, $\varphi \ll k_{\rm B}T/(M_{\rm S}^2 V_{\rm p})$, where $M_{\rm S}$ is the magnetization of the particle material, and $V_{\rm p}$ is the volume of a particle, $cV_{\rm p} = \varphi$; usually the inequality is close to $\varphi \ll 1$.) Consequently, the MF magnetization M in the field H obeys the Langevin law (with $M \ll H$) and is directly proportional to the concentration c. Then by Eq.(1.18) the integral term in Eq.(1.16) vanishes, and one obtains simply

$$\vec{f}_{\rm m} = M\vec{\nabla}H . \tag{1.19}$$

(Of course, the integral term in Eq.(1.16), entering as a gradient, can be absorbed into the pressure and forgotten in the absence of discontinuities.)

That the result (1.19) is not trivial becomes evident if one attempts to calculate $\vec{f}_{\rm m}$ *statistically* as the volume-averaged force on the gas of dipoles (magnetic particles) in an external field. The force on a single dipole is indeed a scalar product of its momentum and the gradient of some microscopic field. The analogous problem of computing the "effective" or "local" field arises in the long-developed and quite subtle theories of dielectric media with dipolar molecules. The analogy is formal though (cf. §31 of [95]), e.g. averaging

the microscopic magnetic field gives the magnetic induction $\vec{B}$, while the averaged electric field gives the intensity $\vec{E}$. Here we only note that Eq.(1.19) was obtained by a macroscopic thermodynamical argument. (See also §8 of [98].)

Eq.(1.15) allows us to introduce the potential of the self-magnetic (demagnetizing) field $\vec{H} - \vec{H}_0 = -\vec{\nabla}\psi_{\rm s}$ of the MF volume in the uniform applied field $\vec{H}_0$. Since $\vec{B} = \vec{H} + 4\pi\vec{M}$, Eq.(1.14) gives the Poisson equation in three dimensions for $\psi_{\rm s}$:

$$\Delta\psi_{\rm s} = 4\pi \,{\rm div}\, \vec{M}$$

with appropriate conditions at infinity. Its solution is

$$\psi_{\rm s}(\vec{r}_0) = -\int_{R^3} \frac{{\rm div}\vec{M}(\vec{r})}{|\vec{r}_0 - \vec{r}|}\, {\rm d}V\,. \tag{1.20}$$

At the boundary S between magnetic and non-magnetic media there is a jump in the magnetization $\vec{M}$, and ${\rm div}\vec{M}$ becomes a delta function there. Equivalently, instead of integrating the delta functions, a corresponding integral over S can be added to the right-hand side of Eq.(1.20):

$$\psi_{\rm s}(\vec{r}_0) = -\int_{R^3\setminus S} \frac{{\rm div}\vec{M}(\vec{r})}{|\vec{r}_0 - \vec{r}|}\, {\rm d}V + \int_S \frac{M_{\rm n}(\vec{r})}{|\vec{r}_0 - \vec{r}|}\, {\rm d}S\,, \tag{1.21}$$

where $\vec{n}(\vec{r})$ is the normal to S outward with respect to the magnetic media. The formulas for the magnetostatic potential can be found in many books on electromagnetism [99]; interestingly, they were first obtained by Poisson, who, apart from all other, was interested in the magnetostatics and founded its mathematical theory. In the electric terminology, if $\psi_{\rm s}$ were the electrostatic potential, then $-{\rm div}\vec{M}$ and $M_{\rm n}$ would be, respectively, the volume and surface densities of charge, both free and induced ones.

The field, potential, magnetization, and force density can be formally expanded in, e.g., volume fraction $\varphi \to 0$: $\vec{H} = \vec{H}_0 + \varphi\vec{H}_1 + \ldots$. Then in the lowest order $\vec{M}$ is directed along $\vec{H}_0$ (or equivalently, along $\vec{B}_0$) and

$$\vec{M} = \frac{\varphi m_0}{V_{\rm p}} \frac{\vec{H}_0}{H_0} + O(\varphi^2)\,,$$

where $m_0 \leqslant m_*$ is the average magnetic moment in the direction of $\vec{H}_0$. Since $\vec{H}_0$ is uniform,

$${\rm div}\vec{M} = \left(\vec{\nabla}\frac{\varphi m_0}{V_{\rm p}} \cdot \frac{\vec{H}_0}{H_0}\right) + O(\varphi^2) = \left(\frac{\vec{H}_0}{H_0} \cdot \vec{\nabla} M\right) + O(\varphi^2)\,.$$

This expression allows to rewrite Eq.(1.21) as

$$\psi_{\rm s}(\vec{r}_0) = \psi_*(\vec{r}_0) + O(\varphi^2)\,, \tag{1.22}$$

where

$$\psi_*(\vec{r}_0) = -\int \left(\frac{\vec{H}_0}{H_0}\cdot\vec{\nabla}M\right)\frac{{\rm d}V}{|\vec{r}_0-\vec{r}|} + \int \frac{H_{0{\rm n}}M\,{\rm d}S}{H_0\,|\vec{r}_0-\vec{r}|} = O(\varphi) \tag{1.23}$$

($\varphi\vec{H}_1 = -\vec{\nabla}\psi_*$). Now we calculate

$$H = \sqrt{H_0^2 + 2\varphi(\vec{H}_0\cdot\vec{H}_1) + O(\varphi^2)} = H_0 + \varphi\left(\frac{\vec{H}_0}{H_0}\cdot\vec{H}_1\right) + O(\varphi^2)\,.$$

Let us adopt the following notation: the magnetic media (MF) will occupy the layer $z = 0\ldots h$ (a Hele-Shaw cell), while $\vec{H}_0$ will be directed either along the z axis (the "perpendicular" field), or along the x axis (the "normal" field; this notation is adopted from [100]). The properties of the media will be further assumed to be constant across the layer: φ, $M = {\rm inv}(z)$. Then the gap-averaged density of the magnetostatic ponderomotive force (1.19) becomes

$$< \vec{f}_{\rm m} >= -\frac{M}{h}\int_0^h \vec{\nabla}\left(\frac{\vec{H}_0}{H_0}\cdot\vec{\nabla}\psi_*\right){\rm d}z + O(\varphi^3)\,. \tag{1.24}$$

In the case of the normal field, the surface integral in Eq.(1.23) vanishes due to $H_{0{\rm n}} = 0$. Then

$$\psi_*(\vec{r}) = -\int \frac{\partial M}{\partial x'}\frac{{\rm d}V'}{|\vec{r}-\vec{r}\,'|}\,, \tag{1.25}$$

$$< \vec{f}_{\rm m} >= -\frac{M}{h}\int_0^h \vec{\nabla}\frac{\partial\psi_*}{\partial x}\,{\rm d}z + O(\varphi^3) = -\frac{M}{h}\vec{\nabla}_\perp\frac{\partial}{\partial x}\int_0^h \psi_*\,{\rm d}z + O(\varphi^3)\,, \tag{1.26}$$

where $\vec{\nabla}_\perp$ is the two-dimensional Laplacian, and it is assumed possible to differentiate outside the integral. Further transformations will be undertaken in §2.4.1.

In the case of the perpendicular field we have $(\vec{H}_0\cdot\vec{\nabla}M) = 0$ and it is the volume integral that vanishes in Eq.(1.23):

$$\psi_*(\vec{r}) = \left(\int_{S_2} - \int_{S_1}\right)\frac{M\,{\rm d}S'}{|\vec{r}-\vec{r}\,'|}\,, \tag{1.27}$$

where S_2 and S_1 are the upper ($z = h$) and lower ($z = 0$) walls of the cell, respectively. The gap-averaged density of the force follows as

$$< \vec{f}_{\rm m} > = -\frac{M}{h}\vec{\nabla}_\perp \int_0^h \frac{\partial \psi_*}{\partial z}\,{\rm d}z + O(\varphi^3) = -\frac{M}{h}\vec{\nabla}_\perp \left(\psi_*|_{z=h} - \psi_*|_{z=0}\right) + O(\varphi^3)$$
$$= -\frac{2M}{h}\vec{\nabla}_\perp \psi_*|_{z=h} + O(\varphi^3)\,. \qquad (1.28)$$

For future reference, we expand Eq.(1.27):

$$\psi_*|_{z=h} = \int\limits_{S_2} \left(\frac{1}{\sqrt{(x-x')^2 + (y-y')^2}} - \frac{1}{\sqrt{(x-x')^2 + (y-y')^2 + h^2}} \right) M\,{\rm d}S'\,. \qquad (1.29)$$

This approximation for the magnetic force was also employed by others (e.g. [101], §4.6 of [15], [102]). Note that $M = m_0 c$ in our description with a constant m_0. The degree of magnetic saturation is not important. The forces (1.26), (1.28) and the resulting flow are in general not potential in the miscible case owing to the inhomogeneity of c.

Chapter 2

Linear stability analysis of a miscible interface in a Hele-Shaw cell

2.1 Miscible interfaces in a Hele-Shaw cell: an overview and model

In a magnetic fluid, the transport processes allow an extra control parameter: the applied magnetic field. They attract scientific interest because of their specific cooperative nature, since the self-magnetic field of the colloid as a whole influences the magnetophoretic motion of colloidal particles and leads to the field-dependent anisotropic effective diffusion.

However, as we have discussed in the Introduction, even if the external field is uniform, the self-magnetic field can give rise to a convective instability.[1] In a thin plane layer with rigid transparent walls (a Hele-Shaw cell), miscible instabilities with MF's can be observed directly with a microscope. In the experiment [1] MF and its pure carrier liquid were brought into contact in a Hele-Shaw cell forming a narrow straight "diffusion front." In the *perpendicular* (to the cell) external field, the interface developed an intricate labyrinthine pattern, while a peak pattern was obtained in the *normal* field (i.e. in the field applied along the cell perpendicularly to the front). The pattern length scale was approximately as small as the layer thickness (less than 10^{-2} cm). Having quickly formed, the patterns were gradually blurred out by diffusion.

[1] This term should be understood in our context as an instability of a quiescent state with respect to convection and not as the opposite to the "absolute" instability of a flow.

Recently, the diffusion in magnetic fluids under an applied magnetic field was investigated [2, 103, 104, 105] by the forced Rayleigh scattering (FRS) on the optical gratings induced in thin layers (between transparent plates) of MF's heated by an intensive non-uniform illumination ("pumping") [106]. By exposing the layer for a long enough time, a stationary grating – usually a periodic array of parallel stripes – was created. After the pumping is switched off, thermal inhomogeneities relax almost immediately, whereas the concentration grating decays gradually. This allowed to determine the effective diffusion coefficient of magnetic particles. If the magnetic field was applied along the layer parallel to the concentration gradients (in the "peak" configuration with respect to the stripes), the effective diffusion coefficient was observed to increase up to several times as the field increased. This effect was attributed [2, 103] to the magnetophoresis in the self-magnetic field. However, the mixing might have also been enhanced through breaking the one-dimensionality of the concentration distribution. The magnetophoresis alone is hardly capable of producing this effect [107]. Even though the occurrence of microconvection was not checked in these FRS experiments, such possibility should be investigated. And indeed, very recently, reported were the first experimental indications of a microconvection in the FRS setup [3, 108].

In this regard the experiments [109] also deserve mentioning; their interpretation was controversial [109, 110, 4]. An MF layer was heated by a focused perpendicular laser beam. The diffraction pattern was observed to loose its axisymmetric shape if the perpendicular magnetic field was raised above a critical value. Further on, if in addition a field was applied along the cell, the diffraction pattern would oscillate. While the authors of the experiment believe that a convection sets in there, it is argued in [110] that the circular symmetry is lost owing to a *static* instability akin to that of magnetic bubbles in a Hele-Shaw cell, with the concentration gradients playing the role of an effective surface tension (§1.2). The nature of observed effects remains unclear. (See also [111].)

In a circular geometry, a miscible MF flow in a Hele-Shaw cell under a perpendicular field was recently simulated in [68] and an intensive fingering was reported.

An instability of the Darcy flow of magnetic fluids in porous media in the field applied along the concentration gradients (the peak configuration) was studied in [112]. To extend these results to the case of a Hele-Shaw cell, its finite thickness must be taken into account at deriving the self-magnetic field of MF. We will consider several concentration distributions along the cell in order to be close to real experimental conditions. The case of an isolated miscible interface admits a pen-and-paper analysis for both orientations of

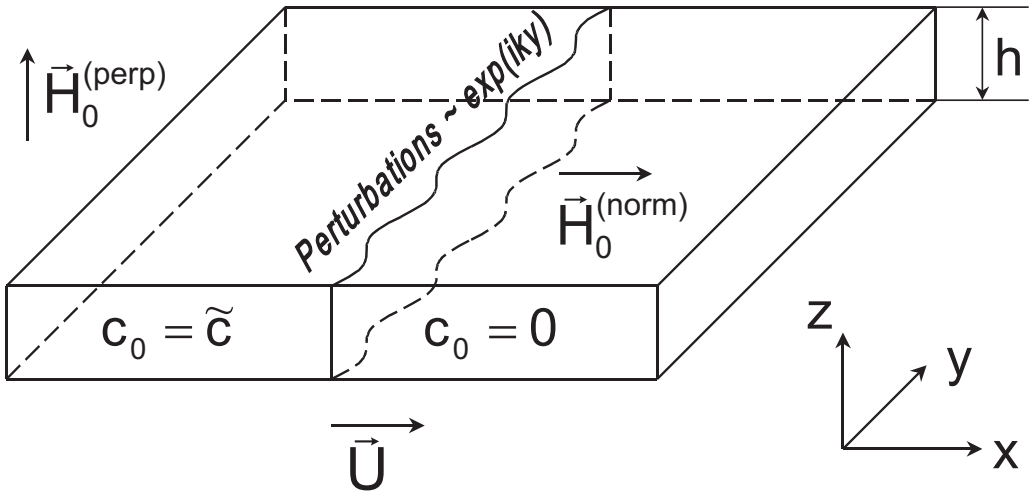

Figure 2.1: A sketch of a Hele-Shaw cell with a perturbed step-like concentration distribution.

the field. Studying the smoothed step-like and Gaussian (an isolated stripe; it will be studied only in the normal field) distributions allows to assess the impact of smearing on stability. Besides, the continuous formulation of the problem makes it possible to incorporate the Brinkman (Darcy–Stokes) equation for the Hele-Shaw flow that is an improvement over the conventional Darcy law (§1.3). The array of sharp parallel stripes specifically reproduces the periodicity of the FRS grating.

We will consider a MF confined in a horizontal Hele-Shaw cell of spacing h. An inhomogeneous gap-invariant concentration of magnetic particles serves to model a particular case of a miscible MF pair in contact. (Indeed, generally one would expect two MF's to have e.g. different diffusion coefficients, etc.) The MF concentration $c(x, y)$ (the number of magnetic particles per unit volume) is assumed constant across the cell, and the whole problem is to be rendered two-dimensional by averaging across the cell gap.

According to §1.2, we take the two-dimensional mass-averaged MF velocity field $\vec{v}$ to satisfy

$$\operatorname{div} \vec{v} = 0\,, \tag{2.1}$$

and the convection–diffusion equation holds:

$$\frac{\partial c}{\partial t} + (\vec{v} \cdot \vec{\nabla})c = D\Delta c\,, \tag{2.2}$$

where D is a constant diffusion coefficient. According to §1.1, the magnetophoresis is not taken into account.

The flow is governed by the Brinkman (Darcy–Stokes) equation for the gap-averaged variables [see Eq.(1.13) in §1.3]:

$$-\vec{\nabla}p + (\eta\Delta - \alpha)\vec{v} + \vec{f}_{\rm m} = 0\,, \tag{2.3}$$

where p is the pressure, $\vec{v}$ is the velocity (relative to the walls), η is the viscosity, and $\alpha = 12\eta/h^2$ is the friction coefficient estimated for the Poiseuille velocity profile. We remind (§1.3) that we can expect the full Eq.(2.3) to be valid for $\eta = \text{const}$; however, in the Darcy case it holds also at the concentration-dependent viscosity $\eta = \eta(c)$. $\vec{f}_{\rm m}$ stands for the gap-averaged density of the magnetostatic body force that depends on the field orientation.

2.2 The miscible stability problem and the continuous spectrum[2]

Let us consider the linear stability of some one-dimensional concentration distribution $c_0(x, t_0)$. The miscible basic flow is time-dependent due to diffusion so that a quasi-steady-state approximation (QSSA) must be adopted to study the linear stability by means of the normal-mode analysis at some moment t_0 [33]. Hereby we discard the further diffusion of the basic state as the flow perturbations evolve; their diffusion is taken into account, however. Technically, this amounts to "freezing" the time-dependent coefficients in the linearized perturbation equations. QSSA is considered [33] valid for diffused enough interfaces. Non-QSSA attempts were an exception [31], though recently a quite general QSSA-free approach to the long-wave linear stability of miscible interfaces was suggested [113]. Note also the boundary conditions introduced in [20] that render the basic flow with diffusion steady and can perhaps be used experimentally to create a controlled diffusion front (the solute spreads by diffusion upwards into a vertical Hele-Shaw cell whose open bottom side is immersed into a large reservoir, with a downward flow of the solvent opposing the spreading). In principle, a time-independent basic state can be maintained also by a chemical reaction [114].

Keeping in mind the situation of slow displacement and weak external field, we introduce h and h^2/D as space and time scales, respectively, to

[2] "It should be kept in mind that the subject of instabilities in an infinite domain is intrinsically difficult, in particular because of the appearance of problems related to the continuous spectrum. Many seemingly innocent questions have, to date, not even the beginning of a satisfactory mathematical answer..." (P. Collet and J.-P. Eckmann, *Instabilities and Fronts in Extended Systems*, Princeton University Press, 1990.)

render our independent variables dimensionless. Further on, we scale the concentration, velocity, magnetic potential, viscosity, friction coefficient, and pressure with their respective reference values $\tilde{c}$, D/h, $\tilde{c}m_0h$, $\tilde{\eta}$, $\tilde{\alpha} = 12\tilde{\eta}/h^2$, and $\tilde{\alpha}D$. We preserve the same notation for the dimensionless variables.

Now we take the curl of Eq.(2.3) and linearize it along with Eq.(2.2) about the basic state. Since the coefficients of the linearized equations depend only on x (and on the "frozen" time t_0 which enters as a parameter), we can separate out the variables t and y, as one would do if no integral terms were present. Thus we expand a velocity disturbance into discrete Fourier modes $\left\{v'_x(x;k), v'_y(x;k)\right\} \exp(iky + \lambda(k)t)$ (and likewise we expand the perturbations of c and ψ), where λ is a temporal growth increment of the mode of a dimensionless wavenumber k. We proceed with a singled out mode.

The linearized Eq.(2.2) becomes now

$$\frac{\mathrm{d}^2 c'}{\mathrm{d}x^2} - (k^2 + \lambda)\, c' = v'_x \frac{\partial c_0}{\partial x}\,, \tag{2.4}$$

The flow incompressibility immediately yields

$$ikv'_y = -\frac{\mathrm{d}v'_x}{\mathrm{d}x}\,. \tag{2.5}$$

In the next paragraphs we will present the further steps of the stability analysis in the case of magnetic fluids. In the rest of the present paragraph, we will explore some general issues concerning the stability analysis. This matter will be of no direct use further in the work. In particular, let us consider now in some detail the occurrence of the continuous spectrum, since we will encounter later (in §2.3) a linearized problem that can possess no discrete spectrum. In order to clarify the issue without technical complications, we temporarily set $\vec{f}_{\mathrm{m}} = 0$, omit the Brinkman term in Eq.(2.3), and take $\alpha = \mathrm{const}$.

Making use of the incompressibility, one obtains now the linearized Eq.(2.3) simply as

$$\frac{\mathrm{d}^2 v'_x}{\mathrm{d}x^2} - k^2 v'_x = 0\,. \tag{2.6}$$

The equations (2.4) and (2.6) together with the boundary conditions (that c' and v'_x vanish) at infinity compose an eigenvalue problem.

However, it can be readily seen that at any λ the boundary conditions are not satisfied. Thus there are no normal modes. Under some conditions, we will meet the same difficulty in our analysis of complete MF equations. However, it is the behaviour of infinitesimal perturbations that is of interest to us. Their dynamics is nevertheless governed by the linearized system.

The decomposition into normal modes [115] is only a convenient way, but not always an appropriate one, to reduce the problem for an arbitrary perturbation into a simpler problem for the single-mode solutions, whose temporal behaviour is given by a compact dispersion relation.

Let us outline briefly a not rigorous argument (ch. 4 of [116], §7.10 of [117]) by which a generalization of the usual normal-mode approach can be obtained. Many assumptions, reservations, etc. will be omitted to make the idea clear. Consider a linear operator L whose set of eigenfunctions $u_k(x)$, $L\,u_k = \lambda_k u_k$, is complete:

$$u = \sum_k \alpha_k u_k$$

for an arbitrary $u(x)$. Then

$$L\,u = \sum_k \alpha_k \lambda_k u_k\,,$$

and we can introduce other operators by the following formal definition:

$$f(L)\,u = \sum_k \alpha_k f(\lambda_k) u_k\,.$$

Let us consider $f(t) = 1/(\lambda - t)$:

$$f(L)\,u = \sum_k \frac{\alpha_k u_k}{\lambda - \lambda_k}\,. \tag{2.7}$$

Obviously, this $f(L)$ is the inverse of $-(L - \lambda E)$, E being the identity operator. Now if L is a differential operator, the inverse is expressed through a Green's function G:

$$f(L)\,u = -\int G(x,\xi,\lambda) u(\xi)\,\mathrm{d}\xi\,. \tag{2.8}$$

Integrating Eqs.(2.7) and (2.8) over a large circle in the λ plane and taking the residues at the poles in Eq.(2.7), we obtain

$$u(x) = -\frac{1}{2\pi i} \oint \mathrm{d}\lambda \int G(x,\xi,\lambda) u(\xi)\,\mathrm{d}\xi\,. \tag{2.9}$$

Thus the decomposition of a function in terms of the eigenfunctions of L is related to the Green's function of $L - \lambda E$. From Eq.(2.9) it follows that

$$-\frac{1}{2\pi i} \oint G(x,\xi,\lambda)\,\mathrm{d}\lambda = \delta(x - \xi)\,. \tag{2.10}$$

The resulting formulas hold in fact for a wider class of situations than one might think.

To be more specific, let us write down our system (2.4), (2.6). We have a generalized eigenvalue problem:

$$L \begin{pmatrix} c' \\ v'_x \end{pmatrix} = \lambda B \begin{pmatrix} c' \\ v'_x \end{pmatrix} ,$$

where

$$B = \begin{pmatrix} 1 & 0 \\ 0 & 0 \end{pmatrix}$$

and

$$L = \begin{pmatrix} \dfrac{\mathrm{d}^2}{\mathrm{d}x^2} - k^2 & -\dfrac{\partial c_0}{\partial x} \\ 0 & \dfrac{\mathrm{d}^2}{\mathrm{d}x^2} - k^2 \end{pmatrix} .$$

In this case the Green's function becomes a Green's matrix (§16.5 of [118]).

For illustration purposes let us consider, however, the trivial case $\partial c_0/\partial x = 0$. Then the equations for c' and v'_x decouple so that the Green's function for the concentration given by

$$(L_{11} - \lambda E)\, G(x, \xi, \lambda) = \delta(x - \xi)$$

can be easily found as

$$G = \frac{-1}{2\sqrt{k^2 + \lambda}} \exp\left(-|x - \xi|\sqrt{k^2 + \lambda}\right) .$$

Now we want to integrate G over the circle of an infinite radius. G is analytic in λ with the exception of a branch cut $\lambda \in (-\infty, -k^2)$, on the upper side of which we choose $\Im\mathrm{m}\,\sqrt{k^2 + \lambda} > 0$. The sum of the integral over the circle and the integral over the branch cut (both paths are followed in the same direction) equals zero by Cauchy's theorem. The integral over the branch cut is easy to evaluate, and we obtain the following formula:

$$-\frac{1}{2\pi i} \oint G(x, \xi, \lambda)\, \mathrm{d}\lambda = \frac{1}{2\pi} \int_{-\infty}^{-k^2} \frac{\cos\left(|x - \xi|\sqrt{-(k^2 + \lambda)}\right)}{\sqrt{-(k^2 + \lambda)}}\, \mathrm{d}\lambda , \qquad (2.11)$$

where the square root takes on its arithmetic value. In accordance with Eq.(2.10), the right-hand side indeed reduces to a delta-function by a well-known representation

$$\int_{-\infty}^{+\infty} \exp(ikx)\, \mathrm{d}k = 2\pi\delta(x) .$$

Eq.(2.9) takes on the form

$$c'(x) = \frac{1}{2\pi} \int\limits_{-\infty}^{-k^2} \frac{\mathrm{d}\lambda}{\sqrt{-(k^2+\lambda)}} \int\limits_{-\infty}^{+\infty} \cos\left(|x-\xi|\sqrt{-(k^2+\lambda)}\right) c'(\xi)\,\mathrm{d}\xi =$$

$$\int\limits_{-\infty}^{-k^2} \frac{\mathrm{d}\lambda}{2\pi\sigma} \left(\cos(\sigma x) \int\limits_{-\infty}^{+\infty} c'(\xi)\cos(\sigma\xi)\,\mathrm{d}\xi + \sin(\sigma x) \int\limits_{-\infty}^{+\infty} c'(\xi)\sin(\sigma\xi)\,\mathrm{d}\xi \right) \quad (2.12)$$

(here $\sigma = \sqrt{-(k^2+\lambda)}$). This is nothing else but the desired decomposition of (the k-th y-mode of) an arbitrary instantaneous concentration field in terms of functions of a prescribed temporal behaviour $\sim \exp(\lambda t)$. If the Green's function had pole singularities in addition to the branch cut, there would appear a sum of residues in Eqs.(2.11), (2.12) corresponding to the decomposition into the conventional normal modes. The inner integration in Eq.(2.12) would still give the coefficients of the decomposition. We remind that usually the expansion is implicit, and normal modes are analyzed from the beginning. However, we have a decomposition in terms of functions that do not satisfy the boundary conditions at infinity, where the functions are only bounded but do not vanish. The corresponding eigenvalues λ are said to belong to the so-called *continuous spectrum* of the stability operator as opposed to the discrete spectrum (§12 in [118]). (Indeed, one has to integrate over the continuous spectrum but sum over the enumerable set of discrete eigenvalues.) Although every eigenfunction of the continuous spectrum is not admissible in the sense of the boundary conditions, their continuous infinite set can represent a valid vanishing perturbation. The situation is the same as with the Fourier integral (our illustration (2.12) is a version of the Fourier decomposition). Infinity of the domain is a root of the continuous spectrum. Indeed, shift the boundary conditions to finite points, and the continuous spectrum will usually condense into a countable set of discrete eigenvalues. (Another common cause for the continuous spectrum to emerge is the singularity of coefficients.)

A by-product of our analysis (2.12) is that $\lambda \le -k^2$, i.e. every perturbation belonging to the continuous spectrum will disappear. Of course, with our simplifications, it follows directly from the diffusion equation that any disturbance will. Thus the continuous spectrum can be neglected if one asks about the instability. How general is this conclusion?

Later we will study situations where the analogue of Eq.(2.6) will contain additional, integral terms related to the magnetic field, which will render the stability operator integro-differential. Analysis of the inverse operator and its singularities seems to be intractable. A finite number of discrete modes

will appear; the discrete eigenvalues will have either $\Re\mathrm{e}\,\lambda > -k^2$ or $\Im\mathrm{m}\,\lambda \neq 0$ (it is easy to see that complex-valued eigenvalues come in conjugate pairs).

Nevertheless, Eq.(2.4) remains valid and has the following property. As in our problems $\partial c_0/\partial x$ and other variable coefficients vanish at infinity, the convection–diffusion equation (2.2) and the analogue of Eq.(2.6) always decouple at infinity. Thus we will have the same behaviour of the eigenfunctions at infinity. If the conditions of vanishing are imposed there, the discrete eigenfunctions result that can be real or complex valued, while the corresponding eigenvalues can be stable or unstable. If we demand that the solutions be only bounded, the continuum eigenfunctions result. In this case it is guaranteed, by virtue of Eq.(2.4), that λ is real and negative. Of course we realize that this argument, extended from [39], is not rigorous, still we believe the conclusion is right.

In the spectral theory ([119, 120]) the exact definitions of the discrete, continuous, and the so-called residual spectrum are given. The linear ordinary differential operators do not possess the residual spectrum (p.184 of [117], p.200 of [116]). The spectral theory for the self-adjoint operators is especially well developed. We will obtain complex-valued eigenvalues though, which automatically implies that the problem is not self-adjoint. For the Sturm-Liouville problem, there are many simple criteria allowing to judge upon the spectrum merely by coefficients. The continuous spectrum of the boundary-value problems is quite important in quantum mechanics [121].

In hydrodynamics, the most studied stability problem is that of the inertial instability (governed by the Orr-Sommerfeld equation) of the viscous parallel shear flow, and its inviscid limit. The continuous spectrum of the problem in the unbounded domain is discussed, e.g., in [122, 123, 124]. The complete and mathematically rigorous approach to the linear stability problem with time-invariant coefficients is to solve the initial-boundary-value problem for an arbitrary perturbation, which allows to take the continuous spectrum into account in a natural way. This is usually achieved through the one-sided Laplace transform of the equations in time combined with the Fourier transform in those spacial variables of which the coefficients are independent ([125, 126, 127, 128]; see also [129], §2.3.2 in [130]). At inverting the solution obtained in the transform space, the poles in the variable of the Laplace transform correspond to the discrete eigenmodes, while the branch cuts correspond to the continuum eigenfunctions, much the same as for the above-demonstrated technique employing the Green's function. Indeed, the homogeneous linear stability equations such as Eq.(2.4) for $c' \exp(\lambda t + \ldots)$, etc, are exactly the equations for the Laplace-transformed Fourier modes of linear perturbations of $c(t, \ldots)$, etc, but without the inhomogeneous terms due to initial conditions. Integrating over the unstable part of the contin-

uous spectrum, one obtains that the associated temporal behaviour is non-exponential (§47.1 in [131]).

We would like to touch briefly the so-called transient-growth phenomena [132, 133, 134]. It turns out that the notion of linear stability must be generalized to describe the observed phenomena more adequately. Consider the case of non-orthogonal eigenfunctions, all of them decaying monotonically in time (a linearly stable situation). Then possible are their linear combinations such that they, being initially small, grow temporarily because of the difference in growth rates between individual modes. A simplistic analogue is the early behaviour of $\exp(-t) - \exp(-2t) \sim t$. The transient growth can be so substantial (orders of magnitude) that the disturbance enters the non-linear regime, where its fate is no longer controlled by the linear theory.

We also just mention the so-called energy methods in (non-linear) stability theory that are based on the estimates of solutions to differential equations (§§VI.8–9 in [135], [136], [137]). If the flow is found to be non-linearly stable, it is of course stable with respect to infinitesimal disturbances as well. Hydrodynamic stability problems are treated from the stand-point of the non-equilibrium thermodynamics in [138].

The theory of the hydrodynamic stability is a respectable but demanding field[3] at the interface between fluid mechanics and applied mathematics. As a reference, we would recommend [131]; for a detailed overview of inertial instabilities and transition, see Chapter 2 of [139].

2.3 The labyrinthine instability

In the next four paragraphs,[4] we will consider the magnetic field applied perpendicularly to the cell and the "labyrinthine" instability it causes. Then the gap-averaged density of the magnetostatic body force $\vec{f}_{\mathrm{m}}$ is given by Eq.(1.28) as

$$\vec{f}_{\mathrm{m}} = -2h^{-1} m_0 c \vec{\nabla} \psi \,. \tag{2.13}$$

Here m_0 is an average particle moment component along $\vec{H}_0$, and by Eq.(1.29),

$$\psi(\vec{r}, t) = m_0 \int c(\vec{r}\,', t) K\left(\vec{r}\,' - \vec{r}\right) \mathrm{d}S' \tag{2.14}$$

with $K(\vec{\rho}) = 1/\rho - 1/\sqrt{\rho^2 + h^2}$.

[3] "Research on hydrodynamic stability has been deep but narrow..." (P. G. Drazin and W. H. Reid, [131].)

[4] Results of §2.3 were mostly published in [140] and communicated in part as [141, 91] and at [9].

2.3.1 Derivation of the dispersion relation

We investigate the linear stability of the *initially* step-like concentration distribution (i.e. of the straight "front" separating half-planes each occupied by its respective MF). For the sake of generality, a steady displacement of the fluid perpendicularly to the front with the velocity U relative to the walls is also allowed for, which, at the concentration-dependent viscosity, allows us to take the Saffman–Taylor mechanism of instability into account. We can allow for viscosity variations only in the Darcy case.

We adopt the (x,y) Cartesian rectilinear reference frame that moves with the velocity $\vec{U}$, the x axis being directed along the $\vec{U}$ vector (Fig. 2.1). The quiescent state is then as follows:

$$\vec{v}_0 = 0\,, \tag{2.15}$$

$$\partial c_0/\partial t = \partial^2 c_0/\partial x^2\,, \tag{2.16}$$

$$-\partial p_0/\partial x - \mathrm{Pe}\,\alpha - 2\,\mathrm{Cm}\,c_0\,\partial\psi_0/\partial x = 0\,, \tag{2.17}$$

$$\psi_0 = \int_{-\infty}^{+\infty} c_0(\xi + x, t_0)\ln\left(1+\xi^{-2}\right)\mathrm{d}\xi\,, \tag{2.18}$$

where $\mathrm{Pe} = Uh/D$ is the Péclet number.[5] The dimensionless group

$$\mathrm{Cm} = \frac{(\tilde{c}m_0)^2}{\tilde{\alpha}D} \tag{2.19}$$

is the ratio of the time h^2/D it takes for diffusion to act over the characteristic distance h to the time $h^2\tilde{\alpha}/(\tilde{c}m_0)^2$ of the advection due to the magnetic force. In fact, the gap width h is introduced as the characteristic length by the magnetic field – through the dimensional form of Eq.(2.18). The driving force being due to a self-magnetic field, Cm is quadratic in magnetization. Hence Cm parallels the magnetic Rayleigh number $\sim (\partial M/\partial T)^2(\Delta T/h)^2h^4$ characterizing a thermomagnetic instability [142] of a thin MF layer in a uniform perpendicular field with a temperature difference ΔT imposed across the layer. However, even though Cm resembles the magnetic concentration (solute) Rayleigh number, it has nothing to do with gradients across the cell. Cm is essentially independent of the viscosity, for the Stokes drag entering the Einstein formula for D and the friction coefficient $\tilde{\alpha}$ both vary linearly with $\tilde{\eta}$ (so that $\mathrm{Cm} \sim (\tilde{c}m_0)^2h^2a/(k_\mathrm{B}T)$, where k_B is the Boltzmann constant). As MF saturates, a field increase cannot yield an arbitrarily high Cm with a given MF sample (unless a thicker cell is taken). For the only available

[5] Everywhere we use "ln" for the natural logarithm and "lg" for the decimal one.

experimental situation [1] ($h = 0.01$ cm, $H_0 = 100$ Oe, MF saturated magnetization of 10 G) we substitute reasonable guesses for the missing values ($a = 5 \times 10^{-7}$ cm for the radius of a particle, and 500 G for the particle material magnetization), which yields $\mathrm{Cm} \approx 10^4$.

Interestingly, the dimensional analysis of the problem (the Π-theorem [143]) with constant coefficients reveals that only one more dimensionless parameter could in principle emerge: $h^3\tilde{c}$. Obviously, we are working in the limit $h^3\tilde{c} \gg 1$ (moreover, $h^3\tilde{c} \gg h/a$ by Eq.(1.1)).

As described in §2.2, we expand all disturbances into discrete Fourier modes $\sim \exp(iky + \lambda(k)t)$. Then, introducing the McDonald (modified Bessel) function

$$K_0(x) = \int_0^\infty \frac{\cos(xt)\mathrm{d}t}{\sqrt{t^2+1}}\,, \tag{2.20}$$

the perturbation of the potential is expressed as

$$\psi' = 2\int_{-\infty}^{+\infty} c'(\xi + x)\left(K_0(k\,|\xi|) - K_0(k\sqrt{\xi^2+1})\right)\mathrm{d}\xi\,. \tag{2.21}$$

The linearized CDE has already been obtained as Eq.(2.4). Taking into account the incompressibility of the flow, Eq.(2.5), one obtains the linearized curl of Eq.(2.3) as

$$\begin{aligned}\frac{1}{k^2}\frac{\mathrm{d}}{\mathrm{d}x}\left[-\frac{\eta}{12}\frac{\mathrm{d}^3 v_x'}{\mathrm{d}x^3} + \left(k^2\frac{\eta}{12} + \alpha\right)\frac{\mathrm{d}v_x'}{\mathrm{d}x}\right] + \frac{\eta}{12}\left(\frac{\mathrm{d}^2 v_x'}{\mathrm{d}x^2} - k^2 v_x'\right) - \alpha v_x' \\ - \mathrm{Pe}\,\frac{\mathrm{d}\alpha}{\mathrm{d}c}c' - 2\,\mathrm{Cm}\left(c'\frac{\partial\psi_0}{\partial x} - \psi'\frac{\partial c_0}{\partial x}\right) = 0\,.\end{aligned} \tag{2.22}$$

The appearance of Eq.(2.22) is somewhat misleading, since it is valid, in its full form, only at $\eta = \mathrm{const}$, when the term with the Pe factor vanishes. However, a varying viscosity is allowed in the Darcy approximation when $(h/L)^2 = k^2 + \|\mathrm{d}^2/\mathrm{d}x^2\| \ll 1$, where L is the two-dimensional (in the plane of the cell) flow scale. Recalling the definition of α we find that the terms *explicitly* containing η should be omitted to have the Darcy case.

Equations (2.21)–(2.22) compose a system of linear ordinary differential and integro-differential equations. Imposing the relevant boundary conditions

$$c' = v_x' = 0 \tag{2.23}$$

at $x = \pm\infty$ yields an eigenvalue problem for the system (these conditions refer to the eigenfunctions of the discrete spectrum, §2.2).

We start with the Darcy case $L^2 \gg h^2$ in the formal limit $t_0 = 0$ when the concentration distribution is step-like. This linear stability problem can be

solved analytically. Let c, α, and $\mathrm{d}\alpha/\mathrm{d}c$ be equal 1, a_1, and b_1, respectively, if $x < 0$ and 0, a_2, and b_2 if $x > 0$. From Eq.(2.18) we calculate the magnetic potential ψ_0 of the basic state:

$$\partial\psi_0(x,0)/\partial x = -\ln\left(1 + x^{-2}\right) . \tag{2.24}$$

Equations (2.4), (2.22) in both half-planes $x < 0$ and $x > 0$ take on the form

$$\mathrm{d}^2c'/\mathrm{d}x^2 = (k^2 + \lambda)\, c' , \tag{2.25}$$

$$k^{-2}\,\mathrm{d}^2v_x'/\mathrm{d}x^2 - v_x' = a_{1,2}^{-1}\, c' \left(b_{1,2}\,\mathrm{Pe} - 2\,\mathrm{Cm}\ln\left(1 + x^{-2}\right)\right) . \tag{2.26}$$

Now, we demand that the discrete perturbation modes vanish at infinity and introduce the following conditions at the discontinuity:

$$[v_x']_{-0}^{+0} = 0 , \tag{2.27}$$

$$[\mathrm{d}c'/\mathrm{d}x]_{-0}^{+0} = v_x'(0)\,[c_0]_{-0}^{+0} , \tag{2.28}$$

$$[c']_{-0}^{+0} = 0 , \tag{2.29}$$

$$[\alpha(c_0)\mathrm{d}v_x'/\mathrm{d}x]_{-0}^{+0} = -2\,\mathrm{Cm}\,k^2\psi'(0)\,[c_0]_{-0}^{+0} . \tag{2.30}$$

The jump conditions (2.27), (2.28), and (2.30) are obtained from the integral form of Eqs.(2.1)–(2.3) and essentially represent, respectively, the conservation of mass, species, and momentum (the latter amounts here to the pressure continuity). Condition (2.29) corresponds to a phenomenological law (the first Fick's law) and perhaps has no immediately apparent physical interpretation in the sharp-interface limit. It may be deduced from Eq.(2.4) e.g. by "balancing" the delta functions (p. 41 in [144]). Even though the reduced Eqs.(2.25), (2.26) are purely differential, the non-local nature of the problem survives through the boundary condition (2.30).

From Eqs.(2.25) and (2.29) it follows that

$$c'(x) = A\exp(-sk|x|) , \tag{2.31}$$

where A is the dimensionless amplitude of the perturbation mode, and

$$s = \sqrt{1 + \lambda/k^2} . \tag{2.32}$$

For the concentration to vanish at infinity we suppose (§2.2)

$$\Re\mathrm{e}\, s > 0 . \tag{2.33}$$

The perturbation of the field is found from Eq.(2.21) as $\psi'(0) = 4AJ(s,k)/k$, where

$$J(p,q) = \int_0^{+\infty} \exp(-pz) \left(K_0(z) - K_0(\sqrt{z^2+q^2}) \right) \mathrm{d}z \,.$$

From Eq.(2.26) we obtain ($s \neq 1$)

$$v_x' = C_{1,2} \exp(k|x|) + D_{1,2} \exp(-k|x|) + A a_{1,2}^{-1} b_{1,2} \,\mathrm{Pe}\, (s^2-1)^{-1} \exp(-sk|x|)$$
$$- A a_{1,2}^{-1} \,\mathrm{Cm}\, k \left[\exp(+k|x|)\, \mathrm{g}(|x|, k(s+1)) - \exp(-k|x|)\, \mathrm{g}(|x|, k(s-1)) \right] , \tag{2.34}$$

where

$$\mathrm{g}(z,a) = \int_0^z \exp(-a\zeta) \ln\left(1+\zeta^{-2}\right) \mathrm{d}\zeta \,,$$

and $C_{1,2}$, $D_{1,2}$ are the dimensionless amplitudes in their respective domains. (For a neutral perturbation, $s = 1$, the necessary expressions are the recovered as the limit of the written ones.) In order for the velocity to vanish at infinity we demand

$$C_{1,2} = A a_{1,2}^{-1} \,\mathrm{Cm}\, k\, \mathrm{f}(k(s+1)) \,, \tag{2.35}$$

where

$$\mathrm{f}(a) \equiv \mathrm{g}(+\infty, a) = 2\left(\gamma + \ln a - \mathrm{ci}\, a \cos a - \mathrm{si}\, a \sin a\right)/a \,, \tag{2.36}$$

$\gamma = 0.5772\ldots$ is the Euler constant, and

$$\mathrm{si}\, x = -\int_x^{+\infty} \frac{\sin t}{t} \mathrm{d}t \,, \quad \mathrm{ci}\, x = -\int_x^{+\infty} \frac{\cos t}{t} \mathrm{d}t$$

are the integral sine and cosine functions. Conditions (2.27)–(2.30) now yield

$$D_{1,2}/A = 2ks - a_{1,2}^{-1} \,\mathrm{Cm}\, k\, \mathrm{f}(k(s+1)) - a_{1,2}^{-1} b_{1,2} \,\mathrm{Pe}/(s^2-1) \tag{2.37}$$

and the dispersion relation

$$\frac{a_1+a_2}{2} ks + \mathrm{Cm}\left[2J(s,k) - k\,\mathrm{f}(k(s+1))\right] + \frac{b_1+b_2}{4} \frac{\mathrm{Pe}}{s+1} = 0 \,. \tag{2.38}$$

Equation (2.38), solved for λ, in a zero field agrees with the expressions obtained previously by other authors (e.g. [36] at a constant isotropic dispersion). However, it is now obvious that the dispersion relation and Eq.(2.33) should preferably be written in terms of s rather than λ. In dimensional variables, the gap width h at $\mathrm{Cm} = 0$ drops out of Eq.(2.38), as it should do.

Given that $b_{1,2} > 0$, an unstable displacement occurs for the non-magnetic fluid at negative Péclet numbers (Fig. 2.1). Concentration–viscosity profile is often [33] assumed exponential, $\eta \sim \exp(Rc)$, in which case $(b_1 + b_2)/(a_1 + a_2) = R$. Note that contrary to the immiscible case, the dispersion relation (2.38) does not involve the viscosity contrast $a_2 - a_1$ due to a different nature of perturbations and boundary conditions (see p. 10).

At any Cm only the solutions of Eq.(2.38) that satisfy the condition (2.33) correspond to admissible, vanishing at infinity perturbations and thus comprise a discrete eigenvalue spectrum. (A similar observation was made in [39]; see §2.2.) Obviously, an arbitrary initial data cannot be decomposed in terms of a finite set of discrete normal modes alone. The continuous part of the perturbation spectrum ($\Re\mathrm{e}\, s = 0$) consists of improper eigenfunctions that are only bounded as $x \to \pm\infty$. These elementary perturbations are stationary ($\Im\mathrm{m}\, \lambda = 0$) and stable ($\lambda \leqslant -k^2$).

In the case when both the applied field and the displacement favour the instability, the dispersion relation (2.38) may lead to a double-humped $\lambda(k)$ curve. The presence of two preferred wavelengths may result in an interesting mode competition and interaction. But further on in the present article we restrict ourselves to the case $\alpha(c) = \tilde{\alpha} = \mathrm{const}$, i.e. in the dispersion relation (2.38) we set

$$a_1 = a_2 = 1\,, \quad b_1 = b_2 = 0\,. \tag{2.39}$$

This renders the system insensitive to the displacement and Pe is no longer a control parameter. For a sharp interface, however, conditions (2.39) are not as restrictive as for a diffused one. Indeed, according to Eq.(2.38), an arbitrary $\alpha(c)$ at no displacement can be absorbed in a rescaled Cm, in which case there is no loss of generality in imposing $a_1 = a_2 = 1$. This way or that, relation (2.38) implicitly defines the possibly multiple-valued $\lambda = \lambda(k, \mathrm{Cm})$ dependence to be explored in detail in the next paragraph.

2.3.2 The stability diagram and the asymptotic analysis of the dispersion relation[6]

At $\mathrm{Cm} = 0$ (the pure convective diffusion) no discrete modes are present. For small Cm the following expression may be derived from Eq.(2.38) by differentiating the implicit function $s = s(\mathrm{Cm})$:

$$\lambda = -k^2 + \mathrm{Cm}^2 \left(k\,\mathrm{f}(k) - 2J(0,k)\right)^2 + O(\mathrm{Cm}^3)\,, \tag{2.40}$$

[6] "Divergent series are the invention of the devil, and it is shameful to base on them any demonstration whatsoever... by using them one can draw any conclusion he pleases..." (Niels Henrik Abel, 1828).

where $J(0,q) = \frac{1}{2}\pi\,(1 - e^{-q})$. Owing to Eq.(2.33), the parentheses in Eq.(2.40) must be positive, which condition is equivalent to $k > k_0 = 1.673$.

For an arbitrary Cm the number of eigenvalues was checked by applying the Cauchy principle of argument [145] to the left-hand side of Eq.(2.38), with the latter being regarded as a function $h(s)$ of a complex variable s in the half-plane (2.33). Consider a semicircle C of a large radius in the half-plane $\Re\mathrm{e}\, s > 0$, closed by a segment $\Re\mathrm{e}\, s = 0$. Then the number of zeroes the left-hand side of Eq.(2.38) has within the semicircle is equal, in the absence of poles, to the number of winds the image $h(C)$ makes around the origin.[7]

The dispersion curves are presented in Fig. 2.3 ($k > k_0$) and Fig. 2.4 ($k < k_0$). We begin with the case $k > k_0$, when just one solution to Eq.(2.38) for a given Cm exists. This mode is stationary. The value $\mathrm{Cm}_{\mathrm{cr}} = 5.572$ appears to be critical, with the mode losing its stability at $k_{\mathrm{cr}} = 5.343$. The most dangerous wavenumber quickly increases with Cm, which is to be discussed below. At $k = k_0$ the value $s = 0$ satisfies the dispersion relation (2.38) with any Cm. As k varies slightly, the solution to Eq.(2.38) departs from zero and either becomes admissible in the sense of Eq.(2.33) or not. Indeed, as soon as k gets smaller than k_0, one discrete mode disappears (if $\mathrm{Cm} < \mathrm{Cm}_0 = 7.135$) or emerges ($\mathrm{Cm} > \mathrm{Cm}_0$). In general, if $k < k_0$, either no solutions or two (complex-conjugate or real distinct) solutions exist. The occurrence of two modes is illustrated by Fig. 2.4 (which extends Fig. 2.3). If the pair is stationary, we term "dominant" the mode with larger increment, referring to the other one as "secondary." Fig. 2.5 presents the classification of solutions in the k, Cm plane. There is a long-wave region on the parameter plane that corresponds to the absence of the discrete modes.[8] If $\mathrm{Cm} < \mathrm{Cm}_0$, the region spans over the whole $0 < k < k_0$ range, but it contracts at larger Cm (the region h of Fig. 2.5). Further on, the dispersion relation (2.38) subject to the constraint (2.33) has two complex-conjugate solutions in the regions f, g (with the frequency of oscillations tending to zero on the border curves 3 and 4); these two solutions are real in c–e; at entering the regions a, b the secondary mode disappears. Closing the path of the clockwise circular "walk" over the stability map, we observe a disappearance of the only mode on the a–h boundary. On the whole, the complexity of Fig. 2.5 is largely due to the condition (2.33), for there always are two solutions to the standalone dispersion relation (2.38), either real or complex.

The neutral curves for oscillatory and stationary modes intersect in the

[7] The idea of this beautiful application of the complex analysis is due to Professor A. Cēbers.

[8] "What happens then with a small disturbance?" – this apparently simple question, asked by Professor J.-C. Bacri, has in fact motivated us to investigate the issue of the continuous spectrum (§2.2).

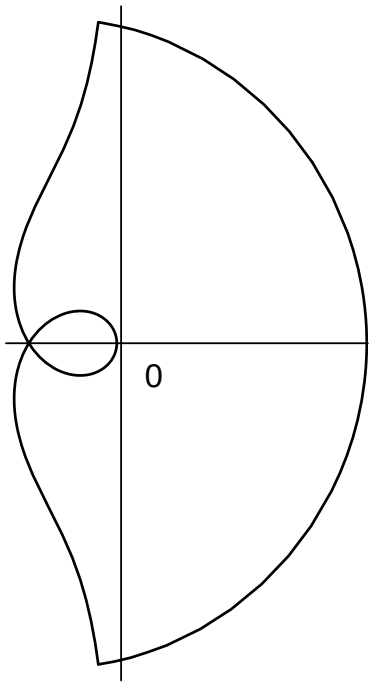

(b) $k = 1.70$, Cm $= 30$: 1 mode.

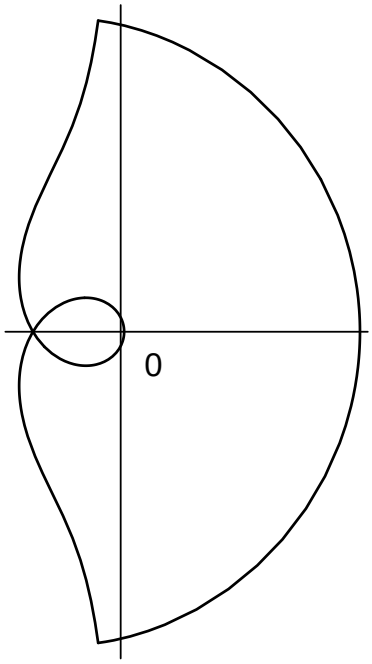

(c) $k = 1.65$, Cm $= 30$: 2 modes.

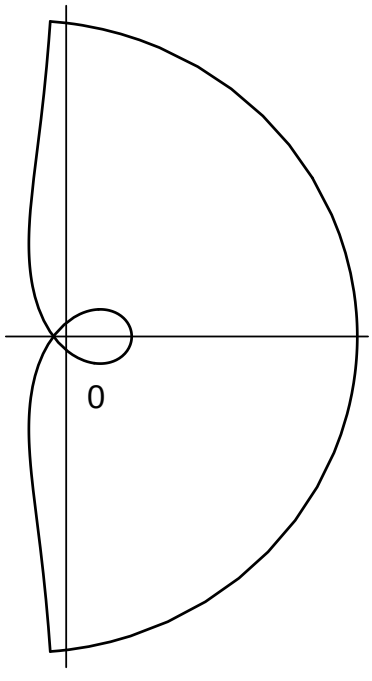

(g) $k = 1.0$, Cm $= 15$: 2 modes.

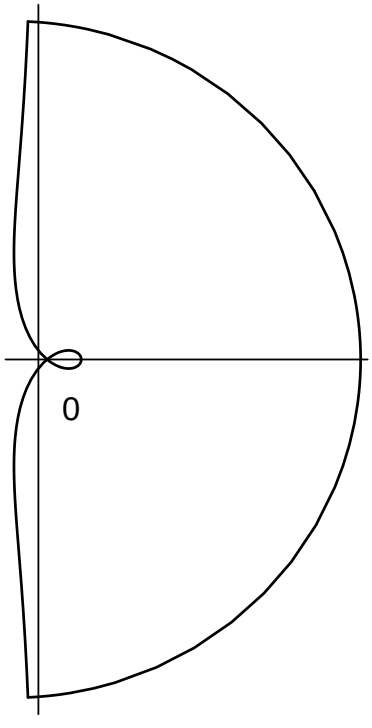

(h) $k = 1.0$, Cm $= 9$: no modes.

Figure 2.2: The number of discrete modes as the number of winds around the origin: an application of the Cauchy principle of argument. Plotted is the image of a large semicircle in the half-plane $\Re\mathrm{e}\, s > 0$ under the complex transform generated by the dispersion relation (2.38), (2.39). The plots are labelled according to the lettering of the stability diagram (Fig. 2.5).

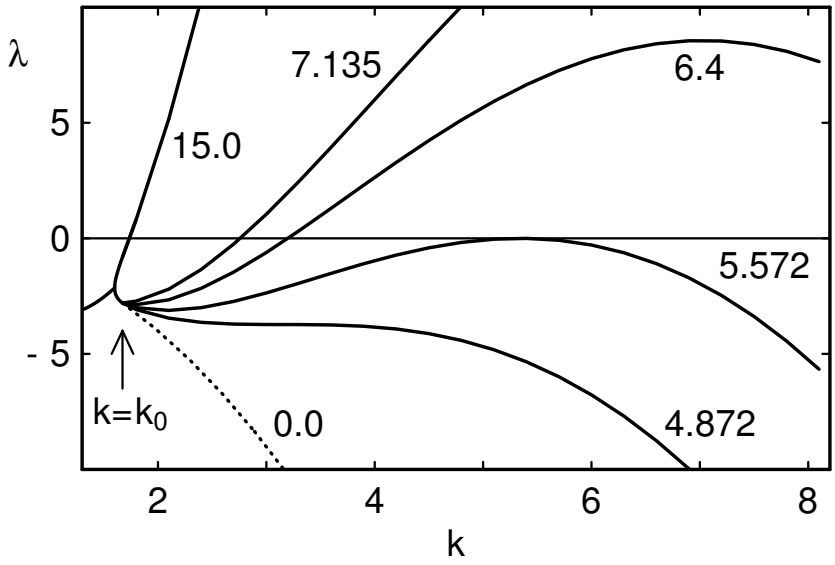

Figure 2.3: The growth rate – wavenumber dependence for short wavelengths $k > k_0$. Numbers near the curves indicate the corresponding Cm values. The dotted curve is the zero-field limit $\lambda = -k^2$. Only the Cm = 15.0 curve extends leftwards beyond k_0 (where a $\Re\mathrm{e}\,\lambda$ segment is visible).

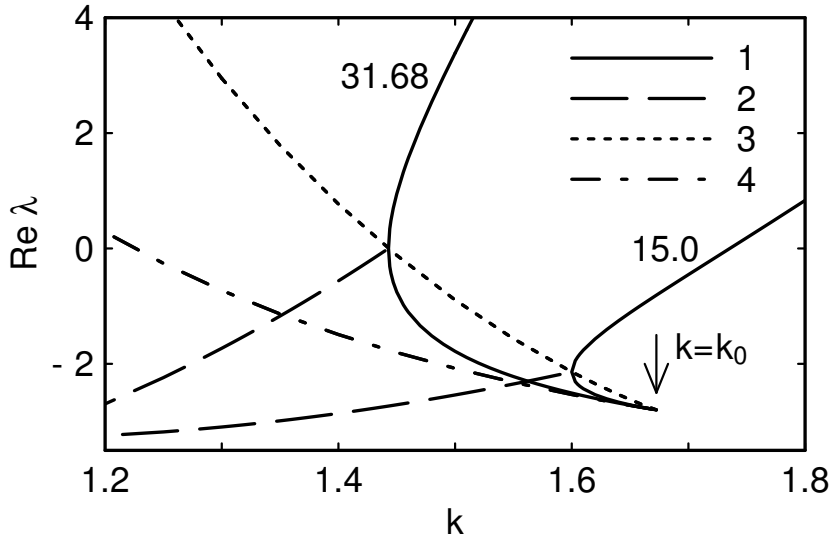

Figure 2.4: The growth rate – wavenumber dependence for $k < k_0$. 1 – the pair of real increments; 2 – the real part of two complex-conjugate increments; 3 – along this curve the two increments converge; 4 – the secondary increment in the infinite field.

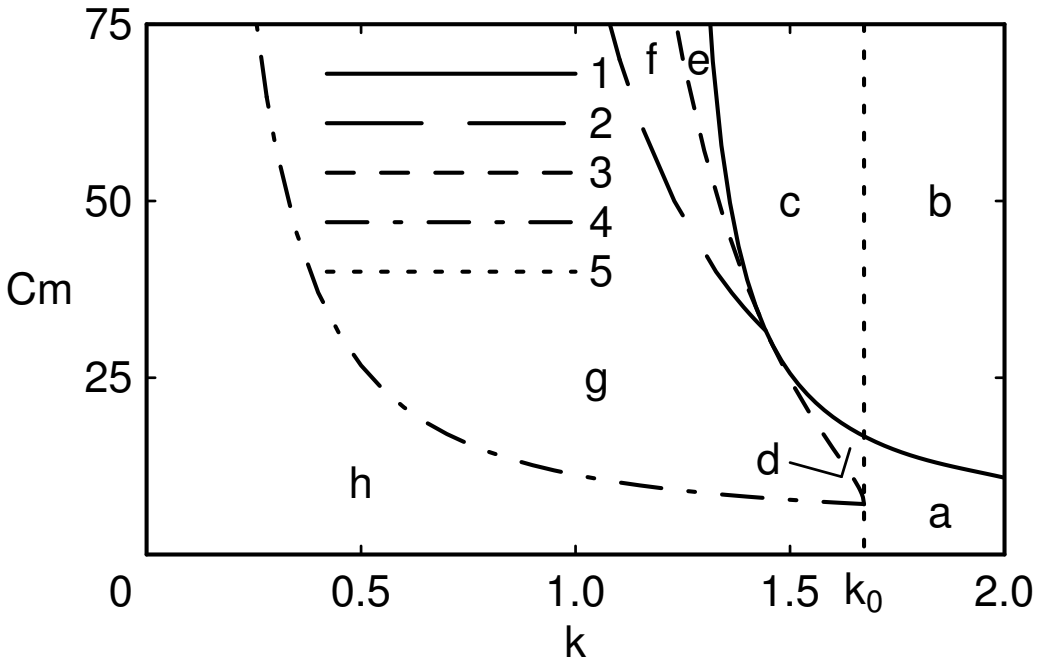

Figure 2.5: The stability diagram and classification of modes. 1, 2 – the neutral curves for the stationary and oscillatory instabilities, respectively; 3 – the boundary of the domain of the oscillatory instability; 4 – the lower boundary ($\Re\mathrm{e}\, s = 0$, $\Im\mathrm{m}\, s \neq 0$) of the region of the discrete spectrum; 5 – $k = k_0$ ($s = 0$). There is one stationary mode in the regions a, b; two stationary modes in c–e; two complex-conjugate oscillatory modes in f, g; no admissible modes in h.

point $k = 1.443$, $\mathrm{Cm} = 31.68$. To the right of this point along the real neutral curve (curve 1 in Fig. 2.5), a perturbation mode (the dominant one in d or the only one in a) loses its stability as Cm increases. On the contrary, since the secondary increment diminishes with the field (see Fig. 2.4), to the left of the point (in e) along the real neutral curve the secondary mode acquires stability as Cm increases. This branch of the neutral curve has an asymptote $k = 1.225$ (i.e. however intense, the field cannot stabilize a long-wave secondary mode, see the curve 4 in Fig. 2.4). The field destabilizes the complex-conjugate modes: the neutral curve 2 in Fig. 2.5 corresponds to a long-wave cutoff. Two complex-conjugate modes imply the presence of an oscillatory convection. Its physical origin will be addressed in §2.3.3. Here we just remark that the convective self-oscillations sought in [146, 147] are very different in that they involve temperature and concentration gradients *across* the cell (as well as additional diffusive effects).

The dispersion relation (2.38) calls for an approximate representation that would enable us to derive simple, explicit asymptotic formulas for some relationships found above. The structure of Eq.(2.38) suggests exploring the limit of large increments rather than a common long-wave expansion. Specifically, the left-hand side of relation (2.38) is asymptotically expanded in s in the limiting case

$$|s| \to \infty\,, \quad |s| \gg 1/k\,. \tag{2.41}$$

The senior terms of the expanded equation read:

$$ks/(2\,\mathrm{Cm}) - s^{-1}F(k) + s^{-2}\left(\ln(ks) + \gamma - 1\right) + \ldots = 0\,, \tag{2.42}$$

where $F(q) = \ln(q/2) + K_0(q) + \gamma$. The first two terms in Eq.(2.42) immediately give a single mode

$$\lambda = -k^2 + 2\,\mathrm{Cm}\,kF(k)\,. \tag{2.43}$$

The diffusive smearing of the perturbations is responsible here for the $-k^2$ term that replaces the known for the immiscible case cubic-in-k damping term in Eq.(3.36) due to the surface tension. Relation (2.43) also reveals the fact that the diffusion is of no influence when $\mathrm{Cm} \to \infty$ (for the $-k^2$ term becomes negligible) and that the diffusion coefficient D drops out from the dimensional growth increment – magnetization dependence. In other words, $h^2/(\mathrm{Cm}\,D) = h^2\tilde{\alpha}/(\tilde{c}m_0)^2$ should be chosen as a true time scale of the instability. In a strong field the new scale becomes much less than several hours (the typical value of h^2/D). In the $\mathrm{Cm} \to \infty$ limit from Eq.(2.43) one recovers the result of [101] for the comb-like instability in zero gravity

and with zero surface tension. (The only difference is a factor of 2, which is due to the inviscid nature of the non-magnetic ambient liquid used in [101], i.e. $a_2 = 0$.) It can be inferred also that the QSSA validity must improve as $\mathrm{Cm} \to \infty$, since the time scale of perturbations varies inversely with Cm, whereas the basic distribution is Cm independent. The results of [101] required no QSSA at all.

In the second approximation we solve the three-term Eq.(2.42) to find at a small k some important corrections to Eq.(2.43). If Cm is large enough for the given k, another real s to satisfy Eq.(2.42) exists (the secondary mode). As Cm increases, this s asymptotically approaches from above a constant value $4/k^2$ (which corresponds to the curve 4 of Fig. 2.4), while the dominant eigenvalue (2.43) increases without bound. On the contrary, if the field decreases, the two roots approach one another and converge at $s = 6/k^2$ (curve 3 of Fig. 2.4) with $1/\mathrm{Cm_B} = (1/216)k^5(-\ln k)$ (curve 3 of Fig. 2.5). The roots become complex-valued and conjugate. As the field decreases further, the frequency of oscillations grows rapidly and attains a maximum of $\Im\mathrm{m}\,\lambda \approx 20/k^2$ at about half the $\mathrm{Cm_B}$. The pair of oscillatory modes gains stability at $(2/27)\mathrm{Cm_B}$, having $\Im\mathrm{m}\,s \approx \Re\mathrm{e}\,s = 2/k^2$ (i.e. the frequency of the neutral oscillations is asymptotically $\Im\mathrm{m}\,\lambda = 8/k^2$), which corresponds to the curve 2 of Fig. 2.5. Thus, given a fixed $k \ll 1$, the range of unstable oscillations covers about a *decade* in Cm. (However, the oscillatory mode is not dominant at a fixed large Cm.) Finally, at much lower Cm values, the solutions fail to satisfy the conditions (2.41); indeed, on the boundary of the domain of the discrete spectrum (curve 4 of Fig. 2.5) we have $k\,\Im\mathrm{m}\,s \sim 1$ ($\lambda \sim -1$).

The validity of the presented asymptotic analysis was verified, among many other means, by direct evaluation of the dispersion relation.

2.3.3 Physical mechanism of oscillations[9]

In this paragraph we attempt to explain the mechanism of the instability in physical terms. To this end, a feedback is established between a driving force and the motion it causes. For clarity, we analyze the case of no displacement. We will be using primed capitals to denote a fully qualified perturbation: $c - c_0 \sim C'(x, y, t) = \Re\mathrm{e}\,[c'(x)\exp(\lambda t)]\cos(ky)$, etc. Let us consider the

[9] "The apparent indication of some form of instability or growth by the linearized plane wave analysis requires rather more by way of interpretation than might at first sight be supposed." (P. C. Clemmow and J. P. Dougherty, *Electrodynamics of Particles and Plasmas*, Addison-Wesley, 1969, §6.1.1.)

linearized dimensionless Eqs.(2.3) and (2.13):

$$-\vec{\nabla}P' - \alpha\vec{V}' + \vec{F}_1' + \vec{F}_2' = 0\,, \tag{2.44}$$

where $\vec{F}_1' = -2\,\mathrm{Cm}\,C'\vec{\nabla}\psi_0$, $\vec{F}_2' = -2\,\mathrm{Cm}\,c_0\vec{\nabla}\Psi'$, and $\vec{V}' = \{V_x', V_y'\}$. The perturbation $\vec{F}_2'$ of the magnetic force is peculiar to plane layers of polarizable media in a perpendicular field, and we are not aware of instabilities of different origin driven by an analogous force. We note that $F_{1\,y}' = 0$, and at $x = 0$ additionally $F_{2\,x}' = 0$ (eigenfunctions V_x', C', and Ψ' have all been found to be even in x). Importantly, it is only at the interface that the velocity field has direct influence upon the concentration and thus is of interest for our purposes.

If the stationary instability sets in, the mechanism seems rather clear. Close enough to the interface, a positive concentration perturbation C' gives rise to a force in the x-direction: $F_{1\,x}' > 0$. The force naturally induces a likewise-directed velocity disturbance ($V_x' > 0$). This velocity advects inhomogeneous basic concentration at $x = 0$ (Eq.(2.28)) so as to increase the concentration perturbation. Diffusive smearing competes the self-intensification (as expressed by Cm). All in all, a "superparamagnetic" ferrofluid parcel is entrained into a stronger resulting field, i.e. into the region of smaller demagnetizing influence of MF. (This is the case for the above-mentioned thermomagnetic instability [142] as well.)

Now we turn to the intriguing nature of a self-sustained oscillatory convection that is also predicted for the system. We begin with establishing an overall pattern of the normal modes that is exemplified by Fig. 2.6. An oscillating x-component of the velocity causes by turns positive and negative concentration variations at the interface. The variations are spread outwards by diffusion and form two semi-infinite sequences of vanishing spots. The spots are alternately either rich or deficient in suspended matter, with new spots being continuously "born" at $x = 0$ (as shown in Fig. 2.6). The process reminds one of "heat waves", or also of a one-dimensional diffusion over a semi-axis with an oscillating source at the end-point. Specifically, according to Eq.(2.31),

$$C' = A\exp(\mu t - ak|x|)\cos(bk|x| - \omega t)\cos(ky)\,, \tag{2.45}$$

where $s = a + ib$ and $\lambda = k^2(s^2 - 1) = \mu + i\omega$. Essential is that the sequences propagate *away* from $x = 0$ (in both directions) at a velocity $w = \omega/(bk) = 2ak > 0$. As for the velocity $\vec{V}'$, from the curl of Eq.(2.44) it may be seen that concentration spots at $x \neq 0$ owing to $\vec{F}_1'$ are associated with the local flow vorticity $\mathrm{rot}_z(\alpha\vec{V}') = 2\,\mathrm{Cm}\,(\partial\psi_0/\partial x)\,\partial C'/\partial y$. According

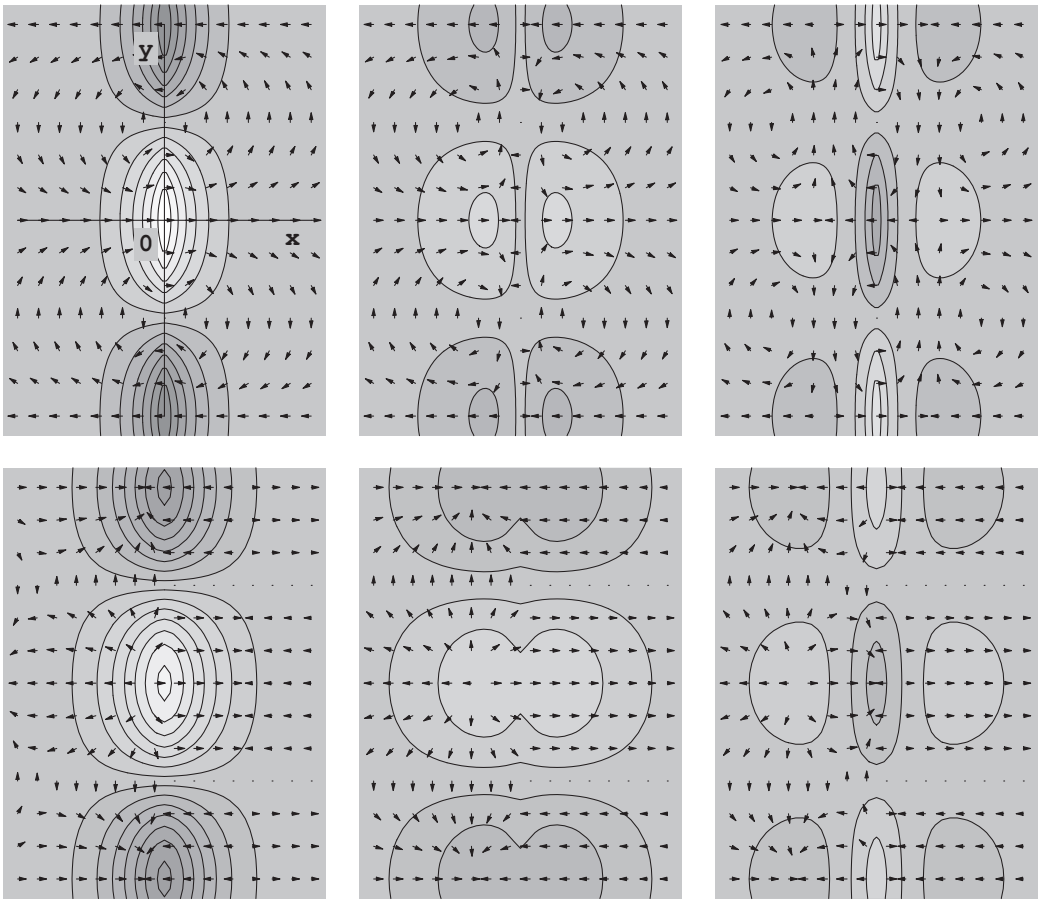

Figure 2.6: Example of an oscillatory perturbation mode ($t_0 = 0$, the Darcy approximation, $k = 1.2$, Cm $= 53.88$, neutral, of a period $T = 1.246$) plotted over $k|y| \leqslant \pi$, $k|x| \leqslant 3\pi/4$. Upper panels: concentration (*contours*) and velocity (*arrows*). Lower panels: the field potential (*contours*) and the density of the magnetic force $\vec{F}_1' + \vec{F}_2'$ (*arrows*). Light and dark areas correspond to positive and negative values, respectively. Arrow lengths depend non-linearly on vector magnitudes. Left to right: $t = 0$; $T/4$; $T/3$. By $t = T/2$, the $t = 0$ pattern is exactly inverted throughout. The basic concentration is non-zero at the left-hand side of every panel ($x < 0$).

to Eq.(2.30), the velocity component V_y' is discontinuous at the interface (it changes sign), so it is set to zero at $x = 0$ when plotting Fig. 2.6.

What is the restoring force reversing the velocity at $x = 0$? Such reversal is evidently important for the overall pattern inversion. As stated above, the direct action of the magnetic force at $x = 0$ is always to amplify the concentration perturbation. Then Eq.(2.44) leaves the only possibility: the pressure gradient across the interface may oppose the force, and $\partial P'/\partial x$ is periodically larger in magnitude than $F_{1\,x}'$. (The latter was never the case with the stationary instability). One local origin of the counter-pressure may be easily identified. By ensuring the flow incompressibility, the pressure involves the y-component $F_{2\,y}'$ of the force into balance. This $F_{2\,y}'$ is zero outside MF, but inside MF it is directed against $\vec{\nabla}\Psi'$ (Fig. 2.6), i.e. approximately against $\vec{\nabla}C'$ (since Ψ' is a smoothed version of C'). Along this side of the interface, the force tends to stretch y-wise the region of positive C', thereby creating a depression inside MF that favours an inward motion and hence the transport of negative C'. In like manner, if C' is negative, an excess pressure induced inside MF would provide a positive $\partial C'/\partial t$. Thus the oscillatory regime is indirectly enabled by $F_{2\,y}'$.

In the above analysis a weak divergence of $F_{1\,x}'$ at $x = 0$ has been left out of account. However, an integrable force density may be redistributed over an arbitrarily narrow stripe containing the interface line, which would not affect our conclusions. This applies also to the counter-pressure gradient. Note that $F_{1\,x}' - \partial P'/\partial x$ remains finite as $x \to 0$.

Obviously, oscillations are possible so far as certain phase relations exist between the velocity, competing forces, and concentration. The eigenfunctions are out of phase even if taken at the same point. Indeed, Eq.(2.45) at $y = 0$ and $x = 0$ becomes simply $C' = A\exp(\mu t)\cos(\omega t)$. However, from the jump condition (2.28) it follows that at this point $V_x' = 2Ak\,\Re\mathrm{e}\,[s\exp(\lambda t)] = 2Ak|s|\exp(\mu t)\cos(\omega t + \arg s)$. The velocity disturbance is always ahead of the concentration (with the time difference $(\arg s)/\omega$). This may be noticed in Fig. 2.6: at a quarter period, the concentration must be exactly zero at $x = 0$, but the velocity has the "negative" direction already and has worked for some time to decrease C' locally. This phase shift must also be attributed to the pressure, for the x-component of the magnetic force oscillates in phase with the concentration. Since $\partial P'/\partial x$ and $\alpha V_x'$ sum to make a force of a zero lag, it is quite evident that the pressure must fall behind with C'. (Strictly speaking, since the force is divergent at $x = 0$, the pressure gradient is a sum of an unbounded part that must be in phase with the force, and a finite part that lags behind.) The importance of the $F_{2\,y}'$ contribution to the pressure at $x = 0$ has been established above. The force $F_{2\,y}'$ is determined

by the perturbation of the field potential Ψ'. But Ψ' *must* lag behind the concentration at $x = 0$ for the following simple reason: it is defined through a smoothing (over x) integral operator acting upon a specific time-dependent concentration distribution. Namely, the concentration inhomogeneities travel away from $x = 0$, so that averaging across the interface involves the earlier-delivered ones. Therefore the potential at $x = 0$ falls behind with C', and the time lag may be easily expressed as $-[\arg J(s,k)]/\omega > 0$. In particular, at a quarter period the potential at the interface is non-zero yet. In short, after $\vec{F}_1'$ and diffusion have worked to produce a large enough concentration spot, $\vec{F}_2'$ takes over and initiates the reversion.

On the whole, self-oscillations occur through the spatial and temporal interplay between diffusion and advection, with the latter being driven by concentration inhomogeneity (via the magnetic force). Since diffusion is crucial for such oscillations to occur, they are absent in the well-studied immiscible case.

2.3.4 Labyrinthine instability of a diffused interface: numerical stability analysis

One might expect the stability features found for small k in §2.3.2 to persist in the case of the more general Brinkman equation. Unfortunately, it is for the weakly diffused interfaces that our numerical results for the Darcy approximation prove rather different from those obtained without it.

The case $t_0 > 0$ is studied both in the Darcy approximation ($L^2 \gg h^2$) and without it. The viscosity is assumed constant. To obtain an algebraic eigenvalue problem from Eqs.(2.4), (2.21)–(2.23), the spatial derivatives are approximated (with the second order) with finite differences, while the involved integral operator with a logarithmically singular kernel is handled as follows. The logarithm is subtracted from the kernel and a simple quadrature rule based on it as a weight function is constructed; the rule is exact for piecewise-linear integrand functions; a smooth remainder is integrated by the trapezoidal rule. To be resolved are several spatial scales: of the basic concentration distribution; of the basic field [which vanishes as $1/x^2$ for $|x| \gg \max(1, \sqrt{t_0})$]; of the perturbations [in a weak field these extend beyond $1/k$, see Eq.(2.31)]. This is partially achieved by adopting a non-uniform grid. Grid points are uniformly distributed along the z axis, where $z = x/\sqrt{x^2 + a^2}$ is a transform of the physical coordinate x (along the basic-state gradients). In the present calculations we take $a = \sqrt{t_0} + 5 + 5/k$ with N grid points. The results are checked against the change in N. Normally we focus upon the dominant mode. The spectrum of the resulting matrix

Cm	Wavenumber k								
	0.14	0.2	0.3	0.5	0.7	1.0	1.4	2.0	3.0
300	2*	2*	2* / 2	3	3 / 2	3 / 2	3 / 2	3 / 2	3 / 2
150	2*	2*	2*	2	3 / 2	2	2	3 / 2	3 / 2
100	2*	2*	2*	2* / 2	3 / 1	2	2	2	3 / 2
75	2*	2*	2*	2* / 2	2 / 1	2 / 1	2	2	2
50	0	2*	2*	2* / 2	2 / 1	1	2 / 1	2	2
30	0	0	2*	2* / 2	2 / 1	1	1	2 / 1	2 / 1
20	0	0	0	2*	2* / 1	1	1	1	2 / 1
10	0	0	0	0	2* / 1	1	1	1	1
5	0	0	0	0	0 / 1	1	1	1	1
3	0	0	0	0	0 / 1	1	1	1	1

Table 2.1: The number of numerical modes at $t_0 = 0.01$ for various k, Cm values. The Darcy and Brinkman results, where different, are separated by a slash. An asterisk denotes two complex-conjugate modes (counted both in the preceding number). The case $k = 0.14$ is computed with N=320; for other columns N=288. To compare with Fig. 2.5 (p. 42).

becomes quite "dense" for $t_0 > 1$, which prevents from efficient solving by power method for just this mode alone. We resort to a standard eigenvalue finder to calculate the whole discrete spectrum. The cases explored include t_0=0.01; 0.03; 0.1; 0.3; 1; 3; 10; 30; 100 with k in the range $0.05 \ldots 20$ (17 values) and Cm in the range $3 \ldots (3 \times 10^4)$ (32 values). Many Figures to be introduced in this paragraph are curve fits of the pointwise data.

For the smallest t_0 values we numerically obtain a satisfactory agreement with our Darcy analytic findings. In particular, the absence of the discrete modes (region h in Fig. 2.5) indeed manifests itself as an absence of the matrix eigenvalues satisfying $\Re\mathrm{e}\, s > 0$. The number of eigenvalues given by both numerical codes is listed in Table 2.1 for the smallest t_0 tried.

Given fixed t_0, k, and Cm, a rough threshold value of N exists such that the number of modes does not change upon further grid refinement. The smaller t_0 and k, the higher the threshold, which makes the respective results computationally more expensive. As t_0 increases, the oscillatory "tongue" on the k, Cm plane (regions f, g in Fig. 2.5) shrinks and shifts to smaller wavenumbers, and the domain of no modes (region h) behaves correspondingly. As early as at $t_0 = 1$, even with our best resolution $N = 320$, we could locate neither oscillatory modes nor the absence of any modes in the whole k range, while both were still present at $t_0 = 0.3$, $k \leqslant 0.2$. Exam-

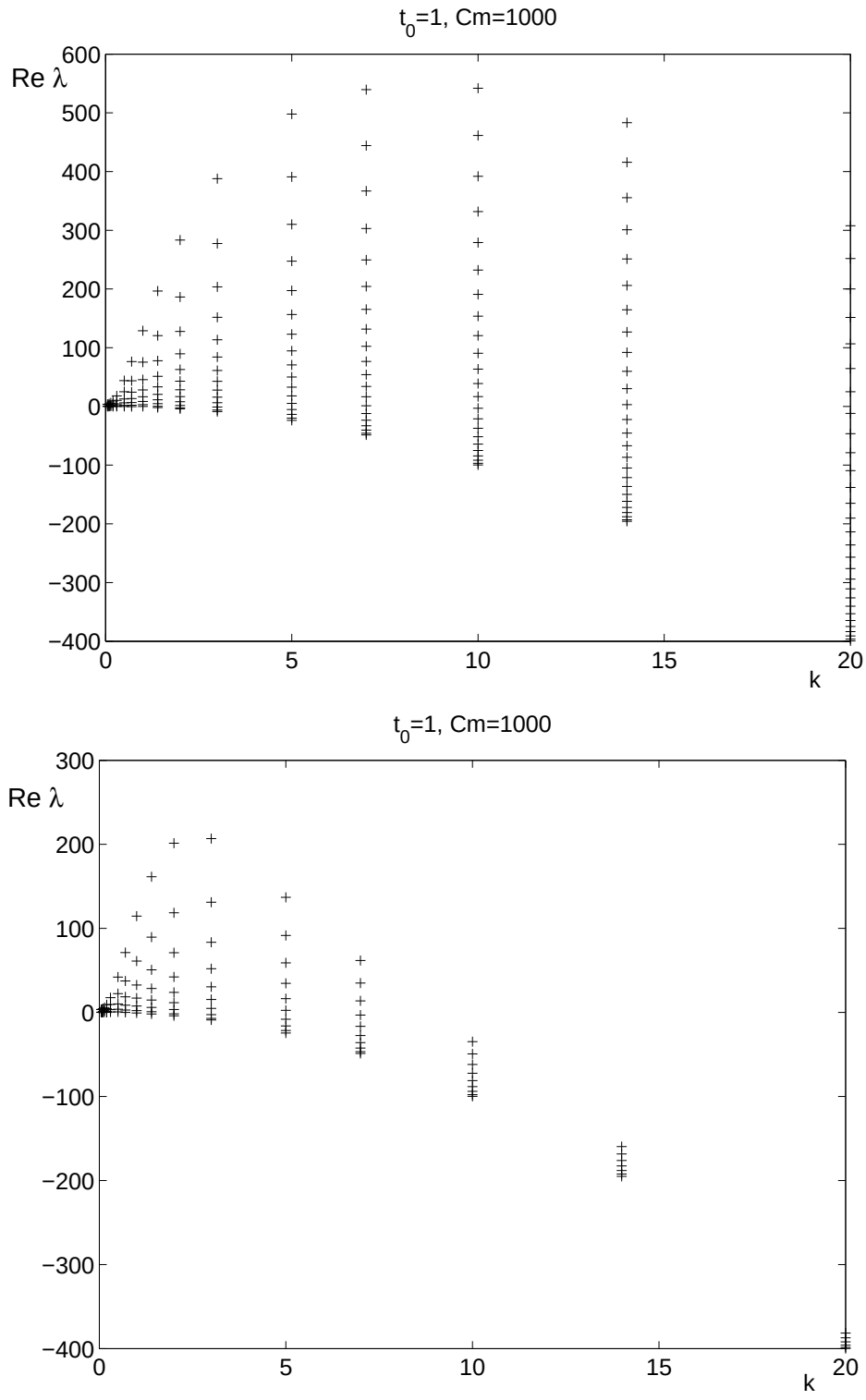

Figure 2.7: An example of the full (discrete) spectrum of growth increments: the Darcy law (top) and the Brinkman equation (bottom). N=160, $t_0 = 1$, $\mathrm{Cm} = 1000$.

ining the numerical oscillatory modes, and both Darcy and Brinkman ones, suggests that at $t_0 > 0$ the presented mechanism of oscillations does not change essentially. For $t_0 \geqslant 1$ all the numerical modes are stationary, and their number increases with t_0 and Cm (being artificially limited by N). For the Darcy case, the number also increases with k. As to the Brinkman case, the number follows more or less the Darcy pattern for small k, but attains a maximum at some k value, being at larger k well lower than it is in the Darcy case (Fig. 2.7).

The growth increment of the dominant mode is plotted in Figs. 2.8, 2.9. For the Darcy approximation we observe an unlimited shift of the most dangerous wavelength towards the successively shorter scales as the field increases, which invalidates the approximation for a weak field already. Besides, large-k concentration being gap-invariant contradicts intuition, especially in the miscible case. Relaxing the Darcy approximation inhibits the instability at shorter scales and leads to a new effect: as Cm increases, the most dangerous wavelength tends to a limiting value that is of the order of h, or unity in the dimensionless notation (Fig. 2.10), and that weakly depends on the thickness of the diffused interface (Fig. 2.11). It remains to be seen how this wavelength dynamics is related to finger coarsening at early stages (cf. [113] for the Darcy case). The linearly most dangerous wavelength is often compared against the typical length of a non-linear pattern. Unfortunately, the latter cannot be recovered with certainty from the experimental photographs [1]. However, if we admit that they all are of the same scale, the typical length may be estimated to be as small as about one third of the gap width (thus considerably smaller than allowed by Figs. 2.10, 2.11). In this case the assumption of a gap-invariant concentration is questionable, though it may be argued that the apparent length scale might have decreased by a tip-splitting at a non-linear stage.

For both the Darcy and the Brinkman cases, the growth rates are asymptotically ($\mathrm{Cm} \to \infty$) linear in Cm for any fixed k value. As a function of k, the rescaled by Cm growth rate in the Brinkman case approaches a limiting curve as $\mathrm{Cm} \to \infty$ (plotted in Fig. 2.12; cf. Fig. 3 of [88]), while the growth increment of the most dangerous wavelength roughly scales as Cm/t_0 for $t_0 \geqslant 1$ (Fig. 2.13). Relative to QSSA it deserves mentioning that the rate of change of the basic state $(1/c_0)\,\partial c_0/\partial t_0$ is independent of Cm and decreases as $1/t_0$ at $x = \sqrt{t_0}$, but not slower than $t_0^{-3/2}$ for any fixed x. Strictly speaking, we can expect QSSA to hold if $1/|\lambda| \ll c_0/\left(\partial c_0/\partial t_0\right) = \sqrt{\pi} t_0\, \mathrm{erfcx}(\xi)/\xi$ for all range of $\xi = x/(2\sqrt{t_0})$ wherein the solution is localized (which is obviously not the case with a sharp interface). The function $\mathrm{erfcx}(z)$ is defined as $\mathrm{erfcx}(z) = \exp(z^2)\,(1 - \mathrm{erf}(z))$ and thus asymptotically $\mathrm{erfcx}(z)/z \sim 1/(\sqrt{\pi} z^2)$ as $z \to$

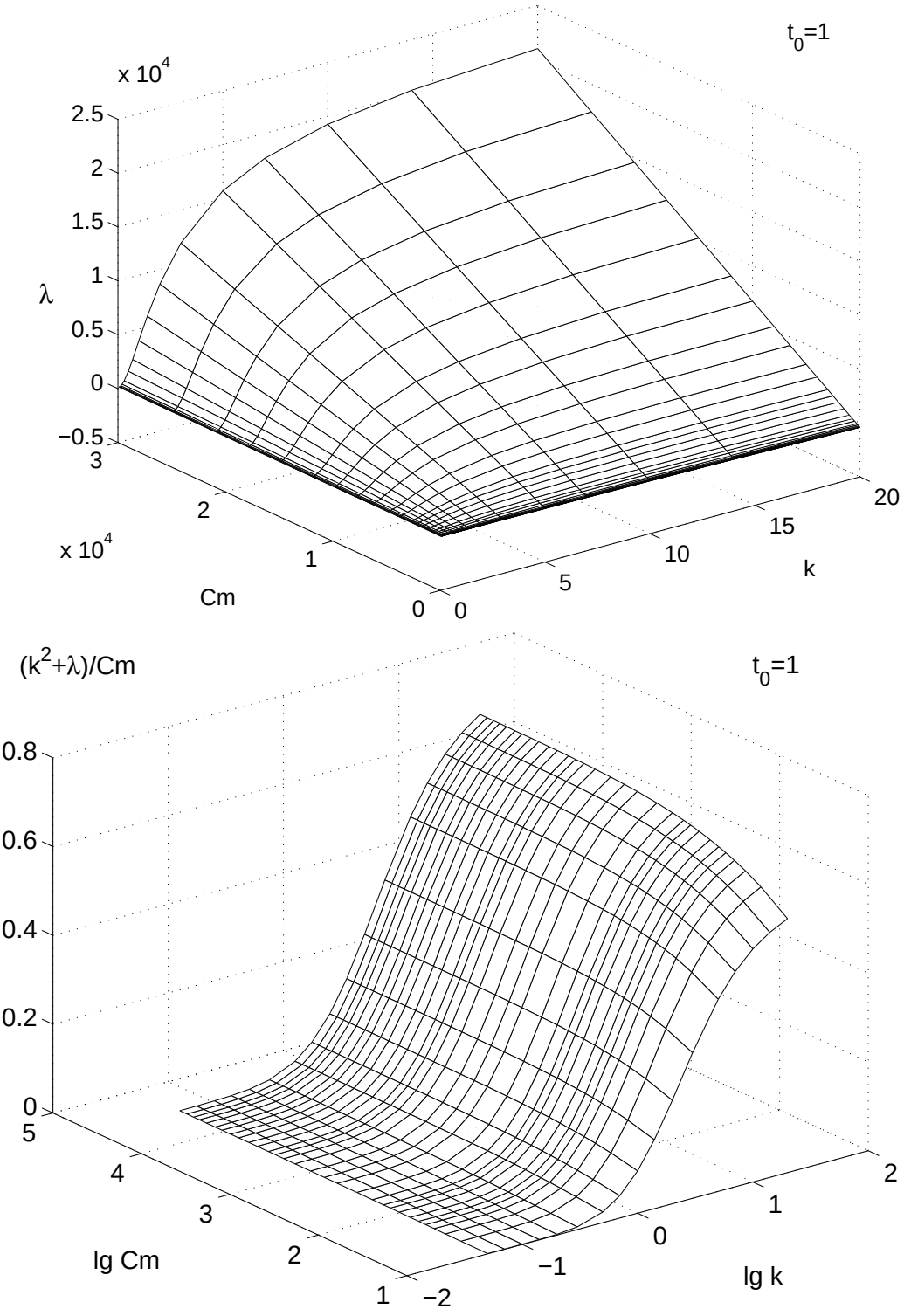

Figure 2.8: The dominant mode for the Darcy equation. N=160, $t_0 = 1$.

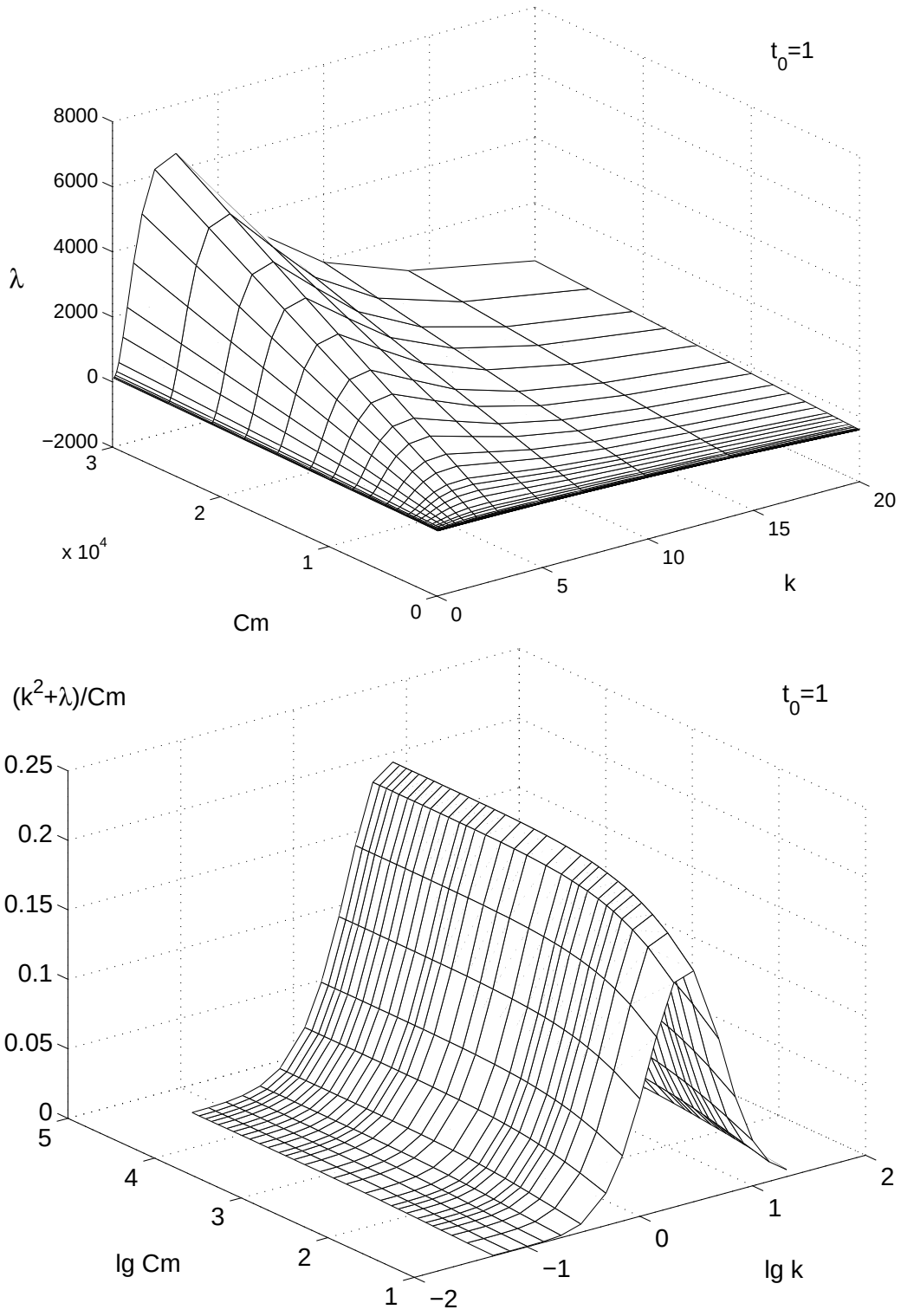

Figure 2.9: The dominant mode for the Brinkman equation. N=160, $t_0 = 1$.

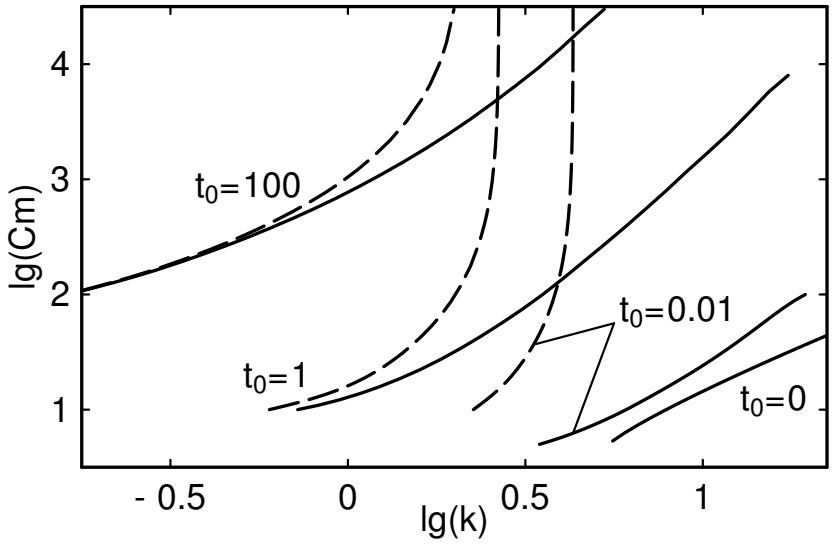

Figure 2.10: The most unstable wavenumber: Darcy (*solid lines*) vs. Brinkman (*dashed lines*). Results for the diffused interfaces are numerical; the Darcy result for $t_0 = 0$ is obtained analytically. N=160 (N=256 if $t_0 = 0.01$).

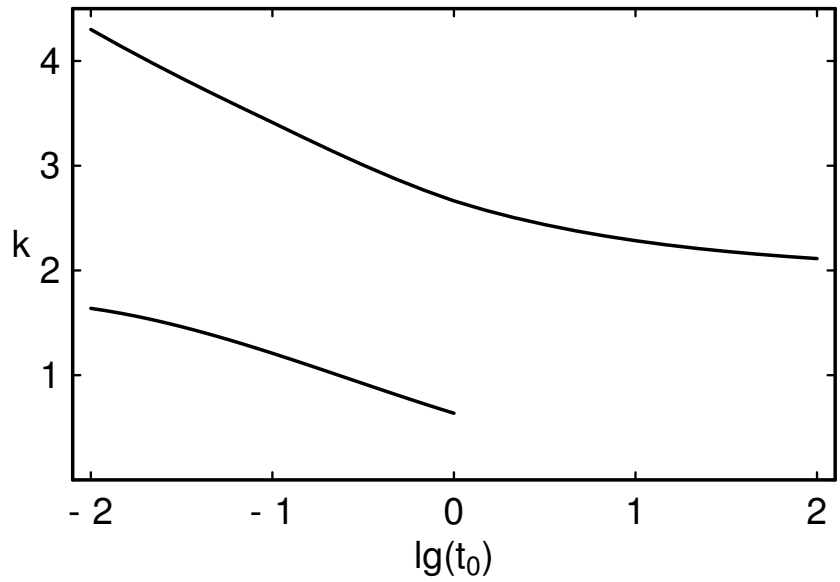

Figure 2.11: The asymptotic (Cm $\to \infty$) most unstable wavenumber (*top*) and the critical wavenumber (*bottom*) vs. the diffusion time. The Brinkman case (N=160).

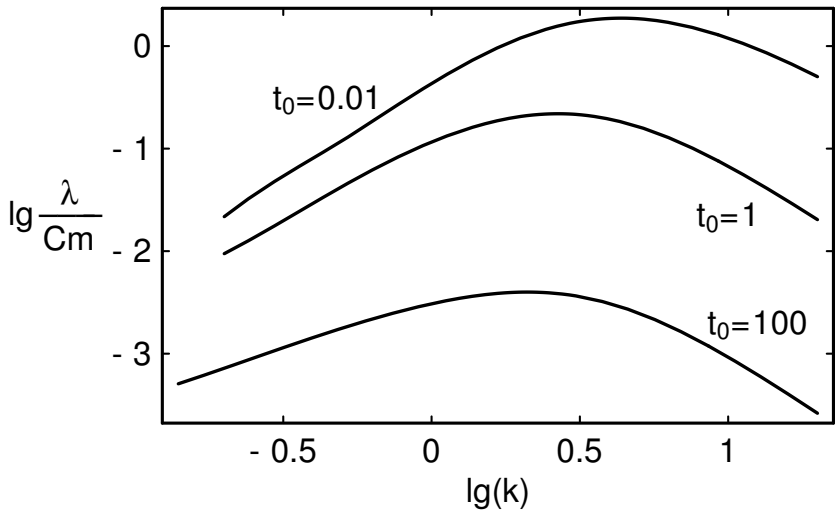

Figure 2.12: The asymptotic (Cm $\to \infty$) growth increment – wavenumber dependence in the Brinkman case. N=160 (N=256 if $t_0 = 0.01$).

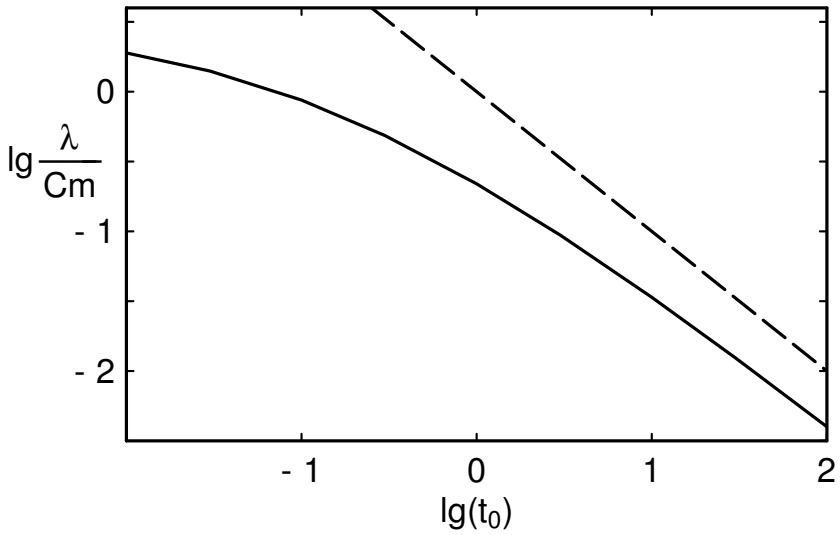

Figure 2.13: Variation of the asymptotic (Cm $\to \infty$) increment of the most unstable mode with the diffusion time t_0 in the Brinkman case (*solid line*, N=160); the $1/t_0$ apparent scaling (*dashed line*).

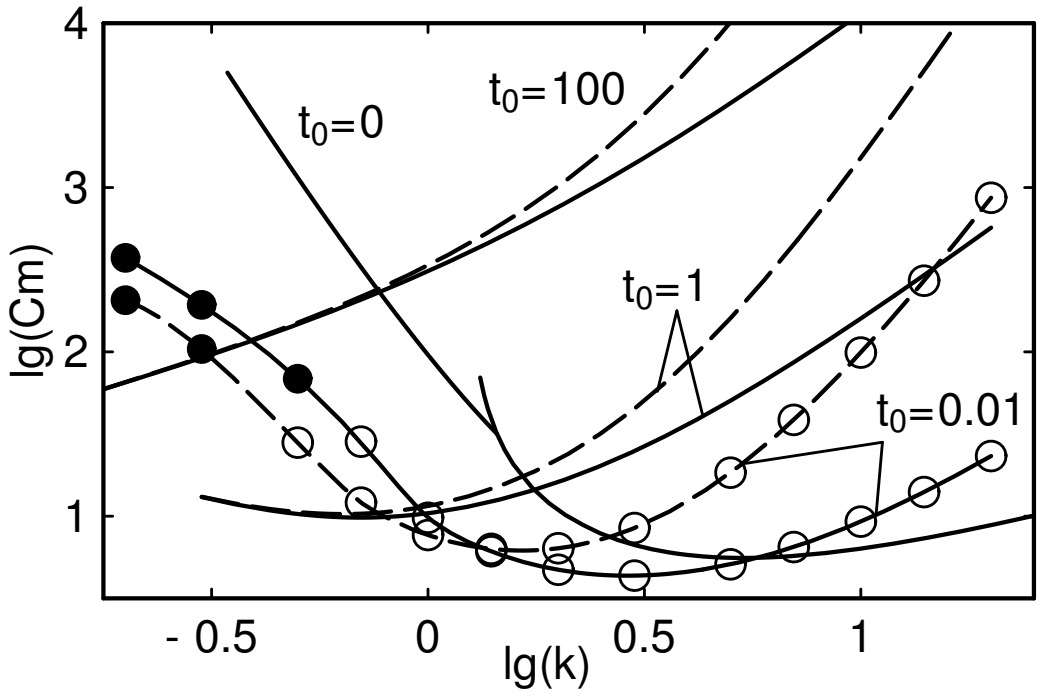

Figure 2.14: Evolution of the Darcy neutral curves (*solid lines*) vs. Brinkman ones (*dashed lines*) as the interface diffuses. The $t_0 = 0$ Darcy curve is obtained analytically (Fig. 2.5). On the $t_0 = 0.01$ curves (N=256), empty circles denote a stationary mode, while the filled ones stand for an oscillatory pair. The other neutral curves (N=160) correspond to stationary modes.

$+\infty$ and $\mathrm{erfcx}(z)/z \sim 1/z$ as $z \to +0$.

As the basic state diffuses out, the critical wavenumber decreases somewhat (Fig. 2.11). Fig. 2.14 presents the neutral curves and leads to the following conclusions about the long-wave perturbations ($k < 1$). First, it is only when t_0 is not small that the inequality $\|\mathrm{d}/\mathrm{d}x\| \ll 1$ holds for the eigenfunctions, so that the Brinkman case reduces to the Darcy one. Fig. 2.10 brings more evidence to this point. Conversely, when the interface is sharp enough, higher velocity derivatives in Eq.(2.22) (and additional boundary conditions for the discontinuous problem) come into play if the Brinkman formulation is employed. Table 2.1 ($t_0 = 0.01$) also exhibits the difference in the number of modes between the cases. Secondly, Fig. 2.14 demonstrates that the interface smearing at an early stage diminishes the stability of the long-wave perturbations. Moreover, they are more unstable for the Brinkman-governed system than for the Darcy-governed one, i.e. adding more dissipation reduces stability. This is not impossible, a celebrated example, though distant one, being the inertial instability (governed by the Orr-Sommerfeld equation) of the viscous planar Poiseuille flow which is stable in the inviscid limit (by the Rayleigh's inflection-point theorem). In the case of the Rayleigh–Taylor instability with miscible fluids, however, analytical dispersion relations are available at $t_0 = 0$ for both Brinkman and Darcy formulations [88], and in the Darcy case the increment appears to be always higher than in the Brinkman case. Finally, we note that the numerically obtained critical Cm for $t_0 = 0.01$ in the Darcy approximation is somewhat lower than the analytically obtained $\mathrm{Cm}_{\mathrm{cr}}$ for the sharp interface. The possibly destabilizing effect of the basic-state diffusion at its early rapid phase was also observed, and also with QSSA, in [39, 38] (cf. also Fig. 18 of [87]). The critical Cm – t_0 dependence will be shown later (Fig. 2.21).

2.4 The peak instability in a Hele-Shaw cell

In the next four paragraphs,[10] we will consider the uniform external magnetic field $\vec{H}_0$ applied in the plane of the cell normally to the interface (along the x-axis, Fig. 2.1). The equations of §2.1 hold, but the gap-averaged density of the magnetostatic body force $\vec{f}_{\mathrm{m}}$ is now given by Eq.(1.26) as

$$\vec{f}_{\mathrm{m}} = -m_0 c \vec{\nabla} \frac{\partial \psi}{\partial x}\,, \tag{2.46}$$

[10]The results of §2.4.1 were mostly published in [148], the results of §§2.4.2–2.4.4 were published as [149]. Besides, all this was presented as [150].

where m_0 is the average magnetic moment of a particle along $\vec{H}_0$. (The particles are non-interacting.) The gap-averaged potential ψ of the self-magnetic field of MF ($\vec{H} = \vec{H}_0 - \vec{\nabla}\Psi$, $\psi =< \Psi >$) reads by Eq.(1.25):

$$\psi = -\frac{m_0}{h} \int_0^h \mathrm{d}z \int_0^h \mathrm{d}z' \int_{-\infty}^{+\infty}\int_{-\infty}^{+\infty} \frac{\partial c(x',y')}{\partial x'} \frac{\mathrm{d}x'\,\mathrm{d}y'}{\left((x-x')^2+(y-y')^2+(z-z')^2\right)^{1/2}} \,. \tag{2.47}$$

2.4.1 Perturbation analysis and a sharp interface in the normal field

In this paragraph, we undertake the stability analysis for a sharp interface under the normal field. The analysis follows largely the lines of §2.3.1 (and §2.2). We again non-dimensionalize Eqs.(2.2), (2.3), (2.46), and (2.47) introducing h and h^2/D as space and time scales, respectively. The concentration, magnetic potential, viscosity, friction coefficient, and pressure are scaled with their respective reference values $\tilde{c}$, $\tilde{c}m_0h$, η, α, and αD. The existing notation is kept for the dimensionless variables.

Let us consider the linear stability of the quiescent state for some concentration distribution $c = c_0(x,t_0)$ in the external field $\vec{H}_0$. We again employ the quasi-stationary-state approximation (QSSA) and "freeze" the coefficients of linearized equations to simplify significantly the analysis. We introduce two-dimensional normal modes: $c(x,y) = c_0(x,t_0) + c'(x)\,\mathrm{e}^{\imath ky+\lambda t}$, $\vec{v} = \vec{v}\,'(x)\mathrm{e}^{\imath ky+\lambda t}$, etc. The linearized Eqs.(2.3), (2.46) are

$$-v_x' - \frac{\mathrm{d}p'}{\mathrm{d}x} - \mathrm{Cm}\,c'\frac{\partial^2\psi_0}{\partial x^2} - \mathrm{Cm}\,c_0\frac{\mathrm{d}^2\psi'}{\mathrm{d}x^2} = 0\,, \tag{2.48}$$

$$-v_y' - \imath kp' - \mathrm{Cm}\,\imath kc_0\frac{\mathrm{d}\psi'}{\mathrm{d}x} = 0\,. \tag{2.49}$$

Expressing v_y' by incompressibility from Eq.(2.5) and the pressure perturbation p' from Eq.(2.49), one rewrites Eq.(2.48) as

$$\frac{1}{k^2}\frac{\mathrm{d}}{\mathrm{d}x}\left[-\frac{1}{12}\frac{\mathrm{d}^3v_x'}{\mathrm{d}x^3} + \left(\frac{k^2}{12}+1\right)\frac{\mathrm{d}v_x'}{\mathrm{d}x}\right] + \frac{1}{12}\left(\frac{\mathrm{d}^2v_x'}{\mathrm{d}x^2} - k^2v_x'\right) - v_x' - \mathrm{Cm}\left(c'\,\frac{\partial^2\psi_0}{\partial x^2} - \frac{\partial c_0}{\partial x}\,\frac{\mathrm{d}\psi'}{\mathrm{d}x}\right) = 0\,. \tag{2.50}$$

Eq.(2.4) is the linearized equation for the concentration perturbation. From

Eq.(2.47) the derivative of the potential follows as

$$\frac{\partial\psi}{\partial x} = 2\int\limits_{-\infty}^{+\infty}\int\limits_{-\infty}^{+\infty}(x-x')\frac{\partial c}{\partial x'}\,J\left(\sqrt{(x-x')^2+(y-y')^2}\right)\,\mathrm{d}x'\,\mathrm{d}y' \qquad (2.51)$$

with $J(\rho) = (\sqrt{\rho^2+1}-\rho)\Big/\rho^2$. Then the magnetic potential ψ_0 induced by the basic distribution $c_0(x,t_0)$ is given by

$$\frac{\partial\psi_0}{\partial x} = 2\int\limits_{-\infty}^{+\infty}\frac{\partial c_0}{\partial x'}\,\left[2\arctan\frac{1}{x-x'} - (x-x')\ln\left(1+\frac{1}{(x-x')^2}\right)\right]\mathrm{d}x'\,, \qquad (2.52)$$

so that

$$\frac{\partial^2\psi_0}{\partial x^2} = 4\pi\frac{\partial c_0}{\partial x} - 2\int\limits_{-\infty}^{+\infty}\frac{\partial c_0(\xi+x)}{\partial\xi}\ln\left(1+\frac{1}{\xi^2}\right)\,\mathrm{d}\xi\,. \qquad (2.53)$$

The field perturbation is also calculated from Eq.(2.51) as

$$\frac{\mathrm{d}\psi'}{\mathrm{d}x} = 4\int\limits_{-\infty}^{+\infty}(x-x')\frac{\mathrm{d}c'}{\mathrm{d}x'}\,J_0(x-x',k)\,\mathrm{d}x' = 4\pi c' + 4\int\limits_{-\infty}^{+\infty}c'(\xi+x)J_1(\xi,k)\,\mathrm{d}\xi\,, \qquad (2.54)$$

where $J_1(\eta,k) = \mathrm{d}\,(\eta J_0(\eta,k))/\,\mathrm{d}\eta - \pi\delta(\eta)$ is only logarithmically singular, and

$$J_0(\xi,k) = \int_0^\infty \cos(k\zeta)\,J\left(\sqrt{\zeta^2+\xi^2}\right)\,\mathrm{d}\zeta\,.$$

Now we are in position to solve analytically the stability problem for a straight sharp interface if the simpler Darcy law is assumed for the flow instead of Eq.(2.3). The corresponding version of Eq.(2.50) is recovered by omitting the terms that involve division by 12, while other equations of this paragraph remain valid.

Let us consider a step-like concentration distribution: $\partial c_0/\partial x = -\delta(x)$. Then Eqs.(2.52), (2.53) immediately give

$$\left[\frac{\partial\psi_0}{\partial x}\right]_{-0}^{+0} = -4\pi\,, \quad \frac{\partial^2\psi_0}{\partial x^2} = 4\pi\frac{\partial c_0}{\partial x} + 2\ln\left(1+\frac{1}{x^2}\right)\,. \qquad (2.55)$$

At the discontinuity of c_0 additional conditions hold [cf. Eqs.(2.27)–(2.30) in §2.3.1]. Three of them are the same as in the case of the perpendicular field: the continuity of c' and v'_x and $[\mathrm{d}c'/\mathrm{d}x] = v'_x\,[c_0]$. Only the condition for the

jump of the pressure differs. It can be derived by integrating Eq.(2.50) over x along the interval $(-\delta, +\delta)$ and taking the limit $\delta \to 0$:

$$\frac{1}{k^2}\left[\frac{\mathrm{d}v'_x}{\mathrm{d}x}\right]_{-0}^{+0} = \mathrm{Cm}\left(c'(0)\left[\frac{\partial\psi_0}{\partial x}\right]_{-0}^{+0} - \frac{\mathrm{d}\psi'(0)}{\mathrm{d}x}\left[c_0\right]_{-0}^{+0}\right). \tag{2.56}$$

This relation can also be derived as a balance of pressures in the same way as it has been done for the perpendicular field. If one wishes not to deal with magnetic forces divergent at the interface where magnetic properties change, the "magnetic pressure" (§5.2 of [14]) can be introduced instead. Indeed, Eq.(5.23) of [14] translated into the CGS units reads $[p] = 2\pi M_{\mathrm{n}}^2$, where M_{n} is the magnetization normal to the interface. Upon linearization and non-dimensionalization we obtain $[p'] = 4\pi\,\mathrm{Cm}\,c'$. We also have from Eqs.(2.49), (2.5) at $x \neq 0$:

$$p' = -\frac{1}{k^2}\frac{\mathrm{d}v'_x}{\mathrm{d}x} - \mathrm{Cm}\,c_0\frac{\mathrm{d}\psi'}{\mathrm{d}x}\,.$$

Now with Eq.(2.55) we recover Eq.(2.56).

The solution of Eq.(2.4) is again simply

$$c' = A\exp(-sk|x|)\,, \tag{2.57}$$

where $s = \sqrt{1+\lambda/k^2}$ as before. Eq.(2.50) at $x \neq 0$ becomes

$$\frac{1}{k^2}\frac{\mathrm{d}^2v'_x}{\mathrm{d}x^2} - v'_x = 2A\,\mathrm{Cm}\exp(-sk|x|)\ln\left(1+\frac{1}{x^2}\right).$$

The solution of this equation that vanishes at infinity and is continuous at $x = 0$ reads

$$\begin{aligned} v'_x &= C\exp(-k|x|) \\ &\quad - Ak\,\mathrm{Cm}\,\exp(+k|x|)\int_{|x|}^{+\infty}\exp(-kx'(s+1))\ln\left(1+\frac{1}{x'^2}\right)\mathrm{d}x' \\ &\quad - Ak\,\mathrm{Cm}\,\exp(-k|x|)\int_{0}^{|x|}\exp(-kx'(s-1))\ln\left(1+\frac{1}{x'^2}\right)\mathrm{d}x'\,, \end{aligned} \tag{2.58}$$

The boundary conditions on the derivatives of the velocity and concentration then give, respectively,

$$-2Ck - 2Ak^2\,\mathrm{Cm}\,\mathrm{f}\,(k(s+1)) = -4\pi Ak^2\,\mathrm{Cm} + k^2\,\mathrm{Cm}\,\frac{\mathrm{d}\psi'(0)}{\mathrm{d}x}\,, \tag{2.59}$$

$$2As = C - Ak\,\mathrm{Cm}\,\mathrm{f}\left(k(s+1)\right), \tag{2.60}$$

where $\mathrm{f}\,(a)$ is defined by Eq.(2.36).

To obtain a dispersion relation from Eqs.(2.59), (2.60), the field perturbation $\mathrm{d}\psi'(0)/\mathrm{d}x$ must be found from Eq.(2.54):

$$\frac{\mathrm{d}\psi'(0)}{\mathrm{d}x} = 4A(\pi + \hat{J}(s,k)) \tag{2.61}$$

with

$$\hat{J}(s,k) = \int_{-\infty}^{+\infty} \exp(-sk|\xi|)J_1(\xi,k)\,\mathrm{d}\xi\,. \tag{2.62}$$

Then the dispersion relation for the growth increment follows as

$$s/\mathrm{Cm} + \hat{J}(s,k) + \mathrm{f}\left(k(s+1)\right) = 0\,. \tag{2.63}$$

It yields a single monotonous perturbation mode. After some manipulations, it is possible to obtain the neutral curve in the following form:

$$\frac{1}{\mathrm{Cm}} = \frac{\pi}{2} + \frac{2}{3k} - \frac{2-k^2}{3}K_1(k) - \frac{k}{3}K_0(k) + \left(1 - \frac{k^2}{3}\right)\mathrm{Ki}_1\,(k) - \mathrm{f}\,(2k)\,, \tag{2.64}$$

where K_0 is the Macdonald function (2.20),

$$\mathrm{Ki}_1\,(k) = \int_k^\infty K_0(t)\mathrm{d}t\,,$$

and $K_1 = -K_0{}'$. The neutral curve is shown in Fig. 2.15. For $k \to 0$ it may be expanded as

$$\frac{1}{\mathrm{Cm}} = k\Big(\frac{5}{2} - \gamma - \ln(8k) + O(k)\Big)\,. \tag{2.65}$$

This approximation becomes unsatisfactory at $k \approx 0.3$ already where it falsely predicts a minimum (Fig. 2.15). For $k \to \infty$ the neutral curve behaves asymptotically as follows:

$$\frac{1}{\mathrm{Cm}} \sim \frac{\pi}{2} + \frac{1}{k}\left(\frac{2}{3} - \gamma - \ln(2k)\right)\,. \tag{2.66}$$

The critical field is $\mathrm{Cm}_{\mathrm{cr}} = 2/\pi$. Our dispersion relation and neutral curve should be compared against that of [112] for the case of porous media, which at zero displacement read $2s^2 = \mathrm{Cm} + 1 - \sqrt{1 + 2\,\mathrm{Cm}} = \mathrm{inv}(k)$ and $\mathrm{Cm} = 4 = \mathrm{inv}(k)$, respectively. Nevertheless the critical Cm's are comparable. Despite the finite thickness of the Hele-Shaw cell, the critical wavenumber is infinite. This indicates of course that at small scales our analysis

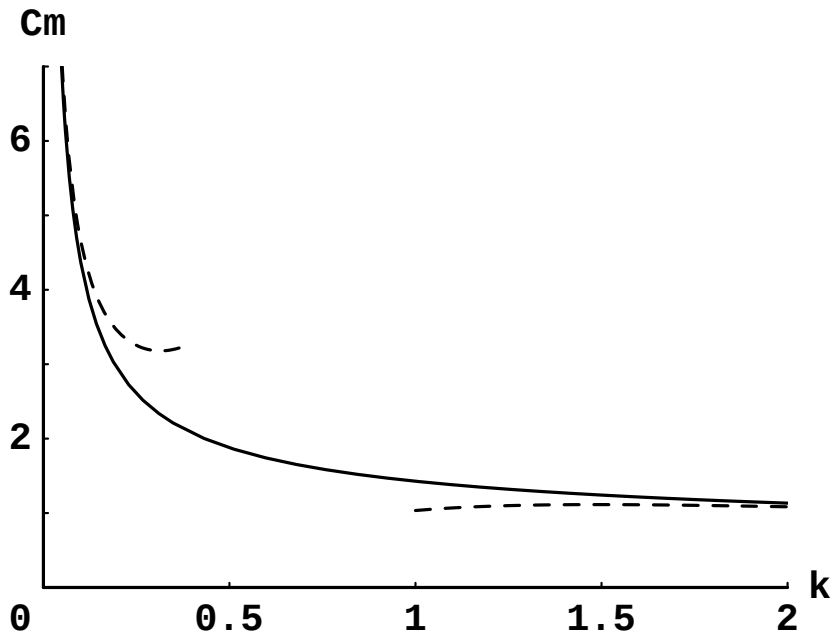

Figure 2.15: The exact neutral curve for the miscible "peak" instability (*solid line*) in a Hele-Shaw cell and its asymptotic behaviour (*dashed lines*).

in inadequate. The real concentration distribution (for which the Rayleigh scattering technique was applied) does not correspond to a sharp interface; it rather resembles a diffused transition layer between two miscible magnetic liquids. At studying a diffused interface, it is desirable to use the Brinkman (Darcy-Stokes) equation to ensure adequate description of the Hele-Shaw flow at short scales. But before these problems are addressed, let us check first the effect of the periodicity of the concentration distribution.

2.4.2 A periodic stripe pattern in the normal field.

In this section we analyze the stability of the periodic array of parallel MF stripes in a Hele-Shaw cell. The applied magnetic field is directed perpendicularly to the stripes. The interface between a stripe and the adjacent pure carrier liquid is sharp. Then, if the simpler Darcy law is again assumed for the flow instead of Eq.(2.3), the stability problem can be solved analytically. The coefficients of the linearized equations in §2.4.1 and the boundary conditions change in the present case. Let us consider the $2L$-periodic array of

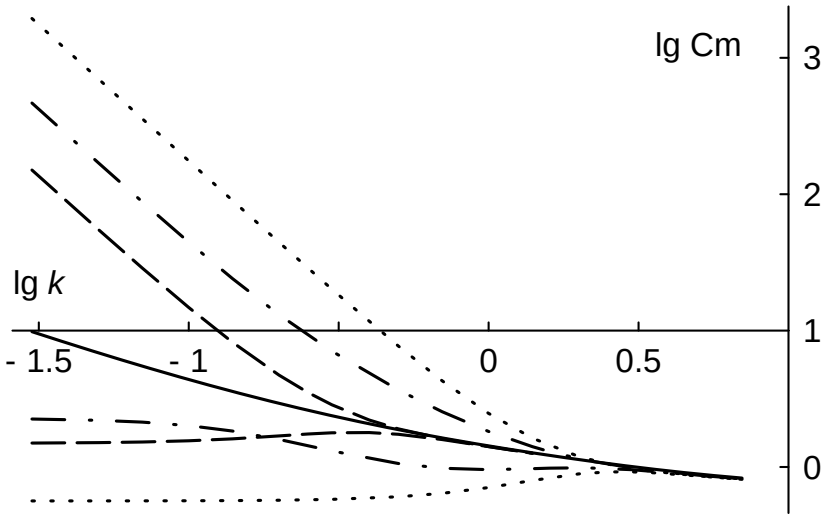

Figure 2.16: The neutral curves for the instability of the periodic array of sharp stripes in the Darcy flow. *Dotted lines*: $L = 2$, $l = 1$; *dash-dotted lines*: $L = 10$, $l = 1$; *dashed lines*: $L = 10$, $l = 5$; *solid line* (from Fig. 2.15): $L \to \infty$, $l \to \infty$.

stripes, the stripe width being $2l$ ($l < L$). Then

$$\frac{\partial c_0}{\partial x} = \sum_{m=-\infty}^{+\infty} \left[\delta(x - 2mL + l) - \delta(x - 2mL - l)\right] ,$$

which, according to Eq.(2.53), gives

$$\frac{\partial^2 \psi_0}{\partial x^2} - 4\pi \frac{\partial c_0}{\partial x} = -2 \ln \frac{\Phi(x + l)}{\Phi(x - l)} ,$$

where $\Phi(y) = 1 + \sinh^2(\pi/(2L)) / \sin^2(\pi y/(2L))$.

With the exception of the magnetic potential, whose perturbation ψ' needs to be evaluated numerically through an infinite sum, the due procedure is much the same as in the previous paragraph. Writing down general solutions of linear homogeneous Eqs.(2.50), (2.4) for every domain where c_0 is constant, one makes use of the jump conditions and periodicity to obtain a linear algebraic system for the amplitudes of eigenmodes. The dispersion relation follows as the zero determinant of this system. Lengthy details of this straightforward derivation are omitted. The resulting dispersion relation is of the form $F(s, \mathrm{Cm}, k, L, l) = 0$, where $s = \sqrt{1 + \lambda/k^2}$. In fact, F is polynomial in Cm, which facilitates finding the roots of the dispersion relation. As common [15] for the problems with the self-magnetic field, a kind of "reciprocity" relation holds: $F(s, \mathrm{Cm}, k, L, l) = F(s, \mathrm{Cm}, k, L, L - l)$, i.e. inverting

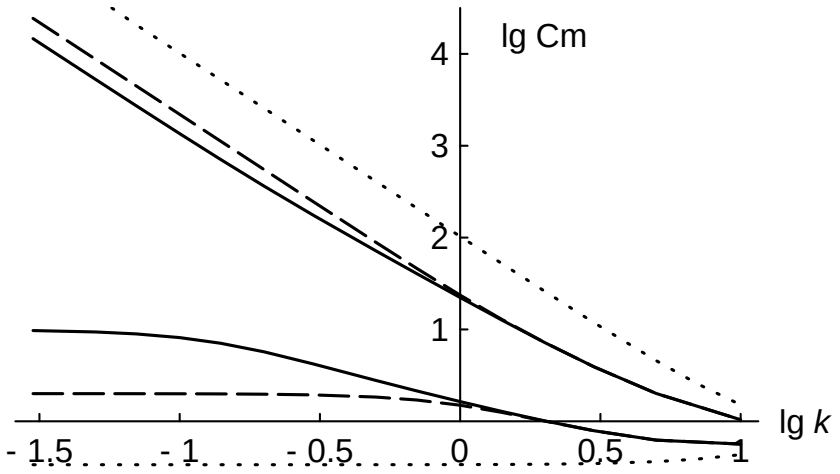

Figure 2.17: The neutral curves for the instability of the periodic array of narrow ($l = 0.1$) sharp stripes in the Darcy flow. *Dotted lines*: $L = 0.2$; *dashed lines*: $L = 2$; *solid lines*: $L = 10$.

the underlying stripe pattern (MF $\leftrightarrow$ non-MF) does not change the flow and its stability. Indeed, for an arbitrary concentration distribution $c(x, y)$, the formal change of sign and the shift by a constant (here $\tilde{c}$) together modify our initial Eqs.(2.3), (2.46), (2.47), and (2.2) only insignificantly. (The modification consists in the addition to the pressure that further drops out both from the equations and from the jump conditions.)

Computing the neutral curves ($\Re\mathrm{e}\,\lambda = 0$), we found no oscillatory neutral modes, so that the "exchange of stabilities" takes place at the threshold. For all values L, l that we tried, the neutral curves appear to have two branches. The upper branch corresponds to the undulation (bending) mode, in which the perturbed velocity at the opposite edges of each stripe is of the same direction. The critical mode is the "peristaltic" one, in which the edges of a stripe spread away in the opposite directions or move toward one another. As l increases (along with L), the mutual influence of the edges vanishes. Therefore, at $l \to \infty$ the branches converge (the higher the wavenumber k, the faster) to the neutral curve for the instability of the sharp discontinuity obtained in the preceding paragraph. At fixed L, l the convergence also seems to be the case as $k \to \infty$ (Figs. 2.16, 2.17). In fact, since we evaluated the dispersion relation only approximately, it cannot be excluded that at some point the two modes fully coalesce into a single one.

We note in conclusion that in the periodical stripe pattern a second perturbation mode exists. This peristaltic mode becomes unstable at finite (and rather low) Cm values even in the limit of large wavelength (Figs. 2.16, 2.17).

A comparison of several sharp-interface neutral curves obtained in the

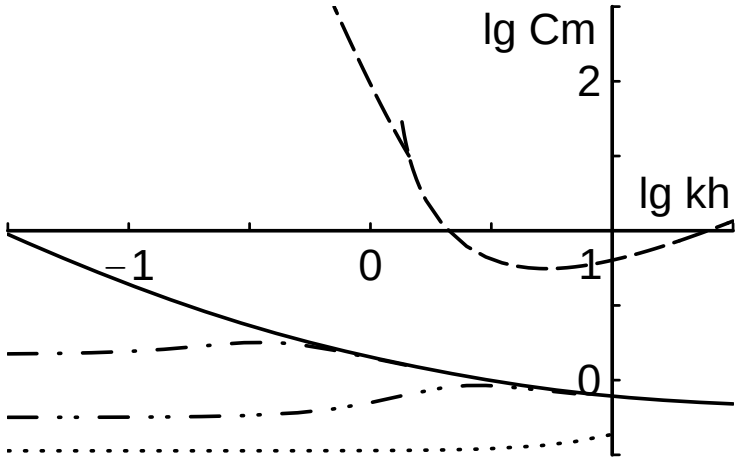

Figure 2.18: The neutral curves for the sharp interface (the Darcy flow): the labyrinthine (*dashed line*) and peak (*solid line*) instabilities of an isolated interface; the peristaltic mode of the peak instability of an array of stripes (*dash-dotted line*: $L = 10$, *dash-dot-dotted line*: $L = 2$, *dotted line*: $L = 0.2$; $l = L/2$ for all).

present work is made in Fig. 2.18.

2.4.3 Numerical stability analysis of a diffused interface in the normal field.

Substituting Eqs.(2.53), (2.54) into Eq.(2.50) yields, together with Eq.(2.4) and boundary conditions, an eigenvalue problem that is generally similar to the one considered in §2.3.4. Thus we follow the same procedure to discretize the problem. Unlike the case of the labyrinthine instability, the kernel J_1 of the integro-differential equation (2.50) is itself expressed through an integral. We represent the kernel as $J_1(\eta, k) = J_2(\eta, k) - K_0(k\eta) + k\eta\, K_1(k\eta)$ ($k > 0$, $\eta > 0$). As $\eta \to 0$, $J_1(\eta, k)$ becomes logarithmically singular, while J_2 remains finite:

$$J_2(\eta, k) + \frac{\pi k}{2} \mathrm{e}^{-k\eta} = k\ \mathrm{Ki}_1\,(k) + K_0(k) - k\, K_1(k) + O(\eta^2)\,.$$

We resolved this problem by constructing a quadrature rule based on the kernel J_1 as a weight function. The rule is exact for piecewise-linear integrand functions. The equations were solved on a non-uniform grid. Grid points were uniformly distributed along the z-axis, where $z = x \,/\sqrt{x^2 + a^2}$. We took $a = \sqrt{t_0} + 5 + 5/k$ with N grid points. The spatial derivatives were approximated (with the second order) with finite differences. The whole

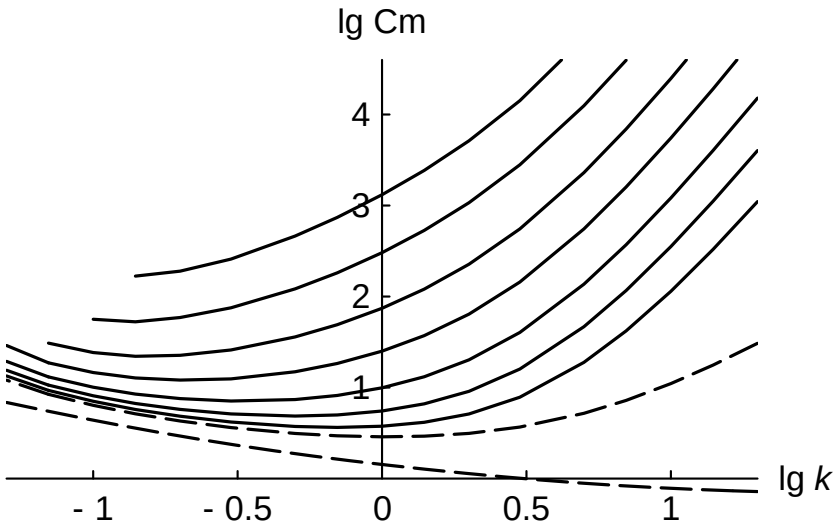

Figure 2.19: The neutral curves for the instability of the originally step-like concentration distribution in the Brinkman flow (*solid lines*, $t_0 = 0.03$; 0.1; 0.3; 1; 3; 10; 30 bottom to top) and in the Darcy flow (*dashed lines*, $t_0 = 0.03$ for the upper curve, $t_0 = 0$ for the lower analytical one repeated from Fig. 2.15).

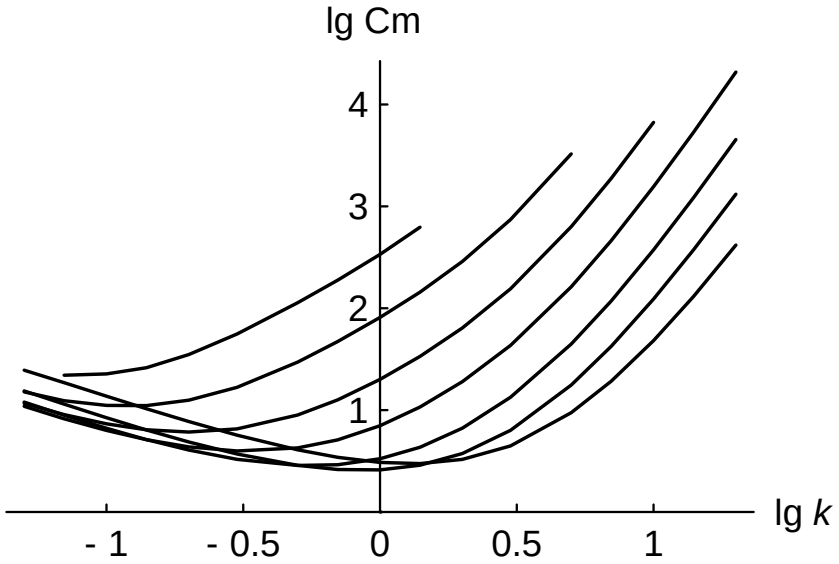

Figure 2.20: The neutral curves for the instability of the Gaussian concentration distribution in the Brinkman flow. Right to left: $t_0 = 0.03$; 0.1; 0.3; 1; 3; 10; 30.

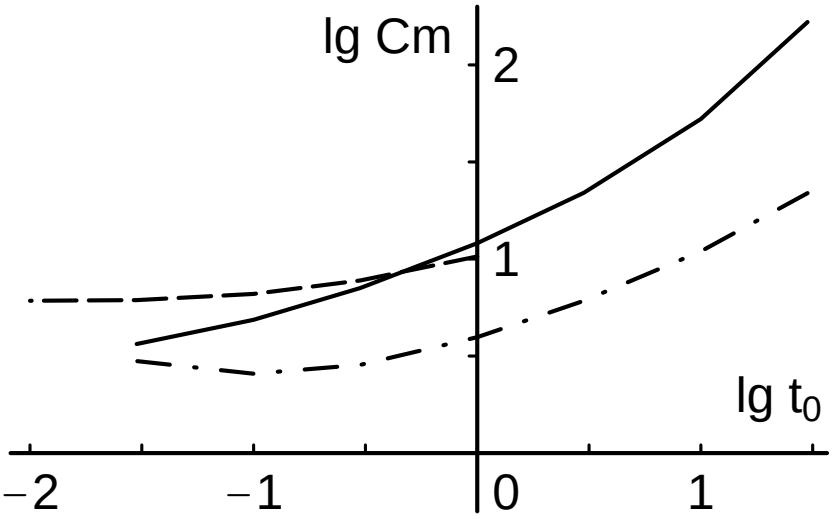

Figure 2.21: The critical Cm number as the basic concentration distribution diffuses out in the Brinkman flow: the labyrinthine (*dashed line*) and peak (*solid line*) instabilities of a single initially step-like interface $c_1(x)$; the peak instability of a Gaussian stripe $c_2(x)$ (*dash-dotted line*).

spectrum of the algebraic system for a given (k, Cm) pair was obtained by a standard eigenvalue finder. Since eigenfunctions of the discrete spectrum are required to vanish at infinity, numerical real eigenvalues $\lambda \leq -k^2$ must be discarded [see §2.2, Eqs.(2.4), (2.33)]. In many cases several valid eigenvalues were obtained. However, we traced only the highest (dominant) one. All the results presented correspond to $N = 512$ but were checked against the change in resolution.

We did the numerical stability analysis for two basic concentration distributions $c_0(x, t_0)$: $c_1 = 0.5\,\mathrm{erfc}\,(0.5x/\sqrt{t_0})$ and $c_2 = \exp\,(-0.25x^2/\,t_0)$, where t_0 is the time elapsed since the distribution was step-like or delta-function-like, respectively. Both distributions are normalized by the maximum concentration value, which for the Gaussian one (c_2) implies a progressive scaling down of the Cm number as the diffusion process evolves. Generally, t_0 in our analysis may just parametrize a family of instantaneous "frozen" distributions that not necessarily result from the diffusion of a definite initial one. The cases explored include $t_0 = 0.03;\ 0.1;\ 0.3;\ 1;\ 3;\ 10;\ 30$ with 17 k values within the range $0.05 \ldots 20$ and 18 Cm values such that $4\pi t_0\,\mathrm{Cm}$ ranged from 0.2 to (1×10^5). (For $t_0 = 10,\ 30$ additional series of computations with higher Cm numbers were undertaken as well).

For both concentration distributions the dominant normal mode was found to be stationary. The neutral curves of the instability are plotted

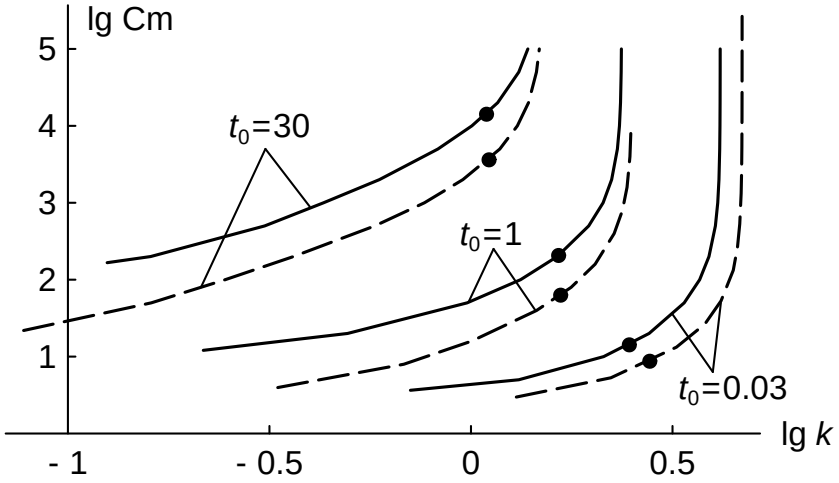

Figure 2.22: The Cm dependence of the most unstable wavenumber for the initially step-like concentration distribution (*solid lines*) and for the Gaussian one (*dashed lines*) in the Brinkman flow. Black circles correspond to $\lambda = 10$.

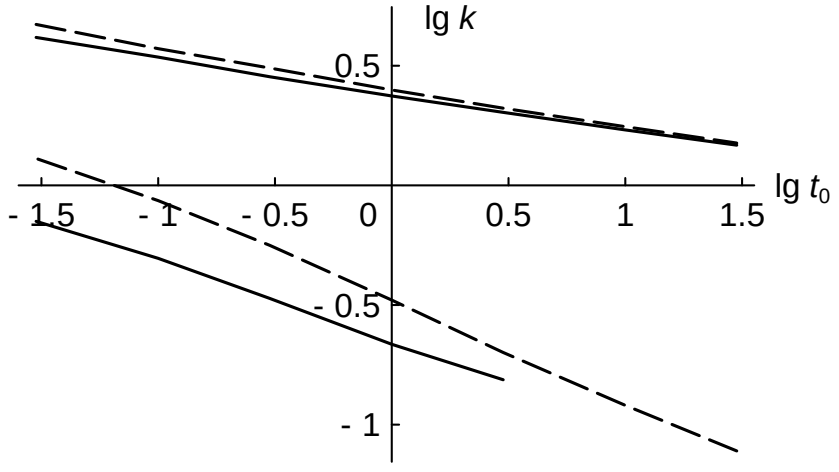

Figure 2.23: The most unstable wavelength at infinite Cm (*top*) and the critical wavelength (*bottom*) for the initially step-like concentration distribution (*solid lines*) and for the Gaussian one (*dashed lines*) at various t_0 values in the Brinkman flow.

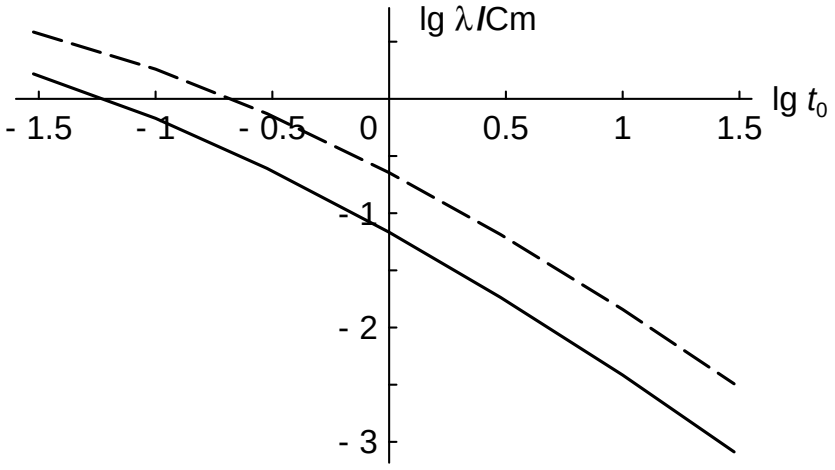

Figure 2.24: The asymptotic (Cm $\to \infty$) value of the λ/Cm ratio for the initially step-like (*solid line*) and Gaussian (*dashed line*) concentration distributions in the Brinkman flow.

in Figs. 2.19, 2.20 for the originally step-like concentration distribution and for the Gaussian one, respectively. Along with the curves for the Brinkman flow at various t_0 values, two neutral curves for the Darcy flow are also plotted in Fig. 2.19: the one obtained analytically in §2.4.1 for $t_0 = 0$ and the numerical one for $t_0 = 0.03$. These curves demonstrate that numerical results are consistent with earlier analytic findings. Besides, the Darcy critical Cm numbers are just a little lower than the Brinkman ones. In the rest of the Section we will consider the Brinkman flow only. The critical Cm numbers provided by Fig. 2.21 generally increase as the concentration gradients get smoother (even though their amplitude is fixed). Therefore, to verify experimentally the onset of convection, it may be appropriate to switch on the field as soon as the desired distribution develops and not earlier. The Gaussian distribution proves to be less stable than the c_1 one for all t_0's tried. The Cm dependence of the most dangerous wavenumber is presented in Fig. 2.22. As Cm increases, the most unstable wavelength tends to the limit of several gap widths, as summarized in Fig. 2.23. While being typical for the microconvection in a Hele-Shaw cell, such behaviour is not reproduced by the Darcy law (see §2.3.4). It should be noted that the limiting ("saturation") wavelength is almost the same for both distributions and weakly depends on t_0. The growth increment λ increases along the curves (upwards) plotted in Fig. 2.22. Their lower end-points correspond to $\lambda = 0$ (and thus to the minimum of the neutral curves in Figs. 2.19, 2.20). Since the validity of QSSA improves as the instability growth rate increases, the Cm numbers that correspond to $\lambda = 10$ are also given in Fig. 2.22. For large Cm the

increment of the most unstable wavenumber is asymptotically linear in Cm. This indicates that the proper time scale of the problem becomes $h^2/(\mathrm{Cm}\, D)$ (p. 43). The limit of the λ/Cm ratio is given in Fig. 2.24.

2.4.4 A comparison to FRS experiments

In the FRS case the developed models concern the situation when the thermal variations have relaxed already after the light source was switched off. Though thermodiffusion is no longer in action, the concentration structure is still present, because it requires much longer time to vanish [106]. Note that only the experiment [3] specifically concerned the convection in the FRS setup. We begin with discussing other cases, where the instability was neither sought nor detected; its presence can now be judged upon by evaluating the corresponding Cm number. As for t_0 for the diffused distributions, it will be taken to be unity, since the pattern period is comparable to h.

Let us estimate the maximum Cm number attained in works [2, 103]. The magnetization of the particle material (maghemite) is $M_\mathrm{S} = 4 \times 10^2$ G, while the magnetic radius of particles is $a_\mathrm{m} = 6$ nm. In the highest field $H_0 = 1.4 \times 10^3$ Oe used, the magnetization of such paramagnetic colloid becomes almost saturated. The diffusion coefficient D of particles of the hydrodynamic radius $a_\mathrm{h} = 15$ nm may be found by the Einstein–Stokes formula. Then, if the average MF concentration c_av is substituted for $\tilde{c}$ in the Cm definition (p. 34), for the colloid of the volume fraction $\varphi_\mathrm{av} = 0.09$ in a $h = 0.01$ mm thick cell one obtains $\mathrm{Cm} = 7 \times 10^4$.

However, it is the concentration modulation (and not c_av) that is responsible for the instability. The concentration difference δc between the dark and bright fringes in the developed grating was in fact introduced above as $\tilde{c}$ and may differ considerably from the average concentration; unfortunately, it was not measured [2, 103]. Nevertheless it may be estimated considering the preceding stage of the FRS experiment. Refs. [147, 151, 106] analyze this steady-state regime, when the light source is still on, and the non-uniform heating sustains the concentration pattern through thermodiffusion (assuming the absence of any convection at this stage). In particular, in these works the amplitudes of the spatial Fourier modes of the temperature are derived in the framework of the two-timescale model. In our case the formulas for the first mode of the time-averaged temperature T_0 would be $T_0 = \theta \cos qx + \mathrm{const}$ with

$$\theta = \frac{2I[1 - \exp(-a_\mathrm{p} h)]}{Sh(q^2\chi + \rho c_\mathrm{p}/\tau_0)}$$

where I is the average power of the pumping laser, S is the overall area of the periodic interference pattern, $q = 2\pi/\Lambda$, Λ is the fringe pattern period, a_p,

χ, ρ, and c_p are the MF absorption coefficient, thermal conductivity, density, and specific heat capacity, respectively. (At 532 nm $a_\mathrm{p}/\varphi = 2 \times 10^4$ cm^{-1} [152], so for $\exp(-a_\mathrm{p} h) \ll 1$ the constant mean value at $\varphi = \varphi_\mathrm{av}$ may be used.) The τ_0 constant is the characteristic time of the thermal decay due to the heat flux through the walls. Since in the steady state the net diffusive flux is zero, we have $\mathrm{d}\varphi_0/\mathrm{d}x = -S_\mathrm{T}^* \varphi_0 \, \mathrm{d}T_0/\mathrm{d}x$, where the Soret coefficient S_T^* is employed. Integrating this relation between the adjacent minimum and maximum, one derives the variation of the relative volume fraction as $\delta\varphi/\varphi_\mathrm{av} = 2 \sinh(|S_\mathrm{T}^*|\theta)/\,\mathrm{I}_0(|S_\mathrm{T}^*|\theta)$, where I_0 is the modified Bessel function of the first kind. Substituting $I \leq 0.2$ W, $S = 3 \times 10^{-7}$ m^2, and $\Lambda = (2 \ldots 6.5) \times 10^{-5}$ m [2, 103], $\tau_0 = 1.9 \times 10^{-4}$ s [152], $S_\mathrm{T}^* = -9 \times 10^{-2}$ K^{-1} [153] and taking χ, ρ, and c_p values to equal those of water, we obtain $\theta = (1.5 \ldots 4)$ K and $\delta\varphi/\varphi_\mathrm{av} = 0.3 \ldots 0.7$. This corresponds to $\mathrm{Cm} = (0.5 \ldots 4) \times 10^4$.

Then from Fig. 2.21 it may be inferred that the instability indeed develops in the circumstances of the FRS experiment [2, 103] as soon as the pumping is switched off. However, the microconvection intensifies mixing and thus destroys the concentration inhomogeneity that feeds the instability. Though the non-linear stage of the process in the periodical concentration structure is unclear, it is possible that having disturbed the original structure, the microconvection vanishes soon after its onset (similar to what was observed in [1]). Subsequently, only the diffusion is in operation, which could have hindered the identification of the convection phenomenon. We remind that Refs. [2, 103, 154] attributed the increase of the diffusion coefficient in the applied magnetic field solely to the transport effects. It should be noted also that convection may be in fact essentially three-dimensional, so that our 2D approach cannot describe it correctly. Anyway, the convective instability, if present, impacts the FRS measurements of the diffusion coefficient in the applied magnetic field. The onset of the threshold convection will be probably marked by a break on the $D_\mathrm{eff}(H_0)$ (effective diffusion coefficient – applied field) curve, which makes more detailed measurements desirable.

The Cm number was much lower in the experiment [105], mostly owing to a less powerful light source. For the MF magnetization of 7.8 G, $\varphi = 2.14\%$, $h = 0.1$ mm, $D = 6.1 \times 10^{-11}$ m^2/s, $\eta = 4.2 \times 10^{-4}$ kg/(m s) (toluene at 50°C), and $\delta\varphi = 0.126\%$ (also found [105, 155] from the two-timescale model) we have $\mathrm{Cm} = 7 \times 10^2$. Still this value probably exceeds the critical one.

Let us also estimate the Cm number attained in [1], where an instability was observed directly at a diffusion front in the normal field. Given $h = 0.1$ mm, $H_0 = 200$ Oe, and $\varphi M_\mathrm{S} = 10$ G and substituting reasonable guesses for the missing values $a_\mathrm{m} = 5$ nm, $a_\mathrm{h} = 8$ nm, and $M_\mathrm{S} = 500$ G, one obtains $\mathrm{Cm} = 4 \times 10^4$. This value is indeed high enough for the instability to develop.

Finally, we turn to a very recent FRS experiment [3, 108], where a con-

vection is detected in the field parallel to the temperature gradient while the light source is on. The temporal behaviour of the intensity of the diffracted pattern cannot be explained by diffusive processes alone. In particular, in the steady-state regime the intensity is observed to fluctuate about a mean value. The results [3] are presented in terms of the magnetic solute Rayleigh number $\mathrm{Rm} = 48\pi(L/h)^2\,\mathrm{Cm}/\mu$, where μ is the permeability (we will take $\mu = 1$), and the variation of the diffusion coefficient with the field is neglected. At $2L = 3 \times 10^{-3}$ cm and $h = 1 \times 10^{-2}$ cm, the observed critical $\mathrm{Rm} \approx 1.7$ translates into $\mathrm{Cm} \approx 0.5$. This value is in a remarkably good accordance with our prediction (the dotted line in Figs. 2.17, 2.18) despite the fact that temperature inhomogeneities are not allowed for in our model. To our knowledge, this experiment is the only one that provides a direct quantitative test for our theory.

Chapter 3

The Saffman–Taylor instability with immiscible ferrofluids

3.1 The free-boundary problem

3.1.1 The context of the problem

The phenomenon of viscous fingering in a Hele-Shaw cell became widely known thanks to the classical paper by Saffman and Taylor [10]. We are not going to present the overview of this vast field [156, 157, 30, 158, 11, 159], mentioning only the basic facts. In [10], as a less viscous fluid displaced a more viscous one, the former was observed to penetrate the latter taking on, *in the plane of the cell*, the shape of a finger. The finger shape was registered for several fluid pairs; as the surface tension (the reverse capillary number) tended to zero, the finger width was observed to decrease approaching one half of the cell width. The asymptotic shapes observed at a small surface tension were found to fit closely the analytically obtained solution, provided one substitutes 1/2 for the relative width of the finger. The analytical solution at zero surface tension (Eq.(3.35)) involves the relative finger width λ as an undetermined parameter. Many other exact solutions are known at zero surface tension, e.g. [160], but this problem is ill-posed and some solutions become singular in finite time. (Few known exact solutions for a non-zero surface tension describe quite artificial flows, e.g. [161].) The surface tension regularizes the problem in the sense that, e.g., at a finite capillary number Ca (defined on p. 79), the amplitude of the disturbance required for a secondary instability of the tip of the finger is $\sim \exp(-\sqrt{\mathrm{Ca}} \cdot \mathrm{const})$ ([11], §IX.6). How and why does a small but non-zero surface tension select the $\lambda = 1/2$ shape from all other? The problem attracted an extreme interest in 1980's, and tremendous mathematical and experimental effort was exerted in order to

understand the "selection" problem. In the work [162], the problem of width selection by surface tension was addressed along with the issue of stability of steady fingers. For steady-state ST fingers with surface tension a system of non-linear integro-differential equations was obtained which allowed to find a unique finger width for any given surface tension. (Later it turned out that in fact, there is a discrete set of solutions, but other ones are unstable. It is also noteworthy that the analysis in [162] of the finger stability was inconclusive.) The solvability condition for the equations of McLean & Saffman gave a mathematical understanding of how a shape gets selected at small surface tensions (§§VIII.2–VIII.4 of [11]). The main complication in the selection problem is that apparently small effects are not negligible and lead to a qualitatively different behaviour. Analytically, it turned out that exponentially small terms are of primary importance in certain asymptotic expansions ("asymptotics beyond all orders"). This is the reason why many earlier analytic attempts failed (cf. the "undetected inconsistency" in [162], etc.). The surface tension, however small it be, is crucial for the selection since it comes with interfacial curvature and is a singular perturbation (a structurally unstable problem). A classical analogue, also from fluid mechanics, is the relation between viscous and inviscid flows as distinguished by viscosity that comes with higher velocity derivatives. Experimentally, fingers were observed to undergo some instabilities such as tip-splitting and to be "pathologically" sensitive to various artificial perturbations, transforming into strikingly beautiful patterns. Thus, fractal patterns were obtained at the viscous displacement of non-Newtonian fluids, both miscible and immiscible [163, 164, 165]. These examples are particularly relevant to our case since we also study a "complex fluid."

The immiscible Hele-Shaw flow with magnetic fluids under the influence of the perpendicular magnetic field was extensively analyzed and modelled by A. Cēbers with collaborators. Their first work on the subject [166] develops a so-called boundary-integral formulation of the problem for an MF droplet confined in a Hele-Shaw cell. The method was applied [166, 167, 168] to the analysis of the over-extension (i.e. peristaltic) and bending (i.e. undulation) instabilities of MF drops as well as multi-lobe shapes. The treatment of the integral terms describing magnetic interactions was improved in [168]. These and some other numerical results are accumulated in §4.7 of [15]. For a later work, see [169], where modelled was vertex-splitting and a long-time behaviour of a drop similar to the rearrangement of the Steiner trees, and [170]. Rising bubbles in a vertical Hele-Shaw cell filled with a ferrofluid were simulated by the algorithm e.g. in [171]. However, these works dealt with the radial geometry (for experimental results, see e.g. [172]). In [173], a single MF stripe was modelled, and its undulations and side-branching were

obtained. The rupture of a MF layer in a vertical cell was simulated in [174]. Of interest to us is the rectilinear geometry that was modelled in [175, 176]. Our treatment of magnetic terms (§3.1.5) will be quite close to that of [175], which, in its turn, was adapted from [168]. Tip-splitting under artificial perturbations was studied in [175]. In [176] a longer magnetic Saffman–Taylor finger was simulated as well as a branched structure.

Now let us mention very briefly the analyses of the labyrinthine instability and related issues (for a general presentation, see §4.6 of [15]). In [177], the threshold of instability was obtained. In [178], a variational formalism is developed for the dynamics of dipolar domains. In [179], a weakly nonlinear analysis of the viscous fingering with MF's in a perpendicular field was undertaken, while in [100], the Kelvin–Helmholtz instability in a Hele-Shaw cell is addressed and some other results are summarized. In [6], the important notion of the effective surface tension (p. 133) is overviewed.

All the above research on the immiscible Hele-Shaw flow with ferrofluids was undertaken for the magnetic field perpendicular to the cell, in which "perpendicular" configuration a labyrinthine instability was known to be possible since mid-1970's. Of the three physically selected mutually perpendicular orientations of the magnetic field, the one tangential to the straight interface and parallel to the cell is known to be stabilizing (e.g. [100], or Refs. 6, 7 of [175]). The other potentially destabilizing configuration is the "normal" one, when the field is directed parallel to the cell, but normally to the interface line. Then a (Hele-Shaw version of the) peak pattern can be observed [180, 7, 181]. The interface dynamics in this case has not yet been simulated. In the present work, we report such preliminary simulations for the first time. The study of the normal-field instability will be deferred to §3.4, and we begin with the perpendicular configuration.

However, a systematic study of the immiscible labyrinthine instability in a rectilinear geometry is also lacking. In this second half of our work, we will develop the approach of the above-cited work [176]. It requires elaboration (e.g., in terms of accuracy) and extension to enable the computation of richly branched, highly ramified in the long run "dendritic" structures.

The latter motivation emerges in the light of the new experimental data [12, 7, 181]. In [12], the Rayleigh–Taylor instability was explored in the perpendicular field. A comparison of the observed near-critical (in the sense of stability) behaviour to the linear stability theory was undertaken. Some reported [12] features of the far-from-threshold pattern will be commented upon in §3.3.2. In [7], the viscous fingering with ferrofluids was investigated in both perpendicular and normal configurations, and the relative width of the magnetic ST finger was measured (in the perpendicular case). Finger-like patterns will be simulated in §3.3.1. For further details about these

experiments, we refer the reader to these original works [12, 7]. To be close in our simulations to the experimental conditions, let now us estimate the relevant values of the dimensionless parameters. (For their definitions, see p. 79 and p. 84 later). For the Saffman–Taylor experiment [12, 181], the Hele-Shaw cell used was $T = 2$ cm wide and its gap was $h = 0.1$ cm thick. The magnetic Bond number Bm was of the order of unity. MF of the dynamic viscosity coefficient $\eta_2 = 0.35$ g/(cm · s) was displaced by air of a negligible viscosity $\sim 10^{-3}\eta_2$, so that At = 1. The surface tension at the interface was evaluated to be $\sigma = 60$ g/s^2. Then the flow rate $Q = u_0 hT$ of 600 ml/h corresponded to Ca $\approx 12u_0\eta_2/\sigma = 7/120$. Experiments were done in the range of flow rates $(0.1 \dots 10)Q$, i.e. Ca did not exceed unity there. As for the Rayleigh–Taylor experiments [7, 181], $T = 14$ cm, $h = 5 \times 10^{-2}$ cm. An MF of the dynamic viscosity coefficient $\eta_2 = 1.4$ g/(cm · s) and density $\rho_2 = 1.7$ g/cm^3 rests on top of white spirit, whose viscosity is $\eta_1 = \eta_2/140$, and density is $\rho_1 = 0.8$ g/cm^3. Therefore $1 - \mathrm{At} \approx 2\eta_1/\eta_2 \approx 1.4 \times 10^{-2}$. Besides, taking into account the surface tension at the interface, $\sigma = 12$ g/s^2, one obtains the gravitational Bond number as Bg ≈ 0.18 (we will use later the value 3/16). The magnetization curve presented in Fig. 3.4 of [181] allows to determine that at the external field of 23 kA/m the MF magnetization was about 21 kA/m (21 G), while at 40 kA/m it becomes $M = 24$ kA/m (24 G). (By the way, these values question the validity of our approximation of a magnetization negligibly small with respect to the applied field.) This corresponds to the magnetic Bond numbers Bm = 3.675 and 4.8, respectively.

3.1.2 Formulation of the problem

Consider a vertical Hele-Shaw cell filled with two fluids (Fig. 3.1).[1] Each of them may be magnetic. The cell is supposed infinite in both directions. Let us reference the two fluids by an index i. Their viscosity, density, and magnetization are denoted by η_i, ρ_i, and M_i, respectively. As with the miscible fluids, we may describe the gap-averaged flow in a cell of the thickness h by the Darcy law or by the Brinkman equation. The latter option, however, will not be explored in this Chapter, as it complicates the problem substantially. In each fluid, the Darcy law reads:

$$-\vec{\nabla} p - \alpha_i(\vec{v} + \vec{u}_0) + \rho_i \vec{g} + \vec{f}_{\mathrm{m}} = 0\,, \tag{3.1}$$

where p is the pressure, $\alpha_i = 12\eta_i/h^2$ is the friction coefficient, $\vec{u}_0$ is the constant injection velocity at infinity relative to the cell walls, $\vec{v}$ is the velocity in the reference frame moving with $\vec{u}_0$, and $\vec{g}$ is the free-fall acceleration.

[1] Please observe that we interchange the x and y axes relative to the previous definition.

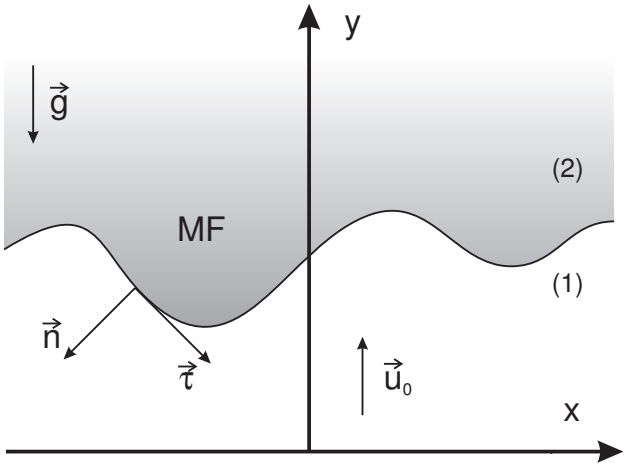

Figure 3.1: The geometry of the immiscible problem.

When p, $\vec{v}$ and other variables are evaluated at the interface, we will also assign the index to them to distinguish at which side of the interface the variable is taken. With the exception of the last paragraph, in this Chapter we will consider a field perpendicular to the cell. The gap-averaged density of the magnetic ponderomotive force $\vec{f}_{\rm m}$ is the same as for the miscible problem (see Chapter 1). However, since in the region S_i occupied by the i-th fluid the corresponding concentration is constant now, $\vec{f}_{\rm m}$ becomes potential away from the boundary: $\vec{f}_{\rm m} = -(2M_i/h)\vec{\nabla}\Psi$, where the scalar magnetostatic potential on one of the walls is

$$\begin{aligned}\Psi(\vec{r}_0) &= \left[M_1 \int_{S_1} + M_2 \int_{S_2}\right] K\left(\vec{r}-\vec{r}_0\right) \mathrm{d}^2\vec{r} \\ &= (M_2 - M_1) \int_{S_2} K\left(\vec{r}-\vec{r}_0\right) \mathrm{d}^2\vec{r} + \text{const}\,,\end{aligned} \tag{3.2}$$

and $K(\vec{\rho}) = 1/\rho - 1/\sqrt{\rho^2+h^2}$. We note parenthetically that with a sharp interface, it can be advantageous to use an alternative formulation for the magnetic force (the "current" formulation as opposed to our "charge" one); for details, see [171, 102, 6, 182]. Both fluids are incompressible: $\operatorname{div}\vec{v} = 0$. At the interface between the fluids the normal velocities are equal (the kinematic boundary condition): $v_{1\rm n} = v_{2\rm n}$, while the tangential velocities may differ. Therefore the flow vorticity is infinite at the interface. For the fluids are immiscible, the Laplace law holds at the interface (the dynamic boundary condition): $p_2 - p_1 = \sigma\kappa$, where σ is the surface tension, and κ is the curvature positive if the region 2 is locally convex.

Strictly speaking, the interface is not two-dimensional. In [183, 184] as-

ymptotic boundary conditions at the immiscible interface in a Hele-Shaw cell were derived that took into account the film of a viscous fluid that is left during the displacement at the walls, and the transverse variations of the meniscus shape. According to this theory, owing to the meniscus, σ should have been replaced with $(\pi/4)\sigma$ plus a presumably constant term [10]. However, since the reference experiments [7, 181, 12, 180] are conducted with prewetted cell walls and surface tension was measured *in situ* there in a certain way, we will assume that σ is already rescaled, and ignore other effects due to the contact angle being dependent upon the displacement velocity, etc.

Then from (3.1) it is obvious that the Saffman–Taylor and Rayleigh–Taylor problems for a vertical cell are identical in the Hele-Shaw approximation and transform one into another by substitution $\rho_i\vec{g} \leftrightarrow -\alpha_i\vec{u}_0$. The flow is unbounded but we demand that it is periodic in the lateral direction (i.e. perpendicularly to $\vec{u}_0$), the period being T ($T \gg h$). Note that owing to the non-locality of $\vec{f}_{\rm m}$, the stated problem is different from that of a laterally bounded flow, while for non-magnetic fluids one problem is typically substituted by the other. The issue of the horizontally bounded cell will be touched in §3.1.5. The Hele-Shaw flow with the magnetic ponderomotive force (3.1) was first studied by Cēbers [101].

As in the miscible problem, the gap-averaged magnetic force translates the transverse dimension h through the length scale of the magnetic force into the 2D problem. Now we will render the problem dimensionless by introducing h and $h^3(\alpha_1 + \alpha_2)/\sigma$ as length and time scales, correspondingly. The time scale is characteristic for the relaxation of an interfacial perturbation of dimension h by the surface tension alone. If a viscosity difference, buoyancy, or magnetic effects dominate, then thus non-dimensionalized times can be far from unity for a physically selected phase of the process (e.g. when non-linear effects come into play, etc.). Other choices for the scales are also possible and are used in the literature, but neither of them is universally convenient and physical in every limit. For example, at studying the "dendritic structures" (§3.3), whose scale is much less than T, it is reasonable not to introduce T into the dimensionless parameters that will enter the equations. Quite similar solutions may be expected for the dendritic problems that in dimensional variables differ only in the value of the imposed period T, and this similarity should remain evident in the dimensionless formulation. To non-dimensionalize the "dynamical" variables containing the unit of mass, we use the surface tension that is almost always required anyway to regularize the problem (see §3.2.1). Then we arrive at the following equation in

dimensionless variables $\vec{r}$, p, $\vec{v}$, κ (for them the existing notation is kept):

$$-\vec{\nabla}p - \frac{\alpha_i}{\alpha_2+\alpha_1}\,\vec{v} - \left(\frac{\alpha_i}{\alpha_2-\alpha_1}\,\mathrm{Ca} + \frac{\rho_i}{\rho_2-\rho_1}\,\mathrm{Bg}\right)\vec{e}_y - \frac{M_i}{M_2-M_1}\,\mathrm{Bm}\,\vec{\nabla}I_\mathrm{m} = 0\,, \tag{3.3}$$

where $\vec{e}_y$ is the unit vertical vector (see Fig. 3.1), and

$$I_\mathrm{m}(\vec{r}_0) = \int_{S_2}\left(\frac{1}{|\vec{r}-\vec{r}_0|} - \frac{1}{\sqrt{(\vec{r}-\vec{r}_0)^2+1}}\right)\mathrm{d}^2\vec{r} \tag{3.4}$$

(the integration is performed over the non-dimensionalized S_2). The following dimensionless groups have been introduced:

1. the modified capillary number $\mathrm{Ca} = h^2u_0(\alpha_2-\alpha_1)/\sigma = 12u_0(\eta_2-\eta_1)/\sigma$;
2. the gravitational Bond number $\mathrm{Bg} = h^2g(\rho_2-\rho_1)/\sigma$;
3. the magnetic Bond number $\mathrm{Bm} = 2(M_2-M_1)^2h/\sigma$.

The dynamic boundary condition at the interface becomes $p_2 - p_1 = \kappa$.

Introducing the effective pressure

$$\tilde{p} = p + \left(\frac{\alpha_i}{\alpha_2-\alpha_1}\,\mathrm{Ca} + \frac{\rho_i}{\rho_2-\rho_1}\,\mathrm{Bg}\right)y + \frac{M_i}{M_2-M_1}\,\mathrm{Bm}\,I_\mathrm{m}\,, \tag{3.5}$$

one can rewrite Eq.(3.3)

$$\vec{v} = -\left[(\alpha_2+\alpha_1)/\alpha_i\right]\vec{\nabla}\tilde{p}\,. \tag{3.6}$$

Thus the flow is potential away from the interface, the potential being $\varphi = -\left((\alpha_2+\alpha_1)/\alpha_i\right)\tilde{p}$, but at the interface the vorticity is infinite. The dynamic boundary condition gives

$$-(\alpha_2\varphi_2 - \alpha_1\varphi_1)/(\alpha_2+\alpha_1) = \tilde{p}_2 - \tilde{p}_1 = \kappa + (\mathrm{Ca}+\mathrm{Bg})\,y + \mathrm{Bm}\,I_\mathrm{m}\,. \tag{3.7}$$

Note that in (3.7) the right-hand side is known. According to what has been said above on the identity of the Saffman–Taylor and Rayleigh–Taylor instabilities, the effects of Ca and Bg are additive. Besides, individual M_i have dropped out from the equations governing the velocity, and now only the combination $(M_2-M_1)^2$ enters the problem (via Bm). It means again that it is not important which of the fluids is (more) magnetic, i.e. the solution will remain the same if the fluids are interchanged (the "reciprocity", cf. §2.4.2). Without any loss of generality, we may assume that the (more) magnetic fluid is always above the other, regardless of their densities and viscosities.

The flow being two-dimensional, the stream function[2] can also be introduced:

$$v_x = \partial\psi/\partial y, \qquad v_y = -\partial\psi/\partial x\,. \tag{3.8}$$

The kinematic boundary condition at the interface may be expressed via the stream function as $\partial(\psi_2 - \psi_1)/\partial\tau = 0$, where $\vec{\tau}$ is the unit tangent vector of the interface, or, adjusting the unimportant constant, simply

$$\psi_2 = \psi_1\,. \tag{3.9}$$

Given the initial interface, the above equations allow to compute the instantaneous "material" (Lagrangian) velocity at the interface. The velocity component normal to the interface gives the rate of deformation of the interface. This allows to integrate the system with respect to time to obtain the shape evolution. Note that the boundary conditions hold at the boundary throughout the process without change, while the boundary itself evolves and its determination is the aim of the analysis. Thus our problem falls into the category of *moving*-boundary problems that are rather common in fluid mechanics – groundwater and free-surface flows, water waves (such problems are commented upon in §3.2.1), etc. Interestingly, if the evolution is expected to end up with a certain final stationary state, determining this unknown state is a *free*-boundary problem [185]. (There is some confusion in the literature regarding what the free-boundary problem and the moving-boundary one precisely are; sometimes the terms are used interchangeably.)

On the other hand, at a given moment of time, we have a boundary-value problem (BVP). We have established that the two-dimensional flow in consideration is incompressible and potential within both domains. Then it follows immediately that both the potential and ψ are harmonic, i.e. we have an elliptic BVP for one of these unknown functions that needs to be solved a large number of times in the course of the domain evolution.

The BVP will indeed be solved, step by step, in the present work. However, before turning to the issue of how this should be done, let us mention briefly a moving-boundary problem of a quite different origin that turns out to be equivalent to computing a Hele-Shaw flow. The problem naturally admits a very different approach not requiring to solve the Laplace equation (it is "generated" instead) and resolve the boundary conditions explicitly. We are speaking of the so-called diffusion-limited aggregation (DLA) and stochastic methods stemming from it [11]. The DLA process was originally understood as the Brownian motion of tiny particles released far from the first fixed one either one by one or as a steady flux; if a particle doesn't escape to infinity, it sooner or later touches and sticks to some of the particles that have

[2] Avoid confusing it with the magnetic potential.

"aggregated" earlier. The probability density for a particle to be at a given point away form the cluster obeys the Laplace equation but equals zero at the boundary of the aggregate. The boundary moves at a velocity proportional to the gradient of the probability density. The growing aggregates turned out fascinating [186] and having a fractal dimension (≈ 1.7 for a planar case), which raised extreme interest [187] to this apparently simple model. Very quickly the exact analogy was noticed between DLA and the pattern formation in viscous displacements in porous media [188]. It also became possible to incorporate the effect of surface tension [157] into a two-dimensional DLA to have a complete analogy with a Hele-Shaw model as well. Here we regard the DLA model as suggesting another point of view on our problem. The discrete "random-walk" methods were indeed used to model the Hele-Shaw flow (e.g. [189, 190]).

3.1.3 Alternative formulations of BVP

In principle, it is possible to solve the Laplace equation directly in both domains e.g. by finite differences, satisfying the somehow approximated boundary conditions. For the elliptic BVP's in two dimensions, however, a number of alternative mathematical formulations is available, some of which offer numerically more efficient treatment. In this paragraph we will give a brief (and incomplete) account of these analytical approaches.

The first such example is the restatement of BVP as the variational problem for the functional for which the original PDE is the Euler-Lagrange equation (the "Dirichlet principle"). This can always be done for self-adjoint problems. This variational problem may be solved by the Galerkin (or other projection) method with basis functions of local support, which constitutes the finite-element method [191].

Another example are the powerful complex-analytic methods whose application to fluid dynamics in two dimensions is long established. The conformal mapping technique reduces BVP to the computation of the conformal map of the unit disk onto the given domain or vice versa, which leads to an integral equation for the map (§§V.8, V.9, VI.4 in [192]). (The map is simply related to the Green's function of BVP, e.g. [145].) Moreover, if for some domain the map is known, the map for a slightly deformed domain at the next time step may be approximated by special efficient methods [145]. On the application of such methods to the Hele-Shaw flow (also with surface tension), see §3.2.1.

Yet another example from this theory are the methods of singular integral equations with Cauchy-type kernels (further referred to as the Cauchy-type, or singular, integral equations) [193, 194] – the main tool for studying various BVP's of the theory of analytic functions. Interestingly, our problem can also

be posed in the form studied in the literature on the Cauchy-type integral equations. Indeed, for the complex potential $\Phi = \varphi + i\psi$ our kinematic boundary condition may be rewritten as $\Im\mathrm{m}\left(\frac{\mathrm{d}(\Phi_2-\Phi_1)}{\mathrm{d}z}(\tau_x + i\tau_y)\right) = v_{2n} - v_{1n} = 0$. The dynamic condition at $\alpha_1 = \alpha_2$ is $\Re\mathrm{e}\left(\frac{\mathrm{d}(\Phi_2-\Phi_1)}{\mathrm{d}z}(\tau_x + i\tau_y)\right) = v_{2\tau} - v_{1\tau} = -2\frac{\mathrm{d}}{d\tau}(\tilde{p}_2 - \tilde{p}_1)$, and this latter function is known for a given interface (3.7). In other words, known is the jump of $(\tau_x + i\tau_y)\frac{\mathrm{d}\Phi}{\mathrm{d}z}$. This problem is a particular case of the following problem solved analytically in [194]: find a piecewise-analytical function (i.e. the one analytical away from some contour in the complex plane) by a given jump at the contour of a linear combination (with continuous complex-valued coefficients) of the sought function, its derivatives of given orders, and contour integrals of the function multiplied by some Fredholm kernels (zeroes in our case). For the exact formulation see §35 of [194], where this problem is called "the boundary problem of the Riemann type with the boundary condition that contains derivatives"; a variety of other BVP's are considered there as well.

The theory of BVP's for analytic functions is closely related to (and more general than) the classical potential theory. Indeed, consider the Cauchy-type integral defined as

$$\tilde{\Phi}(z) = \frac{1}{2\pi i}\oint_C \frac{\mu(t)\mathrm{d}t}{t - z}\,. \tag{3.10}$$

Away from the contour C parametrized by a real s and defined by $t = t(s)$, $\tilde{\Phi}(z)$ is an analytic function of a complex variable z, μ being the density of the Cauchy-type integral. If $z \in C$, the contour integral is taken in the sense of the principal value [193, 194, 145]. Then it is easy to demonstrate ([193], §10 in [194]) that the imaginary part of the Cauchy-type integral with the real density $\mu(t(c))$ is the single-layer logarithmic potential

$$\frac{1}{2\pi}\oint_C \frac{\mathrm{d}\mu}{\mathrm{d}s}\ln|t - z|\mathrm{d}s\,, \tag{3.11}$$

with density $\mathrm{d}\mu/\mathrm{d}s$, while the real part of the Cauchy-type integral is exactly the double-layer potential. In like manner, the formulas for the jump at the contour of potentials and their derivatives are related to the Sokhotski-Plemelj formulas for the Cauchy-type integral, etc.

Employing a potential to resolve the boundary condition results again in an integral equation on the potential density (the equation is real, however). The potential is usually chosen so as to avoid the ill-posed Fredholm equations of the first kind, while welcome are the Fredholm equations of the second kind and, to a certain extent, the singular integral equations ("sometimes blessings in disguise" [195]). Having obtained the density, the harmonic function in

question is found at any point from the definition of the potential (i.e. by integration). It is this technique that is called *the boundary-integral method*. More precisely, it is an indirect boundary-integral method, since the problem is solved through an intermediate function: the potential density. The direct boundary-integral methods involve only the functions that are contained in the original formulation and are obtained usually as follows. According to the main Green's identity for the contour $C : \vec{\rho} = \vec{\rho}(s)$ and an arbitrary harmonic function u [196],

$$\Omega u(\vec{r}) = \frac{1}{2\pi} \oint_C \left(u(\vec{\rho}) \frac{\partial}{\partial n_\rho} \ln|\vec{\rho} - \vec{r}| - \frac{\partial u(\vec{\rho})}{\partial n_\rho} \ln|\vec{\rho} - \vec{r}| \right) \mathrm{d}s \,,$$

where $\partial/\partial n_\rho = (\vec{n}, \partial/\partial\vec{\rho})$, and $\Omega = 2\pi$ ($\Omega = 0$) if $\vec{r}$ points inside (outside) C, and $\Omega = \pi$ if $\vec{r} \in C$. This formula allows to take into account the Dirichlet or Neumann boundary conditions, leading immediately to an integral equation.

3.1.4 The integral equation

In this paragraph we will present the boundary-integral formulation of the problem developed by Cēbers [175, 176]. We will use the single-layer potential to present the stream function in both domains:

$$\psi(\vec{r}) = \frac{1}{2\pi} \int_{-\infty}^{-\infty} \gamma(s') \ln|\vec{\rho}(s') - \vec{r}| \mathrm{d}s' \,, \tag{3.12}$$

where s' is the arclength parameter. The integration is carried out along the infinitely long interface that is a closed curve on the Riemann sphere. Eq.(3.9) is satisfied automatically by the single-layer representation. To determine γ and solve the problem, we have to satisfy now only the dynamic boundary condition (3.7). To express the condition through ψ, we differentiate Eq.(3.7) along the interface and take into account one of the Cauchy-Riemann conditions for the complex potential ($\partial\varphi/\partial\tau = -\partial\psi/\partial n$, $\partial/\partial n = (\vec{n}, \partial/\partial\vec{r})$):

$$(\partial/\partial n)(\alpha_2\psi_2 - \alpha_1\psi_1)/(\alpha_2 + \alpha_1) = (\partial/\partial\tau)\left[\kappa + (\mathrm{Ca} + \mathrm{Bg})\, y + \mathrm{Bm}\, I_\mathrm{m}\right] . \tag{3.13}$$

Now we need the formula for the normal derivative of the single-layer potential at the contour. The formula is in our notation as follows (e.g. §II.6 of [197], §IV.1 of [135], §IV.5 of [196]):

$$\left(\frac{\partial}{\partial n} \int_{-\infty}^{-\infty} \gamma(s') \ln|\vec{\rho}(s') - \vec{r}| \mathrm{d}s' \right)\Bigg|_{\vec{r}\to\vec{\rho}(s)} = \pm\, \pi\gamma(s) + \int_{-\infty}^{-\infty} \gamma(s') \left(\frac{\partial}{\partial n} \ln|\vec{\rho}(s') - \vec{r}| \right)\Bigg|_{\vec{r}=\vec{\rho}(s)} \mathrm{d}s' \,, \tag{3.14}$$

where the upper (lower) sign holds if $\vec{r}$ points to the domain for which $\vec{n}$ is the inward (outward, respectively) unit normal. Let us introduce

$$\left(\frac{\partial\psi}{\partial n}\right)_0 = \frac{1}{2\pi}\int_{-\infty}^{-\infty}\gamma(s')\left(\frac{\partial}{\partial n}\ln|\vec{\rho}(s')-\vec{r}|\right)\Big|_{\vec{r}=\vec{\rho}(s)}\mathrm{d}s'\,. \tag{3.15}$$

Then Eq.(3.14) gives

$$\frac{\partial\psi_1}{\partial n} = +\frac{\gamma}{2}+\left(\frac{\partial\psi}{\partial n}\right)_0, \qquad \frac{\partial\psi_2}{\partial n} = -\frac{\gamma}{2}+\left(\frac{\partial\psi}{\partial n}\right)_0. \tag{3.16}$$

Substituting these equations into (3.13) finally yields

$$-\frac{\gamma}{2}+\mathrm{At}\left(\frac{\partial\psi}{\partial n}\right)_0 = \frac{\partial}{\partial\tau}\left[\kappa+(\mathrm{Ca}+\mathrm{Bg})\,y+\mathrm{Bm}\,I_\mathrm{m}\right], \tag{3.17}$$

where the dimensionless viscosity Atwood ratio is introduced:

$$\mathrm{At} = \frac{\alpha_2-\alpha_1}{\alpha_2+\alpha_1} = \frac{\eta_2-\eta_1}{\eta_2+\eta_1}\,. \tag{3.18}$$

The three parameters listed on p. 79, At, the dimensionless period T, and the initial conditions determine our problem completely.

As soon as this integral equation is solved for γ, the velocities at each side of the interface can be obtained by differentiating ψ by definition (3.8). Essentially we need only the normal velocity that is equal to $\partial\psi/\partial\tau$. The actual tangential velocity is discontinuous at the interface according to (3.14), but we may take whatever value is convenient; we take the average velocity, though other choices are also used in the literature. Then the differentiation of the single-layer potential can be carried out effectively inside the integral (3.12).

$$\left\{\begin{matrix}v_x\\v_y\end{matrix}\right\} = \frac{1}{2\pi}\,\mathrm{v.p.}\!\int_{-\infty}^{-\infty}\gamma(s')\left(\left\{\begin{matrix}+\partial/\partial y\\-\partial/\partial x\end{matrix}\right\}\ln|\vec{\rho}(s')-\vec{r}|\right)\Big|_{\vec{r}=\vec{\rho}(s)}\mathrm{d}s'\,. \tag{3.19}$$

This equation completes the formal solution for a given time step.

To obtain computable formulas, let us first expand Eqs. (3.15) and (3.19). We introduce complex variables $z = x+iy$, $z'(s') = \rho_x + i\rho_y$. Then

$$\left(\frac{\partial}{\partial x}\ln|\vec{\rho}(s')-\vec{r}|\right)\Big|_{\vec{r}=\vec{\rho}(s)} = \frac{1}{2}\frac{\partial}{\partial x}[\ln(z'-z)+\ln(z'^*-z^*)] = -\Re\mathrm{e}\,\frac{1}{z'-z}\,,$$

and analogously

$$\left(\frac{\partial}{\partial y}\ln|\vec{\rho}(s')-\vec{r}|\right)\Big|_{\vec{r}=\vec{\rho}(s)} = +\Im\mathrm{m}\,\frac{1}{z'-z}\,.$$

Therefore

$$v_x - iv_y = \frac{1}{2\pi i}\oint_C \frac{\gamma(z')\mathrm{d}z'}{z'-z}\,. \tag{3.20}$$

Employing the formula of integration by parts in the Cauchy-type integral (§3.5 in [194]), this equation could have also been derived immediately owing to the connection (3.10), (3.11) between the complex flow potential Φ, the flow function $\Im\mathrm{m}\ \Phi$ (3.12), and velocities. In fact, Eq.(3.20) solves the equation $\Delta\psi = -\omega$, where ω is the vorticity concentrated along C as a vortex sheet.

Now let us make use of the periodicity: $\gamma(z'+mT) = \gamma(z')$ for any integer m. Then, if C' is a part of C that comprises the full period,

$$\begin{aligned} v_x - iv_y &= \frac{1}{2\pi i}\sum_{m=-\infty}^{+\infty}\oint_C \frac{\gamma(z')\mathrm{d}z'}{z'-z+mT} \\ &= \frac{1}{2\pi i}\int_{C'}\gamma(z')\mathrm{d}z'\sum_{m=-\infty}^{+\infty}\frac{1}{z'-z+mT} \\ &= \frac{1}{2Ti}\int_{C'}\gamma(z')\cot\frac{\pi(z'-z)}{T}\mathrm{d}z'\,. \end{aligned} \tag{3.21}$$

The just-used formula

$$\sum_{m=-\infty}^{+\infty}\frac{1}{z+m\pi} = \cot z$$

is cited in [145] (p.402) as known to Leonard Euler back in 1742.

The obtained expressions follow in the real form:

$$\begin{aligned} v_x(s) &= -\frac{1}{2T}\ \mathrm{v.p.}\!\int_0^L \gamma(s')\frac{\sinh b\cosh b}{\sin^2 a+\sinh^2 b}\,\mathrm{d}s'\,, \\ v_y(s) &= +\frac{1}{2T}\ \mathrm{v.p.}\!\int_0^L \gamma(s')\frac{\sin a\cos a}{\sin^2 a+\sinh^2 b}\,\mathrm{d}s'\,. \end{aligned} \tag{3.22}$$

Here $a = \pi\left(x(s')-x(s)\right)/T$, $b = \pi(y(s')-y(s))/T$, and L is the length of the interface. We remind that the principal value of the singular Cauchy-type integral (3.20) must be taken.

Eq.(3.15) can be represented in the same manner since

$$\left(\frac{\partial\psi}{\partial n}\right)_0 = -n_x v_y + n_y v_x = -(\tau_x v_x + \tau_y v_y)\,.$$

It enables us to obtain the final form of the integral equation on γ:

$$\gamma(s) + \frac{\mathrm{At}}{T}\int_0^L \gamma(s')\frac{\tau_y(s)\sin a\cos a - \tau_x(s)\sinh b\cosh b}{\sin^2 a + \sinh^2 b}\,\mathrm{d}s' = -2\frac{\partial}{\partial\tau}\left[\kappa + (\mathrm{Ca}+\mathrm{Bg})\,y + \mathrm{Bm}\,I_\mathrm{m}\right]. \quad (3.23)$$

Note that the limiting value of the fraction in the integrand as $s' \to s$ is

$$\frac{T}{2\pi}\left(\tau_y\frac{\mathrm{d}^2x}{\mathrm{d}s^2} - \tau_x\frac{\mathrm{d}^2y}{\mathrm{d}s^2}\right).$$

The kernel of the integral equation is non-singular and smooth, so that Eq.(3.23) is the Fredholm integral equation of the second kind.

We end up this paragraph with a remark that the case of negative At numbers needs not to be studied separately – owing to a symmetry present in our equations, it reduces to that of positive At's. Indeed, consider two interfaces, one of which is a reflection of the other with respect to $y = 0$ axis. For clarity, let us set $\mathrm{Ca} = 0$. The first interface has the more viscous and heavy fluid above and the less viscous and light one below, so that $\mathrm{At} = \mathrm{At}^* > 0$, $\mathrm{Bg} = \mathrm{Bg}^* > 0$. The second interface is formed by two other fluids: on the top there is a heavier but less viscous fluid, while a light and more viscous one is below, and their properties are such that $\mathrm{At} = -\mathrm{At}^* < 0$, and $\mathrm{Bg} = \mathrm{Bg}^*$. We also demand that the magnetic Bond number be the same. Now consider Eq.(3.23) for the two cases. Its right-hand sides differ only in sign, since so do y and κ, while the I_m's in sum give a constant, cf. Eq.(3.2). If we now demand that γ also take on the exactly opposite value, so will do the integral term of Eq.(3.23), so that the latter equation in both cases will be equivalent. Then it is easy to see from Eq.(3.22) that v_x will be the same in both cases, but v_y will have different signs, thus preserving the relation between the interfaces. In other words, the solution of a problem with $\mathrm{At} = -\mathrm{At}^*$ is exactly the solution of the same problem with $\mathrm{At} = +\mathrm{At}^*$ but turned upside down. Therefore it suffices to study only non-negative At's in the range $0 \ldots 1$.

3.1.5 The magnetic force and the ST finger in a laterally bounded cell

Let us carry out some analytical work on transforming the expression (3.4) for the magnetic integral I_m. First we transform it by Green's formula

$$\int\limits_G \left(\frac{\partial Q}{\partial x} - \frac{\partial P}{\partial y}\right)\mathrm{d}x\,\mathrm{d}y = \oint\limits_{\partial G^+} P\mathrm{d}x + Q\mathrm{d}y\ :$$

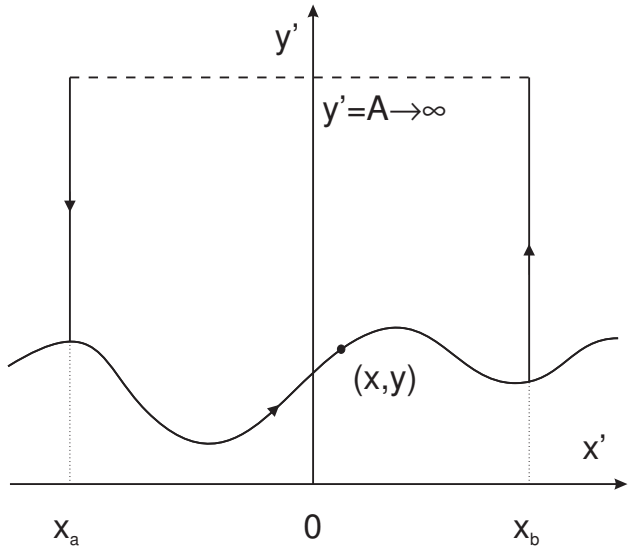

Figure 3.2: The contour of integration for the magnetic term.

$$
\begin{aligned}
I_{\mathrm{m}}(\vec{r}) &= \int \left(\frac{1}{|\vec{r}\,' - \vec{r}|} - \frac{1}{\sqrt{(\vec{r}\,' - \vec{r})^2 + 1}} \right) \mathrm{d}^2 \vec{r}\,' \\
&= \int_{-\infty}^{+\infty} \tau_x(s') \ln \frac{y - y' + \sqrt{(x-x')^2 + (y-y')^2}}{y - y' + \sqrt{(x-x')^2 + (y-y')^2 + 1}} \, \mathrm{d}s' \,.
\end{aligned}
\tag{3.24}
$$

Here and further x', y' mean $x(s'), y(s')$, and x, y mean $x(s), y(s)$. We will consider now a finite integration contour shown in Fig. 3.2. Then owing to the τ_x factor, the integration contour is effectively divided into two parts only. In the part where the integration is done at $y' = A$, the integrand tends as $A \to +\infty$ to the expression $-\ln\left[1 + (x - x')^{-2}\right]$, giving the following contribution to the integral:

$$
\begin{aligned}
I'_{\mathrm{m}}(s) = (x_b - x) \ln \left(1 + \frac{1}{(x_b - x)^2} \right) + (x - x_a) \ln \left(1 + \frac{1}{(x - x_a)^2} \right) \\
+ 2 \left(\arctan(x_b - x) + \arctan(x - x_a) \right) \,.
\end{aligned}
\tag{3.25}
$$

If $|x_{a,b}| \to \infty$, I'_{m} tends to 2π and drops out upon differentiation (3.23). Nevertheless, Eq.(3.25) will be needed as we are going to truncate the domain of integration. Besides, I'_{m} is quite important in the case of the finite geometry that will be discussed later in this paragraph.

The periodic interface will be tracked by $N + 1$ marker points. Marker points have numbers $n = 0 \ldots N$, with the last point ($n = N$) being the first one ($n = 0$) for the next period. The "number variable" n, as we will call

it, may be regarded as a curve parameter another than the arclength $s(n)$. Taking then the periodicity into account, we represent Eq.(3.24) as

$$I_{\mathrm{m}}(s) = \int_{n-N/2}^{n+N/2} \tau_x(s') \ln F\left(\frac{x-x'}{T}, \frac{y-y'}{T}\right) \frac{\mathrm{d}s'}{\mathrm{d}n'} \mathrm{d}n' - T \ln T + I'_{\mathrm{m}}(s) + I''_{\mathrm{m}}(s)\,, \tag{3.26}$$

where only one logarithm evaluation is needed per point s',

$$F(u,v) = \frac{1}{v + \sqrt{u^2+v^2+1}} \prod_{\substack{m=-\infty \\ m\neq 0}}^{+\infty} \frac{v + \sqrt{(u-m)^2+v^2}}{v + \sqrt{(u-m)^2+v^2+1}}\,, \tag{3.27}$$

and

$$I''_{\mathrm{m}}(s) = \int_{n-N/2}^{n+N/2} \tau_x(s') \ln\left(y - y' + \sqrt{(x-x')^2+(y-y')^2}\right) \frac{\mathrm{d}s'}{\mathrm{d}n'} \mathrm{d}n'\,. \tag{3.28}$$

Note that with our moving limits of integration in Eq.(3.26), the periodicity of the magnetic force is ensured. The integrand in Eq.(3.26) is always smooth, while in I''_{m} it is logarithmically singular at $s' = s$, so we integrate it by parts to obtain

$$\begin{aligned} I''_{\mathrm{m}}(s) = \int_{n-N/2}^{n+N/2} & \frac{\tau_x(s')(y-y') - \tau_y(s')(x-x')}{\sqrt{(x-x')^2+(y-y')^2}} \frac{\mathrm{d}s'}{\mathrm{d}n'}\,\mathrm{d}n' - T \\ & + (x-x_A) \ln\left(y - y_A + \sqrt{(x-x_A)^2+(y-y_A)^2}\right) \\ & - (x-x_B) \ln\left(y - y_B + \sqrt{(x-x_B)^2+(y-y_B)^2}\right)\,. \end{aligned} \tag{3.29}$$

Here $x_A = x(n - N/2)$, $x_B = x(n + N/2)$, and $y_A = y_B = y(n \pm N/2)$.

In general, the product (3.27) cannot be calculated in a closed form. Although it may be evaluated numerically using the series transformation and convergence acceleration techniques, in the calculations that will be presented here we will satisfy ourselves with taking a finite number of terms $M = \max m$ and truncating the rest. This corresponds to $x_a = x_A - MT$, $x_b = x_B + MT$ in Eq.(3.25). This formulation of the magnetic force is not identical to that of [175, 176].

Now our problem is fully determined by the integral equation (3.23), its right-hand side (3.26), (3.25), (3.29), and the velocity integrals (3.22). Now we are in position to develop the numerical procedure of solving these equations. But before, it is convenient now to analyze an important property of the magnetic force that has direct consequences for computations of a laterally bounded flow.

Up to now in this Chapter, under study was a flow with periodic boundary conditions, while the real conditions are at least that of no flux (no normal flow). (The more realistic no-slip condition cannot be generally satisfied with the Darcy equation.) With non-magnetic fluids, as long as symmetric shapes are studied, both conditions are related (but not equivalent). Indeed, $v_x(-T/2) = v_x(+T/2)$ by periodicity, while from symmetry it follows that $v_x(-T/2) = -v_x(+T/2)$. Therefore $v_x(\pm T/2) = 0$, and every symmetric periodic Hele-Shaw flow is necessarily a valid laterally confined one. The reverse statement is true only with one reservation: the symmetric interface must approach the sides ($x = \pm T/2$) at a straight angle. Otherwise, in the periodic problem we effectively have an interface with corners, for which our equations are not valid. This is easy to see.

For example, the integrand

$$\frac{\tau_y(s)\sin a\cos a - \tau_x(s)\sinh b\cosh b}{\sin^2 a + \sinh^2 b}$$

in Eq.(3.23) at $s' = L - s$ takes on the value $\tau_y \cot(2\pi x/T)$ if the interface is symmetric. At $x = 0$, thanks to the symmetry and smoothness, we have $\tau_y = 0$ and the indeterminate form may be resolved to produce a finite result. However, as $x \to \pm T/2$, the limit is generally ($\tau_y \neq 0$) infinity. To establish the sort of singularity, it is necessary to investigate two independent limits: $s \to 0$ and $s' \to L - s$. We failed to adapt the algorithm developed for the periodic boundary conditions to the non-periodic case.

Therefore we see the only tractable way to make the periodic boundary conditions work: to demand that $\tau_y = 0$ at $x = \pm T/2$. In other words, the interface should approach the sides of the cell at a straight angle. This is indeed a common, often implicit though, assumption. For such an interface, both types of boundary conditions are shown above to be equivalent.

Unfortunately, with magnetic fluids the situation is worse. It is likely that a magnetic fluid cannot, at least in our description, develop any corners. The absence of MF in the adjacent periods leads to a singularity of magnetic force at the end-points of the interface. In order to have the non-periodic situation in these transformations, one should set $x_a = x_A = -T/2$, $x_b = x_B = +T/2$, and use the fixed limits of integration $0 \ldots L$. The following exact expression can be easily obtained for the magnetic integral I_{m} (3.24) if the interface is planar:

$$\frac{\mathrm{d}I_{\mathrm{m}}}{\mathrm{d}x} = \frac{1}{2}\ln\frac{1 + (T/2 + x)^{-2}}{1 + (T/2 - x)^{-2}} \tag{3.30}$$

This function is logarithmically divergent at the end-points. (We remark here that with a planar interface, the whole problem may be solved by separation of variables, which was done to check our boundary-integral results.)

Note that I_m enters the effective pressure $\tilde{p}$ (3.5), where its singularity cannot be compensated by infinite $\mathrm{d}p/\mathrm{d}\tau$, the "real" pressure gradient along the interface. Indeed, $\mathrm{d}p/\mathrm{d}\tau$ can have only a finite jump given by the dynamic boundary condition at a regular interface, while the jump of $\mathrm{d}I_\mathrm{m}/\mathrm{d}\tau$ is infinite anyway. Therefore, according to Eq.(3.6), as the effective pressure gradient goes infinite, so does the tangential velocity (at least at one side of the interface). We also observed the non-convergent behaviour of numerical velocities for other (non-planar) interfaces that approached the sides of the cell at a straight angle.

If the boundary of the domain occupied by MF has corners, the problem has no bounded solutions in our model and, of course, cannot be simulated numerically. We stress that this fact has physical grounds rather than numerical ones. The more promontory the element of the interface, the stronger indeed it is pushed outwards by the rest of the MF volume. This can be seen from the dispersion relation (3.36) for a planar interface, where the Bm contribution to the growth increment varies asymptotically as $k \ln k$ for large wavenumbers k. Therefore the physical model must be changed in order to simulate the interfaces that are not tangent to the sides of the cell. Perhaps, the Darcy law and the two-dimensional approach to the magnetic force must be abandoned.

However, if the task is to simulate a magnetic ST finger (see §3.2.4), then the precise conditions at the sides of the cell can be not very important. Then one can demand that the interface comes always *tangent* to the sides and simulate a long finger that will not "feel" this condition. The periodic algorithm is incompatible with it, as we have shown above. Still the boundary-integral technique can be applied to the non-periodic situation with a slight modification. Apart from the way the magnetic force is computed, the kernel of the integral equation and the velocity integrals (3.21)–(3.23) are modified. Besides, the non-periodic case requires that γ be distributed not only along the interface, but also along the sides of the cell. In principle, with such method it is also possible to model an infinite interface that does not approach the sides of the cell at all. This algorithm can be developed in the future.

3.2 The numerical method

3.2.1 Numerical modelling with boundary integral equations

In this paragraph we present an overview of applications of the boundary-integral method introduced above in §3.1.3 – the method that will ultimately

serve us to obtain physical results. The review is method-oriented rather than subject-oriented. As we will see, a considerable amount of research was devoted by computational physicists to "taming" the boundary integrals. Numerical instabilities inherent to the method have considerably complicated and limited its use, and not only in the past. Nevertheless, the job is worth doing thanks to important features shared by some of the approaches, including the boundary-integral method, touched upon in §3.1.3. They lead to an integral equation that involves only the values at the boundary, thus reducing the dimension of the problem by unity. Discontinuities of fluid quantities at the interface are easy to take into account; besides, infinite domains are handled naturally. These features are of course an important advantage both theoretically and for modelling.

Elliptic BVP's are among the most common problem types in physics and engineering, emerging in a very wide range of disciplines. Thus the boundary-integral approach has found its application, for example, in diffraction problems in electromagnetism [198], acoustics, to solve the applied problems of elasticity and viscoplasticity theories [199, 200], etc. The approach is natural and especially effective in the problems where only values at the boundaries are in fact important or wanted, e.g. in the analysis of cracks in the elasticity theory (according to the maximum principle, extremal values of the stress are attained at the boundary). In engineering computations, even the complex-variable formulation via the Cauchy-type integrals is in use [201]. On the evolution of the so-called "method of boundary elements" (BEM) in applied mechanics, see [202]. (BEM essentially is the boundary-integral method coupled with a special approach to the boundary discretization.) Aero- and hydrodynamical applications of boundary integrals are also numerous: Stokes flow [203, 200], scattering of surface gravity waves [199], point-vortex [204] and 3D panel [205] methods in aerodynamics, groundwater flow, inviscid non-linear surface waves, the Kelvin–Helmholtz and Rayleigh–Taylor instabilities. For a recent overview on the boundary integral methods for interfacial flows, see [206]. The first (to our knowledge) numerical simulation of a Hele-Shaw flow with surface tension by the boundary-integral method dates back to 1961 [207]. (On further progress, see later in this paragraph.) Owing to the Darcy law, especially close to our problem are the moving-boundary problems (oil extraction by displacement) of the groundwater filtration (percolation) theory (§XVII.6 of [72], [208], §12.3 in [200]). The conditions at the water–air "interface" in porous media are not quite clear (see references in [209]), but are often assumed to be just those of a continuous pressure. The groundwater problems were solved employing the boundary integrals, sometimes employing the jump of the normal derivative of the single-layer potential (§§XVII.6, XIX.6 in [72], [208]). Of

common use in that field, however, are the complex-analytic methods [72]). See a review [157] on the application of the complex-analytic methods to the Hele-Shaw flow with surface tension; on the recent developments and references, see [159, 210] and §X.3 of [11]. As for the numerical solution of the boundary-integral equations of potential theory, see [211] for a general survey. Remember however that we have an indirect boundary-integral method, with velocity being linked to γ through a singular integral, even though the integral equation *per se* is perfectly Fredholmic. Besides, in our case we need to solve a large number of the BVP's, with solution of the preceding problem being used by the following one.

At this point it is necessary to identify and analyze the problem associated with boundary integrals. A singular integral, in general, can be very sensitive to small changes in its density. Consider

$$f(x) = \text{v.p.}\int_0^\pi [g(x+\alpha) + g(x-\alpha)] \cot\frac{\alpha}{2} \mathrm{d}\alpha = \text{v.p.}\int_{x-\pi}^{x+\pi} g(\alpha) \cot\frac{\alpha - x}{2} \mathrm{d}\alpha$$

and its "singular part" obtained by replacing $\cot z$ with $1/z$. Then it can be rigorously proved that an arbitrarily large change in the principal value f can be caused by an arbitrarily small variation of the density g, provided that the variation is only continuous; if the variation is square-integrable, however, this effect is guaranteed not to take place and f is itself square-integrable in x. The example of the first situation was built, and the statement for the second situation was proved in [212] (§69 and comment 113). The sensitivity of a singular integral to the small change in its density is also discussed in [213] (§§5.1, 5.2, 7.1, 7.2), where special approximations to the density are developed that are not subject to the sensitivity and can be used to evaluate the integrals. In [204] (§13.1) it is pointed out that the sensitivity can reveal itself, upon discretization, as numerical instability in the so-called point-vortex method (see below in this paragraph). It is further suggested in [204] that in order to avoid the instability, the point vortices should be placed approximately halfway between the points where the equation is to be satisfied.

Let us recall now that the very boundary-value problem may be ill-posed (the solution to BVP might not continuously depend on the boundary conditions). For an elliptical operator in a bounded domain, boundary-value problems are ill-posed unless boundary values are specified on all boundaries of the domain. A relevant here example of an ill-posed problem is the Cauchy problem for the Laplace equation for which J. Hadamard constructed his celebrated illustration of ill-posedness (e.g. §III.6 of [135], [214]). In the numerical solution of BVP, the ill-posedness appears as a numerical instability, and the finer the mesh, the worse the result. In an advanced text on numerical

analysis [215] it is shown that the two-dimensional Rayleigh–Taylor instability (RTI) with ideal fluids without surface tension is an ill-posed numerical problem, and it is quite difficult even to soften the ill-posedness. It turns out that some boundary conditions must be given with the exponentially small round-off error; high spatial resolution requires multiple-precision machine arithmetics. It is also pointed out that the application of an arbitrary smoothing is a poor practice. In the dispersion relation for the instability modes of a planar interface, the ill-posedness manifests itself as the unlimited growth of the increment as the wavelength vanishes. (Indeed, as $\mathrm{Ca} \to \infty$ in Eqs.(3.36), (3.40) introduced later, the $-k^3$ term becomes insignificant leading to $\lambda \to \infty$ at $k \to \infty$. The same applies even more to the effect of $\mathrm{Bm} \to \infty$ for both perpendicular and normal field orientations.) In the discretized equations, k may not be infinite; instead, the fastest-growing wavenumber corresponds to the numerical mode of smallest wavelength (2 grid points per period – the "sawtooth" mode).

Many physically meaningful and important problems are ill-posed (in an idealized description). We should mention the Kelvin–Helmholtz instability (KHI) that occurs at the flat interface between ideal irrotational incompressible fluids across which the tangential velocity is discontinuous. Under the gravity, surface or internal water waves develop at a horizontal interface. If the configuration is gravitationally unstable, and there is no velocity jump at the interface at infinity, the Rayleigh–Taylor instability ensues, and a non-uniform shear develops even though it was not present initially. The problems of KHI, RTI, and the Saffman–Taylor instability are known to be ill-posed at zero surface tension and to lead to curvature singularities, wave break-ups, etc. in finite time; ill-posedness manifests itself in the corresponding dispersion relations (e.g. §13.7 in [144]) as an unbounded growth rate at large wavenumbers [214]. Note that RTI and ill-posedness can develop even if the upper fluid is of zero density, in the regions of the deformed interface where the local acceleration exceeds the free-fall one [216]. The numerical approximations to these problems proved difficult to obtain even during the regular stage.

Historically, advances in modelling these important problems numerically by the boundary-integral method were ahead of and drove the understanding of the similar method for Hele-Shaw flows. The velocity integrals in these problems of interfaces between two ideal incompressible fluids in two dimensions (referred to as the Birkhoff–Rott integrals in the case of the vortex sheet) are exactly the same as in the Hele-Shaw problem, but the integral equation differs from ours and is related to the Bernoulli's law.

Vortex sheet and point-vortex arrays are a classical subject (e.g. §151 of [73], §§13.62–13.71 of [217], §2.6 of [70]). The first simulation of the dynamics

of the vortex sheet discretized into point vortices, was undertaken in early 1930's by Rosenhead. Even at a low spatial resolution the instability lead to a chaotic motion of the vortices. In 1960's, G. Birkhoff could not obtain the convergence of his results as $N \to \infty$ because of the instability. A common opinion formed that the point-vortex approach is inadequate. In 1965 (published in 1980), the handling of the velocity integrals was improved in the work [218] to take into account the "self-induction" of point vortices (the "van de Vooren correction" discussed later). A real point vortex can drive other vortices but not itself, as known from the hydrodynamics of two-dimensional irrotational flows, e.g. [219]. Thus the (accurately) *discretized* problem for a continuous vortex sheet indeed differs from the *originally discrete* problem for a point-vortex array, though the formulas look almost identical. The number of point vortices was kept low [218] to avoid the instability. Nevertheless, in late 1970's – early 1980's, some new numerical results were obtained with the method. In many works, an arbitrary smoothing was applied, whose effect on convergence was hardly predictable. For later developments, important were the works [220, 221] (no numerical instability was noticed there). Finally, in mid-1980's a correct numerical regularization was developed [222]. Namely, high-wavenumber Fourier modes must be filtered out completely from the solution at every time step if their amplitude is *below* a certain limit. (This is referred to as "the Krasny filtering". Since the solution, while it exists, and the initial conditions should be analytic, the Fourier coefficients must anyway decay quickly with wavenumber.) At small N it may be practical just to do the computations in a higher precision. The filtering allowed to simulate the vortex-sheet evolution from the initial conditions leading to a cusp up to the time of singularity [222]. Yet later, a spectrally accurate quadrature was applied in this problem [223] based upon the results of [224] (the spectral accuracy is discussed in §3.2.3).

For quite a time, also under consideration were various more or less physical regularizations to render the above-mentioned problems well-posed, e.g., by taking into account the surface tension, (additional effects of) viscosity, etc. [214]. In [225], e.g., rigorously proved was the well-posedness of a general interface with surface tension between two ideal irrotational incompressible fluids of different tangential velocities and densities. However, through numerous attempts made by many researchers, a very unpleasant fact became evident in this context that even a physically well-posed continuous problem may upon discretization become an ill-posed one! Many early studies suffered, e.g. [226], from purely numerical high-wavenumber instabilities, and it was not clear why the surface tension cannot damp them. Some early simulations [227, 228] of the Hele-Shaw flow with surface tension were performed by the "vortex-in-cell" (VIC) method, which differs from the point-vortex one

in the smoothing way the velocity is obtained from the vorticity distribution. The success of such eclectic methods was largely due to the mentioned numerical problems with purely boundary-integral methods.

In [229] a perhaps first analysis of the "sawtooth" mode of numerical instability was undertaken and approaches to remove it without indiscreet smoothing were suggested. The important role played by the discretized singular velocity integrals was demonstrated for a spectrally accurate method (using the van de Vooren correction) without surface tension. It is important that singular integrals are not smoothing operators such as common integrals. It can be shown [230] that such singular integrals as in Eq.(3.22) are proportional at small scales to the Hilbert transform $\mathcal{H}$ of γ:

$$\mathcal{H}[\gamma](s) = \frac{1}{\pi}\ \text{v.p.}\!\int_{-\infty}^{+\infty} \frac{\gamma(s')}{s-s'}\,\mathrm{d}s'\,.$$

The Hilbert transform, however, does not alter the amplitude of the Fourier mode:

$$\mathcal{H}[\exp(ikx)] = -i\,\mathrm{sgn}(k)\exp(ikx), \quad \mathcal{H}[1] = 0\,.$$

This quality holds at the discrete level (if singular integrals are computed to the spectral accuracy, see §3.2.3). The spatial instability of boundary-integral methods for two-fluid interfaces was extensively analyzed in [231] by comparing the discrete dispersion relation against the exact continuous one. Trying several conventional discretizations of the interface, derivatives, and the velocity integral, it was revealed why it was so difficult to obtain a numerically stable algorithm. The point was that certain compatibility should exist between the quadrature rule for the singular integral and the way the differentiation is done in other parts of the algorithm. These and related results were presented independently in a series of works [225, 232, 233, 234, 235]. (It was also found there that analysis of the numerical stability at computing a non-linear interface reduces essentially to the simpler question for a flat interface.) Incompatible choices should be rendered stable by a properly applied filtering [232, 234]. Otherwise, numerical modes at high wavenumbers remain unaffected by surface tension, having little in common with exact ones, and grow without bound. In other words, most of seemingly innocent numerical algorithms solve in fact another, ill-posed and unphysical problem, and hence are unstable. A simple example of this behaviour will be given in §3.2.2. We cite here [231]: "we are able to identify the main cause for the growth of the sawtooth mode as the failure ... to represent vorticity created (i.e., redistributed) by surface tension effects. Besides, it was also found that even a slight deviation of the discrete dispersion relation from the continuous one can lead to false spurious non-linear resonances that are another source

of numerical instability (see [229, 231] on Moore's works). These results refer to the case of a vortex sheet with surface tension. Unfortunately, so detailed and delicate numerical analysis is not, to our knowledge, available for the Hele-Shaw flow. Rather, a single spectral method of choice is being advertised in [230] and subsequent works of their group, while stability of other discretizations is poorly covered in the literature.

Described above is a specific sort of numerical instability, sometimes referred to as the "spatial" one. It should not be confused with the "temporal" instability of time integration that we will discuss now. The "spatial" instability remains present even if time integration is carried out exactly (with time continuous). Time integration is numerically stable unless the Courant-Friedrichs-Levy (CFL) constraint on the time step is violated. Observing the constraint guarantees that the round-off errors do not amplify in the course of simulation. The constraint is very stringent for the explicit methods – the ones that use the explicit discrete expression for new marker position solely in terms of old ones. If time marching instead uses implicit formulas for a new position that involve new positions for other markers, the constraint becomes much less restrictive. (In finite-difference methods for partial differential equations, the notions of explicit and implicit templates are extremely important as well.) For our set of equations and explicit method, the CFL condition is [225, 230]

$$(\Delta t)_{\max} \sim (\Delta s)^3_{\min} \,. \tag{3.31}$$

It is $(\Delta s)_{\min}$, the minimum separation of markers in arclength, that constrains the maximum time step $(\Delta t)_{\max}$ for which the explicit time integration is still numerically stable according to (3.31). The constraint is so severe because of the curvature that introduces high-order derivatives. It has also limited seriously the previous research. An implicit method is difficult to obtain, but it allows to choose the time step from considerations of approximation only. Nevertheless, in [230] an effectively implicit time-integration method was developed. In this approach, the interface is represented not in the Cartesian coordinates but in the tangent angle – arclength ones, in order to have simple "linear" expression for the curvature. Further on, the "small-scale decomposition" is applied to the velocity integral, which reveals that at short scales, it behaves essentially like a Hilbert transform on the density of the potential. The latter admits implicit treatment in the Fourier space. The equations are set up in such way that the arclength remain equal automatically. For details, we refer the reader to [230, 182]. (But mind the remark in [231] that in order to have high accuracy, the low-order implicit time-stepping of [230] can in fact require a yet smaller time step than a high-order explicit marching would do.) Though this technique is a significant

advance, allowing to compute the evolution in quite large time steps, we will not employ it, being satisfied with an explicit time-marching.

It is worth mentioning that it is possible to solve the integral equation and compute the velocity integrals at the computational cost of $O(N)$ instead of the standard $O(N^2)$ if fast summation methods are used, such as the method of local corrections or a fast multipole method, and if special interface parametrization is used. Such methods are used (e.g. [230]) occasionally in computations with large N. The overall computational cost of a method hereby becomes only $O(N \ln N)$ per time step. (In our problem such effectiveness is more difficult to achieve, if possible at all, because of magnetic integrals.)

The boundary-integral methods discussed in this paragraph are indirect, i.e. some auxiliary function (the density γ of potential) must be computed first, enabling one to have further two velocity components. However, direct boundary-integral methods for Hele-Shaw flows with surface tension also exist and deserve mentioning. The integral equation is originally formulated for the normal velocity in these methods (the tangential velocity being not important). We refer the reader to [236] for a working example of such method and for references to other such formulations.

In conclusion, we note that the boundary-integral method cannot tackle problems involving topological changes and may require modifications to model singularity formation at the interface. Such problems are treated with ease employing the level-set approach [233], where a two-dimensional interface is considered to be an isoline of level (i.e. height) of a three-dimensional and rather smooth shape. For this and other related computational techniques, see also [8].

3.2.2 Interface and curvature

The periodic interface is tracked by $N+1$ marker points and is in fact defined by their coordinates x, y. A general interface requires a parametric representation. Markers are always uniformly distributed in the "number variable" (this quality is important at dicretizing the integrals, see §3.2.3). The arclength, or natural, parametrization of the interface will also be needed.

To have the arclength s, every time step of the algorithm begins with computing the lengths of the interface curvilinear segments between the markers. This is done through the spline representation of the interface.

A cubic spline is a special case of the cubic Hermite interpolating function. The latter function is a piecewise-polynomial (cubic) interpolant with continuous first derivative [237]. In general, d_i – the values of the derivative at the knots – must also be supplied. However, they may be uniquely defined

by the additional condition of continuity of the interpolant's second derivative. (Note that the periodicity of the function being interpolated is in fact never needed, but first and second derivatives must be periodic.) This condition singles out the cubic spline from other Hermite cubic interpolants and leads to a linear algebraic system on d_i, as discussed in detail in [237]. The $N \times N$ matrix a_{ij} of the system is cyclic tridiagonal, i.e. it contains non-zero elements at the main diagonal $j = i$, two adjacent diagonals $j = i \pm 1$, and two elements at the corners that arise due to the periodicity: $i = 0, j = N-1$ and $i = N-1, j = 0$. Such matrices also arise at solving the second-order PDE's with periodic boundary conditions by finite differences. There exist methods of the Gauss elimination that take $O(N)$ operations. One of them is the standard tridiagonal (Thomas) algorithm applied to the matrix without the two elements, with the obtained solution being corrected using the Sherman–Morrison formula (§2.7 in [195]). We, however, use the the periodic version of the tridiagonal algorithm [238, 239].

Now that we can interpolate by splines, let us describe how the interface parametrization proceeds.

1. First, fit two splines parametrized by the number variable n to the arrays of x_i and y_i. Then compute

$$\int_i^{i+1} \sqrt{\left(\frac{\mathrm{d}x}{\mathrm{d}n}\right)^2 + \left(\frac{\mathrm{d}y}{\mathrm{d}n}\right)^2}\,\mathrm{d}n$$

   for all i using the derivatives of the interpolating splines and the 7-point Gauss quadrature rule [237, 240]. This allows to ascribe to every point its arclength coordinate along the interface.

2. Secondly, reinterpolate x_i and y_i by a new pair of splines parametrized by the arclength $\tilde{s}$ computed at the previous step, and compute the new arclength values.

3. Thirdly, repeat the second step iteratively until convergence – till the moment when the overall perimeter of the interface stabilizes to a prescribed relative accuracy.

Throughout our code, we will assume that $(\mathrm{d}x/\mathrm{d}\tilde{s})^2 + (\mathrm{d}y/\mathrm{d}\tilde{s})^2 \equiv 1$ (i.e. $\tilde{s}$ is the true arclength s) for thus constructed "self-consistent" splines.

As soon as the interface is interpolated, we may check how uniformly the markers are distributed along it. We remind that the minimum separation of markers in arclength should not be too small because of the CFL constraint (3.31). The flow in our problem is such that the Lagrangian markers will

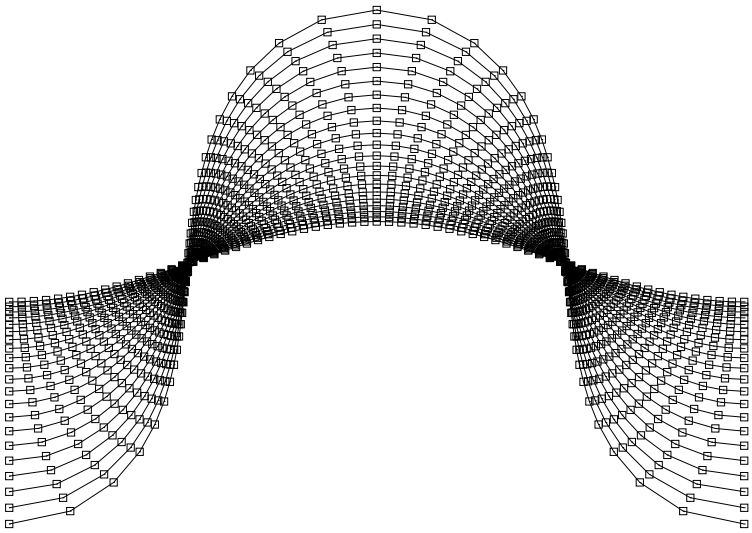

Figure 3.3: The differential clustering of initially equidistant markers as the interface evolves.

cluster into crowded groups in the course of interface evolution, leading to prohibitively short time steps and leaving other parts of the interface underresolved (Fig. 3.3). It is necessary to redistribute the markers from time to time, which is done in the code as follows. As soon as the interface is interpolated, we check if the minimum and maximum arclength separations are within the prescribed margins. If any is not, the new positions are calculated at an equal (and allowed) distance one from another, possibly changing the number of markers. Then the interface is reinterpolated (as described above) again using the new markers.

In our code the redistribution is a relatively rare event; most time steps are performed without it. Sometimes the redistribution can have a smoothing effect on solution [241]. Another possible approach is to use a non-Lagrangian tangential velocity that can be chosen to automatically keep markers uniformly distributed. On this and other approaches to redistribution and/or new marker deletion and insertion, see e.g. [209], Appendix B of [242], [243, 230], and §6.3 in [203].

The curvature is given by

$$\kappa = (y''x' - x''y')/(x'^2 + y'^2)^{3/2}\,,$$

where primes denote the differentiation with respect to a curve parameter. If the interface is parametrized by arclength, the curvature simplifies to $\kappa =$

$(\mathrm{d}^2y/\mathrm{d}s^2)/\tau_x$ (where $\tau_x = \mathrm{d}x/\mathrm{d}s$ as before). However, we observed this form to lead to numerical instability, so in the code we used

$$\kappa = \tau_x \, \mathrm{d}^2y/\mathrm{d}s^2 - \tau_y \, \mathrm{d}^2x/\mathrm{d}s^2 \, .$$

To have the curvature, we need to accurately and reliably compute the derivatives of the interface-defining functions.

It is well-known ([244], §4.12 in [237]) that the cubic spline interpolation of a smooth enough function offers the accuracy of $O(h^4)$, h being the (maximum) distance between the knots. The n-th derivative of the spline approximates the n-th derivative of the function to the order $(4-n)$. However, in the special case of a periodical function interpolated over its period (i.e. if the spline boundary conditions are periodic), the accuracy of the spline derivatives can be improved owing to the fact (see [245] and references therein) that the asymptotic error of the first derivative of a periodic cubic spline remains $O(h^4)$ at a knot. Higher derivatives may be had to the same order through the following procedure. First, one fits a spline to the function and computes the spline's first derivatives at the knots. To these values, another spline is fit then; its derivative will be an excellent, $O(h^4)$ approximation to the second derivative of the original function. (Note that the second derivative of the original spline would be only h^2 accurate.) Yet higher derivatives may be obtained in the like manner. This technique was referred to as the "spline-on-spline" method (§2.5 in [244]), later as the "successive" or "iterated" splines. It was used in the boundary-integral problems already in [226]; with quintic splines it was used in [242].

We have just discussed the behaviour of the approximation error for a given function and its derivatives as the mesh is refined. However, a computation is generally done once with a predefined number of markers, the mesh being refined (doubled) for the purpose of stability rather than approximation. Thus the reverse situation is also of interest: the mesh is fixed, and one tests how good the approximation is for the derivatives of various trial functions, for which the Fourier modes $\exp(ikx)$ are naturally chosen. The work [231] analyzed several ways to interpolate a function uniformly sampled over a period of 2π. It was demonstrated that the quality of the spline representation deteriorates as k approaches the "Nyquist frequency" which is defined as the highest wavenumber $k_{\max} = N/2$ visible to the N-point mesh (the period being 2π). The derivatives of the interpolating spline at the knots are underestimated, and the smoothing is characterized by the error factor [233, 234, 231]

$$E_{\mathrm{s}}(kh) = \frac{3}{2+\cos(kh)} \frac{\sin(kh)}{kh} \, ,$$

where $h = 2\pi/N$ is the uniform spacing. In a sense, even the periodic-spline approximation to the derivative is local like the one by finite differences. In compliance with the previous passage, $1 - E_\mathrm{s} \sim (kh)^4/180$ as $h \to 0$. The "sawtooth" (Nyquist) mode has 2 sampling points per period that are the points of extremum for the interpolating spline, whose derivative therefore vanishes at the knots, $E_\mathrm{s}(\pi) = 0$. This property is a difficulty [231] for a straightforward spline-on-spline procedure. The sawtooth mode does not contribute to the computed interface curvature and is not damped by the surface tension. Thus it can be a source of the numerical instability (of a simple "spatial" one); as we have discussed already, the surface tension should be enabled to act upon high numerical wavenumbers (see Section 3.2.1).

3.2.3 Discretization of integrals

Integral operators enter the formulation of our problem three times:

- in the magnetic force (quadrature);
- in the potential density (an integral equation);
- in the velocity (singular quadrature).

We shall consider these cases one by one.

The first issue are the numerically accurate quadratures in the magnetic force (3.26), (3.29). Essentially we have our data in the tabular form: the values of the integrand are known at the marker points, the markers being equispaced in the number variable. Then it is natural and convenient to use the Hermite cubic quadrature [237]. Consider the Hermite cubic interpolating function (see §3.2.2) with equidistant knots of spacing h – a piecewise-cubic polynomial $c(x)$ with continuous first derivative. It is fully defined by two arrays: the one of function values y_i and the one of derivatives d_i. Since the error of the Hermite interpolation of a smooth function is $O(h^4)$ (see above), the original integral can be approximated by the integral of $c(x)$ yielding an interpolatory quadrature rule of the polynomial degree 4. The integral of $c(x)$ is given by a remarkably simple formula (§5.8 in [237]):

$$\int_{x_1}^{x_n} c(x)\mathrm{d}x = \sum_{i=1}^{n} \alpha_i y_i + (d_1 - d_n)h^2/12\,, \tag{3.32}$$

where

$$\alpha_i = \begin{cases} h/2 & \text{if } i = 1 \text{ or } i = n, \\ h & \text{otherwise.} \end{cases}$$

Obviously, the sum in Eq.(3.32) is the standard compound rectangle rule, while the other term is a correction that improves the accuracy. Note that the correction term involves the derivatives only at the ends of the segment of integration. In our code the derivatives of the integrand functions at the endpoints are computed analytically from the expressions (3.26), (3.29). Note that in order to evaluate (3.29), the segment should be divided into two parts at the point $s' = 0$ because the integrand is non-smooth there, and the rule (3.32) should be applied to both parts separately.

The second task is to solve the integral equation (3.23) for the potential density γ. There are several methods available for the numerical solution of the Fredholm integral equations of the second kind. In [166, 167, 168, 175, 176] the Galerkin method is used. The simplest yet efficient method consists, however, in replacing the integral operator with a quadrature rule:

$$f(s) = \gamma(s) + \int_a^b \gamma(s')K(s,s')\mathrm{d}s' \approx \gamma(s) + \sum_j w_j \gamma(s_j)K(s,s_j)\,, \qquad (3.33)$$

where K is the kernel of Eq.(3.23) including the prefactor At/T, f is its right-hand side, w_j are the quadrature weights, and s_j are the quadrature nodes. The formula (3.33) evaluated at the nodes $s = s_i$ reduces the problem to a system of linear algebraic equations. This direct approach to solve an integral equation is usually called the (mechanical) quadrature method and occasionally is referred to as the Nyström method. The latter term should preferably be used if on obtaining $\gamma(s_i)$ the values of γ at an *arbitrary* point s are found through Eq.(3.33) used as an interpolation formula (the "Nyström interpolation"). For our purposes it suffices to have γ at the nodes s_i only.

Next, which quadrature rule should be chosen? The advice of the "Numerical Recipes" [195] is that "for smooth, non-singular problems, nothing beats Gaussian quadrature...". Indeed, it is obvious that the dimensionality of the algebraic system should be kept as low as possible, the accuracy being fixed. The Gauss quadrature rules are generally the most efficient in this sense – for a given number or nodes, they provide the highest algebraic accuracy (i.e. they exactly integrate algebraic polynomials of the highest order) among other interpolatory rules. However, our case is not a general one. The kernel is periodic, the right-hand side and γ are periodic as well, and the markers are equidistant in the number variable. Then there exists an appealing alternative that we will employ [211]. The following result is important (§6.4 in [215]; also formulated in other textbooks on numerical analysis, in [223], etc.). For a periodic function being integrated over its period, the N-point compound rectangle rule is exact for trigonometric polynomials of the order $N-1$, which is the highest possible order for a N-point rule. Such algo-

rithms are called spectrally accurate, of infinite accuracy $\sim \exp(-\text{const} \cdot N)$, or saturation-free.

The system of linear algebraic equations is solved for $\gamma(s_i)$ by simple iterations (this method is sometimes referred to as Richardson's one, §2.3 in [246], the fixed-point iteration, or as successive substitutions, since the system originates from the Fredholm equation of the second kind):

$$\gamma^{i+1}(s) = f(s) - \sum_j w_j \gamma^i(s_j) K(s, s_j)\,. \tag{3.34}$$

The initial guess γ^0 is taken from the previous time step. In [233] it is suggested to use the γ_0 extrapolated from several previous time steps. If a redistribution has occurred at the beginning of the step, the old γ at new marker positions is found by the spline interpolation. At the first time step, the right-hand side is taken as the initial guess. On convergence of the iterations, see [221, 216, 233, 243]. The condition to stop the process is that the relative change (as compared to the previous iteration) of the absolute value of any γ component no longer exceeds the prescribed threshold (i.e. the error should be small in the "continuous" norm). More effective iterative methods such as GMRES [182, 247] can also be applied.

Now let us turn to the third question – how the principal-value integrals (3.22) can be computed numerically. They have the form

$$I(\infty) = \text{v.p.}\!\int_0^N g(n, n')\,\mathrm{d}n'\,,$$

where n, n' are the number variables, g is N-periodic in both variables and singular but Cauchy-integrable at $n' = n$. At the marker points $n \in [0 \ldots N)$ takes the values $0 \le n_i = i < N$. A possible approach is to resolve the singularity, which leads to the "van de Vooren correction" [218] to the rectangle quadrature rule with the singular point omitted. The accuracy of the corrected rule is determined by the way the derivatives that enter the correction term are computed; with the Fourier differentiation, the corrected rule becomes spectrally accurate. Equivalently, the singularity can be subtracted [218], leading to the spectral accuracy [223]. However, there exists a simpler very accurate method. Integrating by the (compound) rectangle rule, let us simply omit the node that corresponds to $s' = s$ (the "point vortex method")

$$I(\infty) \approx I(N) = \sum_{\substack{j=0 \\ j \ne i}}^{N-1} g(s_i, s_j)\,,$$

Then it turns out that the relative (and hence absolute) error introduced hereby is not just $O(1/N)$, but, in addition, does not contain any algebraic terms of higher order [224, 223]. Then this $O(1/N)$ term can be exactly eliminated by the classical Richardson extrapolation [238] restoring the spectral accuracy [224, 223]. The Richardson extrapolation in this case consists in the following. Let $N+1$ be odd; the error term to eliminate is C/N, where C is a constant. Consider the same rule with a halved number $N/2+1$ of points, i.e. the point with $j=i$ is omitted as before, but starting with it every other point is skipped as well:

$$I(N/2) = 2 \sum_{\substack{j=0 \\ j\neq i \\ i+j \text{ even}}}^{N-1} g(s_i, s_j)\,,$$

Here the term is $2C/N$. Then it follows that in the combination

$$2\,I(N) - I(N/2) = 2 \sum_{\substack{j=0 \\ i+j \text{ odd}}}^{N-1} g(s_i, s_j)\,,$$

the error terms cancel out, which leads to a spectrally accurate approximation of $I(\infty)$. This is known as the alternate-point (or alternating) trapezoidal (or rectangle) rule. We will use this rule, for which, we remind, N should be even.

Yet another issue is an efficient evaluation of the trigonometric functions in Eqs.(3.22), (3.23). Indeed, at every time step there are approximately N^2 pairs of $x_j - x_i$ and $y_j - y_i$ of which trigonometric or hyperbolic functions must be computed. However, it is possible to decrease the count of function evaluations down to N using the formulas [229]

$$\sinh(z - z') = \sinh z \cosh z' - \sinh z' \cosh z\,,$$

$$\cosh(z - z') = \cosh z \cosh z' - \sinh z \sinh z'\,,$$

and analogous trigonometric identities. The functions in the right-hand side are computed once during a time step. The tables of these values are used subsequently in Eqs.(3.22), (3.23).

Note that the form of denominator in Eq.(3.22) is so chosen as to avoid the cancellation of digits as $s' \to s$ that would occur if it were replaced with $\cosh^2 b - \cos^2 a$. This point was made in [218].

3.2.4 Characterization and validation

In the previous paragraphs we have described a single time step of the algorithm. Before turning to its verification, we must complete the definition of the algorithm by specifying how the problem is integrated in time. Operation count per time step is $O(N^2)$ for the equation setup (magnetic force, matrix to solve the integral equation), solving for γ (operations with the matrix), and evaluation of the velocity integrals. Then, if the perimeter increases approximately linearly with model time (Saffman–Taylor fingers) (and since markers are distributed approximately evenly along the interface), a computing time needed to calculate up to a certain model time is a cube of the model time. This imposes a practical prohibition to compute further than a certain model time.

Given the expenses of computing the velocities of the markers, we perform the time integration of the system by the explicit two-step Adams-Bashfort method. At the first time step or after a redistribution of markers has occurred, the second order Runge–Kutta method is employed. Both methods are of the second order of approximation in the time step Δt. The time step is fixed throughout the run. Higher temporal convergence is not reasonable because it is the stability constraint (3.31), and not the approximation, that really limits from above the time step $\Delta t \sim 1/N^3$ in our computations. Since the error of the spatial approximation will be found to be asymptotically $1/N^4$, the error of the second-order time integration behaving as $(1/N^3)^2$ is negligible at high N.

The program is written portably in the C programming language and compiled with the free Digital Mars compiler [248]. Throughout the code, we compute indiscriminately in the 80-bit "long-double" floating-point arithmetic (ca. 20 decimal digits). With an Intel® PC, this is anyway the lowest (or the only) hardware precision. Multiple precision defers the onset of numerical instabilities and is good for computing nearly ill-posed problems (§3.2.1). The algorithm requires $O(N^2)$ memory at At $\neq 0$ because of the matrix of the integral operator. The matrix is computed once per time step and stored to be reused several times as the corresponding linear system is iterated. With $N = 3000$ markers the matrix takes about 100 Mbytes of RAM.

Now we will verify the correctness of our implementation of the algorithm to prove its suitability for the modelling. This will be done in a number of ways. The code of course passes simple "internal-consistency" checks. It passes the periodicity test (a comparison of results obtained with shifted initial conditions). Doubling the period also gives consistent results, i.e. two equal patterns are obtained side by side, each being equal to the pattern

obtained with a single period. The volume of each fluid must conserve by formulation; the numerically computed volume is of course non-zero and increases with time, but is checked to remain reasonably low. (Other integral invariants should also be constant and can be checked [218, 226].)

Note that we don't use any explicit filtering. Smoothing other than that naturally associated with the spline approximation (p. 100) is not present in the presented computations. We were able to do many computations without any visible signs of instability or irregularity in the plots of the interface, the right-hand side (rhs) of the integral equation Eq.(3.23), its solution γ, or velocities. However, in some rare cases we did observe that, independently of the time step size, the $(\kappa + \mathrm{Ca}\, y + \mathrm{Bm}\, I_{\mathrm{m}})$ combination entering the rhs, or rhs itself, developed a small-amplitude zigsaw pattern over some segments of the interface. The amplitude of the zigsaw grew quite slowly with time or saturated at a constant, quite low value. Usually we had to change the spatial resolution to avoid this. We also noticed that too loose marker redistribution conditions could provoke the zigsaw. There was also another, more serious sort of numerical problem. With highly ramified and convoluted interfaces, a numerical blow-up would occur quickly at a very localized segment of high interfacial curvature: say, a dozen consequent markers would have irregular rhs value, velocities, etc. The iterations of the integral equation on γ would no longer converge. This problem caused the computation to stop, and we could not find a remedy against it. By analogy to the two-dimensional interfacial problems for ideal fluids, we may expect that full "spatial" numerical stability can be achieved by application of a certain filter [232, 234]. Other possibilities are also being tried, which is a subject of our ongoing work.

In Fig. 3.4 some numerically computed non-magnetic shapes are compared to the ST finger of a relative width λ. The asymptotic shape of an infinitely long finger with the tip at $x = y = 0$ is given by the formula

$$\exp \frac{\pi y}{(1-\lambda)T} = \cos \frac{\pi x}{\lambda T}\,. \tag{3.35}$$

At any λ, the ST finger is an exact solution of the problem at zero surface tension ($\mathrm{Ca} = \infty$; §3.1.1). As the surface tension is non-zero but small, λ tends to 1/2. Even at larger surface tensions the observed and modelled shapes not predicted by the surface-tension-free theory, are well described by Eq.(3.35) with a suitably adjusted λ (the problem of the finger-width "selection"). If not specified otherwise, for λ we will take the first width maximum, counting from the tip of the finger. As illustrated by Fig. 3.4, the shapes with surface tension near tips are narrower than the ST finger, but already at Ca as small as unity, the correspondence becomes quite close.

A common verification test for a Hele-Shaw numerical code is the compar-

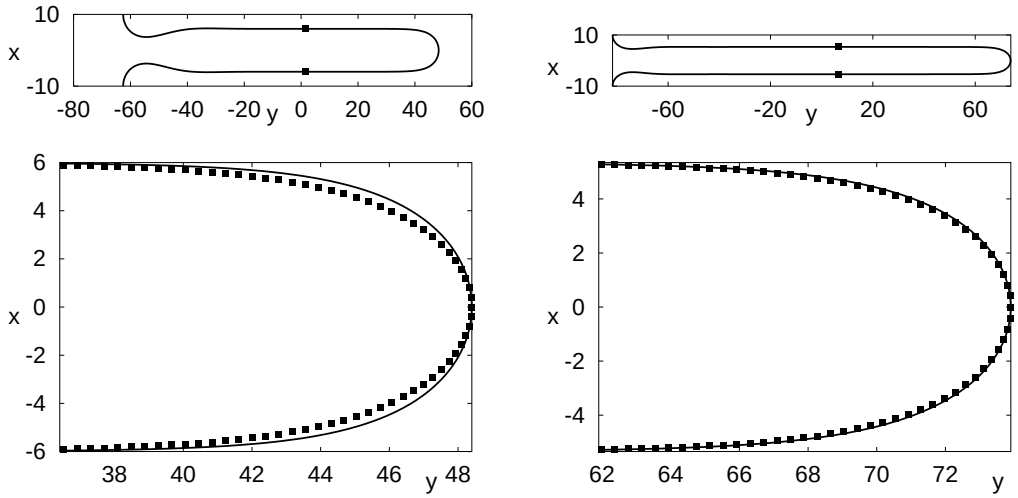

(a) Ca = 0.2, $t = 500$: $\lambda = 0.59979$.

(b) Ca = 1, $t = 100$: $\lambda = 0.53447$.

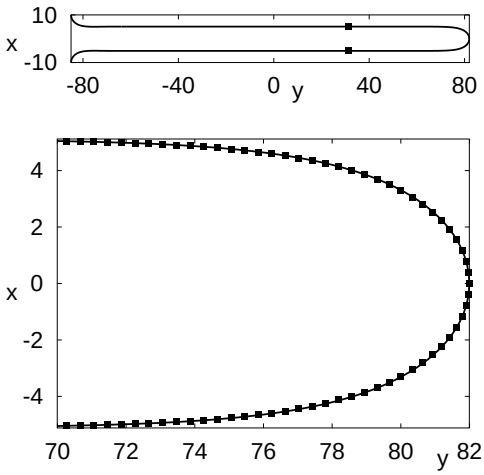

(c) Ca = 5, $t = 20$: $\lambda = 0.51181$.

Figure 3.4: A comparison of the computed finger shape to the classical ST solution. Upper panels: A non-magnetic finger computed with At = 1, $T = 20$, and the initial data $y = 0.02\cos(2\pi x/T)$. Lower panels: The magnified tip of the computed finger (boxes) versus the Ca = ∞ ST finger (solid line) of a relative width λ, which is defined by two points marked (solid boxes) in the corresponding upper panel.

Ca	λ by [162]	$\lambda = b$
1.339824	0.515	0.51538
0.062976	0.640	0.646

Table 3.1: The ST finger width λ – capillary number Ca dependence. Center: results from Table I of [162]. Right: our corresponding numerical results (Bm = 0, At = 1, $T = 31.75$, $M = 3$, $y = 0.03\cos(2\pi x/T)$ and $N = 65$ initially).

ison of the computed λ to the benchmark steady-state results of [162] (§3.1.1). where a unique finger width for a given surface tension was computed. We compute the ST fingers at several Ca, starting with a small cosine-like initial interface perturbation. However, with a time-dependent model the limiting λ can be difficult to recover. Even an apparently developed finger in fact continues to deform. Namely, the lateral segments of its interface can undulate slightly in a symmetric fashion, with humps emerging not far from the tip, travelling slowly away from the nose, and increasing in amplitude in the meanwhile. The distance between the extrema of symmetric humps is natural to be taken for λ. Thus a convention is needed, when and which hump should be used. On the other hand, the amplitude of the undulation being rather small (about the last decimal place in lambda by [162]), we can merely neglect the difference. In Fig. 3.5 this situation is shown for Ca = 0.062976 (the undulations take place at small Ca). We assume that the width of a hump follows approximately the model $\lambda(t) = a/(t - t_0) + b$, where a, b, and t_0 are determined from λ values at several t. This b may be thought of as the steady-state λ, though its precise value can be appreciably model-dependent and should not be attributed too much importance in such cases. Thus, it is clear from Fig. 3.5 that the computed λ may well tend to the McLean&Saffman's limit 0.640 instead of the value $\lambda = b = 0.646$ given by the fit. (Fit parameters were determined by a non-linear estimation procedure available in [249], where the non-linear least-squares Marquardt-Levenberg algorithm is implemented). Note that minute oscillations of the tip curvature were reported in [250], where it was also shown that the these oscillations can grow in amplitude with time leading to a late tip-splitting of a seemingly stationary finger.

Table 3.1 lists two entries of Table I of [162] that were chosen here for being extremal among those given by [162] – the first one corresponds to the smallest surface tension, while the other corresponds to the largest surface tension at which the interface is still linearly unstable. (Lower part of their Table refers to the linearly stable situation.)

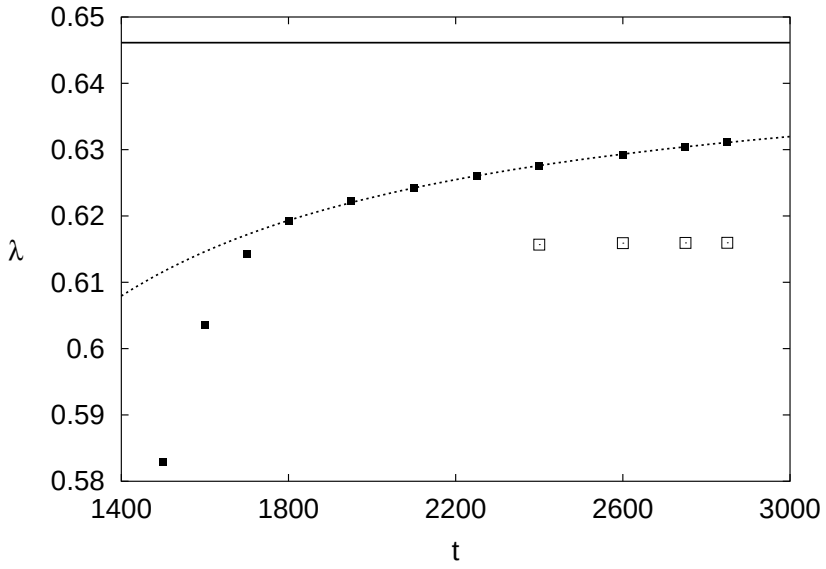

Figure 3.5: Computed finger width λ vs time. Black and empty boxes correspond to two different "humps" (see text). The dotted curve is a fit to a part of the data, and the solid line is curve's asymptote $\lambda = b$.

Now let us compare the computed growth increment to the theoretical dispersion relation [176]

$$\lambda = -k^3 + k\left[\mathrm{Ca} + \mathrm{Bg} + 2\,\mathrm{Bm}\,\left(K_0(k) + \gamma + \ln\frac{k}{2}\right)\right]. \tag{3.36}$$

(We use the same letter for the growth increment and finger width, which should not lead to confusion; the Macdonald function K_0 is given by Eq.(2.20).) Note that if $y \sim \exp(\lambda t)$, then $v_y/y = \lambda$. Let us choose the parameter values with which the summands in Eq.(3.36) are of the same order: $\mathrm{Ca} = 1$, $\mathrm{Bm} = 1$, $T = 2\pi$, i.e. $k = 1$, and $\lambda = 0.610187$. Besides, take $M = 10$, the number of markers as low as $N = 65$, and the interface that was initially just slightly perturbed: $y = 2\pi \times 10^{-7}\cos(2\pi x/T)$. Then for the marker in the middle ($x = 0$, $y = 2\pi \times 10^{-7}$) the computed vertical velocity is found to be $v_y = 3.833196 \times 10^{-7}$, so that $v_y/y = 0.610072$. Comparing this value against the theoretical one, we recover a rather small error in the computed value: 0.02%.

Now let us investigate the quality of the spatial approximation offered by our algorithm. Specifically, we will find the actual rate of convergence of the computed solution to the limit as the grid is refined ($N \to \infty$). We remind that the numerical algorithm was so constructed as to enable the

fourth-order convergence. To check this feature, let us fix the following parameters: Ca = 7/120, Bm = 1.14, At = 1, $T = 20$, $M = 3$, and the initial condition $y = 7\cos(2\pi x/T)$. The initial condition is non-linear in the sense that its amplitude is comparable to the period T, so that the non-linear integral term in Eq.(3.23) can manifest itself. We distribute markers uniformly in x, hence unevenly in arclength, to have the most general case possible. The test consists in running the code with different numbers of markers and comparing the results computed in the first time step (marker redistribution being disabled). Namely, we will pick out several markers that are present at any N and compare their computed velocities as N varies. "By construction," the values are expected to be of the algebraic asymptotic behaviour: $v|_N \sim A + B/N^\alpha$, where $v|_N$ is either v_x or v_y computed with N markers per period. Hopefully we should observe $\alpha = 4$. To verify this, let us multiply N repeatedly by a factor of 2, carrying out the computation with each value. Now notice that

$$\frac{v|_{2N} - v|_N}{v|_{4N} - v|_{2N}} \quad \overset{N\to\infty}{\sim} \quad \frac{1/(2N)^\alpha - 1/N^\alpha}{1/(4N)^\alpha - 1/(2N)^\alpha} = 2^\alpha \,. \tag{3.37}$$

Thus the "apparent" order of convergence is easy to compute having the results for $2N$ and $4N$ along with the ones for N. The results of such test with our code are given in the Table 3.2 for 3 markers: far from the end of the interface, close to it, and immediately at it. The reader may quickly verify, for example, that the ratio (3.37) for v_x at the marker with coordinates $x = -1.875$, $y = 7\cos(2\pi x/T) \approx +5.820$ and for N as high as 1024, is $8550/519 \approx 16.5$. (The deviation from the exact power of two must be attributed to the finite value of N.) The same behaviour is the case for other markers and other quantities (γ, etc.). Hereby the so-called "apparent" spatial convergence of the algorithm is proved to be of the fourth order. Even though we won't necessarily compute at that high resolutions, this property is quite satisfying, for lower (and usually unchecked and unreported) precision of existing previously algorithms was one of their serious drawbacks. In fact, the ultimate goal in this direction might be to construct a (even better) spectrally accurate algorithm for the Hele-Shaw flow with MF's.

In the same manner we can verify the temporal convergence as the time step is diminished. Specifically, the following was done (with the redistribution feature disabled):

- $4n$ time steps, each being equal Δt;
- $2n$ time steps $2\Delta t$;
- n time steps Δt.

Coordinates	N	$v_x \times 10^2$	$v_y \times 10^2$
	32	-7. 234440 452984838804 63000	+8.1 00871 906452581012 4300
	64	-7. 297826 695220566467 7000	+8.1 05130 482414961237 5500
	128	-7. 304908 078187593675 360	+8.1 10591 558746343030 290
$x = -1.875$,	256	-7. 305266 384062836710 22	+8.1 10878 551916856362 17 7
$y \approx +5.820$	512	-7. 305288 399465865115 1 37	+8.1 10896 193374066252 1 10
	1024	-7. 305289 769194312342 0855	+8.1 10897 291015752110 0685
	2048	-7. 305289 854700766376 00519	+8.1 10897 359535596702 00416
	4096	-7. 305289 859894237968	+8.1 10897 363694727385
	32	-0. 271664 5569677863042 1. 000000	-2.30025 0954391177648 2.00000
	64	-1. 211184 109416471383 6500	-4.34511 6893518365033 1500
	128	-1. 217722 229490212754 1500	-4.36056 0334594867185 340
$x = +9.375$,	256	-1. 216234 375601009210 119	-4.35712 0956443009651 27 5
$y \approx -6.865$	512	-1. 216115 418835572680 7 85	-4.35684 5517651677088 1 82
	1024	-1. 216107 566726906089 497	-4.35682 7330862391562 1152
	2048	-1. 216107 069391478064 0314	-4.35682 6178870820950 00728
	4096	-1. 216107 037973773322	-4.35682 6106092765834
	32	+5.583641188300347835e-17	+17.41071 883481683420 3.00000
	64	-1.253608761936364502e-17	+20.37177 215224953303 6100
	128	+1.022876987104293089e-16	+20.43251 766074224400 700
$x = +10$,	256	+3.272935308190616510e-17	+20.42555 393928514361 61 4
$y = -7$	512	-1.322027848250830612e-16	+20.42494 009378124741 4 12
	1024	-1.905082977493328250e-17	+20.42489 891147713024 262
	2048	-3.368252984536326996e-17	+20.42489 629334124457 0164
	4096	-9.493402997760839080e-17	+20.42489 612932692596

Table 3.2: Pointwise convergence of results as the discretization is refined. For three markers, listed are their velocities computed at various N. The rows with the empty N entry contain instead the leading digits of the difference between the values immediately above and below. See the text for details.

The temporal convergence proved to be of the second order.

However, another issue may become important in this regard. As an example, two competing fingers that have developed from the "symmetric" initial conditions (i.e. that have been absolutely identical at the first time step) and have preserved their resemblance to high accuracy till some moment, suddenly can break the symmetry. Which of the two will dominate is determined essentially by the numerical noise, so that computing the same problem with two different time steps (or other numerical parameters) can lead to rather different shapes. This question will be explored in more detail later (§3.3); now we just remark that for the purposes of establishing the convergence, such events must be avoided.

Our code will be further checked in the following paragraph along with presenting the results obtained with it. In particular, we will reproduce and extend the results of Cēbers [176] regarding non-linear patterns exhibited by magnetic fluids in a Hele-Shaw cell.

3.3 Numerical results for the perpendicular field[3]

In this paragraph we will present the results of our numerical simulations. They will be split into two parts: the Saffman–Taylor fingers and the "dendritic" patterns, although the division is not strict. A small-amplitude perturbation, mostly one harmonic of a period T, will be taken as the initial condition. In most cases the initial number of markers will be equal to $N = 32$ or $N = 64$; however, as the interface evolves and its perimeter increases, the number of markers will vary directly, reaching in some cases several thousands. The time step is chosen to be close to the largest one compatible with numerical stability.

3.3.1 Magnetic Saffman–Taylor fingers

We begin with repeating the simulation [176] of a magnetic ST finger. In Fig. 3.6 we present our results obtained with the same physical parameters as in [176]. In particular, Fig. 3.6(a) corresponding to $t = 0.44$ shows excellent agreement with the last panel in Fig.2b of [176] that corresponds to $t = 0.4375$ in our notation (note that gravity was directed upwards in [176]; aspect ratios of the plots are the same). At a later stage, the characteristic "peristaltic"

[3] "...du fait de la difficulté mathématique des modèles de croissance, l'analyse de l'évolution des formes de croissance ne peut se faire en général que de façon numérique." (P. Pelcé, [11], p. 19.)

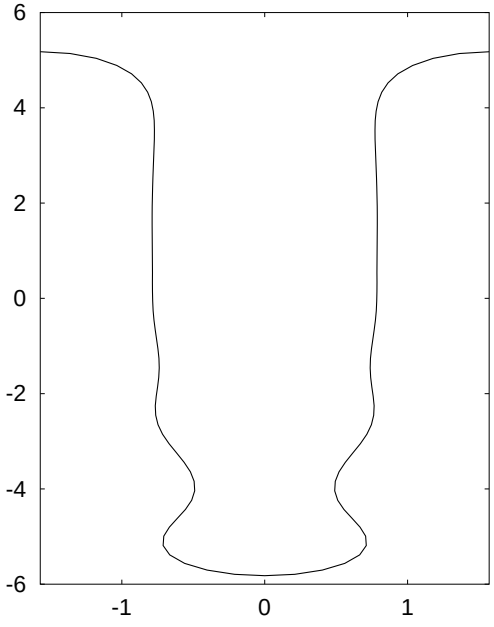

(a) $t = 0.44$.

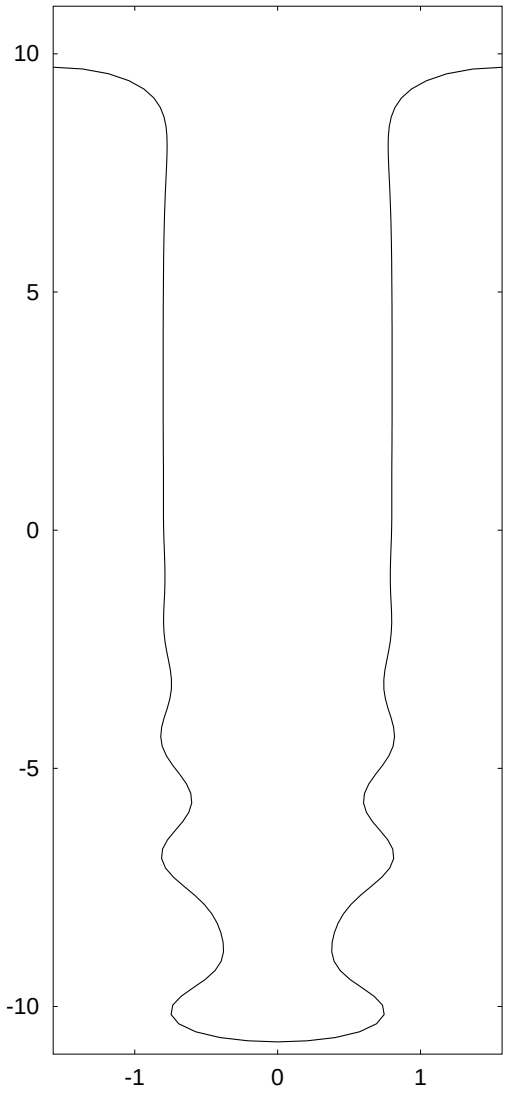

(b) $t = 0.85$.

Figure 3.6: Magnetic fingers computed with Ca = 12, Bm = 7, At = 29/31, $T = \pi$, $M = 3$, and the initial data $y = -0.05\cos(2\pi x/T)$.

		Bm			
Ca	$\mathrm{Bm}_{\mathrm{cr}}$	0.24	0.61	0.93	1.14
7/1200	0.821403	stable	stable	0.521	nonstat.
7/240	0.615011	stable	stable	0.5469	0.508
7/120	0.357022	stable	0.59805	0.54230	0.5117
7/40	0	0.58850	0.55736	0.53107	0.51468
7/12	0	0.54173	0.52999	0.51984	0.51325

Table 3.3: The finger width λ as a function of Ca and Bm. Other parameters: At $= 1$, $T = 20$, $M = 3$, the initial condition is $y = 0.02\cos(2\pi x/T)$, average spacing between markers $\Delta s = 0.61$. $\mathrm{Bm}_{\mathrm{cr}}$ is a critical magnetic Bond number at the given Ca. The entry "nonstat." refers to a non-stationary finger whose sides continuously deform and tip width oscillates too much.

deformations near tips of MF tongues falling down become more pronounced (Fig. 3.6(b)).

Now we will present the width of simulated fingers at various Ca and Bm. The initial condition is set to be a single small-amplitude harmonics of a period T. As in §3.2.4, the relative width λ is measured by the width maximum that is nearest to the tip. The results are listed in Table 3.3 and are also plotted in Fig. 3.7 in the fashion of the experimental Fig. 2.31 of [181] and Fig. 4 of [7]. The fingers are allowed to develop until their width converges to several decimal places, except for the case shown in Fig. 3.8, where the same extrapolation is used as in §3.2.4 (Fig. 3.5, p. 108). However, at low Ca and high Bm numbers the fingers continuously deform "peristaltically" causing the tip width to oscillate. This limits the accuracy of our computed λ. In one case (Ca $= 7/1200$ and Bm $= 1.14$), the deformations are so large in amplitude that no meaningful steady width can be ascribed to the finger (besides, the finger spontaneously looses symmetry after a while and starts undulating, cf. later). That at Bm > 0.9 fingers become unstable was mentioned in [7, 181]. Comparing Fig. 3.7 to the above-mentioned experimental figures, one can notice that in the experiment, but not in our simulations, it was possible to obtain steadily propagating non-linear fingers in linearly stable situations. From our experience with large-amplitude initial conditions and also with finger-shaped ones, we tend to think that this discrepancy cannot be attributed to the difference in initial conditions. Rather, the non-periodicity of the experimental pattern should lead to different stability properties (see the end of §3.1.5; it is likely that the non-periodic situation is more unstable). On the other hand, some qualitative features are reproduced well with our simulation: for a given Ca, λ generally decreases with Bm, and the higher

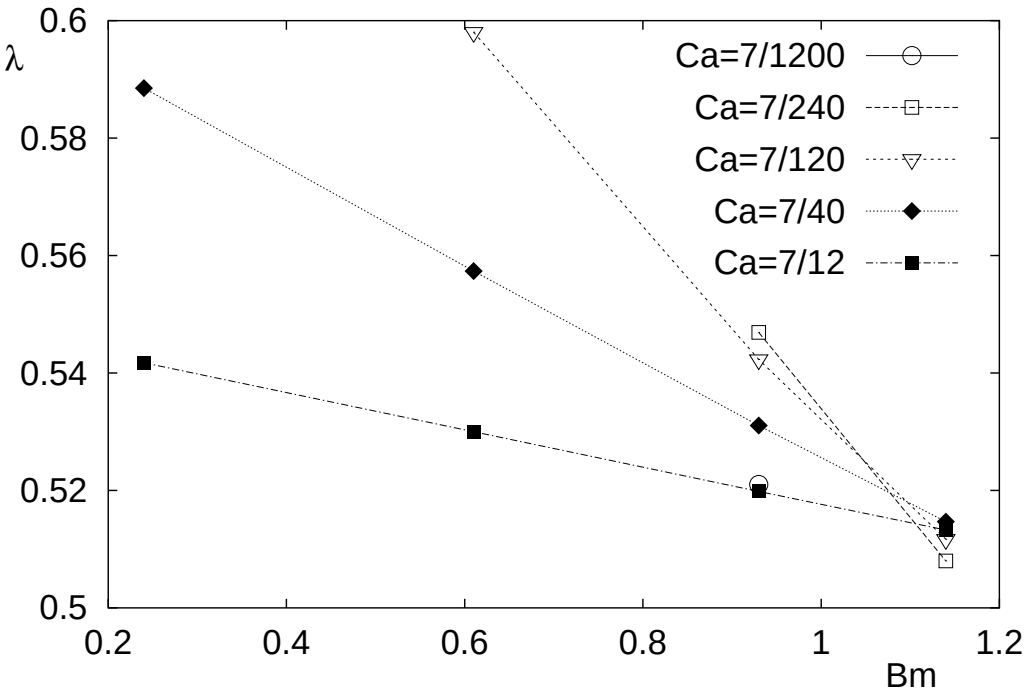

Figure 3.7: A relative magnetic finger width for various Ca and Bm. The data is taken from Table 3.3.

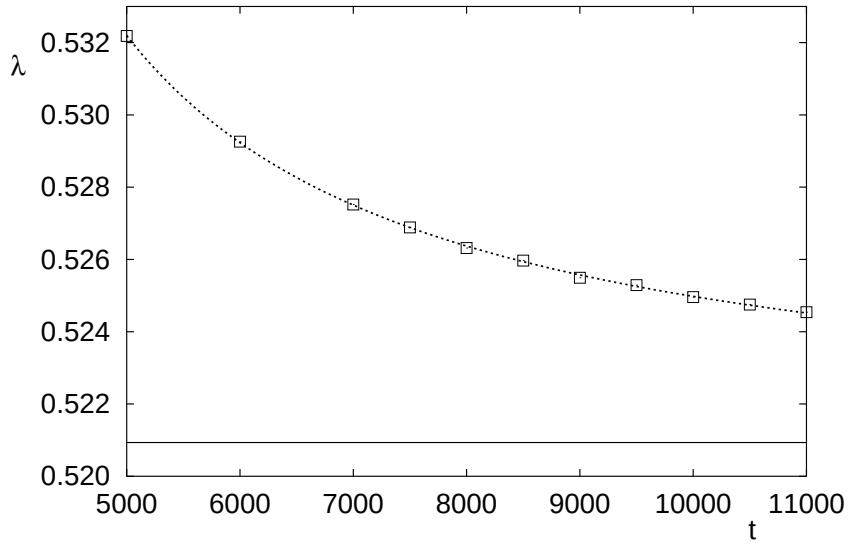

Figure 3.8: Computed magnetic finger width λ versus time. Ca = 7/1200, Bm = 0.93; other parameters are as in Table 3.3. The solid line is curve's asymptote.

Ca, the slower. Note also that at some Bm values, the finger width is a non-monotonous function of Ca having its maximum at an intermediate Ca value. The quantitative agreement with the experiments [181, 7] of the Bacri group is unfortunately not satisfactory, the discrepancy in λ being at low Ca as high as 0.08. We attribute this to the assumed periodicity of the magnetic force (§3.1.5) and to a high magnetization that is in fact not negligible with respect to the applied field (p. 76). None of the computed fingers had $\lambda < 1/2$.

Now we repeat another simulation by Cēbers – the one of a magnetic branched pattern [176]. We find it convenient to present most patterns over a period and a half, having the x-axis horizontal and the y-axis – vertical, if not specified otherwise. Our pattern presented in Fig. 3.9 should be compared against Fig. 3 of [176]. In comparing, we remember that in that simulation of [176], the length scale was twice as long as ours (we preserve the same aspect ratio in Fig. 3.9 though), their time scale was two thirds of ours, their capillary number was defined in a different manner, and their gravity was directed upwards. As early as at $t = 0.5$, our pattern shown in Fig. 3.9(a) looks already quite different from that shown in the panel of [176] corresponding to $t = 0.75$ in their notation. Namely, there are two tongues of falling MF (fingers) per period in [176], with the wider one having started to tip-split already, while Fig. 3.9(a) displays a single three-lobe tongue. A second fin-

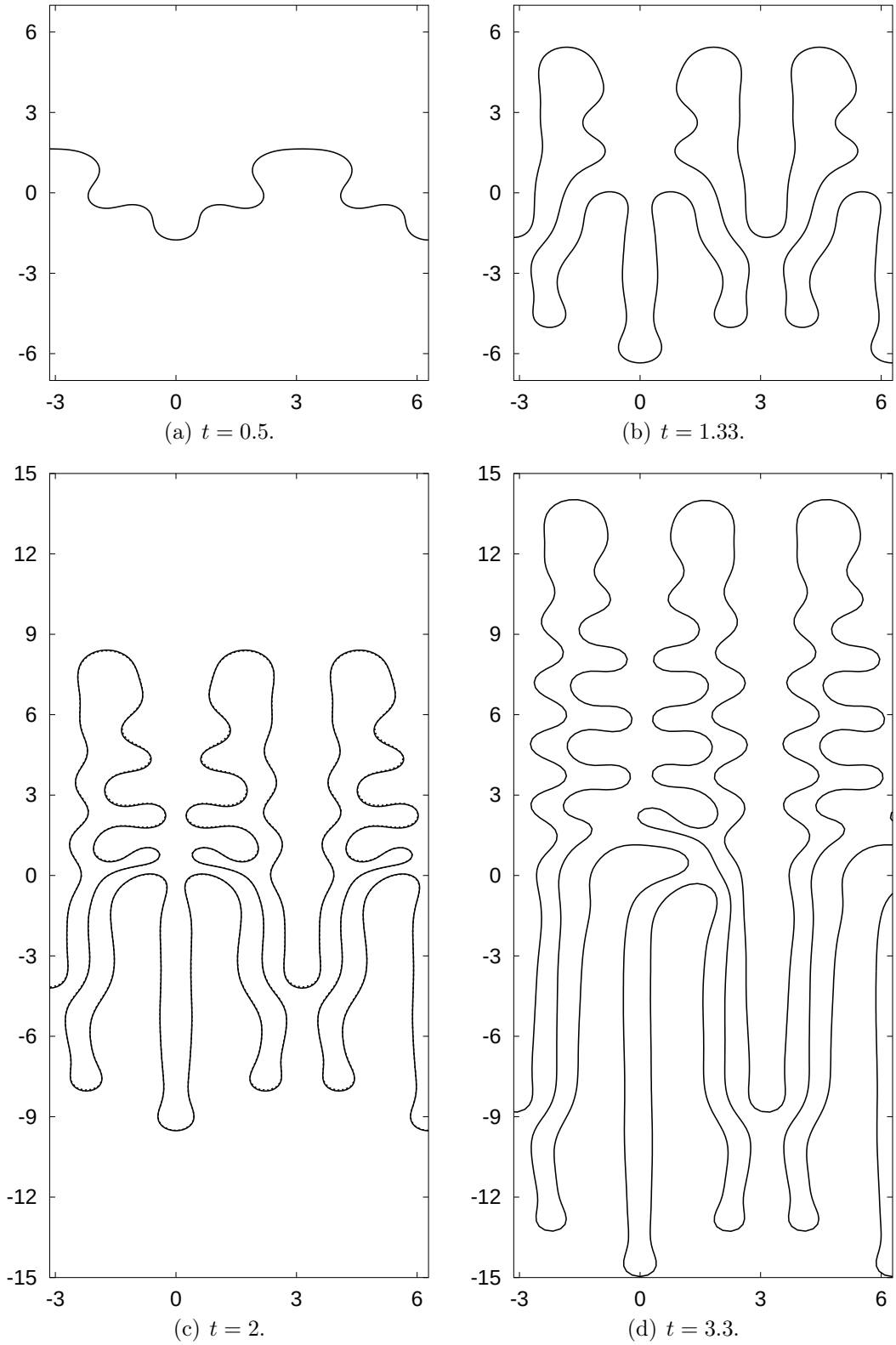

(a) $t = 0.5$. (b) $t = 1.33$.

(c) $t = 2$. (d) $t = 3.3$.

Figure 3.9: An interface computed with Ca = 3, Bm = 7, At = 29/31, $T = 2\pi$, $M = 3$, and the initial data $y = -0.1\cos(2\pi x/T)$.

ger appears at a later stage, but remains weaker than the finger appearing in [176]. Nevertheless, the later structures bear much resemblance to those in [176]. This is evidenced by comparing Fig. 3.9(b) against the corresponding result of [176] ($t = 2$ in their notation, which corresponds to our $t = 4/3$). Indeed, in both cases there are two (long) fingers of emerging non-magnetic fluid. Of the two magnetic fingers, one is split into two (three, in our simulation) lobes and exhibits two (one) "peristaltic" deformations, while the other is partially (completely) shielded. In this regard the conjecture made in [250] may be pointed out that two-lobe and three-lobe tip-splittings are caused by the same instability mechanism and can substitute one another (three-lobe splittings are indeed observed in experiments). As simulation goes on, the peristaltic deformations increase in number and amplitude, becoming side branches. About $t = 2.1$ the symmetry of the interface gets broken. Strictly speaking, broken gets the parity of the interface (its evenness with respect to the $x = 0$ line.) We are able to progress further with the simulation up to $t = 3.3$ (Fig. 3.9(d)). To assess the accuracy of this result obtained with initial $N = 32$, we computed with a twice as high resolution ($N = 64$ initially) up to $t = 2$, which is shortly before the symmetry breaks up. In Fig. 3.9(c), we try to plot the low-resolution results in dots, while the higher-resolution ones are plotted in solid. The two curves are almost indistinguishable, which proves that the accuracy is high enough. Turning back to Fig. 3.9(d), we see that the central finger has shifted towards one of its neighbours. We interpret this as follows: the symmetric position has lost its stability. We believe that the symmetry break-up and the emergence of bifurcation is indeed present in the model. Which of the two new stable positions is selected? This of course is determined by the noise, be it numerical or experimental (later we will see an example of the noise effect). The event can be described physically as the four-arm vertex (located at $(x, y) = (0, 0)$ in Fig. 3.9(c)) being separated into two 3-arm vertices (Fig. 3.9(d)). Such events were previously reported and analyzed for the same problem in the radial geometry [169, 182] and are analogous to the behaviour of two-dimensional foam films attached to several pins. The vertex-splitting is believed to prevent the rupture of shapes by the overextension mechanism. Later we will see a vertex-splitting in other patterns as well.

Simulating another magnetic structure (Fig. 3.10), we will check the effect on the results of the time step size and that of changing the marker redistribution criteria. Surprisingly, the latter effect is quite appreciable (still not drastic). Besides, at plotting the pattern after the loss of symmetry (Fig. 3.10(b)), the interface computed at a decreased time step in fact demanded a reflection with respect to $x = 0$ axis, which shows that small perturbations (noise) can determine which of the two new stable configurations

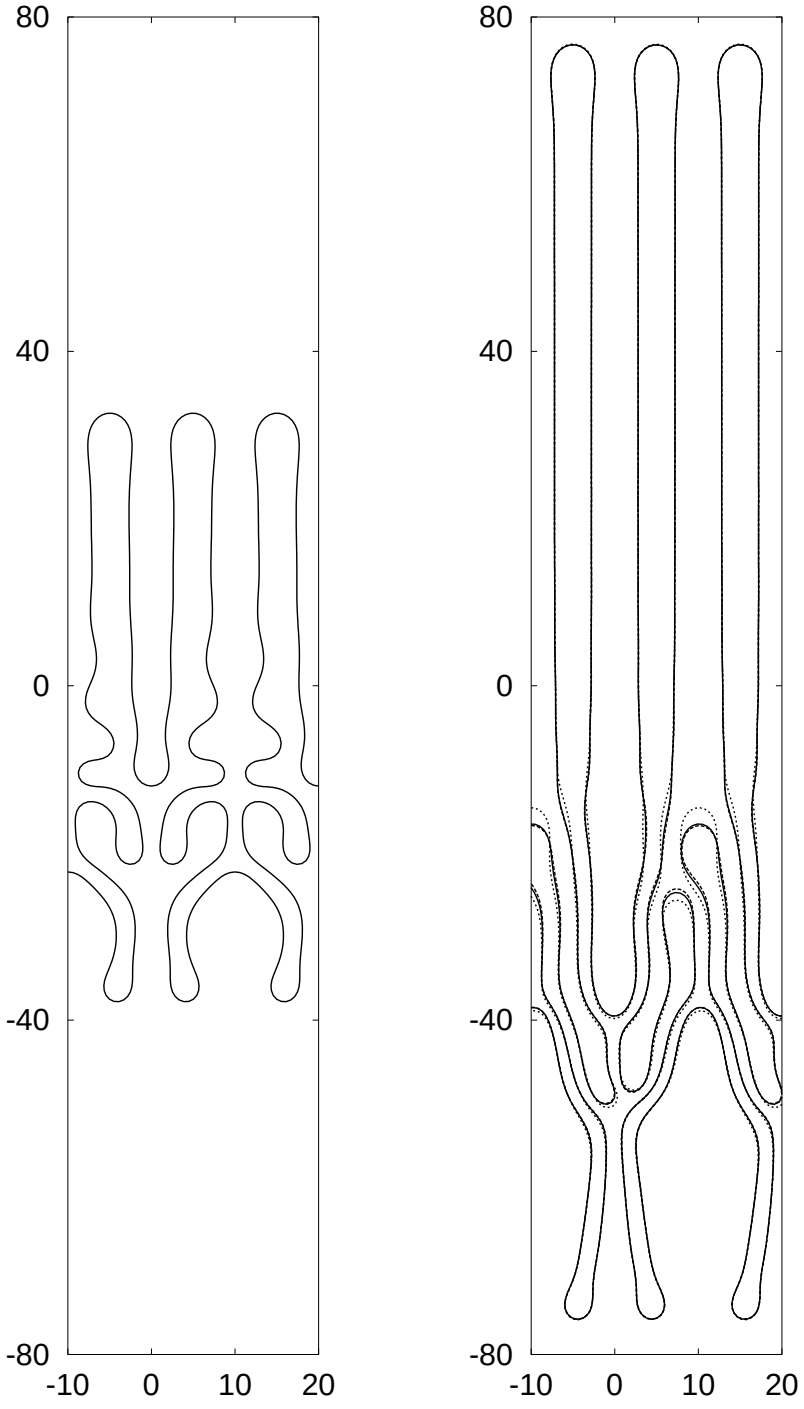

(a) $t = 500$. (b) $t = 990$.

Figure 3.10: An interface computed with Ca $= 0.224/\pi \approx 7.13 \times 10^{-2}$, Bm $= 4.56/\pi \approx 1.45$, At $= 0.92$, $T = 20$, $M = 3$, and the initial data $y = 0.02\cos(2\pi x/T)$. In Fig. 3.10(b), plotted with a dashed line is the interface computed at a decreased time step ($\Delta t = 0.020$ instead of 0.025), the interface plotted with dots is obtained at a tighter arclength spacing constraint: $0.607 < \Delta s < 0.613$ (instead of $0.60 < \Delta s < 0.62$).

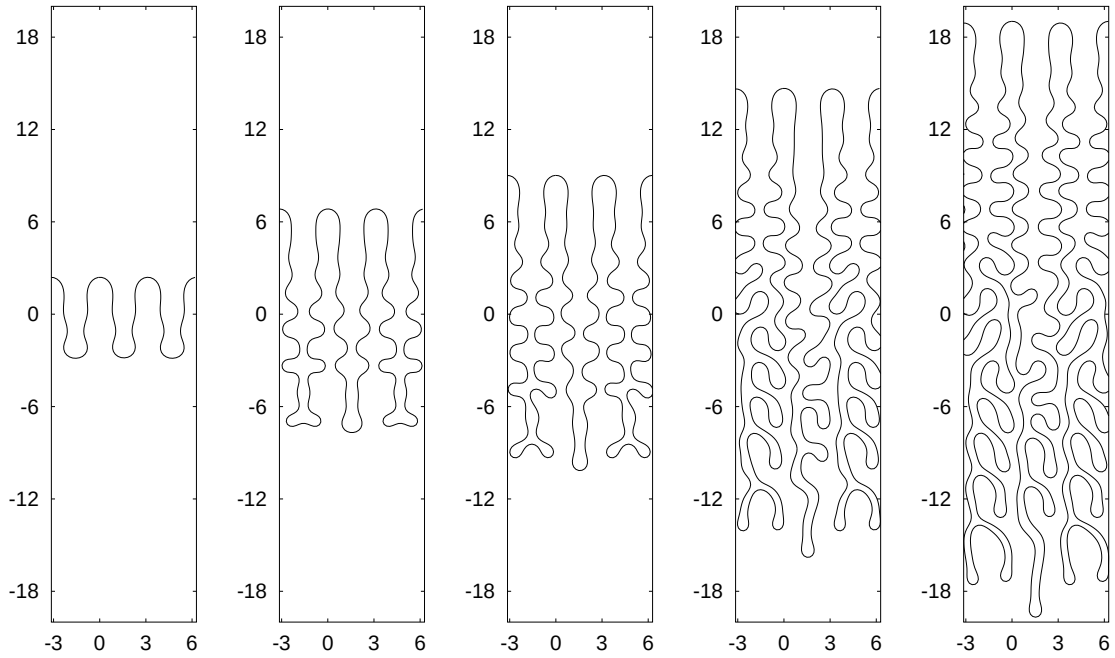

(a) $t = 0.5$. (b) $t = 1.5$. (c) $t = 2$. (d) $t = 3.3$. (e) $t = 4.3$.

Figure 3.11: The competition of two magnetic fingers. Parameters are the same as in Fig. 3.9 with the exception of the initial data $y = 0.1\cos(4\pi x/T) - 0.02\sin(2\pi x/T)$.

is actually chosen.

It may be interesting to see what happens if we rerun the simulation presented in Fig. 3.9 with another initial condition: a harmonic perturbation whose wavelength equals $T/2$, with a superimposed small-amplitude harmonic of the basic period T. The growth increments of the modes, according to the dispersion relation Eq.(3.36), are 17.4 and 6.3, correspondingly. The faster-growing one besides has an advantage in the initial amplitude. So there is no surprise that at an early non-linear stage we have two almost indistinguishable fingers per period (Fig. 3.11(a)). Nevertheless, later on the difference manifests itself (Fig. 3.11(b)), and yet later, the fingers loose their symmetry with respect to the centerline (Fig. 3.11(c)). Notice two-lobe tip-splittings and observe that fingers of the less-viscous fluid tend to undulate, while fingers of the more-viscous one would rather exhibit peristaltic deformations.

Concerning the competition of fingers growing from the initial conditions

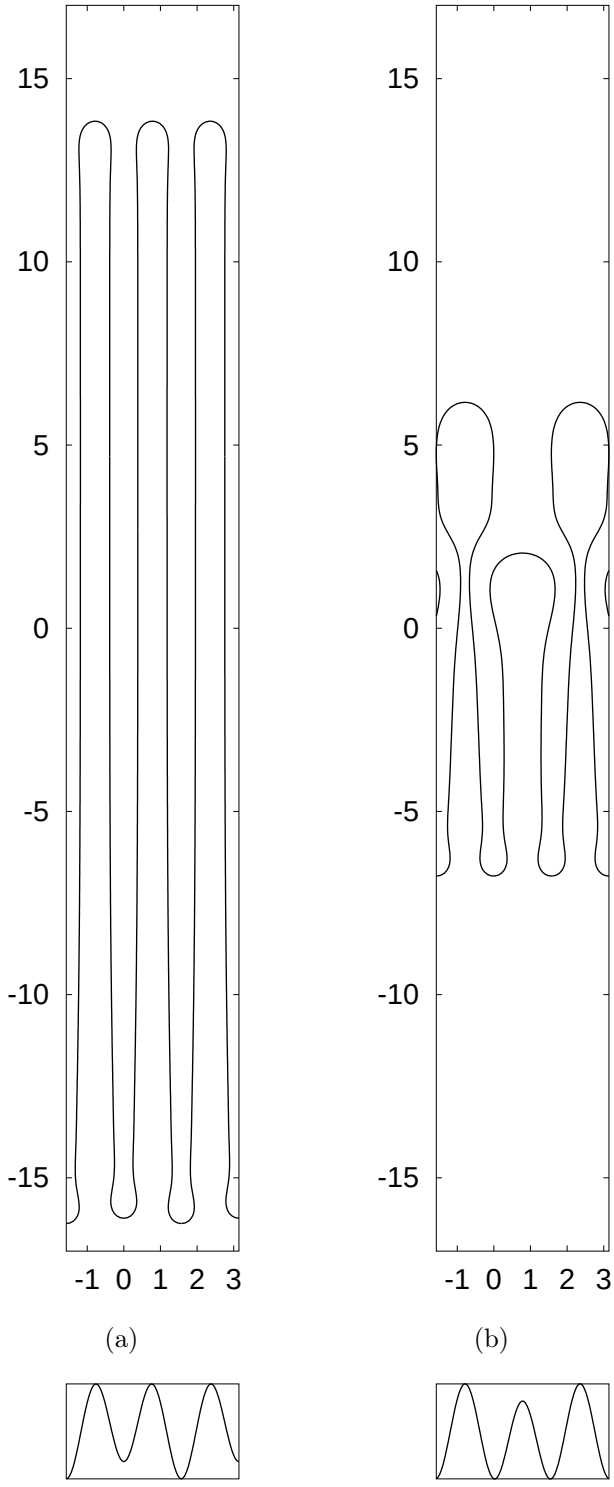

Figure 3.12: Shielding: absent or present? (a): $t = 1.18$, initial shape $y = -0.05\cos(4\pi x/T) + 0.01\cos(2\pi x/T)$; (b): $t = 0.48$, initial shape $y = -0.05\cos(4\pi x/T) - 0.0005\sin(2\pi x/T)$. The initial shapes are schematically shown below. Ca = 12, Bm = 7, At = 29/31, $T = \pi$, and $M = 3$ for both.

of the above sort, we note the important role played by the phase difference between the interacting harmonics. Indeed, compare Figs. 3.12(a) and 3.12(b). In the first case, the (downward) humps of the more-viscous fluid differ in amplitude, while the humps of the less-viscous one do not. The stronger downward finger does not shield with time the shorter one, their difference in length remains small, as if there were some stabilizing mechanism. In the other case, the crests of the wavy interface differ just a little bit, while the hollows are exactly the same. Nevertheless, the higher crest quickly wins over the lower one (Fig. 3.12(b)). Thus we can cautiously infer that fingers of the less-viscous fluid are more susceptible to mutual shielding than fingers of the more-viscous one.

In Fig. 3.13 we present a long finger undergoing repetitive "peristaltic" deformations. In Figs. 3.13(h)–3.13(k) it is shown how the finger looses its symmetry with respect to the centerline. It occurs through the characteristic vertex-splitting already described above.

One more pattern is shown in Fig. 3.14. Contrary to what one might think, the strange shape of the downward finger proves stable.

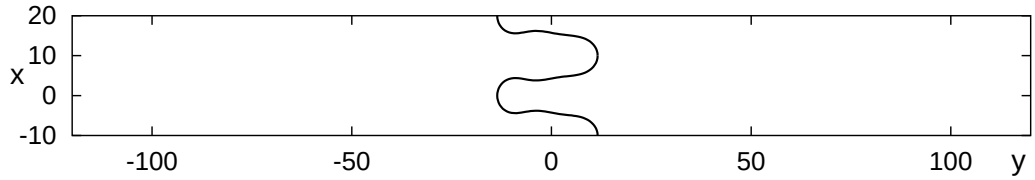

(a) $t = 200$.

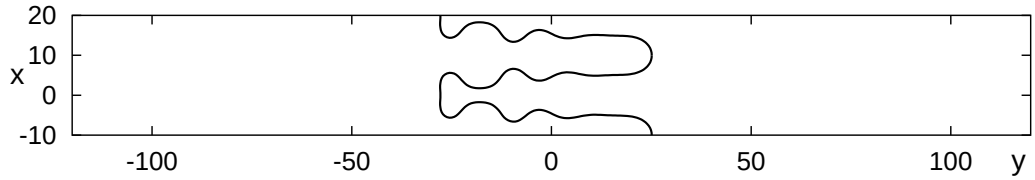

(b) $t = 400$.

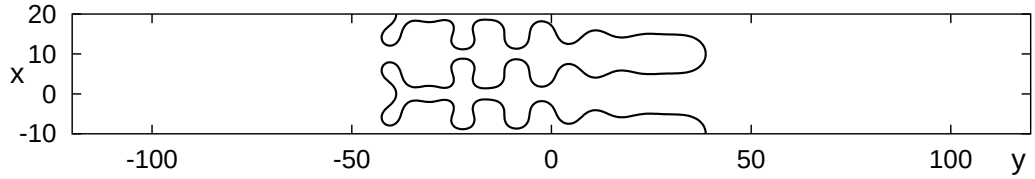

(c) $t = 600$.

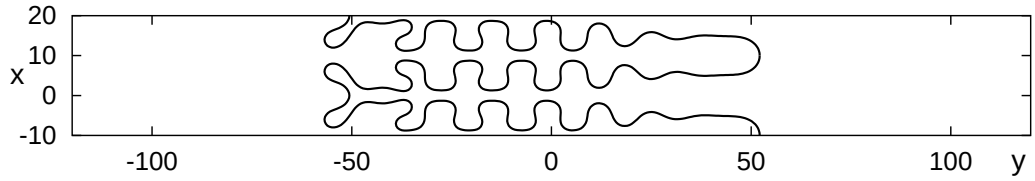

(d) $t = 800$.

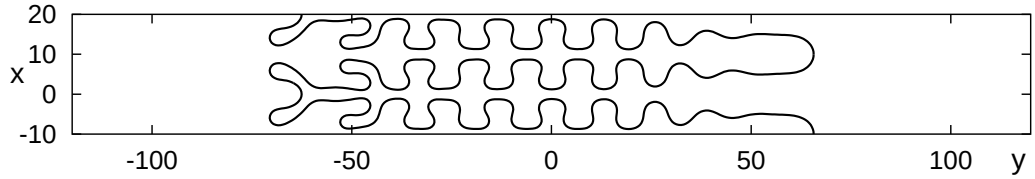

(e) $t = 1000$.

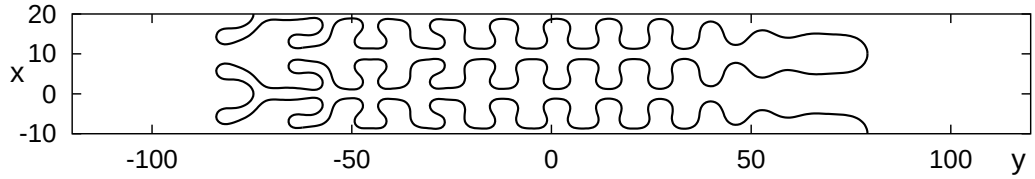

(f) $t = 1200$.

Figure 3.13: A long magnetic finger. Ca $= 7/120$, Bm $= 1.3$, At $= 1$, $T = 20$, $M = 3$; the initial condition is $y = -(1/\pi)\cos(2\pi x/T)$.

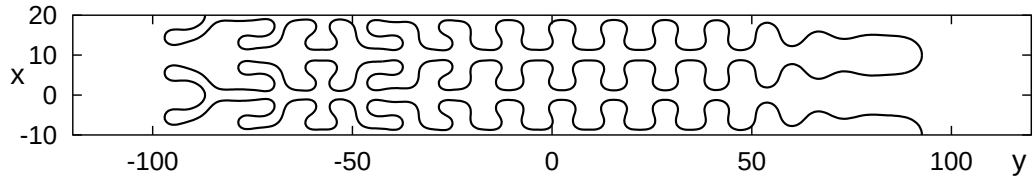

(g) $t = 1400$.

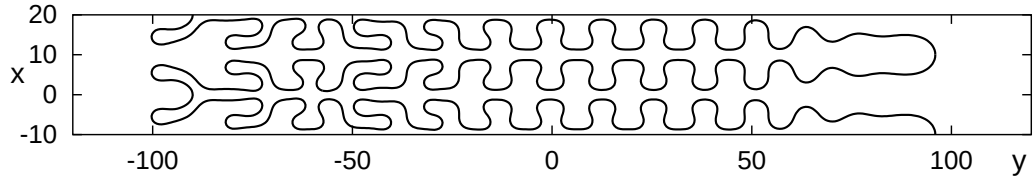

(h) $t = 1450$.

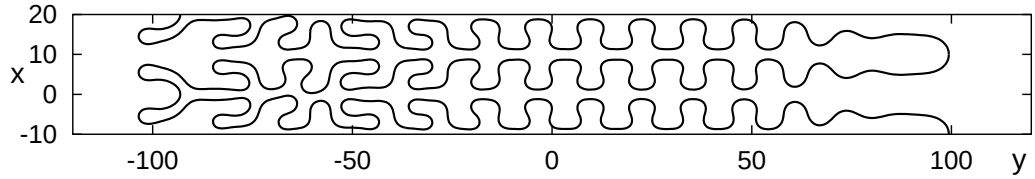

(i) $t = 1500$.

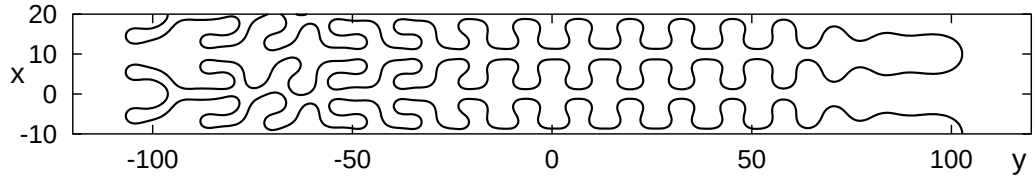

(j) $t = 1550$.

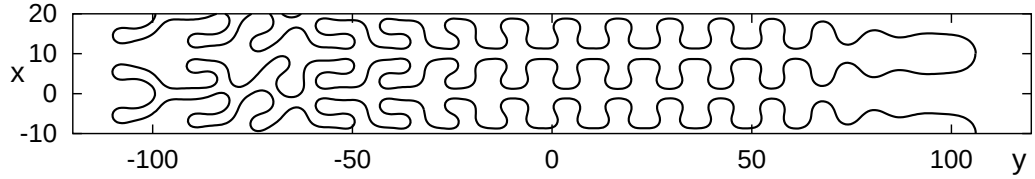

(k) $t = 1600$.

Figure 3.13: A long magnetic finger (continued). A vertex-splitting event.

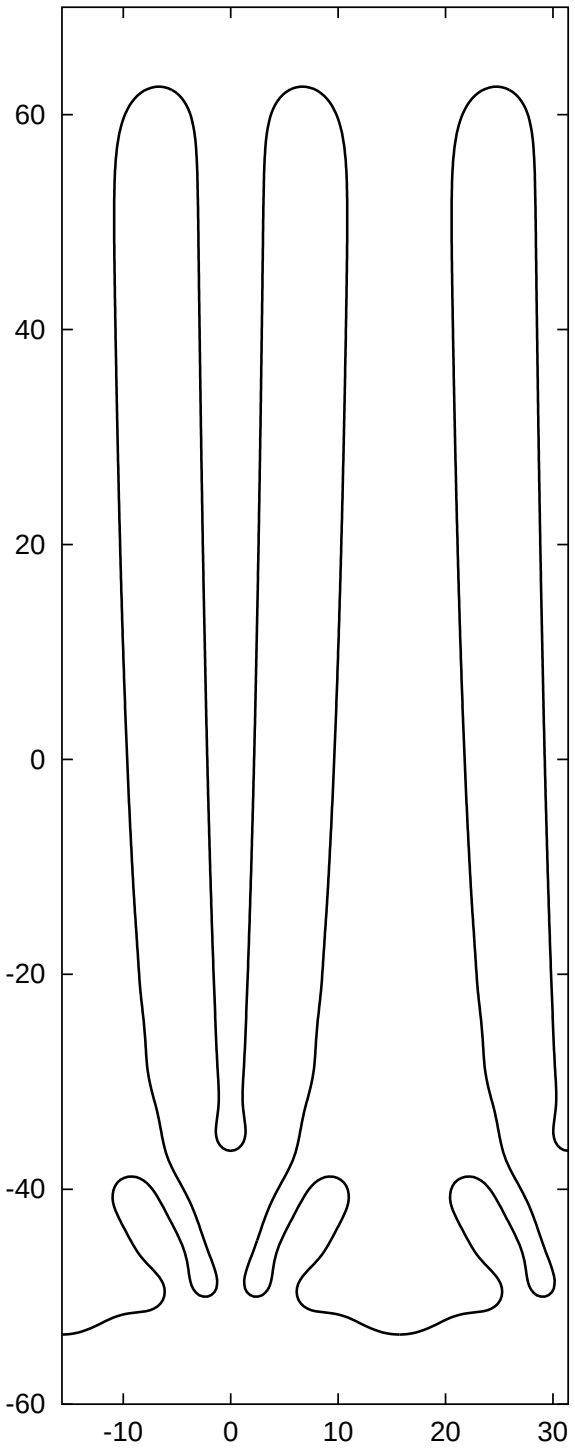

Figure 3.14: Yet another pattern: Ca = 8, Bm = 1, At = 1, $T = 10\pi$, $M = 1$; the initial condition is $y = 0.05\cos(2\pi x/T)$; $t = 9$.

3.3.2 Dendritic patterns

Now we will study the development of a highly convoluted interface that develops at a relatively low capillary number Ca, high Bm, and high viscosity contrast. We will call the more-viscous upper (At > 0) fluid just "liquid", and the less-viscous fluid will be called "air". Tracing the evolution of the interface (Fig. 3.15) reveals some scenarios of pattern formation. Perhaps the most common is the tip-splitting that is the first secondary instability to occur (Figs. 3.15(a), 3.15(b)), both with liquid and air fingers. Some fingers exhibit already the "peristaltic" deformations. At about $t = 14$ the pattern looses its symmetry, and another instability sets in: A peristaltic bulge on a liquid finger flattens out on one side, jutting out on the other (Fig. 3.15(c)). The process ends up with a single side branch (Fig. 3.15(d); the pattern fragments under consideration are marked by a rectangular contour). Thus a retraction of a side branch is possible, which is indeed observed [12]. In parallel, adjacent air fingers also develop corresponding branches, usually upon undulation, as exemplified by Figs. 3.15(e)–3.15(g). Many fingers become shielded and stop evolving shortly after appearing. Interpenetrating side branches form the "hairpin" details [251]. Later stages are marked by the avalanche of tip-splittings by air fingers. Interestingly, liquid fingers never tip-split again, as was noted and explained by the unfavourable (for instability) viscosity contrast in [12]. Near the tips, air tongues are thicker than liquid ones are at their tips. Note that the top-bottom asymmetry in the pattern is caused by a non-zero At (at a non-zero surface tension). We remind (see p. 86) that were At opposite (negative), the pattern would exactly turn upside down to within the noise effect. The sensitivity of patterns to small perturbations is demonstrated by Fig. 3.16, we simulate two patterns that differ only in the sign of At and should coincide in precise arithmetics. However, the numerical results are slightly yet appreciably different because of the numerical error that differs between the two simulations (mostly because of the magnetic integrals being taken over different domains). Inside the contour, one can notice that some side-branchings that have occurred in one case, have not in the other, etc. We stress our belief that this sensitivity is a physical effect and not numerical one. The same numerical observation is made in [178] where it is conjectured that the energy functional has multiple local minima in the space of accessible shapes. The final picture that we were able to obtain without the numerical instability resembles rather closely the patterns observed in the experiments [12, 181].

At Bm $= 4.8$, the pattern formed is shown in Fig. 3.17.

It is interesting to note that the number of fingers per period in Fig. 3.15 is $n = 5 \ldots 6$ long fingers of the same direction, while the period $2\pi/k = 3.5092$

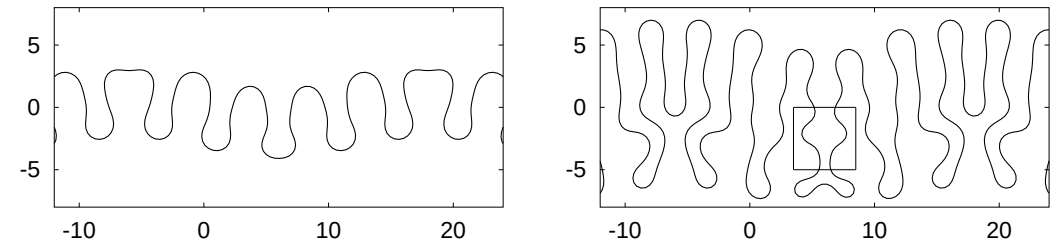

(a) $t = 9$.

(b) $t = 14$.

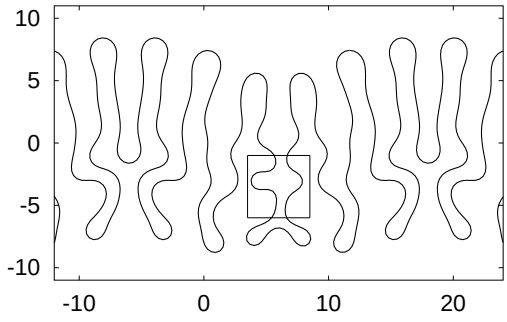

(c) $t = 16$.

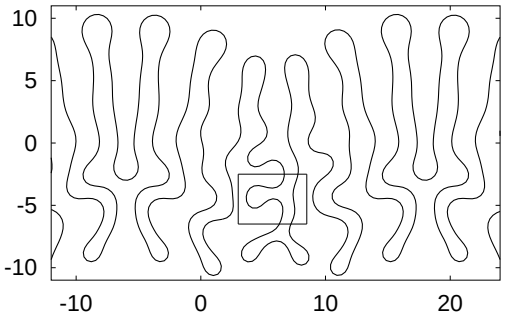

(d) $t = 19$.

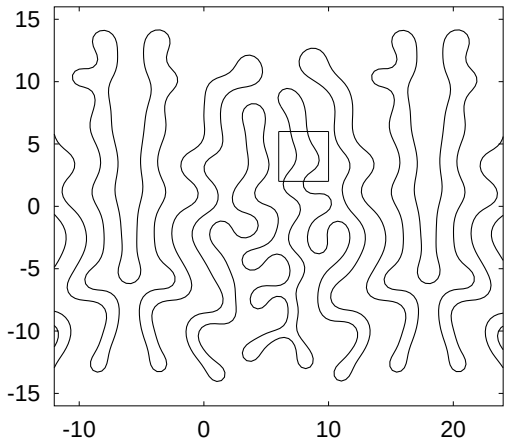

(e) $t = 26$.

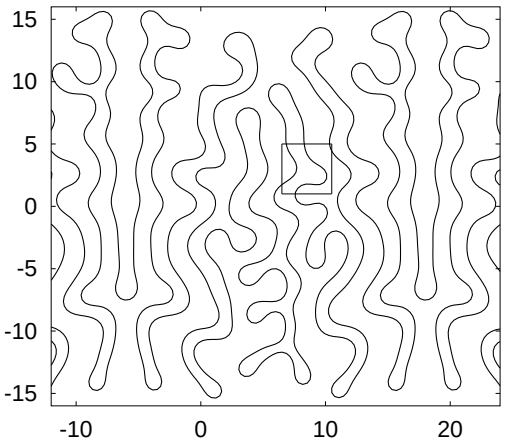

(f) $t = 29$.

Figure 3.15: The development of a magnetic dendrite: Ca = 3/16, Bm = 3.675, At = 0.986, $T = 24$, $M = 3$, and the initial data $y = -0.5\sin(2\pi x/T)$.

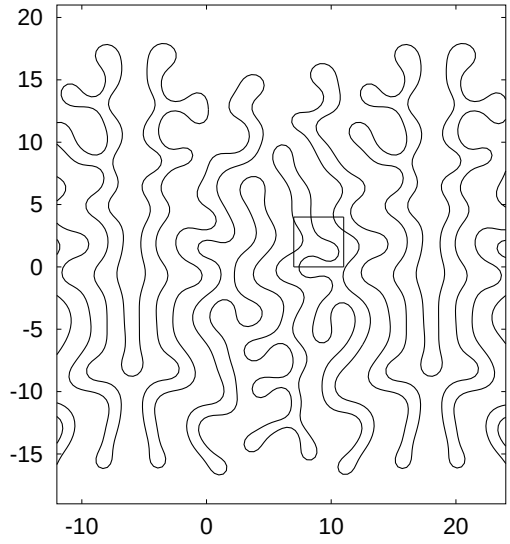

(g) $t = 32$.

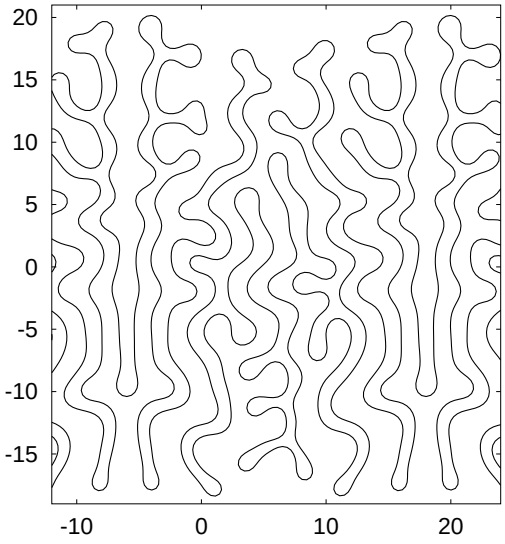

(h) $t = 36$.

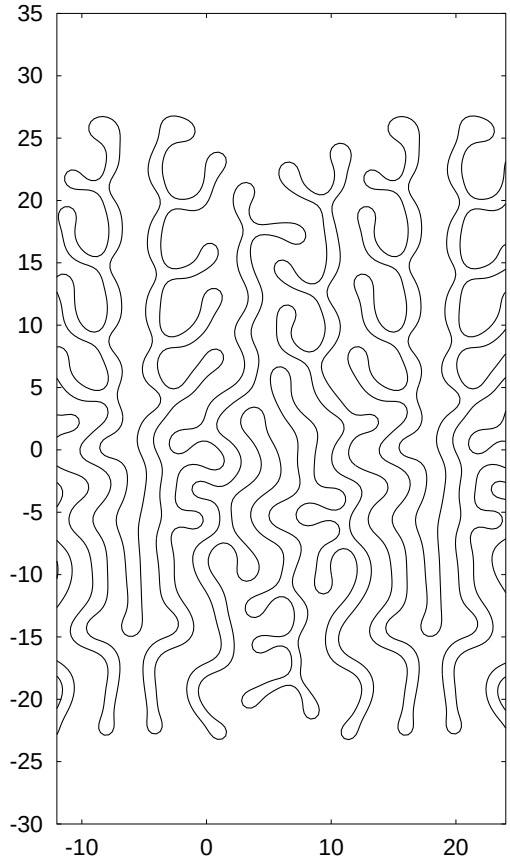

(i) $t = 48$.

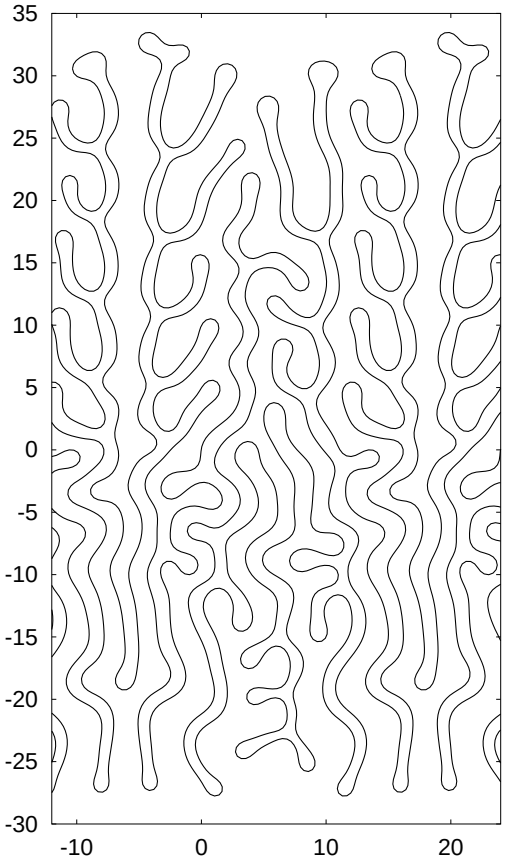

(j) $t = 60$.

Figure 3.15: The development of a magnetic dendrite (continued).

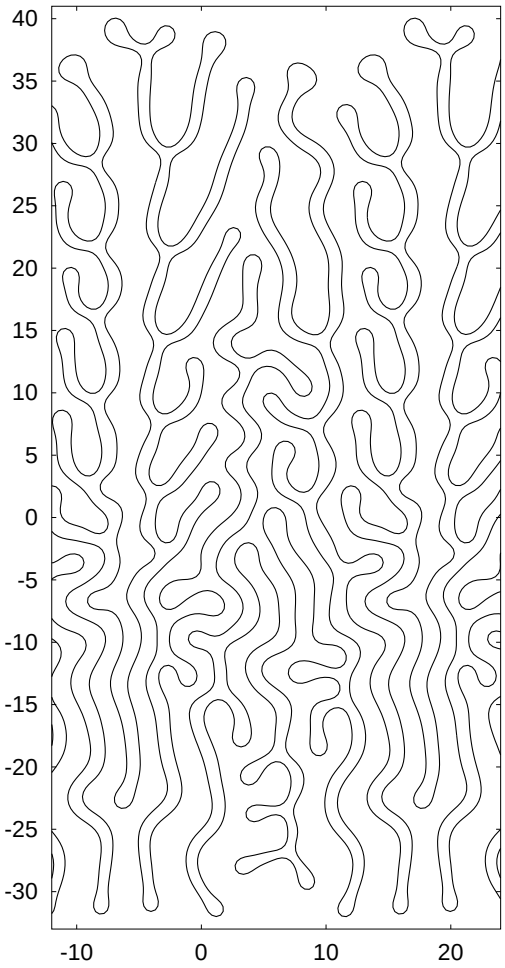

(k) $t = 72$.

Figure 3.15: The development of a magnetic dendrite (continued).

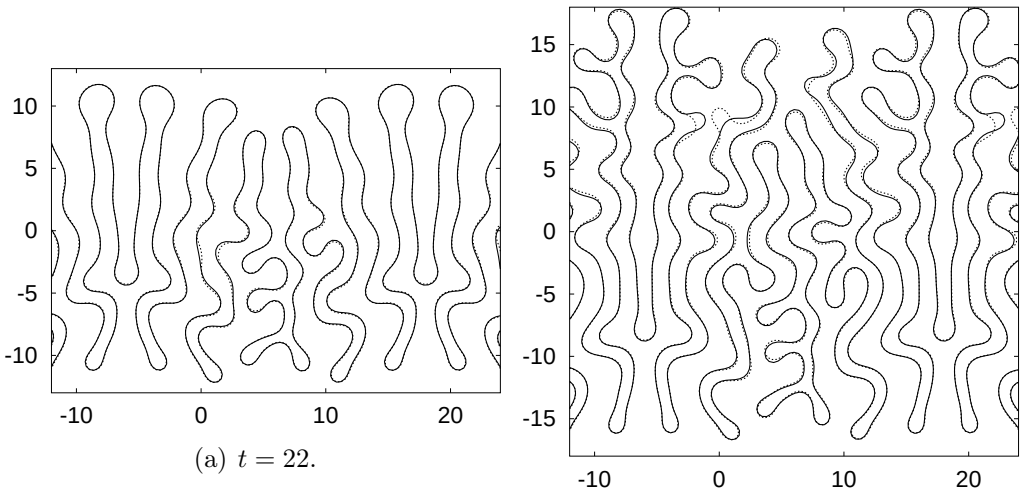

(a) $t = 22$.

(b) $t = 32$.

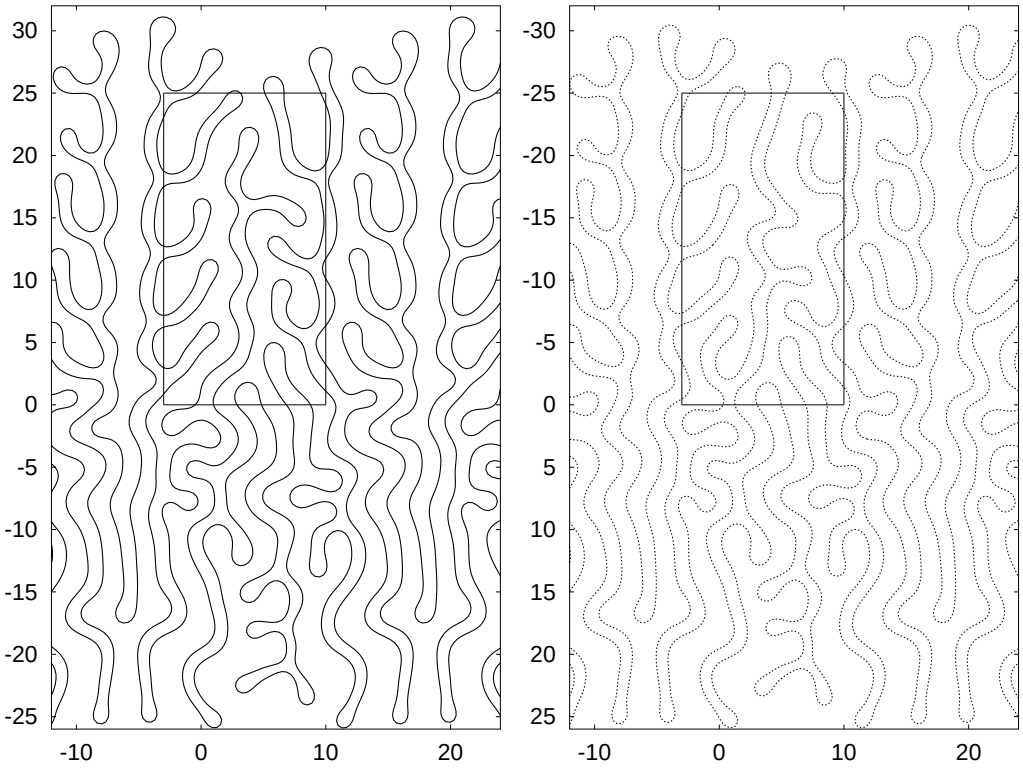

(c) $t = 55$.

Figure 3.16: The sensitivity of pattern formation to small perturbations. The pattern shown in Fig. 3.15 is reproduced in solid lines. The pattern obtained under the same conditions except for the opposite At $= -0.986$ and the opposite initial data $y = +0.5 \sin(2\pi x/T)$ is plotted upside down in dots. (In the last panel the y-axis is reversed explicitly.) While the exact solutions coincide, numerical noise in the two runs was different, which lead to appreciably distinct patterns.

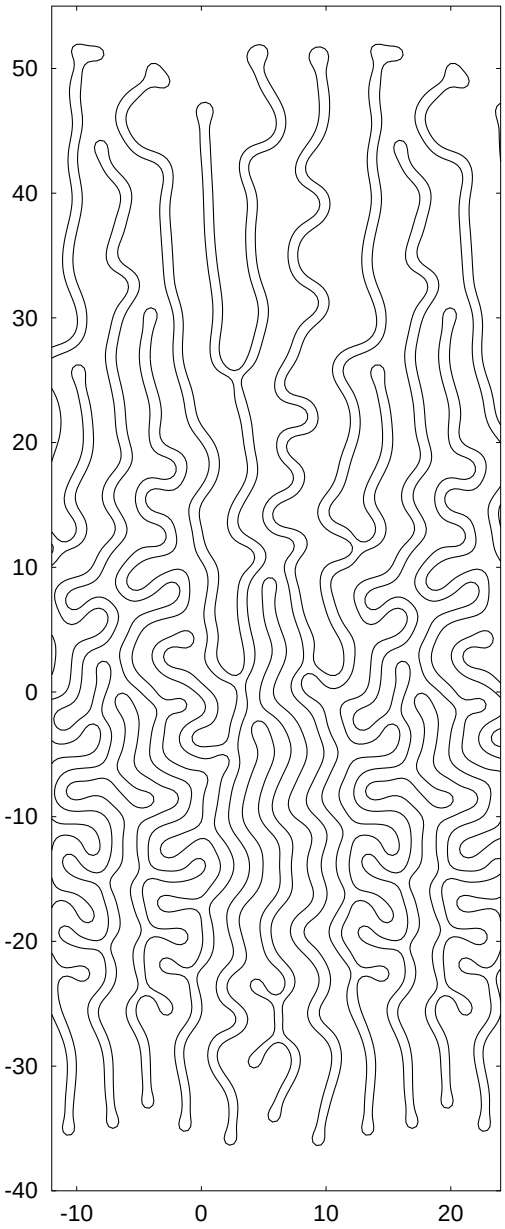

Figure 3.17: A magnetic dendrite at a higher Bm ($t = 64$): Ca $= 3/16$, Bm $=$ 4.8, At $= 0.986$, $T = 24$, $M = 3$, and the initial data $y = -0.5\sin(2\pi x/T)$.

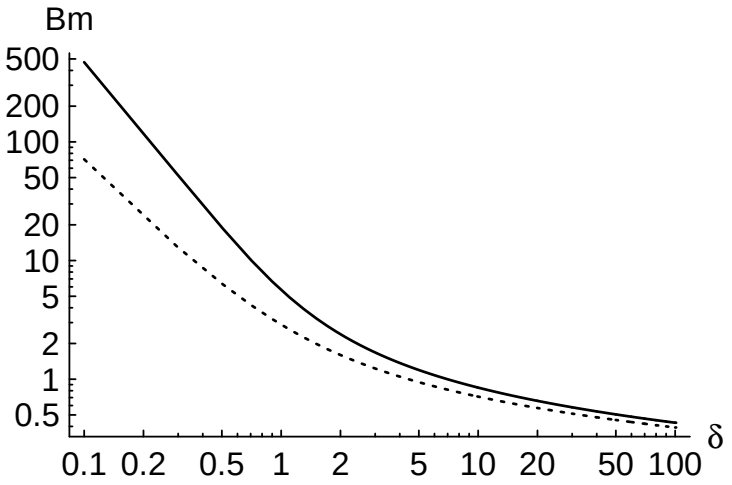

Figure 3.18: The equilibrium width δ of straight magnetic stripes as a function of Bm. Solid line: a stripe in a 2δ-periodic pattern [59]; dotted line: an isolated stripe [252].

of the most dangerous linear mode (for a planar interface) is some 7 times less than $T = 24$. In the same time, the width δ of long fingers measured in the middle of the structure (far from top and bottom) is about $1.2 \ldots 1.4$ for the fingers of both sorts. (The closer to the tip, the thinner the finger, unless the distance from the tip is less than several widths.) The deviation of the width from $T/(2n)$ is due to the "defects" of the structure (side branches, undulation, shielded fingers). Judging by late panels of Fig. 3.15, apart from the drift as a whole, the middle of the structure stops to evolve, which means that internally this region has arrived to a static equilibrium. In this regard let us note that it is possible to compute the magnetic energy (per unit length) of the pattern of long parallel MF stripes [253, 59]. This energy summed with the energy due to surface tension can be minimized at a constant stripe area to yield the equilibrium parameters of the pattern. From formula (11) of [59], in the case when stripes of both kinds are of the same length, it follows that (in our notations)

$$\left(\frac{2\delta}{\pi}\right)^2 \int_0^{\pi/(2\delta)} y \ln\left(1 + \frac{1}{\sinh^2 y}\right) \mathrm{d}y = \frac{2}{\mathrm{Bm}}\,. \tag{3.38}$$

Another particular case of that formula in [59] is the equilibrium width[4] of

[4]Bm is defined in [59, 252] to be one half of ours. Our Bm in SI units is $(\mu_0/(4\pi))\ 2(\Delta M)^2 h/\sigma$, where μ_0 is the "permeability of vacuum."

a single straight stripe [252]:

$$\delta^2 \ln(1+\delta^{-2}) + \ln(1+\delta^2) = 4/\mathrm{Bm}\,. \tag{3.39}$$

These relations are plotted in Fig. 3.18. It may be seen that at Bm = 3.675, $\delta = 1.36$ for the system of parallel straight stripes, which agrees well with our measured finger width of $1.2 \ldots 1.4$. We point out that our fingers are appreciably narrower than the half-period $\pi/k = 1.75$ of the most unstable mode of a planar interface. At Bm = 4.8, the obtained finger width is $1.0 \ldots 1.1$, also in agreement with $\delta = 1.12$ given by Fig. 3.18, and also less than the half-period $\pi/k = 1.40$ of the most unstable mode. Thus the patterns evolve by adapting to the change of preferred spatial scales that takes place in the course of their evolution.

On the other hand, a larger width that the fingers inherit from the linear stage of instability is the equilibrium one for a pattern of parallel stripes at a lower Bm. It is remarkable that the energy of magnetostatic interactions across an undulating stripe (or stripe pattern) undergoing large-wavelength undulations scales with wavelength (at large wavelength where it is more important) the same way the energy due to surface tension does. This allows to introduce [254] the notion of an effective surface tension. This quantity is zero at the critical Bm (see [177], §4.6 of [15] for a single stripe), which is equivalently the equilibrium one defined by Eqs.(3.38), (3.39). The effective surface tension becomes negative at larger Bm values, leading to long-wavelength undulations (cf. simulations of a single stripe in [173]). For the analogy of MF stripe patterns to liquid-crystal smectics, see [6, 13]. Thus it can be expected that a magnetic Bond number too high for a given period will force the fingers to undulate. "Chevrons" and "hairpins" should [254, 255, 62] develop from the undulations in the non-linear regime, as indeed observed experimentally in [13, 251]. Now we can add to this our numerically obtained hairpin-like side branches in Fig. 3.15 and, especially, Fig. 3.17, where they are rather pronounced and regular.

Fig. 3.19 shows the effect of viscosity contrast on the pattern shown in Fig. 3.15 – At = 0 for this simulation, other parameters being the same as in Fig. 3.15. Though the basic mechanisms (tip-splitting, side-branching) are still in operation, the resulting differences are obvious. Notice that the pattern no longer transforms into itself by reflection about the x-axis combined with a translation by a half-period. (In precise arithmetics, the pattern should so transform as long as the initial conditions do.)

Now let us determine how long-range the magnetic interactions between the parts of a branched pattern are. In other words, how small $M = \max m$ in Eq.(3.27) is sufficient at calculating the magnetic force? Fig. 3.20 proves

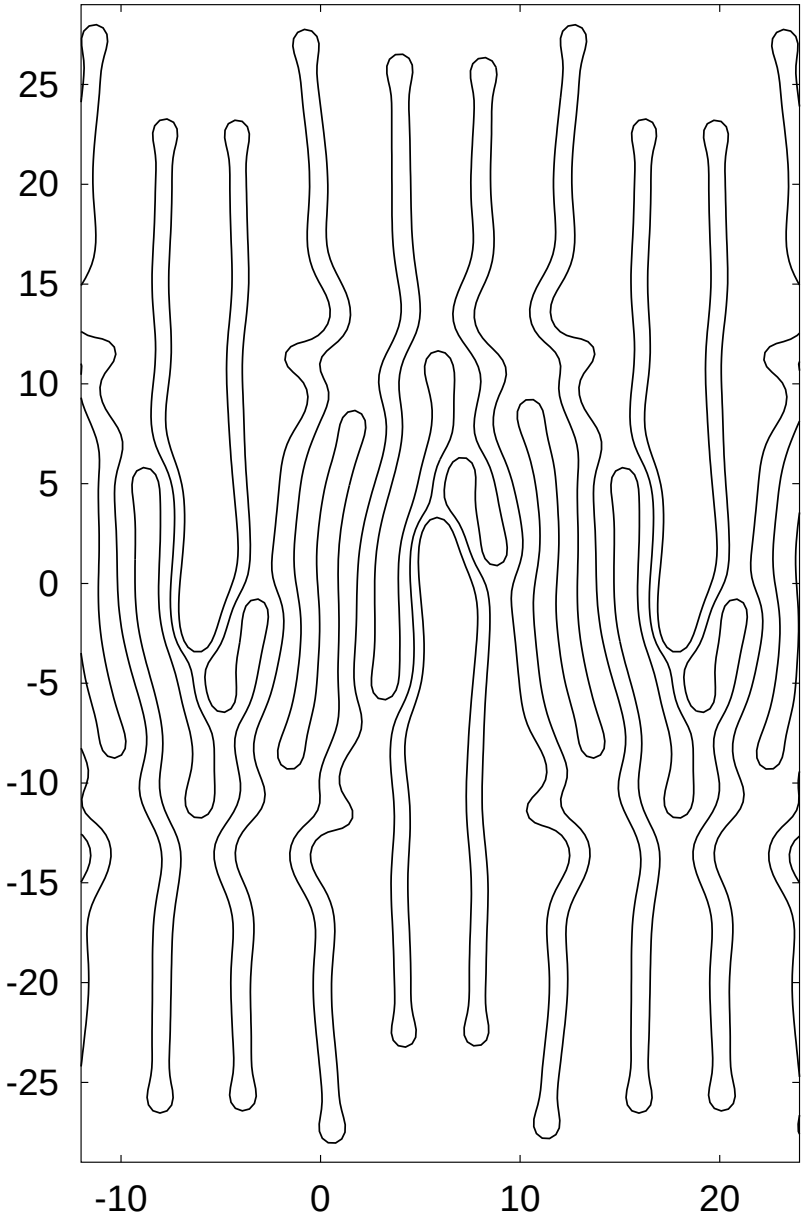

Figure 3.19: A pattern at a zero viscosity contrast: At = 0. Other parameters are as in Fig. 3.15; $t = 55$.

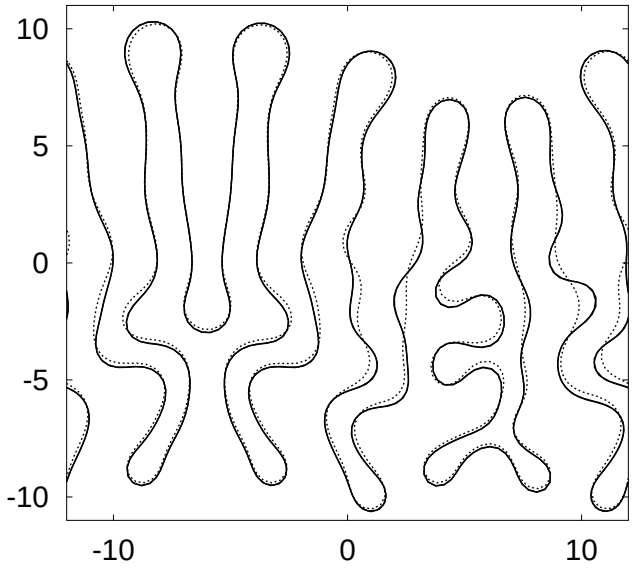

Figure 3.20: On the effective range of magnetic interactions in Fig. 3.15 ($t = 19$). The pattern interface computed at $M = 0$ is plotted with a dotted line. The shapes at $M = 3$ (usual) and $M = 1$, both plotted in solid, are indistinguishable.

that in the case under review just above, $M = 1$ is already a very good approximation, while $M = 0$ is perhaps not. (We remind that $M = 0$ means that interactions with about a half of the period in any direction are taken into account, $M = 1$ implies one period more, etc.) Nevertheless, since anyway not much computing time would be gained (10–20 %), we will normally proceed with $M = 3$ as before.

At low surface tension, we observe other interesting events such as the formation of a pending viscous drop and the air-bubble trapping. Pinching and rupture of the necks cannot be modelled with the present algorithm (cf. [174]); other approaches are capable of handling topological changes, e.g. the level-set algorithm (see p. 97).

In Fig. 3.22 we demonstrate that while the interface can be quite branched and convoluted, it adapts to the driving forces in such a way that they vary in a rather regular manner along the interface. This includes not only vertical segments, but also the side branches.

In Fig. 3.23 we compare the early dynamics of the perimeter in the case of a single finger (Fig. 3.6) against the case of a branched interface (Fig. 3.15). Rapid growth of the interface length in Fig. 3.23(b) at about $t = 6 \ldots 9$ is explained by higher harmonics generated (Fig. 3.15(a)) by the initial imposed

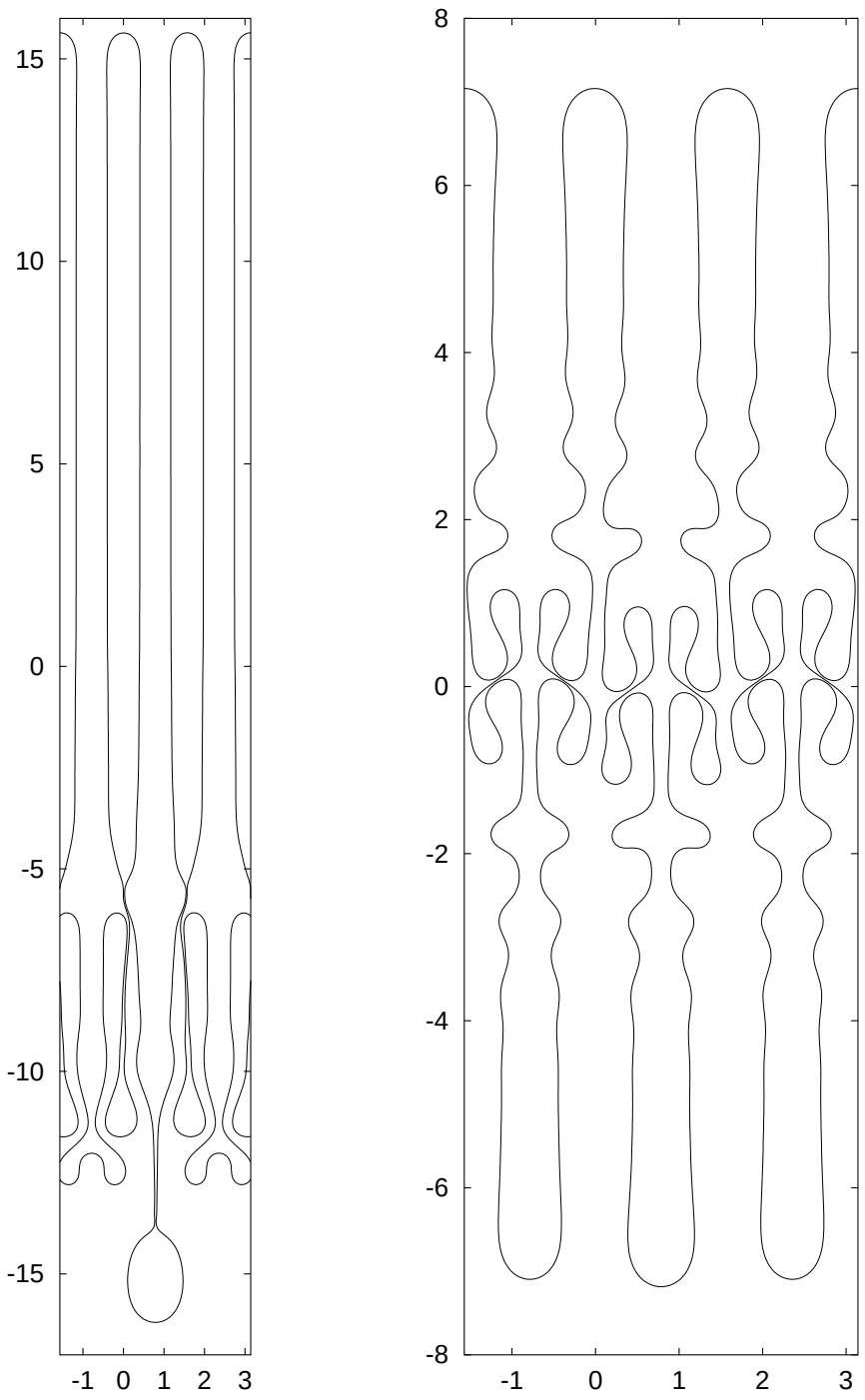

(a) Bm = 10, $t = 0.162$.

(b) Bm = 30, $t = 0.062$.

Figure 3.21: Drops and trapped bubbles. Ca = 100, At = 0, $T = \pi$, $M = 3$, and initially $y = +0.05\cos(4\pi x/T) - 0.01\sin(2\pi x/T)$ for both figures.

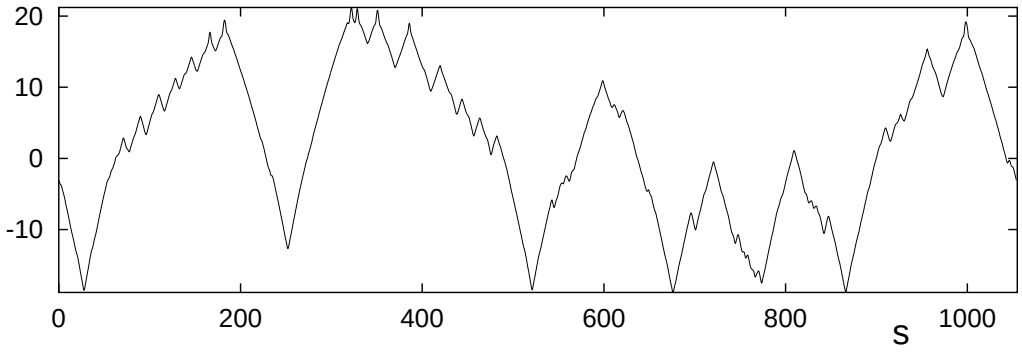

Figure 3.22: The dynamical structure of the branched interface shown in Fig. 3.15(k). The combination $2(\kappa + \mathrm{Ca}\, y + \mathrm{Bm}\, I_{\mathrm{m}}) + \mathrm{const}$, the "forcing" of the integral Eq.(3.23), is plotted versus arclength.

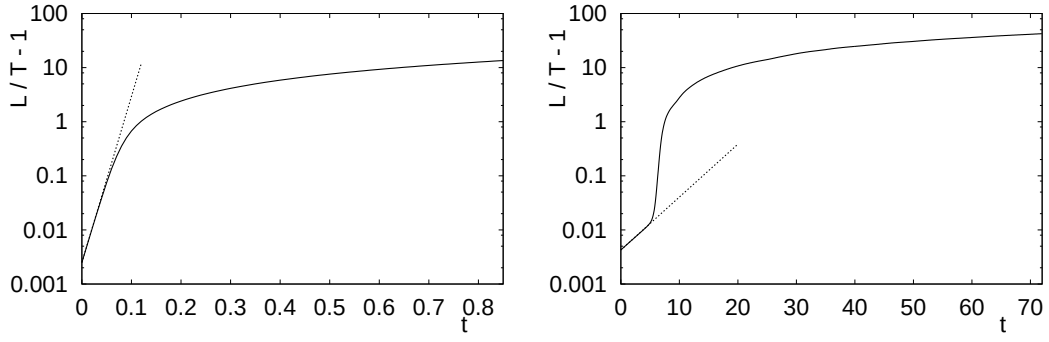

(a) The case of a finger (Fig. 3.6). (b) The case of a branched pattern (Fig. 3.15).

Figure 3.23: Evolution of the perimeter. Solid line: the scaled surplus perimeter $L/T - 1$; dotted line: its early asymptotics $\exp(2\lambda t)$.

mode of the basic period T in the non-linear regime, with the higher harmonics being more unstable than the initial mode. (It is easy to see that the surplus perimeter, $L-T$, of a sinusoidal deformation whose amplitude grows exponentially with rate λ, grows as $\exp(2\lambda t)$ in the linear regime and slows down afterwards to $\exp(\lambda t)$.) In both cases T is larger than the period of the most unstable wavelength. However, the growth rate at the imposed period in the case of the finger is only 1.6 times lower than the growth rate of the most unstable mode, while in the case of the branched interface the ratio is about 24. This explains the difference between Figs. 3.23(a) and 3.23(b) as well as why the imposed mode dominates in the finger case but not in the case of the branched pattern. Later, the perimeter of the branched structure evolves rather smoothly, but somewhat slower that linearly with time. On the contrary, the interfacial length of a developed finger varies linearly with time to an excellent precision, as might be expected.

In conclusion we mention the so-called comb-like instability [256] that essentially is the Rayleigh–Taylor instability of MF's with stable density stratification, $\mathrm{Bg} < 0$. We have made some runs for this situation, finding the obtained patterns to be very similar to the usual case $\mathrm{Bg} > 0$ ($\mathrm{Ca} > 0$). We remark that the present algorithm enables us to verify the non-linear analysis of [257] of the type of bifurcation in the near-critical conditions.

3.4 Numerical results for the normal field

In fact, at this point we have all the ingredients necessary to easily derive the equations of the evolution of an initially straight interface in the "normal" field (i.e. in the "peak" configuration, where the field is perpendicular to the interface and parallel to the plane of the Hele-Shaw cell). The dispersion relation for linearized perturbations of a planar interface [180] can be written in our notation as

$$\lambda = -k^3 + k\left(\mathrm{Ca} + \mathrm{Bg} + 2\,\mathrm{Bm}\, I_{\mathrm{norm}}(k)\right)\,, \tag{3.40}$$

where

$$I_{\mathrm{norm}}(k) = \int_0^{+\infty} \frac{1-\cos(kt)}{t^2}\left(\sqrt{t^2+1} - t\right)\,\mathrm{d}t\,.$$

Both perpendicular (Eq.(3.36)) and normal fields tend to destabilize every wavelength of a perturbed immiscible interface (and the shorter the wavelength, the higher the tendency towards its destabilization by the fields).

Let the field be directed along the y-axis in the geometry of Fig. 3.1. Then to use the formulas derived in §1.4 and Chapter 2.4, we only have to

substitute there x with $-y$ and y with x. Indeed, Eq.(2.46) for the magnetic force at a constant magnetization becomes

$$\vec{f}_{\rm m} = M_i \vec{\nabla} \frac{\partial \psi}{\partial y} \,. \tag{3.41}$$

The (gap-averaged) magnetic potential ψ is written according to the dimensional form of Eq.(2.51) as

$$\frac{\partial \psi}{\partial y} = -\frac{2}{h} \int\limits_{-\infty}^{+\infty} \int\limits_{-\infty}^{+\infty} (y - y') \frac{\partial M}{\partial y'} \, J_{\rm h} \left(\sqrt{(x-x')^2 + (y-y')^2} \right) \, {\rm d}x' \, {\rm d}y' \tag{3.42}$$

with $J_{\rm h}(\rho) = \left(\sqrt{\rho^2 + h^2} - \rho\right) \Big/ \rho^2$. Since we have now two domains of constant magnetization, the derivative of the latter in Eq.(3.42) is zero away from the interface, being in fact a delta function. This allows to perform one of integrations in Eq.(3.42). First imagine that the interface is such that y is a single-valued function of x. Then we immediately obtain (whatever the slope of the interface)

$$\begin{aligned} \frac{\partial \psi}{\partial y} &= -\frac{2(M_2 - M_1)}{h} \int\limits_{-\infty}^{+\infty} (y - y') J_{\rm h} \left(\sqrt{(x-x')^2 + (y-y')^2} \right) \, {\rm d}x' \\ &= -\frac{2(M_2 - M_1)}{h} \int\limits_{-\infty}^{+\infty} (y - y') J_{\rm h} \left(\sqrt{(x-x')^2 + (y-y')^2} \right) \tau_x(s') \, {\rm d}s' \,, \end{aligned} \tag{3.43}$$

where s' is the arclength variable parametrizing the infinite interface. If we remove the limitation of single-valuedness, it suffices to split the (x', y') domain into the pieces where x' can be used as a curve parameter and sum the resulting integrals, obtaining the same final result. If we now proceed with the same further manipulations as we have done for the case of the perpendicular field in §3.3, we will obtain exactly the same equations except for $I_{\rm m}$ (see Eq.(3.24)) which needs to be replaced with

$$\tilde{I}_{\rm m} = \\ {\rm v.p.} \int\limits_{-\infty}^{+\infty} \frac{\sqrt{(x-x')^2 + (y-y')^2 + 1} - \sqrt{(x-x')^2 + (y-y')^2}}{(x-x')^2 + (y-y')^2} (y - y') \tau_x(s') \, {\rm d}s' \,. \tag{3.44}$$

Unlike Eq.(3.24), Eq.(3.44) involves a principal-value integral. We will again truncate the infinite path of integration in same manner as it has been done in §3.1.5. Our ability to simulate extensively the normal-field instability turns out to be seriously limited by violent numerical instabilities. To have a stabler method, some special desingularization of Eq.(3.44) is perhaps needed. Nevertheless we are able to produce a preliminary result presented in Figs. 3.24, 3.25. (Keep in mind that these Figures are stretched y-wise unlike most previous ones.) Interestingly, it proves possible to reproduce the experimentally observed behaviour noted in [7, 181] at Ca $= 7/720$, Bm $= 0.84$, At $= 1$, and $T = 20$, although some our parameter values differ from the experimental ones. Namely, in the transient regime several peaks per period can develop from the initial perturbation of a period T. At this stage, the development is quite fast (Figs. 3.24(a), 3.24(b)). Then the evolution of the dominant peak and its smaller neighbours slows down, as shown in Fig. 3.24(c), with the interfacial period being quite constant. After a while the dominant peak resumes advancing fast, absorbing the smaller ones that recede. Then there is only one peak with straight slopes that develops into a finger with high curvature at the tip. Fig. 3.25 shows the case of the maximum viscosity contrast. The transition from a multiple-peak interface to a single peak occurs in a slightly different way, while the preceding stage shows no difference between the At $= 0$ and At $= 1$ cases. We note also that the At $= 1$ pattern almost restores its symmetry with respect to the $y = 0$ line by about $t = 90 \ldots 100$. In the long run, the fingers take on a typical "fish-like" shape.

The development of the boundary-integral method is under way.

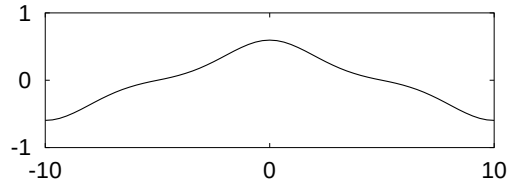

(a) $t = 20$.

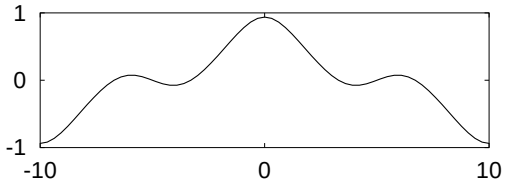

(b) $t = 25$.

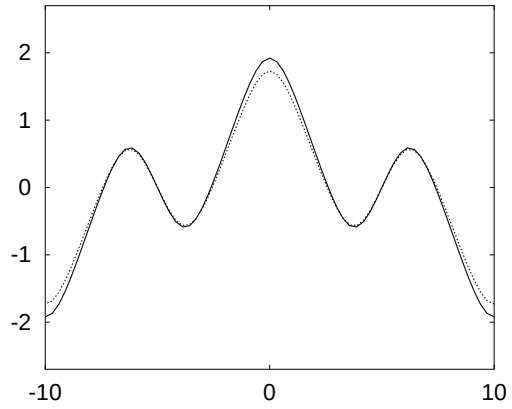

(c) $t = 35$ (dotted line); $t = 40$ (solid line).

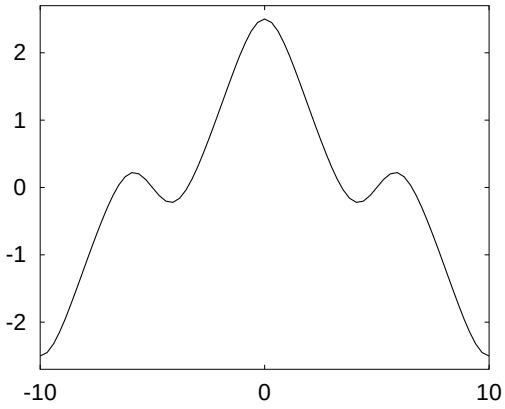

(d) $t = 60$.

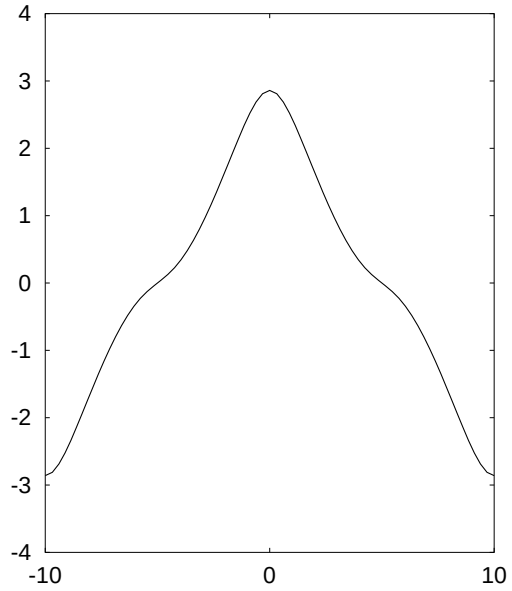

(e) $t = 70$.

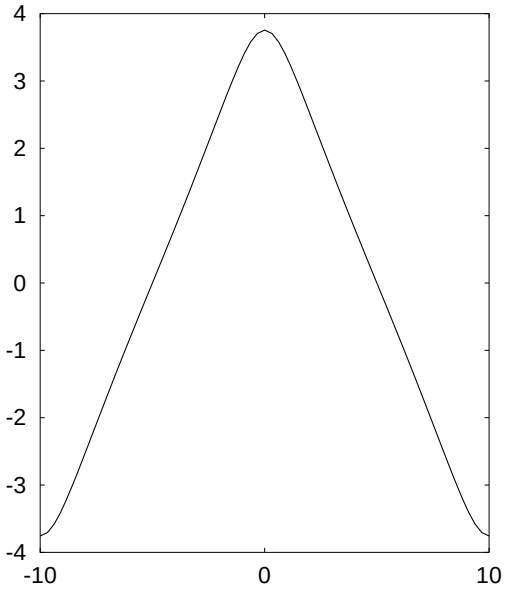

(f) $t = 85$.

Figure 3.24: Development of a magnetic finger in the normal field: Ca = 7/120, Bm = 1.14, At = 0, $T = 20$, $M = 1$, and the initial data $y = 0.2\cos(2\pi x/T)$.

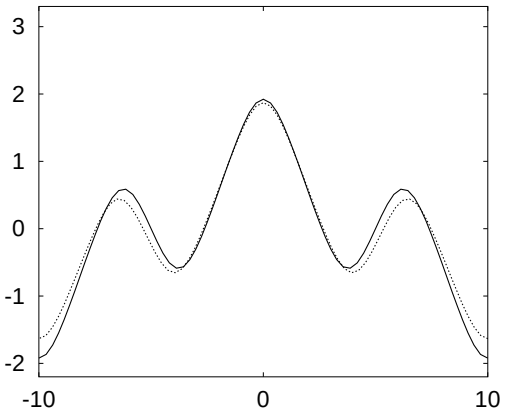

(a) $t = 35$ (dotted line); $t = 40$ (solid line).

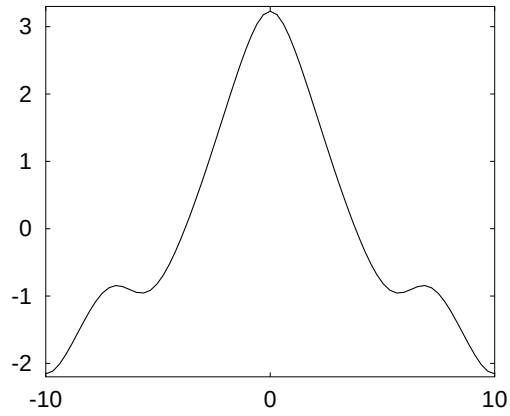

(b) $t = 60$.

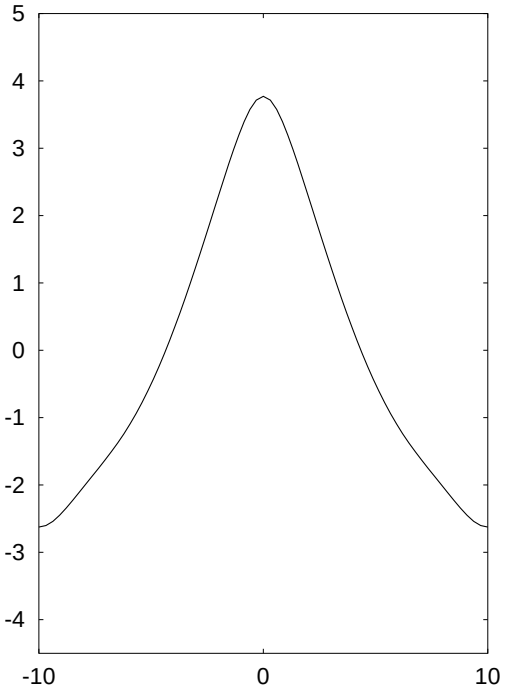

(c) $t = 70$.

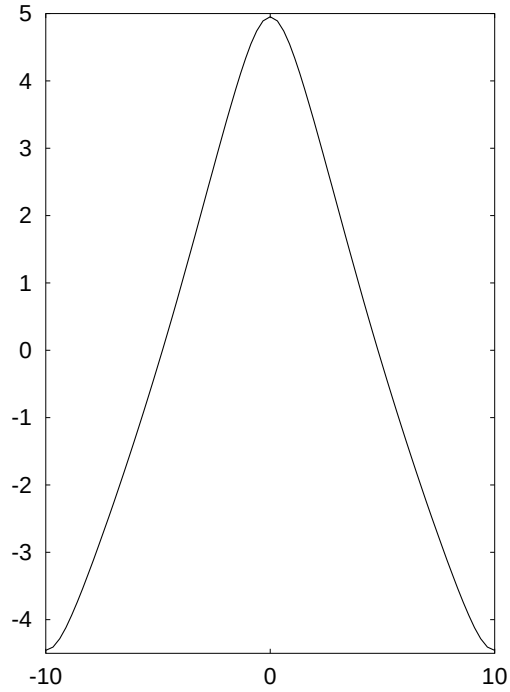

(d) $t = 90$.

Figure 3.25: Development of a magnetic finger in the normal field at infinite viscosity contrast. Parameters are the same as in Fig. 3.24 except for At = 1.

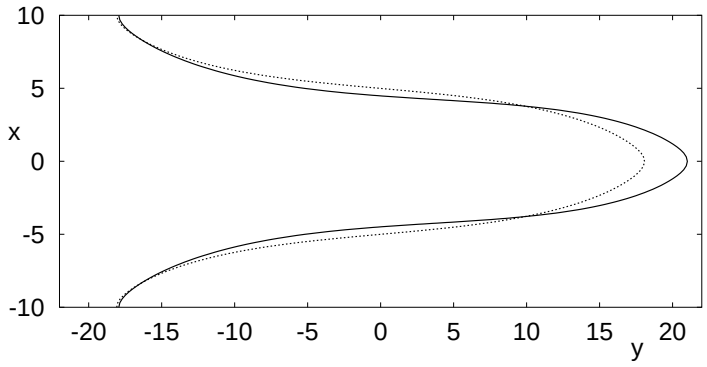

Figure 3.26: The normal-field magnetic fingers at $t = 360$: the At $= 1$ shape (solid line) and the At $= 0$ one (dotted line). Other parameters are the same as in Figs. 3.24, 3.25.

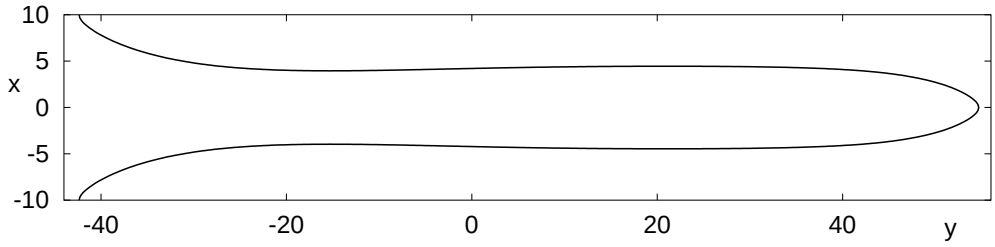

Figure 3.27: A normal-field magnetic finger from Fig. 3.25 at $t = 840$.

Conclusion

In conclusion, the present work analyzes some fluid-mechanical instabilities exhibited by isothermal magnetized ferrofluids in a Hele-Shaw cell. The non-potential driving force of the instability is due to the self-magnetic field of the ferrofluid. By taking the approach of averaging across the gap, we consider both the case of a single fluid with an inhomogeneous (possibly discontinuous) concentration of magnetic particles, and the case of two immiscible magnetic fluids forming a sharp interface with surface tension. Two orientations of the uniform external field are considered: "perpendicular" and "normal" ones.

In the first part, an extensive linear stability analysis is performed for the miscible case with selected basic concentration distributions along the cell that model experimental conditions reported in the literature. For a step-like concentration distribution, we obtain analytically the neutral curves along with the critical wavelength and the critical magnetization. In the perpendicular field, an oscillatory instability and the absence of discrete instability modes are found possible under certain conditions, and the stability diagram is presented. A mechanism of the oscillatory instability mode is explained physically. Self-oscillations occur through the interplay between diffusion and advection driven via a magnetic body force by concentration inhomogeneity. An asymptotic treatment of the dispersion relation is presented as well. These results refer to the known experimental situation when a ferrofluid is brought into contact with its pure carrier liquid, and convective instabilities (the miscible labyrinthine and peak ones) are observed at the diffusion front between the fluids. In the normal field, we additionally consider the stability of a periodic pattern of sharp parallel stripes and find that the peristaltic mode is critical. These results apply to the forced Rayleigh scattering experiments, and our threshold conditions for the onset of microconvection are consistent with recent experimental observations.

The above analysis is carried out with the assumption that the flow is governed by the conventional Darcy law that takes into account only the near-wall friction. The Brinkman equation offers a much better gap-averaged approximation of viscous stresses if the typical flow length scale is expected

to be as small as the gap width. It is the simplest equation that allows to reproduce realistically such Hele-Shaw flows. With both the Brinkman equation and the Darcy law, we undertake the numerical stability analysis of the family of smoothed step-like concentration distributions (in both fields) and of the Gaussian concentration distributions (in the normal field only). The Darcy results for the smoothed step-like distributions are proven to converge to the analytical ones as the interface gets sharper. With the Brinkman equation, we find that it is viscosity (and not diffusion, as one might think) that determines the scale of the instability at strong forcing by rendering the most unstable wavelength comparable to several gap widths. This result proves to be robust, being quite weakly dependent on the basic concentration gradient. We trace the evolution of the neutral curves as the step-like concentration distribution diffuses out. Although the wavelength selection is seriously modified, the critical magnetization is not much affected by the adoption of the Brinkman equation.

In the second half of our study, we model the non-linear dynamics, governed by the Darcy equation, of an immiscible interface between ferrofluids. The boundary-integral method makes modelling efficient by rendering the problem effectively one-dimensional. We describe the corresponding computational technique, indicate some associated pitfalls, and pay proper attention to the validity of the developed algorithm. We note that the Saffman–Taylor finger in a laterally bounded cell cannot be modelled with our approach, although the same problem in the laterally infinite periodic geometry is handled with ease. In the latter case, we observe the decrease of the finger width as the magnetization increases. We also obtain picturesque "dendritic" structures close to those observed experimentally and analyze some aspects of pattern formation such as two-lobe and three-lobe tip-splittings, vertex-splitting, side-branching, and finger shielding. We notice the intrinsic sensitivity of the patterns to small perturbations. The change of the preferable length scale in the course of the pattern evolution is identified as a reason for the complexity of patterns. These results concern the case of the perpendicular field. We also present, here for the first time, some numerical simulations for the normal field. In particular, we obtain a typical finger shape.

As for perspectives, an obvious extension is to unify the miscible and immiscible problems by following the current trend and allowing for the Korteweg stresses at the concentration gradients. The non-linear simulations of the Brinkman-governed miscible and immiscible flows might also be interesting; modelling in three dimensions is an ideal. However, these options would complicate any treatment considerably. Without any doubt, more experiments are needed for the development of the subject. The general context for this is quite favourable thanks to the technological trend towards miniaturization.

List of Figures

1 Magnetic microconvection on a diffused interface. 2

2.1 A sketch of a Hele-Shaw cell. 26
2.2 The number of modes: application of the Cauchy principle of argument. 40
2.3 The growth rate for short wavelengths. 41
2.4 The growth rate for large wavelengths. 41
2.5 The stability diagram. 42
2.6 An oscillatory perturbation mode. 46
2.7 An example of the full spectrum. 50
2.8 The Darcy dominant mode. 52
2.9 The Brinkman dominant mode. 53
2.10 The most unstable wavenumber. 54
2.11 The critical wavenumber and the asymptotic most unstable one for diffused interfaces. 54
2.12 The asymptotic growth increment – wavenumber dependence. 55
2.13 The asymptotic increment of the most unstable mode of diffused interfaces. 55
2.14 Evolution of neutral curves as the interface diffuses. 56
2.15 The neutral curve for the miscible "peak" instability in a Hele-Shaw cell. 62
2.16 The neutral curves for the periodic array of wide stripes . . . 63
2.17 The neutral curves for the periodic array of narrow stripes . . 64
2.18 A comparison of the neutral curves for the peak and labyrinthine instabilities 65
2.19 The neutral curves for the instability of the originally step-like concentration distribution 66
2.20 The neutral curves for the instability of the Gaussian concentration distribution 66
2.21 The critical Cm as the interface diffuses. 67
2.22 The Cm dependence of the most unstable wavenumber 68

2.23 The most unstable wavelength at infinite Cm and the critical wavelength 68
2.24 The asymptotic value of the λ/Cm ratio 69

3.1 The geometry of the immiscible problem. 77
3.2 The contour of integration for the magnetic term. 87
3.3 The differential clustering of initially equidistant markers as the interface evolves. 99
3.4 A comparison of the computed finger shape to the classical ST solution. 107
3.5 Computed magnetic finger width versus time. 109
3.6 A magnetic finger. 113
3.7 The width of a magnetic finger. 115
3.8 Computed magnetic finger width versus time. 116
3.9 Magnetic structure. 117
3.10 Another magnetic structure. 119
3.11 The competition of magnetic fingers. 120
3.12 Shielding and its absence. 121
3.13 A long magnetic finger. 123
3.13 A long magnetic finger (2). A vertex-splitting event. 124
3.14 Yet another pattern. 125
3.15 Development of a magnetic dendrite. 127
3.15 Development of a magnetic dendrite (2). 128
3.15 Development of a magnetic dendrite (3). 129
3.16 The sensitivity of pattern formation to small perturbations. . . 130
3.17 A magnetic dendrite at a higher field. 131
3.18 The equilibrium width of stripes by [59, 252]. 132
3.19 A pattern at a zero viscosity contrast. 134
3.20 The effective range of magnetic interactions 135
3.21 Drops and trapped bubbles. 136
3.22 Dynamical structure of an interface. 137
3.23 Evolution of the perimeter. 137
3.24 A magnetic finger in the normal field at zero viscosity contrast. 141
3.25 A magnetic finger in the normal field at infinite viscosity contrast. 142
3.26 A comparison of the normal-field magnetic fingers. 143
3.27 A long normal-field magnetic finger. 143

List of Tables

2.1 The number of numerical linear modes. 49

3.1 The λ–Ca dependence at Bm = 0. 108
3.2 Pointwise numerical convergence of results. 111
3.3 The width of a magnetic finger. 114

Bibliography

[1] M. M. Maiorov and A. O. Tsebers. Magnetic microconvection on the diffusion front of ferroparticles. *Magnetohydrodynamics*[5], 19(4):376–380, 1983.

[2] J.-C. Bacri, A. Cebers, A. Bourdon, G. Demouchy, B.M. Heegaard, and R. Perzynski. Forced Rayleigh experiment in a magnetic fluid. *Phys. Rev. Lett.*, 74:5032–5035, 1995.

[3] A. Mezulis and E. Blums. Experimental investigations on the microconvective instability in optically induced gratings. In NanoMag2004 [258], pages 35–36.

[4] W. Luo, T. Du, and J. Huang. *Phys. Rev. Lett.*, 87, 059802, 2001. Reply to [110].

[5] J. M. Ottino and S. Wiggins. Introduction: mixing in microfluidics. *Phil. Trans. R. Soc. Lond. A*, 362:923–935, 2004. Full text is available as: <mixing.chem-eng.northwestern.edu/papers/philtrans /Phil_Trans_OttiWigg.pdf>.

[6] A. Cēbers and I. Driķis. Labyrinthine pattern formation in magnetic liquids. In I. Athanasopoulos, G. Makrakis, and J. F. Rodrigues, editors, *Free boundary problems: theory and applications*, volume 409 of *Research Notes in Mathematics*, pages 14–38. Chapman & Hall /CRC, 1999.

[7] G. Pacitto, C. Flament, and J.-C. Bacri. Viscous fingering in a magnetic fluid. II. Linear Hele-Shaw flow. *Phys. Fluids*, 13(11):3196–3203, 2001.

[5]We reference only the English translation of the journal Magnitnaya Gidrodinamika [Магнитная гидродинамика]. The original Russian reference (prior to 2002) can be recovered at the site of the journal <www.mhd.sal.lv/index.html>.

[8] D. M. Anderson, G. B. McFadden, and A. A. Wheeler. Diffuse-interface methods in fluid mechanics. *Ann. Rev. Fluid Mech.*, 30:139–165, 1998. Full text is available as: <math.gmu.edu/~dmanders/WEBDAN/ann_rev.ps>.

[9] Ecole Supérieure de Physique et de Chimie Industrielles. *Proceedings of the International Workshop on Miscible Interfaces*, Paris, France, July 2001.

[10] P. G. Saffman and G. Taylor. The penetration of a fluid into a porous medium or Hele-Shaw cell containing a more viscous liquid. *Proc. R. Soc. London, Ser. A*, 245:312–329, 1958.

[11] P. Pelcé. *Théorie des formes de croissance. Digitations, dendrites et flammes.* EDP Sciences – CNRS Éditions, Les Ulis, Paris, 2000. In French.

[12] G. Pacitto, C. Flament, J.-C. Bacri, and M. Widom. Rayleigh–Taylor instability with magnetic fluids: Experiment and theory. *Phys. Rev. E*, 62(6):7941–7948, 2000.

[13] C. Flament, J.-C. Bacri, A. Cebers, F. Elias, and R. Perzynski. Parallel stripes of ferrofluid as a macroscopic bidimensional smectic. *Europhys. Lett.*, 34(3):225–230, 1996.

[14] R. E. Rosensweig. *Ferrohydrodynamics.* Cambridge University Press, Cambridge, 1985. References are made to the revised Russian edition.

[15] E. J. Blums, A. Cebers, and M. M. Maiorov. *Magnetic Fluids.* Walter de Gruyter, Berlin, 1997.

[16] A. Gailītis. Formation of the hexagonal pattern on the surface of a ferromagnetic fluid in an applied magnetic field. *J. Fluid Mech.*, 82:401–413, 1977.

[17] M. I. Shliomis. Magnetic fluids. *Soviet Physics – Uspekhi*, 17:153, 1974.

[18] L. D. Landau and E. M. Lifshitz. *Fluid Mechanics.* Pergamon, Oxford, 1987.

[19] R. Haase. *Thermodynamik der irreversiblen Prozesse.* Steinkopff, Darmstadt, 1963. In German.

[20] H. H. Hu and D. D. Joseph. Miscible displacement in a Hele-Shaw cell. *Z. Angew. Math. Phys.*, 43(4):626–644, 1992. Full text is available at [259].

[21] O. Manickam and G. M. Homsy. Fingering instabilities in vertical miscible displacement flows in porous media. *J. Fluid Mech.*, 288:75–102, 1995.

[22] T. Y. Liao and D. D. Joseph. Sidewall effects in the smoothing of an initial discontinuity of concentration. *J. Fluid Mech.*, 342:37–51, 1997. Full text is available at [259].

[23] D. Joseph, A. Huang, and H. Hu. Non-solenoidal velocity effects and Korteweg stresses in simple mixture of incompressible liquids. *Physica D*, 97:104–125, 1996. Full text is available at [259].

[24] D. Joseph. Fluid dynamics of two miscible liquids with diffusion and gradient stresses. *Eur. J. Mech. B / Fluids*, 9:565–596, 1990. Full text is available at [259].

[25] P. Galdi, D. D. Joseph, L. Preziosi, and S. Rionero. Mathematical problems for miscible, incompressible fluids with Korteweg stresses. *Eur. J. Mech. B / Fluids*, 10:253–267, 1991. Full text is available at [259].

[26] N. Alikakos, P. Bates, and X. Chen. Convergence of the Cahn–Hilliard equations to the Hele-Shaw model. *Arch. Rat. Mech. Anal.*, 128:165–205, 1994.

[27] H.-G. Lee, J. S. Lowengrub, and J. Goodman. Modeling pinchoff and reconnection in a Hele-Shaw cell. I. The models and their calibration. *Phys. Fluids*, 14(2):492–513, 2002.

[28] H.-G. Lee, J. S. Lowengrub, and J. Goodman. Modeling pinchoff and reconnection in a Hele-Shaw cell. II. Analysis and simulation in the nonlinear regime. *Phys. Fluids*, 14(2):514–545, 2002.

[29] G. I. Taylor. Dispersion of soluble mater in solvent flowing slowly through a tube. *Proc. R. Soc. London Ser. A*, 219:186–203, 1953.

[30] G. M. Homsy. Viscous fingering in porous media. *Annu. Rev. Fluid Mech.*, 19:271–311, 1987.

[31] R. A. Wooding. The stability of an interface between miscible fluids in a porous medium. *Z. Angew. Math. Phys.*, 13:255–266, 1962.

[32] L. Paterson. Fingering with miscible fluids in a Hele-Shaw cell. *Phys. Fluids*, 28(1):26–30, 1985.

[33] C. T. Tan and G. M. Homsy. Stability of miscible displacements in porous media: Rectilinear flow. *Phys. Fluids*, 29:3549–3556, 1986.

[34] C. T. Tan and G. M. Homsy. Stability of miscible displacements in porous media: Radial source flow. *Phys. Fluids*, 30(5):1239–1245, 1987.

[35] Y. C. Yortsos and M. Zeybek. Dispersion driven instability in miscible displacement in porous media. *Phys. Fluids*, 31(12):3511–3518, 1988.

[36] J.-C. Bacri, D. Salin, and Y. C. Yortsos. Analyse linéaire de la stabilité de l'écoulement de fluides miscibles en milieux poreux. *C. R. Acad. Sci. Paris, Ser. II*, 314:139–144, 1992. In French.

[37] J.-C. Bacri, N. Rakotomalala, D. Salin, and R. Wouméni. Miscible viscous fingering: Experiments versus continuum approach. *Phys. Fluids A*, 4(8):1611–1619, 1992.

[38] A. Rogerson and E. Meiburg. Shear stabilization of miscible displacement processes in porous media. *Phys. Fluids A*, 5(6):1344–1355, 1993.

[39] O. Manickam and G. M. Homsy. Stability of miscible displacements in porous media with nonmonotonic viscosity profiles. *Phys. Fluids A*, 5:1356–1367, 1993.

[40] C. T. Tan and G. M. Homsy. Simulation of nonlinear viscous fingering in miscible displacement. *Phys. Fluids*, 31(6):1330–1338, 1988.

[41] C.-Y. Chen and E. Meiburg. Miscible porous media displacements in the quarter five-spot configuration. Part 1. The homogeneous case. *J. Fluid Mech.*, 371:233–268, 1998.

[42] R. A. Wooding. Growth of fingers at an unstable diffusing interface in a porous medium or Hele-Shaw cell. *J. Fluid Mech.*, 39:477–495, 1969.

[43] P. Petitjeans and T. Maxworthy. Miscible displacements in capillary tubes. Part 1. Experiments. *J. Fluid Mech.*, 326:37–56, 1996.

[44] J. Kuang, T. Maxworthy, and P. Petitjeans. Miscible displacements between silicone oils in capillary tubes. *Eur. J. Mech. B / Fluids*, 22:271–277, 2003.

[45] C.-Y. Chen and E. Meiburg. Miscible displacements in capillary tubes. Part 2. Numerical simulations. *J. Fluid Mech.*, 326:57–90, 1996.

[46] C.-Y. Chen and E. Meiburg. Miscible displacements in a capillary tube: Influence of Korteweg stresses and divergence effects. *Phys. Fluids*, 14(7):2052–2058, 2002.

[47] N. Rakotomalala, D. Salin, and P. Watzky. Miscible displacement between two parallel plates: BGK lattice gas simulations. *J. Fluid Mech.*, 338:277–297, 1997.

[48] C.-Y. Chen, L. Wang, and E. Meiburg. Miscible droplets in a porous medium and the effects of Korteweg stresses. *Phys. Fluids*, 13:2447–2456, 2001.

[49] P. Petitjeans and P. Kurowski. Fluides non miscibles / fluides miscibles: des similitudes intéressantes. *C. R. Acad. Sci. Paris, Ser. II B*, 325:587–592, 1997. In French.

[50] M. Legendre, P. Petitjeans, and P. Kurowski. Instabilités à l'interface entre fluides miscibles par forçage oscillant horizontal. *C. R. Acad. Sci. Paris, Ser. II B*, 331 (9):617–622, 2003. In French.

[51] M. Legendre. *Fluides sous vibrations et singularités d'interface.* PhD thesis, Université Paris 6 – Pierre et Marie Curie, Paris, 2003. In French.

[52] P. Petitjeans. Une tension de surface pour les fluides miscibles. *C. R. Acad. Sci. Paris, Ser. II B*, 322:673–679, 1996. In French.

[53] Z. Yang and Y. C. Yortsos. Asymptotic solutions of miscible displacements in geometries of large aspect ratio. *Phys. Fluids*, 9(2):286–298, 1997.

[54] E. Lajeunesse, J. Martin, N. Rakotomalala, and D. Salin. 3d instability of miscible displacements in a Hele-Shaw cell. *Phys. Rev. Lett.*, 79(26):5254–5257, 1997.

[55] S. H. Davis. Hydrodynamic interactions in directional solidification. *J. Fluid Mech.*, 212:241–262, 1990.

[56] E. Lajeunesse, J. Martin, N. Rakotomalala, D. Salin, and Y. C. Yortsos. Miscible displacement in a Hele-Shaw cell at high rates. *J. Fluid Mech.*, 398:299–319, 1999.

[57] E. Lajeunesse, J. Martin, N. Rakotomalala, D. Salin, and Y. C. Yortsos. The threshold of the instability in miscible displacements in a Hele-Shaw cell at high rates. *Phys. Fluids*, 13(3):799–801, 2001.

[58] A. O. Tsebers. Role of surface interactions in stratification of magnetic fluids. *Magnetohydrodynamics*, 18(4):345–350, 1982.

[59] A. Cebers. Transformations of the concentration domain structures of liquid magnetics in plane layers 1. The energetic approach. *Magnetohydrodynamics*, 31(1):58–64, 1995.

[60] A. Cebers. Transformations of the concentration domain structures of liquid magnetics in plane layers 2. Kinetics and the numerical experiment. *Magnetohydrodynamics*, 31(1):65–72, 1995.

[61] A. Cebers. Two-dimensional concentration domain patterns in magnetic suspensions: Energetical and kinetic approach. *Progr. Colloid Polym. Sci.*, 100:101–106, 1996.

[62] A. Cēbers. Instabilities of concentration stripe patterns in ferrocolloids. *Phys. Rev. E*, 61(1):700–708, 2000.

[63] D. Lacoste and T. C. Lubensky. Phase transitions in a ferrofluid at magnetic-field-induced microphase separation. *Phys. Rev. E*, 64, 041506, 2001. See also <arxiv.org/abs/cond-mat/0103429>.

[64] A. Cēbers. The anisotropy of the surface tension at the magnetic-field-induced phase transformations. *J. Magn. Magn. Mat.*, 252:259–261, 2002.

[65] A. O. Tsebers. Three-dimensional structures in planar ferrocolloid layers. *Magnetohydrodynamics*, 24(2):184–188, 1988.

[66] A. O. Tsebers. A general diffusion model of magnetized suspensions and dissipative vortex structures in rotating magnetic fields. 1. *Magnetohydrodynamics*, 25(3):281–285, 1989.

[67] C.-Y. Chen. Numerical simulations of fingering instabilities in miscible magnetic fluids in a Hele-Shaw cell and the effects of Korteweg stresses. *Phys. Fluids*, 15(4):1086–1089, 2003.

[68] C.-Y. Chen and C.-Y. Wen. Numerical simulations of miscible magnetic flows in a Hele-Shaw cell. Radial flows. *J. Magn. Magn. Mater.*, 252:296–298, 2002.

[69] J. Happel and H. Brenner. *Low Reynolds Number Hydrodynamics: With Special Applications to Particulate Media*. Prentice-Hall, Englewood Cliffs, N. J., 1965.

[70] G. K. Batchelor. *An Introduction to Fluid Dynamics*. Cambridge University Press, Cambridge, 1970.

[71] P. Gondret, N. Rakotomalala, M. Rabaud, D. Salin, and P. Watzky. Viscous parallel flows in a finite aspect ratio Hele-Shaw cell: Analytical and numerical results. *Phys. Fluids*, 9:1841–1843, 1997.

[72] P. Ya. Polubarinova-Kochina. *Theory of Groundwater Movement*. Nauka, Moscow, 2nd edition, 1977. In Russian. English translation from the 1st edition was printed by Princeton University Press, Princeton, N. J., 1962.

[73] H. Lamb. *Hydrodynamics*. Cambridge University Press, Cambridge, 6th edition, 1993.

[74] M. van Dyke. *An Album of Fluid Motion*. Parabolic Press, Stanford, California, 1982.

[75] L. Prandtl. *Führer durch die Strömungslehre*. 2nd edition.

[76] H. Schlichting. *Boundary-Layer Theory*. McGraw-Hill, N. Y., L., 6th edition, 1968.

[77] J. Zeng, Y. C. Yortsos, and D. Salin. On the Brinkman correction in unidirectional Hele-Shaw flows. *Phys. Fluids*, 15:3829–3836, 2003.

[78] D. Snyder and S. Tait. A flow-front instability in viscous gravity currents. *J. Fluid Mech.*, 369:1–21, 1998.

[79] M. Rabaud, Y. Couder, and N. Gerard. Dynamics and stability of anomalous Saffman–Taylor fingers. *Phys. Rev. A*, 37:935–947, 1988.

[80] W. Boos and A. Thess. Thermocapillary flow in a Hele-Shaw cell. *J. Fluid Mech.*, 352:305–330, 1997.

[81] J. Huang and B. F. Edwards. Pattern formation and evolution near autocatalytic reaction fronts in a narrow vertical slab. *Phys. Rev. E*, 54:2620–2627, 1996.

[82] M. Böckmann and S. C. Müller. Growth rates of the buoyancy-driven instability of an autocatalytic reaction front in a narrow cell. *Phys. Rev. Lett.*, 85(12):2506–2509, 2000.

[83] D. A. Vasquez and A. De Wit. Dispersion relations for the convective instability of an acidity front in Hele-Shaw cells. *J. Chem. Phys.*, 121(2):935–941, 2004.

[84] A. A. Predtechensky, W. D. McCormick, J. B. Swift, A. G. Rossberg, and Harry L. Swinney. Traveling wave instability in sustained double-diffusive convection. *Phys. Fluids*, 6:3923–3935, 1994.

[85] W. Schoepf. Convection onset for a binary mixture in a porous medium and in a narrow cell: a comparison. *J. Fluid Mech.*, 245:263–278, 1992.

[86] J. Fernandez, P. Kurowski, P. Petitjeans, and E. Meiburg. Density-driven unstable flows of miscible fluids in a Hele-Shaw cell. *J. Fluid Mech.*, 451:239–260, 2002.

[87] F. Graf, E. Meiburg, and C. Härtel. Density-driven instabilities of miscible fluids in a Hele-Shaw cell: Linear stability analysis of the three-dimensional Stokes equations. *J. Fluid Mech.*, 451:261–282, 2002.

[88] J. Fernandez, P. Kurowski, L. Limat, and P. Petitjeans. Wavelength selection of fingering instability inside Hele-Shaw cells. *Phys. Fluids*, 13:3120–3125, 2001.

[89] P. Kurowski, J. Fernandez, L. Limat, and P. Petitjeans. Instabilité gravitationnelle entre fluides miscibles dans une cellule de Hele-Shaw: des petits nombres de Péclet aux grands nombres de Péclet. *J. Phys. IV (France)*, 11:247–253, 2001. In French.

[90] J. Martin, N. Rakotomalala, and D. Salin. Gravitational instability of miscible fluids in a Hele-Shaw cell. *Phys. Fluids*, 14(2):902–905, 2002.

[91] M. Igonin and A. Cebers. Labyrinthine instability of miscible magnetic fluids. *J. Magn. Magn. Mat.*, 252:293–295, 2002. [*Proceedings of the 9th International Conference on Magnetic Fluids*, Bremen, Germany, July 2001].

[92] J. Huang, D. A. Vasquez, and B. F. Edwards. Onset of convection for autocatalytic reaction fronts in a vertical slab. *Phys. Rev. E*, 48:4378–4386, 1993.

[93] P. Kurowski, C. Misbah, and S. Tchourkine. Gravitational instability of a fictitious front during mixing of miscible fluids. *Europhys. Lett.*, 29:309–314, 1995.

[94] G. K. Batchelor and J. M. Nitsche. Instability of stationary unbounded stratified fluid. *J. Fluid Mech.*, 227:357, 1991.

[95] L. D. Landau, E. M. Lifshitz, and L. P. Pitaevskii. *Electrodynamics of Continuous Media*. Pergamon, Oxford, 1984. Translated from the 2nd Russian edition.

[96] I. G. Shaposhnikov and M. I. Shliomis. Hydrodynamics of magnetizable media. *Magnetohydrodynamics*, 11(1):37–46, 1975.

[97] V. V. Gogosov, V. A. Naletova, and G. A. Shaposhnikova. *Hydrodynamics of magnetizable fluids*, volume 16 of *Progress in Science and Technology, Ser. Mechanics of Fluid and Gas*, pages 76–208. VINITI, Moscow, 1981. In Russian. [Гогосов В. В., Налетова В. А., Шапошникова Г. А. Гидродинамика намагничивающихся жидкостей. Итоги науки и техники. Мех. жидк. и газа. – М.: ВИНИТИ, 1981, т. 16, сс. 76–208].

[98] S. R. de Groot and L. G. Suttorp. *Electrodynamics of Continuous Media*. North Holland, Amsterdam, 1972.

[99] W. K. H. Panofsky and M. Phillips. *Classical Electricity and Magnetism*. Addison-Wesley, N. Y., 1962.

[100] J. A. Miranda and M. Widom. Parallel flow in Hele-Shaw cells with ferrofluids. *Phys. Rev. E*, 61:2114–2117, 2000.

[101] A. O. Tsebers. Dynamics of magnetostatic instabilities. *Magnetohydrodynamics*, 17(2):113–121, 1981.

[102] D. P. Jackson, R. E. Goldstein, and A. O. Cebers. Hydrodynamics of fingering instabilities in dipolar fluids. *Phys. Rev. E*, 50(1):298–307, 1994.

[103] J.-C. Bacri, A. Cebers, A. Bourdon, G. Demouchy, B.M. Heegaard, B. Kashevsky, and R. Perzynski. Transient grating in a ferrofluid under magnetic field: Effect of magnetic interactions on the diffusion coefficient of translation. *Phys. Rev. E*, 52:3936–3942, 1995.

[104] G. Demouchy, A. Bourdon, J.-C. Bacri, F. da Cruz, A. Mezulis, and E. Blums. Forced Rayleigh scattering determination of the Soret coefficient and of the thermodiffusion mobility of ferrofluids under applied magnetic field. In Pamir2000 [260], pages 433–438.

[105] A. Mezulis and E. Blums. Two-dimensional determining the transport coefficients under applied magnetic field. In *Proceedings of the Fifth International* Pamir *Conference on Fundamental and Applied MHD*, volume 2, pages (IV) 63–68, Ramatuelle, France, September 2002.

[106] J. Lenglet, A. Bourdon, J.-C. Bacri, and G. Demouchy. Thermodiffusion in magnetic colloids evidenced and studied by forced Rayleigh scattering experiments. *Phys. Rev. E*, 65, 031408, 2002.

[107] A. O. Tsebers. Nonlinear magnetodiffusion problems in the intrinsic field of a particle ensemble. *Magnetohydrodynamics*, 27(2):123–128, 1991.

[108] A. Mezulis and E. Blums. Experimental investigations on the microconvective instability in optically induced gratings. *Magnetohydrodynamics*, 2004. Submitted.

[109] W. Luo, T. Du, and J. Huang. Novel convective instabilities in a magnetic fluid. *Phys. Rev. Lett.*, 82:4134–4137, 1999.

[110] M. I. Shliomis. *Phys. Rev. Lett.*, 87, 059801, 2001. Comment on [109].

[111] A. Cēbers, T. Du, and W. Luo. Temperature-concentration (activator-inhibitor) model of magnetic fluid free surface autooscillations induced by absorption of light. *Magnetohydrodynamics*, 32(3):303–314, 1996.

[112] A. Cēbers. Stability of diffusion fronts of magnetic particles in porous media (Hele-Shaw cell) under the action of an external magnetic field. *Magnetohydrodynamics*, 33(1):48–55, 1997.

[113] Yu. Ben, E. A. Demekhin, and H.-C. Chang. A spectral theory for small-amplitude miscible fingering. *Phys. Fluids*, 14:999–1010, 2002.

[114] A. De Wit. Fingering of chemical fronts in porous media. *Phys. Rev. Lett.*, 87, 054502, 2001.

[115] S. Chandrasekhar. *Hydrodynamic and Hydromagnetic Stability*. Dover, N. Y., 1961.

[116] B. Friedman. *Principles and Techniques of Applied Mathematics*. Wiley, N. Y., 1956.

[117] G. F. Roach. *Green's Functions*. Cambridge University Press, Cambridge, 2nd edition, 1982.

[118] R. Courant and D. Hilbert. *Methoden der mathematischen Physik*, volume 1. Springer-Verlag, Berlin, 2nd edition, 1931. In German.

[119] N. Dunford and J. T. Schwartz. *Linear Operators. Parts I–III.* Interscience, N. Y., 1958–71.

[120] R. G. Cooke. *Linear Operators: Spectral Theory and Some Other Applications.* Macmillan, London, 1953.

[121] L. D. Landau and E. M. Lifshitz. *Quantum Mechanics: Non-Relativistic Theory.* Pergamon, Oxford, 1977.

[122] C. C. Lin. Some mathematical problems in the theory of the stability of parallel flows. *J. Fluid Mech.*, 10(3):430–438, 1961.

[123] C. E. Grosch and H. Salwen. Continuous spectrum of Orr–Sommerfeld equation. 1. Spectrum and eigenfunctions. *J. Fluid Mech.*, 87(1):33–54, 1978.

[124] H. Salwen and C. E. Grosch. The continuous spectrum of Orr–Sommerfeld equation. 2. Eigenfunction expansions. *J. Fluid Mech.*, 104:445–465, 1981.

[125] K. M. Case. Stability of inviscid plane Couette flow. *Phys. Fluids*, 3(2):143–148, 1960.

[126] L. A. Dikii. The stability of plane parallel flows of an ideal fluid. *Dokl. Akad. Nauk SSSR*, 135(5):1068–1071, 1960. In Russian. [Дикий Л. А. Об устойчивости плоскопараллельных потоков идеальной жидкости, Доклады АН СССР, т. 135, N5, сс. 1068–1071 (1960)].

[127] K. M. Case. Hydrodynamic instability and the inviscid limit. *J. Fluid Mech.*, 10(3):420–429, 1961.

[128] L. H. Gustavsson. Initial-value problem for boundary layer flows. *Phys. Fluids*, 22(9):1602–1605, 1979.

[129] R. Menikoff, R. C. Mjolsness, D. H. Sharp, C. Zemach, and B. J. Doyle. The initial value problem for Rayleigh–Taylor instability of viscous fluids. *Phys. Fluids*, 21(10):1674–1687, 1978.

[130] A. Georgescu. *Hydrodynamic Stability Theory.* Nijhoff, Dordrecht, 1985.

[131] P. G. Drazin and W. H. Reid. *Hydrodynamic Stability*. Cambridge University Press, Cambridge, 1981.

[132] L. N. Trefethen, A. E. Trefethen, S. C. Reddy, and T. A. Driscoll. Hydrodynamic stability without eigenvalues. *Science*, 261:578–584, 1993.

[133] W. O. Criminale, T. L. Jackson, and D. G. Lasseigne. The initial-value problem for viscous channel flows. Technical Report NASA CR-195034 ICASE No. 95-6, Institute for Computer Applications in Science and Engineering, NASA Langley Research Center, Hampton, VA 23681-0001, USA, February 1995. Full text is available as: <techreports.larc.nasa.gov/icase/1995/icase-1995-6.pdf>.

[134] P. J. Schmid and D. S. Henningson. *Stability and Transition in Shear Flows*. Springer, N. Y., 2001.

[135] R. Courant and D. Hilbert. *Methods of Mathematical Physics*, volume 2 (*Partial Differential Equations*, by R. Courant). Interscience, N. Y., 1962.

[136] G. P. Galdi and S. Rionero. *Weighted Energy Method in Fluid Dynamics and Elasticity*, volume 1134 of *Lecture Notes in Mathematics*. Springer, Berlin, 1985.

[137] D. D. Joseph. *Stability of Fluid Motions I, II*, volume 27, 28 of *Springer Tracts in Natural Philosophy*. Springer, Berlin, 1976.

[138] P. Glansdorf and I. Prigogine. *Thermodynamic Theory of Structure, Stability and Fluctuations*. Wiley, N. Y., 1971.

[139] A. S. Monin and A. M. Yaglom. *Statistical Hydromechanics*, volume 1. Gidrometeoizdat, Saint-Petersburg, 2nd edition, 1992. In Russian. [Монин А. С., Яглом А. М. Статистическая гидромеханика, т. 1. 2-е изд. – СПб.: Гидрометеоиздат, 1992].

[140] M. Igonin and A. Cebers. Labyrinthine instability of miscible magnetic fluids. *Phys. Fluids*, 15:1734–1744, 2003.

[141] M. Igonin and A. Cebers. Labyrinthine instability of miscible magnetic fluids. In *Proceedings of the 9th Plyos Conference on Magnetic Fluids*, pages 190–195, Plyos, Ivanovo region, Russia, September 2000. In Russian. [Игонин М. Д., Цеберс А. О. Лабиринтная неустойчивость смешивающихся магнитных жидкостей. – В кн.: 9-я Международная Плёсская конференция по магнитным жидкостям (сентябрь 2000 г.). Сборник научных трудов, т. 1, сс. 190–195].

[142] B. A. Finlayson. Convective instability of ferromagnetic fluids. *J. Fluid Mech.*, 40:753–767, 1970.

[143] G. I. Barenblatt. *Scaling, Self-similarity, and Intermediate Asymptotics*. Cambridge University Press, Cambridge, 1996.

[144] G. B. Whitham. *Linear and Nonlinear Waves*. Interscience, N. Y., 1974.

[145] M. A. Lavrentiev and B. V. Shabat. *Methods of the Theory of Functions of Complex Variable*. Nauka, Moscow, 1987. In Russian. [Лаврентьев М. А., Шабат Б. В. Методы теории функций комплексного переменного. – М.: Наука, 1987].

[146] M. I. Shliomis. Convective instability of magnetized ferrofluids: Influence of magnetophoresis and Soret effect, 2001. Full text is available as: <arxiv.org/abs/cond-mat/0106413>.

[147] A. Mežulis. *Mass transport phenomenon in non-isothermic magnetic colloids*. PhD thesis, Université Paris 7 – Denis Diderot, Paris, 1999.

[148] A. Cebers and M. Igonin. Convective instability of magnetic colloid and forced Rayleigh scattering experiments. *Magnetohydrodynamics*, 38(3):265–270, 2002.

[149] M. Igonin. On the microconvective instability of an inhomogeneous magnetic fluid in a Hele-Shaw cell. *Magnetohydrodynamics*, 40(1):53–64, 2004.

[150] M. Igonin and A. Cebers. Magnetic microconvective instabilities in plane layers. In NanoMag2004 [258], pages 37–38.

[151] A. Mezulis, E. Blums, A. Bourdon, and G. Demouchy. Thermodiffusion-induced optical index grating in ferrocolloids: Determination of transport coefficients. In Pamir2000 [260], pages 781–786.

[152] J. Lenglet. *Génération de second harmonique et diffusion Rayleigh forcée dans les colloïdes magnétiques*. PhD thesis, Université Paris 7 – Denis Diderot, Paris, 1996. In French.

[153] A. Mezulis, M. Maiorov, and E. Blums. Transport properties of an ionic magnetic colloid: Experimental study of increasing the ionic strength. In *Proceedings of the 9th International Conference on Magnetic Fluids*, Bremen, Germany, July 2001.

[154] K. I. Morozov. Gradient diffusion in concentrated ferrocolloids under the influence of a magnetic field. *Phys. Rev. E*, 53:3841–3846, 1996.

[155] A. Mežulis. Private communication, 2003.

[156] P. G. Saffman. Viscous fingering in a Hele-Shaw cell. *J. Fluid Mech.*, 173:73–94, 1986.

[157] D. Bensimon, L. P. Kadanoff, S. D. Liang, B. I. Shraiman, and C. Tang. Viscous flows in two dimensions. *Reviews of Modern Physics*, 58(4):977–999, 1986.

[158] K. V. McCloud and J. V. Maher. Experimental perturbations to Saffman–Taylor flow. *Phys. Reports*, 260:139–185, 1995.

[159] S. Tanveer. Surprises in viscous fingering. *J. Fluid Mech.*, 409:273–308, 2000.

[160] S. D. Howison. Fingering in Hele-Shaw cells. *J. Fluid Mech.*, 167:439–453, 1986.

[161] D. G. Crowdy. Hele-Shaw flows and water waves. *J. Fluid Mech.*, 409:223–242, 2000.

[162] J. W. McLean and P. G. Saffman. The effect of surface tension on the shape of fingers in a Hele-Shaw cell. *J. Fluid Mech.*, 102:455–469, 1981.

[163] J. Nittman, G. Daccord, and H. E. Stanley. In Pietronero and Tosatti [187].

[164] L. M. Sander. In Pietronero and Tosatti [187].

[165] H. Van Damme, C. Laroche, L. Gatineau, and P. Levitz. Viscoelastic effects in fingering between miscible fluids. *J. Physique*, 48:1121–1133, 1987.

[166] A. O. Tsebers and A. A. Zemitis. Numerical simulation of MHD instability in the free surface of a gripped drop of magnetic liquid. Part 1. *Magnetohydrodynamics*, 19(4):360–368, 1983.

[167] A. O. Tsebers. A numerical experiment on simulating the MHD instability of the free surface in a trapped drop of magnetic liquid. Part 2. *Magnetohydrodynamics*, 20(2):140–143, 1984.

[168] A. O. Tsebers. Simulating MHD instability in the free surface of a trapped drop magnetic liquid. Part 3. *Magnetohydrodynamics*, 21(2):142–147, 1985.

[169] A. Cēbers and I. Drikis. A numerical study of the evolution of quasi-two-dimensional magnetic fluid shapes. *Magnetohydrodynamics*, 32(1):8–17, 1997.

[170] I. Drikis and A. Cebers. Viscous fingering in magnetic fluids: numerical simulation of radial Hele-Shaw flow. *J. Magn. Magn. Mater.*, 201:339–342, 1999.

[171] A. Cebers. Numerical simulation of the bubble dynamics in a Hele-Shaw cell containing a magnetic fluid. 2. Magnetostatic instabilities. *Magnetohydrodynamics*, 29(2):128–133, 1993.

[172] C. Flament, G. Pacitto, J.-C. Bacri, I. Drikis, and A. Cebers. Viscous fingering in a magnetic fluid. I. Radial Hele-Shaw flow. *Phys. Fluids*, 10:2464–2472, 1998.

[173] A. Cebers. A numerical simulation of the dynamics of bending deformations of the magnetized stripes in Hele-Shaw cells. *Magnetohydrodynamics*, 30(1):20–26, 1994.

[174] A. Cēbers. Topological instability of stripes in Hele-Shaw cells. 1. Viscous instability. *Magnetohydrodynamics*, 33(2):107–115, 1997.

[175] A. O. Tsebers. Numerical simulation of the Saffman–Taylor instability of magnetized liquids. *Magnetohydrodynamics*, 23(1):13–19, 1987.

[176] A. Cēbers. Numerical simulation of Rayleigh–Taylor instability of magnetic fluids. *Magnetohydrodynamics*, 33(2):99–106, 1997.

[177] A. O. Tsebers and M. M. Maiorov. Magnetostatic instabilities in plane layers of magnetizable fluids. *Magnetohydrodynamics*, 16(1):21–27, 1980.

[178] S. A. Langer, R. E. Goldstein, and D. P. Jackson. Dynamics of labyrinthine pattern formation in magnetic fluids. *Phys. Rev. A*, 46(8):4894–4904, 1992.

[179] M. Widom and J. A. Miranda. Viscous fingering patterns in ferrofluids. *J. Stat. Phys.*, 93:411–426, 1998. See also <arxiv.org/abs/cond-mat/9802194>.

[180] C. Flament, S. Lacis, J.-C. Bacri, A. Cebers, S. Neveu, and R. Perzynski. Measurement of ferrofluid surface tension in confined geometry. *Phys. Rev. E*, 53(5):4801–4806, 1996.

[181] G. Pacitto. *Instabilités hydrodynamiques à l'interface de ferrofluides en géométrie confinée*. PhD thesis, Université Paris 7 – Denis Diderot, Paris, 2001. In French.

[182] I. Drikis. *Dynamique non-linéaire de la surface libre d'un liquide magnétique dans une cellule de Hele-Shaw*. PhD thesis, Université Paris 7 – Denis Diderot, Paris, 1999.

[183] C.-W. Park and G. M. Homsy. Two-phase displacement in Hele-Shaw cells: theory. *J. Fluid Mech.*, 139:291–308, 1984.

[184] D. A. Reinelt. The effect of thin film variations and transverse curvature on the shape of fingers in a Hele-Shaw cell. *Phys. Fluids*, 30(9):2617–2623, 1987.

[185] P. N. Vabischevich. *Numerical Methods of Solution of Free-boundary Problems*. MGU Press, Moscow, 1987. In Russian. [Вабищевич П. Н. Численные методы решения задач со свободной границей. – М.: Изд-во МГУ, 1987].

[186] T. C. Halsey. Diffusion-limited aggregation: A model for pattern formation. *Phys. Today*, 53(11):36–42, 2000. Full text is available as: <www.aip.org/pt/vol-53/iss-11/p36.html>.

[187] L. Pietronero and E. Tosatti, editors. *Fractals in Physics*. Proceedings of the Sixth Trieste International Symposium, 9–12 July 1985. North-Holland, Amsterdam, 1986.

[188] L. Paterson. Diffusion-limited aggregation and two-fluid displacements in porous media. *Phys. Rev. Lett.*, 52(18):1621–1624, 1984.

[189] S. Liang. Random-walk simulations of flow in Hele-Shaw cells. *Phys. Rev. A*, 33(4):2663–2674, 1986.

[190] A. Arnéodo, Y. Couder, G. Grasseau, V. Hakim, and M. Rabaud. Uncovering the analytical Saffman–Taylor finger in unstable viscous fingering and diffusion-limited aggregation. *Phys. Rev. Lett.*, 63(9):984–987, 1989.

[191] G. Strang and G. J. Fix. *An Analysis of the Finite Element Method*. Prentice-Hall, 1973.

[192] L. V. Kantorovich and V. I. Krylov. *Approximate Methods of Higher Analysis*. Interscience, N. Y., 1958. Translated from the 3rd Russian edition.

[193] N. I. Muskhelishvili. *Singular Integral Equations: Boundary Problems of Function Theory and Their Applications to Mathematical Physics*. Noordhoff, Groningen, 1953. Translated from the 1st Russian edition.

[194] F. D. Gakhov. *Boundary Value Problems*. Pergamon Press, Oxford, 1966. Translated from the 2nd Russian edition.

[195] W. H. Press, S. A. Teukolsky, W. T. Vetterling, , and B. P. Flannery. *Numerical Recipes in C: The Art of Scientific Computing*. Cambridge University Press, Cambridge, 1992. Full text is available as: <lib-www.lanl.gov/numerical/bookcpdf.html>.

[196] A. N. Tikhonov and A. A. Samarski. *Equations of Mathematical Physics*. Nauka, Moscow, 1977. In Russian. [Тихонов А. Н., Самарский А. А. Уравнения математической физики. – М.: Наука, 1977].

[197] N. M. Gunther. *La théorie du potentiel et ses applications aux problèmes fondamentaux de la physique mathématique*. Gauthier-Villars, Paris, 1934. In French.

[198] D. Colton and R. Kress. *Integral Equation Methods in Scattering Theory*. Wiley, N. Y., 1983.

[199] T. A. Cruse and F. J. Rizzo, editors. *Boundary-Integral Equation Method: Computational Applications in Applied Mechanics*. The American Society of Mechanical Engineers, N. Y., 1975.

[200] C. A. Brebbia, J. C. F. Telles, and L. C. Wrobel. *Boundary Element Techniques: Theory and Applications in Engineering*. Springer, Berlin, Heidelberg, 1984.

[201] T. V. Hromadka II and C. Lai. *The Complex Variable Boundary Element Method in Engineering Analysis*. Springer, N. Y., 1987.

[202] J. O. Watson. Boundary elements from 1960 to the present day. *Electronic J. Boundary Elem.*, 1(1):34–46, 2003.

[203] C. Pozrikidis. *Boundary Integral and Singularity Methods for Linearized Viscous Flow*. Cambridge University Press, Cambridge, 1992.

[204] S. M. Belotserkovsky and I. K. Lifanov. *Method of Discrete Vortices*. CRC Press, Boca Raton, Fl., 1992. Paragraphs are cited by the original Russian edition: Белоцерковский С. М., Лифанов И. К. Численные методы в сингулярных интегральных уравнениях (и их применение в аэродинамике, теории упругости, электродинамике). – М.: Наука, 1985.

[205] Boundary element methods in aerodynamics. Lecture course of the Institut für Aerodynamik und Gasdynamik, Universität Stuttgart. <www.iag.uni-stuttgart.de/luftfahrzeugaerodynamik /download/bem/lecture.pdf>.

[206] T. Y. Hou, J. S. Lowengrub, and M. J. Shelley. Boundary integral methods for multicomponent fluids and multiphase materials. *J. Comp. Phys.*, 169:302–362, 2001. Full text is available as: <www.acm.caltech.edu/˜hou/papers/jcpreview.pdf>.

[207] V. L. Danilov. On the motion of the interface of viscous fluids in a narrow gap. *Dokl. Akad. Nauk SSSR*, 137(2):299–302, 1961. In Russian. [Данилов В. Л. О движении границы раздела вязких жидкостей в узкой щели, Доклады АН СССР, т. 137, N2, сс. 299–302 (1961)].

[208] A. Begmatov. *Problems of Non-Stationary Filtration in Domains with Moving Boundary*. Fan, Tashkent, 1991. In Russian. [Бегматов А. Задачи нестационарной фильтрации в областях с подвижной границей. – Ташкент: Фан, 1991].

[209] A. J. DeGregoria and L. W. Schwartz. A boundary-integral method for 2-phase displacement in Hele–Shaw cells. *J. Fluid Mech.*, 164:383–400, 1986.

[210] B. Gustafsson and A. Vasil'ev. Conformal and potential analysis in Hele-Shaw cells, 2004. <docencia.mat.utfsm.cl/∼avassili /BOOK2.pdf>.

[211] K. E. Atkinson. The numerical solution of boundary integral equations. In I. Duff and G. Watson, editors, *The State of the Art in Numerical Analysis*, pages 223–259. Clarendon Press, Oxford, 1997. Full text is available as: <www.math.uiowa.edu/ftp/atkinson/bie_survey.pdf>.

[212] N. N. Lusin. *An Integral and the Trigonometric Series*. GITTL, Moscow, Leningrad, 1951. Edited and commented by N. K. Bari and D. E. Men'shov. In Russian. [Лузин Н. Н. Интеграл и тригонометрический ряд. – М., Л.: ГИТТЛ, 1951].

[213] G. N. Pihteev. *Approximate Methods for Computing the Cauchy-type Integrals of a Special Kind*. Nauka, Novosibirsk, 1982. In Russian. [Пыхтеев Г. Н. Приближенные методы вычисления интегралов типа Коши специального вида. – Новосибирск: Наука, 1982].

[214] D. D. Joseph and J. C. Saut. Short wave instabilities and ill-posed initial value problems. *Theoret. Comp. Fluid Dynamics*, 1:191–227, 1990. Full text is available at [259].

[215] K. I. Babenko. *Fundamentals of Numerical Analysis*. Nauka, Moscow, 1986. In Russian. [Бабенко К. И. Основы численного анализа. – М.: Наука, 1986].

[216] J. T. Beale, T. Y. Hou, and J. S. Lowengrub. Growth rates for the linear motion of fluid interfaces far from equilibrium. *Comm. Pure Appl. Math.*, 46:1269–1301, 1993.

[217] L. M. Milne-Thomson. *Theoretical Hydrodynamics*. Macmillan, London, 4th edition, 1960.

[218] A. I. van de Vooren. A numerical investigation of the rolling-up of vortex sheets. *Proc. Roy. Soc. London Ser. A*, 373:67–91, 1980.

[219] P. Ya. Kochina. *Selected Works: Hydrodynamics and Percolation Theory*. Nauka, Moscow, 1991. In Russian. [Кочина П. Я. Гидродинамика и теория фильтрации: Избранные труды. – М.: Наука, 1991].

[220] G. R. Baker, D. I. Meiron, and S. A. Orszag. Vortex simulations of the Rayleigh–Taylor instability. *Phys. Fluids*, 23:1485–1490, 1980.

[221] G. R. Baker, D. I. Meiron, and S. A. Orszag. Generalized vortex methods for free-surface flow problems. *J. Fluid Mech.*, 123:477–501, 1982.

[222] R. Krasny. A study of singularity formation in a vortex sheet by the point-vortex approximation. *J. Fluid Mech.*, 167:65–93, 1986.

[223] M. J. Shelley. A study of singularity formation in vortex-sheet motion by a spectrally accurate vortex method. *J. Fluid Mech.*, 244:493–526, 1992.

[224] A. Sidi and M. Israeli. Quadrature methods for periodic singular and weakly singular Fredholm integral equations. *J. Sci. Comput.*, 3:201–231, 1988.

[225] J. T. Beale, T. Y. Hou, and J. S. Lowengrub. On the well-posedness of two fluid interfacial flows with surface tension. In R. E. Caflisch and G. C. Papanicolaou, editors, *Singularities in Fluids, Plasmas and Optics*, Nato Adv. Sci. Inst. Ser. A, pages 11–38. Kluwer, Amsterdam, 1993.

[226] D. I. Pullin. Numerical studies of surface-tension effects in nonlinear Kelvin–Helmholtz and Rayleigh–Taylor instabilities. *J. Fluid Mech.*, 119:507–532, 1982.

[227] G. Tryggvason and H. Aref. Numerical experiments on Hele-Shaw flow with a sharp interface. *J. Fluid Mech.*, 136:1–30, 1983.

[228] G. Tryggvason and H. Aref. Finger-interaction mechanisms in stratified Hele-Shaw flow. *J. Fluid Mech.*, 154:287–301, 1985.

[229] A. J. Roberts. A stable and accurate numerical method to calculate the motion of a sharp interface between fluids. *IMA J. Appl. Math.*, 31:13–35, 1983.

[230] T. Y. Hou, J. S. Lowengrub, and M. J. Shelley. Removing the stiffness from interfacial flows with surface tension. *J. Comput. Phys.*, 114(2):312–338, 1997.

[231] G. Baker and A. Nachbin. Stable methods for vortex sheet motion in the presence of surface tension. *SIAM J. Sci. Comput.*, 19(5):1737–1766, 1998.

[232] J. T. Beale, T. Y. Hou, J. S. Lowengrub, and M. J. Shelley. Spatial and temporal stability issues for interfacial flows with surface tension. *Mathematical and Computer Modelling*, 20(10/11):1–27, 1994.

[233] T. Y. Hou. Numerical solutions to free boundary problems. *Acta Numerica*, pages 335–415, 1995.

[234] J. T. Beale, T. Y. Hou, and J. Lowengrub. Convergence of a boundary integral method for water waves. *SIAM J. Numer. Anal.*, 33(5):1797–1843, 1996.

[235] H. D. Ceniceros and T. Y. Hou. Convergence of a non-stiff boundary integral method for interfacial flows with surface tension. *Mathematics of Computation*, 67(221):137–182, 1998. Full text is available as: <www.ams.org/journal-getitem?pii=S0025-5718-98-00911-9>.

[236] E. B. Hansen and H. Rasmussen. A numerical study of unstable Hele-Shaw flow. *Computers & Mathematics With Applications*, 38:217–230, 1999.

[237] D. Kahaner, C. Moler, and S. Nash. *Numerical Methods and Software.* Prentice-Hall, Englewood Cliffs, N. J., 1989.

[238] R. P. Fedorenko. *Introduction to Computational Physics.* MFTI Press, Moscow, 1994. In Russian. [Федоренко Р. П. Введение в вычислительную физику. – М.: Изд-во МФТИ, 1994].

[239] H. Kalis. *Methods of Approximate Solution of Differential Equations [Diferenciālvienādojumu tuvinātās risināšanas metodes].* Zvaigzne, Riga, 1986. In Latvian.

[240] A. Stroud and D. Secrest. *Gaussian Quadrature Formulas.* Prentice-Hall, Englewood Cliffs, N. J., 1966.

[241] G. R. Baker. A test of the method of Fink and Soh for following vortex sheet motion. *J. Fluid Mech.*, 100:209–220, 1980.

[242] G. R. Baker and M. J. Shelley. On the connection between thin vortex layers and vortex sheets. *J. Fluid Mech.*, 215:161–194, 1990.

[243] W. S. Dai and M. J. Shelley. A numerical study of the effect of surface tension and noise on an expanding Hele-Shaw bubble. *Phys. Fluids A*, 5(9):2131–2146, 1993.

[244] J. H. Ahlberg, E. N. Nilson, and J. L. Walsh. *The Theory of Splines and their Applications.* Academic Press, N. Y., 1967.

[245] M. J. Shelley and G. R. Baker. Order-preserving approximations to successive derivatives of periodic functions by iterated splines. *SIAM J. Numer. Anal.*, 25(6):1442–1452, 1988.

[246] L. A. Hageman and D. M. Young. *Applied Iterative Methods.* Academic Press, N. Y., 1981.

[247] I. Driķis. Some aspects of the numerical simulation of the magnetic fluid pattern formation by the boundary integral equation technique. *Magnetohydrodynamics*, 36(1):1–15, 2000.

[248] W. Bright. Digital Mars C and C++ Compilers, 1999–2004. <www.digitalmars.com>.

[249] T. Williams and C. Kelley. GNUPLOT, 1986–1993, 1998, 2004. <www.ucc.ie/gnuplot/>.

[250] E. Meiburg and G. M. Homsy. Nonlinear unstable viscous fingers in Hele-Shaw flows. II: Numerical simulation. *Phys. Fluids*, 31(3):429–439, 1988.

[251] F. Elias, C. Flament, J.-C. Bacri, and S. Neveu. Macro-organized patterns in ferrofluid layer: Experimental studies. *J. Phys. I (France)*, 7:711–728, 1997.

[252] F. Elias, I. Drikis, A. Cebers, C. Flament, and J.-C. Bacri. Undulation instability in two-dimensional foams of magnetic fluid. *Eur. Phys. J. B*, 3:203–209, 1998.

[253] A. Tsebers. Quantitative relationship governing the appearance of and unique features in the magnetic properties of concentrated domain structures of magnetic colloids in plane slots. *Magnetohydrodynamics*, 26(3):309–313, 1990.

[254] A. Cebers. On elastic properties of stripe structures of a magnetic fluid. *Magnetohydrodynamics*, 30(2):148–155, 1994.

[255] A. Cebers. Liquid magnetic stripe patterns and undulation instabilities. *J. Magn. Magn. Mater.*, 149(1–2):93–96, 1995.

[256] A. O. Tsebers and M. M. Maiorov. Comblike instability in thin layers of magnetic fluid. *Magnetohydrodynamics*, 16(2):126–130, 1980.

[257] A. O. Tsebers. Nature of comb instability. *Magnetohydrodynamics*, 16(3):236–239, 1980.

[258] Institute of Physics, University of Latvia. *Proceedings of the Workshop "Magnetic Forces in Nano- and Biotechnologies"*, Riga, Latvia, September 2004.

[259] D. D. Joseph. Online archive of publications: <www.aem.umn.edu /people/faculty/joseph/archive/life.html>.

[260] *Proceedings of the Fourth International* Pamir *Conference on Magnetohydrodynamics at Dawn of Third Millennium*, volume 2, Presqu'île de Giens, France, September 2000.

ABSTRACT

The dissertation treats analytically and numerically the instabilities exhibited by magnetic fluids in a Hele-Shaw cell under a uniform magnetic field. Considered are both two immiscible magnetic fluids whose interface is a well-defined planar curve and a single fluid with an inhomogeneous gap-averaged concentration of magnetic particles (or a diffused interface between miscible ferrofluids). The inhomogeneous demagnetizing field of a ferrofluid sample excites a two-dimensional convection or modifies the existing flow. In the first part, we undertake a detailed linear stability analysis in the miscible case for selected concentration distributions along the cell. The results apply also to the periodical grating induced in the forced Rayleigh scattering experiments. We demonstrate that the Brinkman equation better describes the viscous dissipation in a Hele-Shaw flow than the conventional Darcy law. We find that viscosity, and not diffusion, renders the length scale of the flow comparable to the cell thickness at strong forcing. In the second half of our study, we model the non-linear dynamics of an immiscible interface between ferrofluids by a boundary-integral method. We describe the modification of the Saffman–Taylor finger by the magnetostatic force. We also obtain "dendritic" structures close to those observed experimentally and analyze some aspects of pattern formation.

KEYWORDS: Ferrofluid – Stability analysis – Mixing – Convection–diffusion – Viscous fingering – Boundary integral equations

RÉSUMÉ

Ce manuscrit décrit analytiquement et numériquement les instabilités d'un fluide magnétique dans une cellule de Hele-Shaw. On considère l'interface entre un fluide magnétique et un autre fluide non magnétique, miscible ou non, soumise à un champ magnétique homogène normal à la cellule ou à l'interface. Le champ démagnétisant est inhomogène à cette interface et génère un mouvement convectif des fluides. Dans la première partie, nous avons utilisé une analyse linéaire de stabilité entre deux liquides miscibles pour une distribution donnée de concentration à l'interface. Les résultats s'appliquent aussi à la stabilité d'un réseau de concentration induit par une expérience de Rayleigh forcé. Nous avons démontré que l'équation de Brinkman décrit mieux la dissipation visqueuse dans une cellule de Hele-Shaw que celle de Darcy. Nous avons trouvé que la viscosité (et non la diffusion massique) donnait à l'écoulement une échelle de longueur de l'ordre de l'épaisseur de la cellule dans le cas des forçages élevés. Dans la seconde partie de notre étude, nous avons modélisé la dynamique non linéaire de l'interface avec une tension superficielle par la méthode des équations intégrales de frontière. Nous avons décrit la modification des doigts de Saffman–Taylor par les forces magnétostatiques. Nous avons obtenu des structures dendritiques proches de celles observées expérimentalement et analysé quelques aspects de la formation des motifs.

MOTS CLÉS: Liquide magnétique – Analyse de stabilité – Mélange – Convection–diffusion – Digitation visqueuse – Équations intégrales de frontière

KOPSAVILKUMS

Disertācijā analītiski un skaitliski tiek analizētas magnētisko šķidrumu nestabilitātes Hele-Šou slānītī homogenā magnētiskā laukā. Aplūkots kā divu nesamaisošos magnētisku šķidrumu gadījums, robeža starp kuriem ir gluda plakana līkne, gan šķidruma gadījums ar nehomogenu pa slāņīša biezumu vidējoto magnētisku daļiņu koncentrāciju. Lielu koncentrācijas gradientu gadījumā pēdējo situāciju var aprakstīt ar asu robežvirsmu starp diviem samaisošiem feroškidrumiem. Feroškidruma atmagnetizējošā lauka nehomogenitāte izsauc divdimensionālu konvekciju vai modificē esošo plūsmu. Disertācijas pirmajā daļā veikta izsmeļoša lineārās stabilitātes analīze samaisošos šķidrumu gadījumā izvēlētiem koncentrācijas sadalījumiem Hele-Šou slāņīša plaknē. Rezultāti piemēroti arī periodiskam koncentrācijas sadalījumam, kurš tiek radīts uzspiestās Releja izkliedes eksperimentos. Mēs parādam, ka Brinkmana vienādojums labāk apraksta viskozo disipāciju Hele-Šou plūsmās nekā tradicionāli apskatītais Darsī likums. Tika atrasts, ka viskozitāte (bet ne difūzija) nosaka plūsmas telpisko mērogu, kurš stipru iedarbību gadījumā ir samērojams ar slāņīša biezumu. Darba otrajā daļā ar robežintegrālvienādojumu metodi tiek modelēta nesamaisošos feroškidrumu robežas nelineārā dinamika. Tiek aprakstītas Safmena–Teilora pirkstu izmaiņas, ko izsauc magnetostatiskie spēki. Mēs iegūstam arī dendrīttipa struktūras, kuras ir tuvas eksperimentos novērojamām un analizējam dažus struktūru veidošanās aspektus.

ATSLĒGAS VĀRDI: Feroškidrums – Stabilitātes analīze – Samaisīšanās – Konvekcija–difūzija – Viskozā pirkstu veidošanās – Robežintegrālvienādojumi